UNIVERSITAT DE BARCELONA

Study of the Secundary Neurulation in the chick embryo, a model to understand neural tube defects

Estudio de la neurulación secundaria en el embrión del pollo, un modelo para entender los defectos del tubo neural

Elena González Gobartt

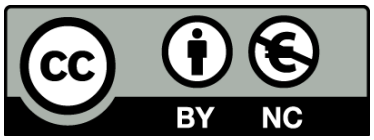

PhD Thesis

Study of the Secondary Neurulation in the chick embryo, a model to understand neural tube defects

Elena González Gobartt

Barcelona, 2019

Programa de doctorado en Biomedicina

Facultad de Biología

Universidad de Barcelona

TESIS DOCTORAL

Study of the Secondary Neurulation in the chick embryo, a model to understand neural tube defects

Estudio de la neurulación secundaria en el embrión de pollo, un modelo para entender los defectos del tubo neural

Memoria presentada por

Elena González Gobartt

Para optar al grado de

Doctora por la Universidad de Barcelona

Esta Tesis Doctoral ha sido realizada en el Departamento de Biología del Desarrollo del Instituto de Biología Molecular de Barcelona (IBMB), perteneciente al Consejo Superior de Investigaciones Científicas (CSIC), bajo la dirección de la Dra. Elisa Martí Gorostiza.

Doctoranda	Directora	Tutora
Elena González Gobartt	Elisa Martí Gorostiza	Marta Pascual Sánchez

Barcelona, Septiembre 2019

A mis padres y a Fer

"*It is not birth, marriage, or death,*
but gastrulation [and neurulation], *which is*
truly the most important time in your life."

Lewis Wolpert

ACKNOWLEDGEMENTS

Han sido muchas las personas con las que me he cruzado durante estos años de tesis y que me han ayudado a elaborarla. Cada una de ellas ha contribuido en mayor o menor medida, pero todas han sido imprescindibles para que hoy esta tesis sea una realidad. Y con ello no solo me refiero a las personas directamente involucradas en el trabajo de laboratorio, sino también a familiares y amigos que me han ayudado, con su apoyo y amistad, a seguir adelante. Sin duda recordaré esta época con nostalgia, y eso es sobre todo por las personas que me han rodeado.

En primer lugar, quiero dar las gracias a mi directora de tesis Elisa. Gracias por haberme permitido realizar la tesis en su laboratorio y por haber sido tan buena jefa durante todos estos años. Le agradezco mucho la confianza depositada en mí y en mi trabajo, la libertad que me ha brindado para pensar por mí misma y por haberme transmitido su pasión por la ciencia. Gracias también por haberme hecho crecer, que 5 años no son pocos, no sólo como científica sino también como persona.

A mis compañeros y excompañeros de laboratorio con los que hemos compartido y disfrutado mucho de este camino. De todos y cada uno he aprendido algo que me llevaré conmigo allá donde vaya. Gracias por iniciarme en la tradición del vermú, que ahora ya tengo más que dominada, por todas las escapadas a la montaña, por el rafting, el kayak y la vía ferrata, por la única calçotada rodeados de pajarillos en jaulas, por ser grandes compañeros de congresos, tanto en las sesiones diurnas como en las nocturnas, y, sobre todo, por ser tan buenos amigos.

A Ireni, mi jefecita, por su paciencia al principio, por enseñarme casi todo lo que sé, y por haberse convertido en mi mentora y en una gran amiga. Juntas hacíamos un equipo increíble. Superamos todas las adversidades, adaptándonos a cada rato a ser científicas, cuidadoras de peces, fontaneras en inundaciones, e incluso psicoterapeutas, y todo ello siempre acompañado de risas sin fin (a veces por no llorar). No sabes cuánto te he echado de menos estos últimos años.

A Gwen, por toda su ayuda en los momentos en los que he estado estancada, por sus grandes ideas, por siempre ver nuevas vías por dónde tirar y por empujarme a seguir en los momentos más duros. No puedo sentir nada más que admiración por él. También por su mente enciclopédica, que recuerda todas las herramientas del laboratorio y que me llevó a hacer arqueología y al fin usarlas. Gracias también por enseñarme a decir "no", algo que aún quizás no tenga del todo aprendido, pero sí presente.

A Mumi le agradezco todo lo que aprendí durante los años en que trabajamos mano a mano: su ojo crítico, su gran capacidad de improvisar y de dar nuevas vueltas de tuerca, y por siempre ver la parte positiva cuando las cosas no salen. Y también por su gran capacidad de relativizar los problemas, algo que nos contagia a todos.

A Luci, mi verdadera compañera de tesis, juntas de principio a fin. Le agradezco el estar siempre disponible para ayudar o enseñar o trastear con los pollitos. También por su apoyo incondicional, todos los buenos y malos momentos compartidos en esta etapa y el hecho de que sea tan buena amiga. No soy capaz de imaginar nadie mejor con quién haber compartido esta experiencia.

A Jose, mi pupilo (ojalá), por ser mi gran apoyo estos últimos años. Desde que ocupó el sitio a mi izquierda los días se me han pasado volando. Gracias por su paciencia infinita, por escucharme siempre y por ponerme los pies en la tierra en mis momentos de drama. Gracias por las bromas, las risas y las

apuestas absurdas con premios absurdos. Y también por no haber usado demasiado el bate que Gwen le regaló.

A Sus, por el gran trabajo que hace cada día y que, aunque quizás no sea tan visible, todos sabemos que el laboratorio se derrumba sin ella. Por ser la mejor técnica del mundo, por su asistencia con las infinitas in situs, con las maxis y los buffers, y por siempre encontrar aquel reactivo olvidado al fondo de aquel tercer cajón de reserva que ninguno de nosotros consiguió encontrar. Por siempre estar ahí con todo y para todo, y siempre con una gran sonrisa.

A todas las personas con las que he coincidido durante mi tesis y que se fueron dejando una gran huella. A Juanito, no solo por su asistencia técnica sino también por la alegría del sur que traías cada día al laboratorio. A Rene, por su gran capacidad como científico, que confío está explotando al máximo en Méjico, y porque sé que siempre tendré un gran amigo esperándome en el DF con los brazos abiertos. A Angie, por sus regresos fugaces al labo que nos daban el chute de energía que tanto necesitábamos. A los estudiantes de máster y carrera con los que coincidí, a Alberto, Carla, Sara, Nere, Marta y Marc, gracias por el soplo de aire fresco.

A todo el laboratorio de Mariona Arbonés. Gracias MariaJo, Isa, Sonia, Juan y Álex, y también a Toni, Blanca y Andrea del laboratorio de Sebastián Pons, por todos esos seminarios compartidos en los que siempre intentaron ayudarme y aportar ideas, contagiándome de su entusiasmo y positivismo. En especial gracias a Isa por ser el conejillo de indias y resolver rápidamente todas mis dudas en la etapa más final.

A Marian Martínez y a todas sus chicas, Raquel, Ale, Stella, Simona y Marta, por su gran compañía, ha sido un placer compartir espacio (y el bodorrio en Grecia) con ellas.

To Bertrand Bénazéraf and his entire lab. I am deeply grateful for offering me the opportunity of joining you in Toulouse and of performing the *in vivo* time-lapse experiments, which I believe are key for this work. Thanks for the time invested on me, not only on my learning but also, together with Dani, on advising me about the uncertain future and for motivating me. Thanks to Guillame Allio for his invaluable assistance in the image processing. Thanks also to all the people in the CBD Toulouse for the welcoming and stimulating work environment they create every day.

A Fernando Martín-Belmonte y a María Delgado, por las alentadoras discusiones, por las ideas aportadas y por abrirme nuevas perspectivas. Gracias también por aquel congreso en Sant Feliu de Guíxols en el que pude aprender de los mejores en el campo de la polaridad celular y del que disfruté muchísimo.

A Elena Rebollo y a Jaume, por poner tanto esfuerzo en que todo funcione como la seda en la Facility de Microscopía y resolver mis problemas técnicos con gran paciencia. Y gracias a todas aquellas personas que me han facilitado material o me han ayudado con algún aparato como Olivier Rosnet, Anghara o Toni P.

Gracias también a Uri y a Ale T. por su gran ayuda en la maquetación de esta tesis. Y a Ale G., por el diseño de la portada.

A los chicos del máster, Ruth, Miriam, Stella, Arnau, Adri y Yari, por la compañía, las ganas, la fuerza y el ánimo compartido durante todo este proceso. Ha sido genial conseguirlo a vuestro lado y a la vez.

A todas las bailarinas de Bollywood, Dancehall, y Afrobeatz que me han acompañado en los momentos en que mi mente y mi cuerpo necesitaban respirar. En especial, gràcies a la Raquel i a la Gemma, qui hagués dit que una dansa tan llunyana ens faria tan properes.

A l'Alba, per aquella nota d'ànims i força sobre la taula, en el moment més oportú, que ho reflexa tot.

A las Homies, por hacer del pisito de Notariat el hogar más acogedor durante mis años de tesis. Gracias por las confidencias, las risas, los baños de realidad y los consejos. A Marina y a Ale, por tratarme desde el principio como una más, como si nos conociésemos desde hace años, y por acabar compartiendo una maravillosa amistad. A Bárbara, si alguien me ha acompañado durante toda la tesis sin duda ha sido ella. Me alegro de haber pasado aquel año entre soporíferas películas mudas y largometrajes de Wong Kar Wai solamente por haberla conocido. Por ser como mi hermana, nunca me cansaré de vivir juntas. Gracias también a los Homies y a las nuevas incorporaciones de Notariat, Armand y Macari, por la compañía y el ánimo en los descansos de la biblioteca, y por vigilar que mis siestas no fuesen nunca demasiado largas.

A mis niñas, Nuna, Vallbo, Torre, Blanes, Mery, Cortins y Moni. Gracias por estar ahí desde siempre, por apoyarme en todo el proceso de la tesis, por escucharme e intentar comprender los líos de la ciencia, y por ser las mejores amigas del mundo.

A en Joan, per haver estat aquest últim any incondicionalment fent-me costat. Per haver-me comprès, per cuidar-me tant i per intentar sempre treure'm un somriure. Gràcies per viure intensament i contagiar-m'ho, i gràcies per la muntanya russa de la que no em vull baixar.

Por último, gracias a mi familia. A mis tías, tío y primos. A mis abuelos, sé que estaríais muy orgullosos de mí. Pero sobre todo gracias a mis padres y a Fer. Por el apoyo constante, por dármelo todo, por aconsejarme y porque espero que algún día estéis tan orgullosos de mí como yo lo estoy de teneros. No hay nada mejor que la familia unida. Esto os lo debo y os lo dedico a vosotros.

INDEX

SUMMARY

Body axis elongation is a hallmark of the vertebrate embryo, which also comprises the morphogenesis of the caudal neural tube (NT). The contribution of bipotential neuromesodermal progenitors (NMPs) to the cranio-caudal elongation of the embryo is beginning to be understood. However, the signalling pathways and tissue remodelling events required for shaping the caudal NT from NMPs remain largely unknown, even though the failure in this process generates caudal neural tube defects (NTDs). The caudal NT in amniote embryos forms by a process termed secondary neurulation (SN). SN shapes a secondary neural tube (SNT) through the lineage restriction and the mesenchymal-to-epithelial transition (MET) of NMPs into neural progenitor cells (NPCs), and the concomitant opening of a lumen *de novo* in the centre of the tissue. In human embryos, the development of the lumbar, sacral, coccygeal and equinal cord largely involves SN. The limited availability of human tissue to perform histological analyses at different developmental stages reinforces the need to use animal models to understand the events shaping the SNT, particularly since NTDs rank among the most common categories of birth defects, affecting 1 in every 1000 established pregnancies worldwide.

Here, we combine the genetic manipulation of the chick embryo with an *in vivo* imaging technique to decipher the cellular events driving SNT formation and to demonstrate that TGF-β/SMAD3 signalling is required for proper SN, since its inhibition results in NTDs with multiple lumens. Our analysis demonstrates that the lineage restriction and the MET of Sox2+ T/Bra+ mesenchymal NMPs into Sox2+ T/Bra- epithelial neural progenitor cells (NPCs) are independent of SMAD3 activity. In the developing SNT, both the neural restriction and the MET tightly associate to the growing basement membrane (BM), which assembles in a dorso-ventral fashion. Hence, the first cells to adopt a neural identity and to undergo MET are those contacting the BM, located in the dorsal periphery of the medullary cord. On the contrary, centrally located cells remain mesenchymal, even to the very end of the process. It is between these two cell populations that small cavities of varied size and shape form, always at a one-cell distance from the BM, being SMAD3 also dispensable for lumen initiation.

We found that the resolution of a single, centrally positioned continuous lumen in the SNT takes place through the intercalation of central cells, rather than through their programmed cell death. Indeed, results show an important novel activity for TGF-β/SMAD3 in the intercalation of central cells during lumen resolution. Notably, cell intercalation is always preceded by a cell division, either a symmetric II, which generates two intercalating daughter cells, or an asymmetric IC, which generates one intercalating and one central daughter cell. These two modes of division associate to different cranio-caudal levels, with II occurring cranially to IC. In addition, a third mode of division, the symmetric CC division, occurs in the caudal tail bud in order to generate two central mesenchymal NMPs and to expand the progenitor pool driving body axis elongation. Finally, we found lengthened primary cilia in sh-SMAD3 electoporated NPCs, a ciliopathy that might compromise the sensory functions of this organelle and ultimately contribute to the failure in central cell intercalation. Altogether, here we describe the cellular events driving SNT formation in the chick embryo and found a TGF-β/SMAD3-associated NTD. We anticipate our findings to be relevant to understand human SN and the embryonic origin of closed NTDs.

RESUMEN

El alargamiento del eje del cuerpo es un sello distintivo del embrión de vertebrados. Los progenitores neuro-mesodérmicos (NMPs) llevan a cabo este proceso, incluyendo la morfogénesis del tubo neural caudal. En amniotas, éste se forma por el proceso conocido como neurulación secundaria (SN). El papel de los NMPs en el alargamiento del eje cráneo-caudal se conoce en mayor medida. Sin embargo, las vías de señalización y los eventos celulares que conforman el tubo neural secundario (SNT) se mantienen ampliamente desconocidos, aun cuando fallos en la SN producen defectos de tubo neural (NTDs).

Aquí combinamos la manipulación genética del embrión de pollo con técnicas de imagen *in vivo* para descifrar los eventos celulares que conducen la formación del SNT y demostrar también que la vía de señalización TGF-β/SMAD3 juega un papel muy importante en este proceso. Así, si ésta es inhibida durante el desarrollo del SNT se generan NTDs caracterizados por la presencia de múltiples lúmenes. Nuestro análisis demuestra que los eventos iniciales de la SN como la restricción de los NMPs en células progenitoras neurales (NPCs) y la subsecuente transición mesénquima-epitelio (MET) son independientes de la actividad de TGF-β/SMAD3. No obstante, la resolución de un único lumen central, posible gracias a la intercalación de las células centrales, requiere la actividad de TGF-β/SMAD3. Por todo ello, creemos que los hallazgos aquí presentados son relevantes para entender el proceso de SN en humano y así desentrañar el origen embrionario de los NTDs.

LIST OF ABBREVIATIONS

AJ	Adherens Junction
AJC	Apical Junctional Complex
aPKC	Atypical Protein Kinase C
BF	Bright-Field
BM	Basement Membrane
BMP	Bone Morphogenetic Protein
BRE	BMP Responsive Element
BSA	Bovine Serum Albumen
CC	Central Central [mode of division]
cCasp3	Cleaved-Caspase 3
CDC	Central Daughter Cell
Cdc42	Cell division control protein 42 homolog
CLE	Caudal Lateral Epiblast
CNH	Chordo-neural Hinge
CNS	Central Nervous System
CS	Carnegie Stage
DLHP	Dorso-Lateral Hinge Point
DLL1	Delta Like canonical Notch Ligand 1
DNA	Deoxyribonucleic Acid
E	Embryonic day
ECM	Extracellular Matrix
EGFP	Enhanced Green Fluorescent Protein
EMT	Epithelial-to-Mesenchymal Transition
EP	Electroporation
FGF	Fibroblast Growth Factor
FOP	FGFR1OP; FGFR1 Oncogene Partner
GDF	Growth Differentiation Factor
GFP	Green Fluorescent Protein
GTP	Guanosine Triphosphate
H2B	Histone H2B
HH	Hamburger and Hamilton stage
hpe	Hours post-electroporation
IC	Intercalating Central [mode of division]
IDC	Intercalating Daughter Cell
IFT	Intraflagellar Transport
II	Intercalating Intercalating [mode of division]
INM	Interkinetic Nuclear Migration
IQR	Interquartile Range

LR	Lumen Resolution
MDCK	Madin-Darby Canine Kidney cells
MET	Mesenchymal-to-Epithelial Transition
MHP	Median Hinge Point
min	minutes
mRNA	Messenger Ribonucleic Acid
ms	milliseconds
MTOC	Microtubule-Organizing Centre
N	Node
NC	Notochord
NMPs	Neuromesodermal Progenitors
NPCs	Neural Progenitor Cells
NSB	Node-Streak Border
NT	Neural Tube
NTDs	Neural Tube Defects
P/S	Penicillin/Streptomycin
PAR	Partitioning Defective
PBS	Phosphate Buffered Saline
PBT	PBS Triton
PCIG	pCAGGS:_ires_GFP
PCM	Pericentriolar material
PCP	Planar Cell Polarity Pathway
PCR	Polymerase Chain Reaction
PFA	Paraformaldehyde
pH3	Phosphorylated-Histone 3
PN	Primary Neurulation
PNT	Pre-Neural Tube [cells]
pre-SN	Pre-Secondary Neurulation [region]
PS	Primitive Streak
PSNT	Pre-Secondary Neural Tube [cells]
RA	Retinoic Acid
Rac1	Ras-related C3 botulinum toxin substrate 1
RFP	Red Fluorescent Protein
R-SMAD	Receptor-regulated SMAD
RT	Room Temperature
S	Somites
S1	SMAD1
S2	SMAD2
S3	SMAD3
S4	SMAD4
S5	SMAD5

SD	Standard Deviation
sem	Standard Error of the Mean
SHH	Sonic Hedgehog
sh-RNA	Short hairpin Ribonucleic Acid
SMAD	Similar to Mothers Against Decapentaplegic
SN	Secondary Neurulation
SNT	Secondary Neural Tube
Sox2	Sex determining Region Y-box 2
T/Bra	T/Brachyury
TB	Tail bud
TBM	Tail bud Mesoderm
TGF-β	Transforming Growth Factor Beta
TJ	Tight junction
TRITC	Tetramethylrhodamine
TZ	Transition Zone
WNT	Wingless
WT	Wild-type
ZO-1	Zonula Occludens-1

INTRODUCTION

Neurulation shapes the Neural Tube

Neurulation is the term that defines the set of dynamic morphogenetic events occurring in the embryo that shape the neural tube (NT). The NT is the embryonic primordium of the brain and spinal cord and forms by two different modes, termed primary and secondary neurulation (Harrington et al., 2009; Lowery and Sive, 2004) (Fig. 1). The mode of neurulation depends on the organism and, in some species, on the cranio-caudal axis level of the embryo. In amniote embryos, the future brain and cranial spinal cord form by primary neurulation (PN), while caudal regions of the NT develop by secondary neurulation (SN). During PN, a flat sheet o f epithelial cells, the embryonic neural plate, invaginates and the bilateral neural folds elevate and fuse with each other to form a hollow NT (Fig. 1A) (Colas and Schoenwolf, 2001; Nikolopoulou et al., 2017; Smith and Schoenwolf, 1987). On the other hand, SN starts when mesenchymal cells undergo mesenchymal-to-epithelial transition (MET) and open a lumen in the centre (Fig. 1B) (Criley, 1969; Griffith et al., 1992). Despite of the striking differences between PN and SN, both mechanisms lead to the same product: a hollow NT.

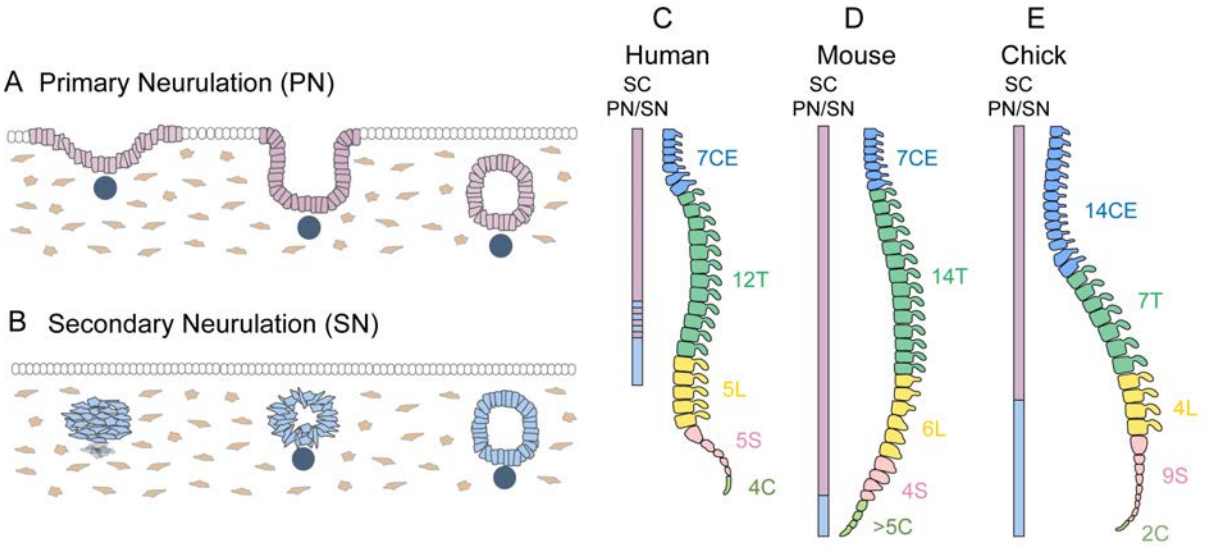

Figure 1. Amniote embryos undergo two modes of neurulation. (A-B) Schematic representations of primary (PN) and secondary neurulation (SN). During PN, the epithelial neural plate (purple) invaginates to form a hollow neural tube (NT). During SN, a mesenchymal mass of cells condense (light blue), apico-basally polarise and open a lumen in the centre to form a hollow secondary neural tube (SNT). The surrounding mesoderm is shown in brown and the notochord appears in dark blue. **(C-E)** Topological correspondence between the different categories of vertebrae, the spinal cord (SC) and the regions of primary and secondary neurulation (PN, purple; SN, light blue) in human, mouse and chick. The change from purple to blue represents the location of the caudal neuropore. In human embryos, the SC does not extend to the spine end and the exact position of the caudal neuropore is still under debate (dotted lines). CE, cervical; T, thoracic; L, lumbar; S, sacral; and C, caudal vertebrae. PN, primary neurulation; SN, secondary neurulation; SC, spinal cord. Adapted from (Dady et al., 2014).

The precise position of the caudal neuropore, the place where primary and secondary NTs fuse, is variable in different organisms (Fig. 1C-E). In human embryos, the junction of the primary and secondary NTs is apposed at the lumbosacral level, therefore development of the lumbar, sacral, coccygeal and equinal cord, largely involves secondary neurulation (O'Rahilly and Muller, 1994;

O'Rahilly and Muller, 2002; Saitsu and Shiota, 2008; Saitsu et al., 2004) (Fig. 1C). Likewise, the caudal neuropore locates at the level of the somite 27 in chick and quail embryos, which corresponds to the transition from the thoracic to the lumbosacral vertebrae (Catala et al., 1995; Criley, 1969; Dady et al., 2014; Le Douarin et al., 1998)(Fig. 1E). On the contrary, SN only occurs at the level of the tail in mouse embryos, starting at somites 32-34 (Nievelstein et al., 1993; Schoenwolf, 1984; Shum et al., 2010) (Fig. 1D).

The morphogenetic events and gene regulatory networks governing PN are beginning to be understood. However, knowledge about SN is still very fragmentary. As will be discussed in following sections, abnormalities in any of these processes can lead to neural tube defects (NTDs) with devastating effects on nervous system function (Greene and Copp, 2014). Classically, open NTDs are attributed to the failure of NT closure during PN, whereas closed NTDs concern mostly the lower trunk issued from SN. Although NTDs rank among the most common categories of birth defects, affecting an average of 1 in every 1000 established pregnancies worldwide (Morris et al., 2016), the exact cellular and molecular events at their origin remain largely unknown.

Primary neurulation shapes the cranial Neural Tube

Primary neurulation (PN) initiates from a pre-existing sheet of epithelial cells, which folds, rolls or bends into a tube. The term "primary neurulation" refers to the "primary body development", as the tissues involved descend from the three germ layers of the early embryo (Holmdahl, 1925). This process has been carefully studied in several vertebrate species (Davidson and Keller, 1999; Morriss-Kay et al., 1994; Peeters et al., 1998; Smith and Schoenwolf, 1991) and even though some variations are found, the basic steps of PN are mostly conserved. Briefly, PN consists on the following steps: i. the formation and shaping of the neural plate; ii. bending of the neural plate and formation of the neural groove; and iii. the final closure of the neural groove to form the NT (Smith and Schoenwolf, 1997).

Neural plate formation and shaping

During early embryonic development, three germ layers (ectoderm, mesoderm, and endoderm) arise from the blastula through the process of gastrulation (Fig. 2). The blastula of non-rodent amniotes forms a flat blastoderm consisting of two epithelial cell layers (the epiblast and the hypoblast) with a space in between (the blastocoel) (Eyal-Giladi and Kochav, 1976; Kochav et al., 1980). The embryo comes entirely from the epiblast, as the hypoblast only contributes to external membranes. At the onset of gastrulation, a groove forms along the midline of the epiblast (the primitive streak, PS) and an enlarged group of cells grows in its cranial portion (the Hensen's node or organizer). Both structures act together to establish the embryo's bilateral symmetry, to define the cranio-caudal axis and to organize gastrulation (Downs, 2009; Mikawa et al., 2004). As a result, epiblast cells move towards the PS, ventrally ingress and bilaterally migrate to generate the endodermal and mesodermal germ layers. The remaining non-ingressing epiblast cells differentiate into the ectodermal layer (Mikawa et al., 2004).

Three sets of cells are then induced in the ectodermal layer and will become separated during PN: the neural plate, the neural crest and the epidermis (Fig. 3A). The process of PN starts when the underlying dorsal mesoderm signals the ectodermal cells above it to elongate into columnar neural plate cells (Keller et al., 1992; Smith and Schoenwolf, 1989). Thus, the neural plate emerges as an epithelial

sheet of cells, which then undergoes convergent extension, leading to its medio-lateral narrowing and rostro-caudal lengthening, so that subsequent bending will form a tube instead of a sphere (Keller et al., 2008).

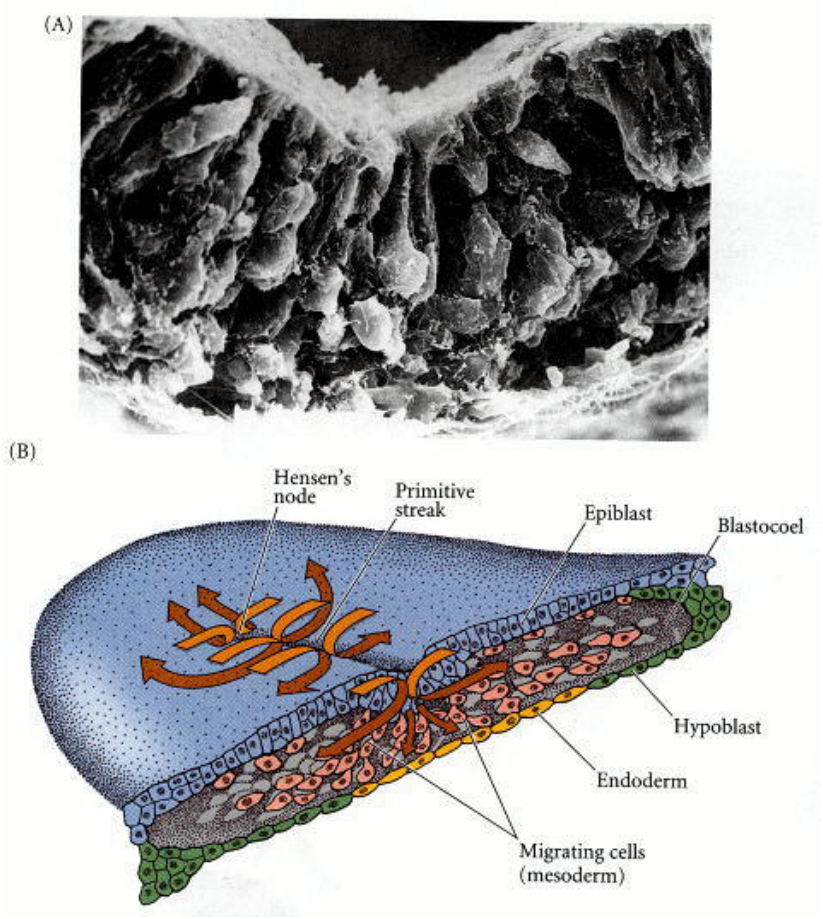

Figure 2. Gastrulation in the chick embryo. (A) Scanning electron micrograph showing epiblast cells ingressing into the blastocoel. **(B)** Scheme of a gastrulating chick embryo. The midline of the epiblast (blue) thickens and forms the primitive streak (PS) and the Hensen's node to organize gastrulation. Epiblast cells move towards the PS (orange arrows) and ingress to generate the endoderm (yellow) and mesoderm (red). Non-ingressing cells will form the ectoderm. The result of this process is that a three-layered embryo is generated. The hypoblast cells of the original blastoderm (green) become displaced by the endoderm and eventually sort out to contribute to the yolk sac. Image from (Gilbert SF., 2000).

Bending of the neural plate

PN continues with the bending, along the cranio-caudal axis of the embryo, of the neural plate. Neural plate bending creates the neural groove and causes the flanking neural folds to elevate and approach each other in the dorsal midline, where they will later fuse to form the closed NT. The main strategy to bend the neural plate consists in defining the hinge points: regions where neural plate cells become wedge shaped and where the epithelium can bend (Copp et al., 2003; Lowery and Sive, 2004). In general, a median hinge point (MHP) is specified along the ventral midline of the embryo, which buckles the neural plate and elevates the neural folds (Fig. 3A-B). Subsequently, two dorsolateral hinge points (DLHPs) form and push the neural folds together so they can fuse across the dorsal midline

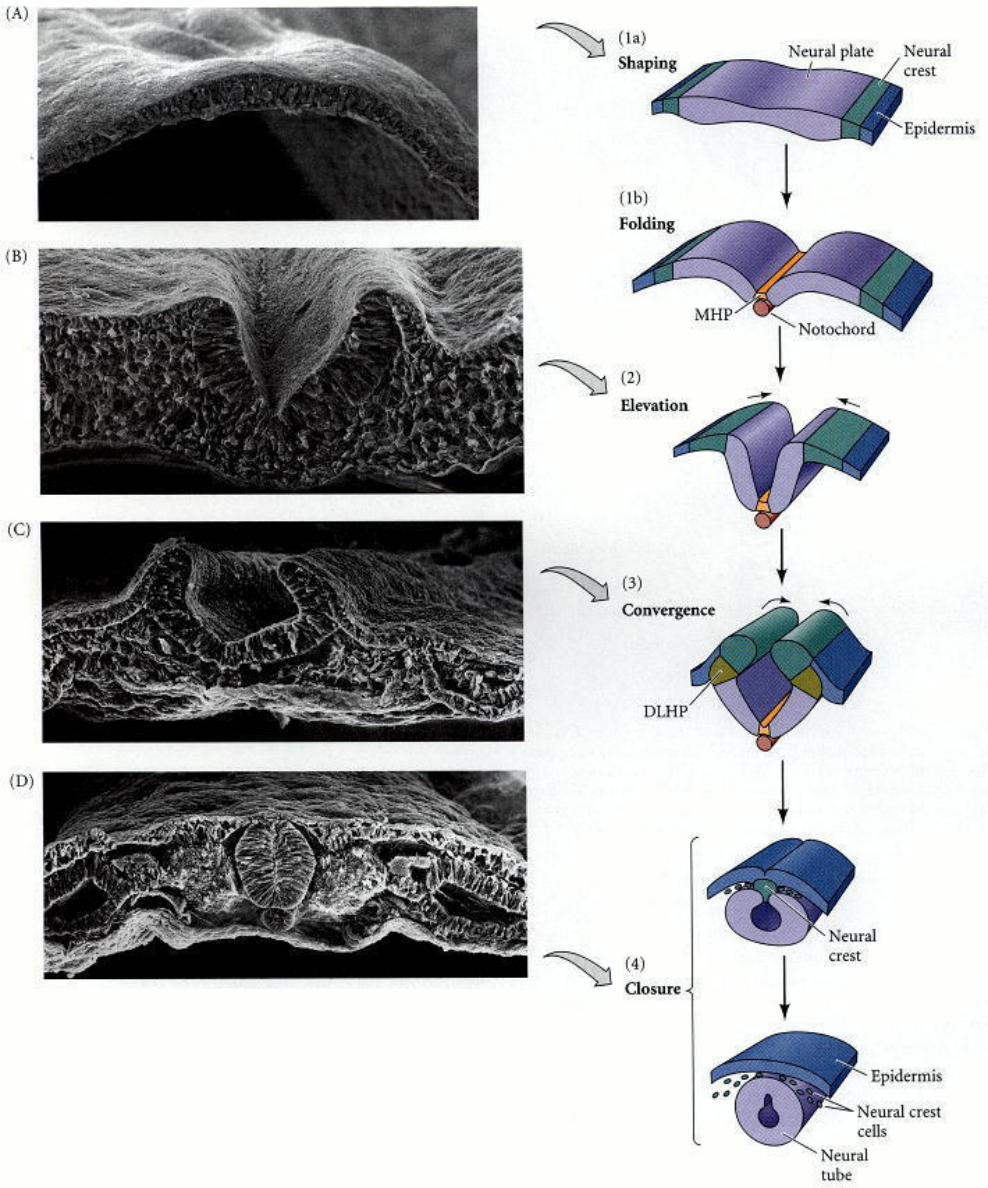

Figure 3. Primary neurulation (PN) in the chick embryo. (A) (A-D, 1-4) Scanning electron micrograph images showing the process of chick PN and associated schemes. **(A, 1)** Three sets of cells are induced in the ectoderm: the neural plate (purple), the neural crest (dark green) and the epidermis (dark blue). The median hinge point (MHP, orange) is then specified and neural plate folding begins. **(B, 2)** The neural folds are elevated and the presumptive epidermis move towards the centre of the tissue (black arrows). **(C,3)** Two paired dorsolateral hinge points (DLHP, light green) bring the neural folds together in the dorsal midline. **(D,4)** The neural folds contact each other and fuse to generate a hollow NT. The neural crest cells disperse. Image from (Gilbert SF., 2000).

(Fig. 3C). However, hinge point number and location differs among species and along the cranio-caudal axis and developmental stage within a single species, and bending can occur without the need of any hinge point, by folding of the entire epithelium (Shum and Copp, 1996; Smith and Schoenwolf, 1991; Ybot-Gonzalez et al., 2002).

MHP cell shape changes are induced by the protein Sonic hedgehog (SHH), secreted from the underlying notochord (Smith and Schoenwolf, 1989); and by antagonistic non-canonical Transforming Growth Factor-beta (TGF-β) and Bone Morphogenetic Protein (BMP) activities (Amarnath and

Agarwala, 2017; Eom et al., 2012; Stottmann et al., 2006). Chick embryos without notochord do not develop MHP cells, and although neural plate bending occurs, the resulting NT has an abnormal morphology (Smith and Schoenwolf, 1989). On the other hand, TGF-β blockade or BMP activation in the ventral midline also disrupt MHP formation, leading to NT closure defects (Amarnath and Agarwala, 2017). Interestingly, the cytosolic interaction of SMAD proteins, the BMP and TGF-β pathway transducers, with proteins of the apico-basal polarity pathway is what modulates TGF-β/BMP-induced MHP cell shape changes.

Dorsal closure of the neural groove

To conclude NT formation, the neural groove must close dorsally (Fig. 3D). The apposed neural folds contact in the dorsal midline via cellular protrusions, adhere and fuse (Pai et al., 2012). Fusion establishes the roof of the NT and separates it from the overlying epidermis. The region between the NT and the epidermal ectoderm originates the neural crest cells, which migrate extensively to generate a wide variety of cell types, such as the entire peripheral nervous system (Huang and Saint-Jeannet, 2004; Mayor and Theveneau, 2013). In the embryo, NT closure initiates at distinct closure points and progresses from them by zipping the open neural groove, in both cranio-caudal and caudo-cranial directions (Cearns et al., 2016). The number and location of closure points and the direction of closure varies among vertebrate species (Copp et al., 2003; Greene and Copp, 2014; Karfunkel, 1974; Nakatsu et al., 2000).

Secondary neurulation shapes the caudal Neural Tube

Although the development of the nervous system is a major area of research, so far the majority of studies have been focused on the primary NT. In contrast, the cellular events and the molecular signals driving the formation of the secondary neural tube (SNT) remain largely unknown. The term "secondary neurulation" refers to the "secondary body development", as the caudal region of the embryo derives from tissue of the undifferentiated tail bud by a process of body axis elongation after more cranial regions have developed (Aires et al., 2018; Bénazéraf and Pourquié, 2013; Griffith et al., 1992; Holmdahl, 1925). The tail bud presents a bipotential population of progenitors that contribute to both neural and mesodermal lineages, termed neuromesodermal progenitors (NMPs) (Henrique et al., 2015; Kimelman, 2016). NMPs at the onset of SN are mesenchymal cells, from which the caudal neuroepithelium will also derive (Duband, 2010). Therefore, in the process of SN there is no structure such as the neural plate from PN. Instead, NMPs condense to form a solid medullary cord, undergo MET and form a single epithelial tube (Catala et al., 1995; Colas and Schoenwolf, 2001; Griffith et al., 1992; Shimokita and Takahashi, 2011).

Notably, the SNT is the first structure that differentiates during secondary body development, even before the notochord (Criley, 1969). The notochord forms slightly later from a ventral mass of densely packed cells, which is continuous with the floor of the forming SNT (Schoenwolf, 1984). This suggests that different developmental pathways must be driving primary and secondary NT formation.

The morphogenesis of the SNT has been investigated in both mouse and human embryos (Nievelstein et al., 1993; O'Rahilly and Muller, 1994; Saitsu et al., 2004; Schoenwolf, 1984), but major conclusions have been drawn from extensive studies in chick (Dady et al., 2014; Schoenwolf and Delongo, 1980; Shimokita and Takahashi, 2011).

Secondary neurulation in human embryos

Contrary to other amniotes, both types of neurulation are observed in parallel in the developing human embryo. PN starts at Carnegie stage 8 (CS8, 18 postovulatory days) and progresses from cranial regions to the caudal neuropore, which closes by 4 weeks of gestation (CS13) (O'Rahilly and Muller, 1994; Saraga-Babic et al., 1995). However, by CS12 (26 postovulatory days), SN has already started caudally (Muller and O'Rahilly, 1987; O'Rahilly and Muller, 2002).

At the level of the caudal neuropore, an overlapping zone exists, where both PN and SN coincide. In this region, tail bud mesenchymal cells are incorporated into the ventral part of the primary NT by MET (Saitsu and Shiota, 2008; Saitsu et al., 2004), an event that has been also observed in developing chick embryos (Dady et al., 2014). Caudally to the overlapping zone, SN occurs as tail bud cells dorsally condense, radially arrange, epithelialize and open multiple cavities (Fig. 4A). Cells located in the centre disappear for cavities to enlarge and coalesce. Finally, SNT formation is completed by CS17-18 (between 5 and 6 weeks of gestation) (Pytel et al., 2007; Yang et al., 2014).

Secondary neurulation in mouse embryos

The caudal neuropore closes in mouse embryos at embryonic day 9.5 (E9.5) (Nievelstein et al., 1993). Contrary to human and chick development, a zone where both PN and SN overlap is absent. In caudal regions, the mouse SNT is directly shaped by two different mechanisms, which associate to the embryo stage (Schoenwolf, 1984).

In early embryos (E9.5-10), the entire mesenchymal region undergoing SN epithelializes and forms the "medullary rosette", where elongated tail bud cells radially arrange around a central small lumen (Fig. 4B). The lumen then expands progressively and the rosette either enlarges by mitosis of the already epithelialized cells or by further recruitment of additional tail bud cells (Schoenwolf, 1984). In older embryos (E11-12), only the dorsal part of the medullary cord initially epithelializes, forming the "medullary plate" (Fig. 4C). Mesenchymal cells are then recruited from the edges of the plate and added to the epithelium to eventually form a tube. In both processes, the incipient secondary lumen appears concomitant with the formation of apical intercellular junctions.

Secondary neurulation in chick embryos

In chick embryos, the caudal neuropore closes at Hamburger and Hamilton stage 12 (HH12) (Costanzo et al., 1982; Hamburger and Hamilton, 1992). At the level of the caudal neuropore, there is an overlapping zone where PN occurs dorsally and SN ventrally (Dady et al., 2014), as observed in human embryos. Within this transitional zone, the NT forms progressively less by PN and increasingly more by SN, craniocaudally. Finally, from the 27th somite onwards, the NT completely derives from SN (Le Douarin et al., 1998; Shimokita and Takahashi, 2011).

Current knowledge of amniote SN mostly comes from research performed in chick embryos. Initial studies provided histological observations of the process (Criley, 1969; Hughes and Freeman, 1974; Jelinek et al., 1969; Klika and Jelinek, 1969), but they give little insight into how SN occurs, mainly due to the poor resolution of the techniques used at the time. Later in the 80's, Schoenwolf and colleagues extended previous observations using scanning and transmission electron microscopy as well as light microscopy of plastic sections (Schoenwolf and Delongo, 1980; Schoenwolf and Kelley, 1980). All these investigations contributed to the establishment of four basic morphogenetic processes

involved during chick SN: (i) segregation of the prospective medullary cord cells, (ii) formation of the medullary cord and differentiation into peripheral and central cells, (iii) formation of multiple lumens and (iv) lumen coalescence into a single central cavity (Fig. 4D).

Morphogenesis of the SNT in chick embryos starts with the aggregation of mesenchymal NMPs on the midline to form a densely packed cylinder of cells, the medullary cord (Catala et al., 1995; Catala et al., 1996; Schoenwolf and Delongo, 1980; Yang et al., 2003). This first segregation from adjacent tissues occurs in a cranio-caudal fashion and is followed by a process of MET, that involves the

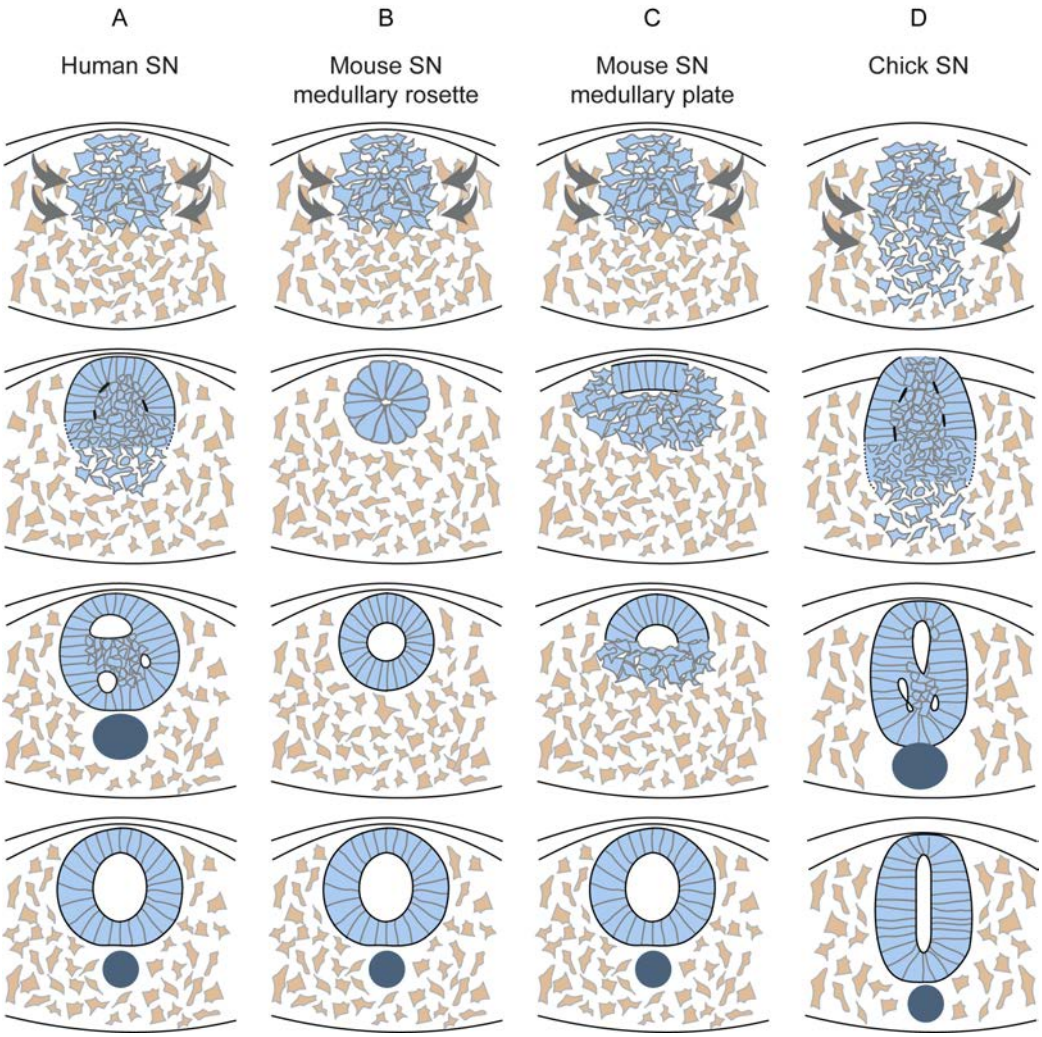

Figure 4. Strategies of amniote secondary neurulation (SN). Schematic representations of human, mouse and chick SN. SN undergoing cells are shown in light blue, the surrounding mesoderm is in brown and the notochord appears in dark blue. **(A)** In human SN, mesenchymal tail bud cells dorsally condense into a solid medullary cord, radially arrange, undergo epithelialization and open multiple lumens. Centrally located cells are cleared from the luminal space and a hollow SNT emerges. Drawings after (Saitsu et al., 2004). **(B-C)** Mouse embryos undergo SN by two different mechanisms. In the medullary rosette mode **(B)**, the whole mass of cells of the medullary cord undergoes MET and opens a lumen in the centre, that later expands. In the medullary plate mode **(C)**, epithelialization first starts in dorsal cells and the epithelium then expands by recruitment of lateral mesenchymal cells. The result of both processes is a hollow SNT. Adapted from (Lowery and Sive, 2004). **(D)** Chick SN begins when mesenchymal tail bud cells condense into the medullary cord, cells located dorsally and in the periphery undergo MET and the epithelialization ventrally propagates. Small lumens open up and then coalesce to form a hollow SNT. Centrally located cells are cleared from the luminal space by unknown mechanisms. Drawings after (Schoenwolf and Delongo, 1980).

formation of a layer of extracellular material between adjacent organ rudiments, intercellular junctions and apico-basal cell polarisation (Schoenwolf and Delongo, 1980; Shimokita and Takahashi, 2011; Yang et al., 2003). The first cord cells to undergo MET are located dorsally and peripherally, and subsequently, the epithelialization propagates ventrally (Shimokita and Takahashi, 2011). Small intercellular junctions first form at the basal outer ends of the elongating peripheral cells and then at their apical inner ends (Schoenwolf and Delongo, 1980; Schoenwolf and Kelley, 1980). The centrally located cells remain mesenchymal, as in the undifferentiated tail bud. Small lumina soon form between the peripheral epithelial and the central mesenchymal cell populations. These small lumina vary in number, size, shape and dorso-ventral location, even though the first lumen often appears dorsally displaced (Schoenwolf and Delongo, 1980). Finally, cavities coalesce to form a central single lumen. For that to happen, central cells must be cleared from the luminal space and the mechanism by which this is achieved remains elusive. Localised apoptosis seems not to be the case (Criley, 1969; Schoenwolf and Delongo, 1980; Shimokita and Takahashi, 2011), but cell death could still play an important role in secondary lumen formation, as central cells may de-attach, freely float in the lumen and finally degenerate. Other possibilities is that central cells migrate caudally, away from SN regions, or that they eventually elongate and become inserted into the lateral walls of the developing NT (Schoenwolf and Delongo, 1980). All observations favour the latter possibility, but since they have been all made in fixed sections, further research is needed to achieve a deeper understanding of this process. Coalescence is finally completed by stage HH35, and the whole NT is transformed into one tube with a single continuous lumen (Yang et al., 2003).

Neural tube defects (NTDs)

Neural tube defects (NTDs) are severe birth defects of the central nervous system that originate during embryogenesis, mainly due to a failure in the process of neurulation. NTDs rank among the most common categories of birth defects (Creasy and Alberman, 1976) affecting an average of 1 in every 1000 established pregnancies worldwide (Morris et al., 2016). Around 20% of individuals with birth defects die *in utero* (Dolk et al., 2010), while 9-10% die during the first year of life (Malcoe et al., 1999). Surviving individuals beyond one year of age are often destined for a life of ill health with repeated medical and surgical interventions. NTDs cover a wide spectrum of clinical severity and the main types are classified into open and closed NTDs, according to the degree of exposure of the neural tissue to the amniotic fluid.

A failure in Primary Neurulation leads to open NTDs

Open NTDs result from a failure of PN. When the dorsal closure of the NT is not completed, the neuroepithelium remains exposed to the environment, leading to its degeneration *in utero* and loss of neurological function below the lesion level. The severity of open NTDs vary with the level of the body axis affected (Fig. 5). Thus, failure of closure at the level of the prospective brain gives rise to anencephaly, which is lethal before or at birth (Fig. 5B). On the other hand, PN failure at the level of the spinal cord results in open spina bifida, a condition compatible with postnatal survival but related to lack of sensation, inability to walk and incontinence (Fig. 5C). In addition, around 10% of NTDs comprise a more extensive lesion in which the entire NT remains open from the midbrain to the low

spine (Fig. 5A). This condition is termed craniorachischisis, and represents the most severe form of NTD, being also lethal (Copp and Greene, 2013; Copp et al., 2015; Greene and Copp, 2014).

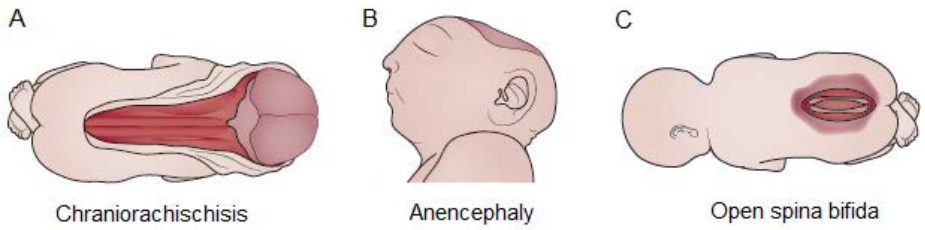

Figure 5. Open neural tube defects (NTDs). Schematic representation of open NTDs, which arise from faulty PN. **(A)** Chraniorachischisis occurs when an extensive region of the NT fails to close, resulting in a completely open brain and spinal cord. **(B)** Anencephaly results from the failure in NT closure at the level of the prospective brain, resulting in an open brain and lack of skull vault. **(C)** Open spina bifida results from the failure in NT closure at the level of the prospective spinal cord. Adapted from (Copp et al., 2015).

A failure in Secondary Neurulation leads to closed NTDs

Closed NTDs occur at sacrococcygeal levels when SN is disturbed. As SN does not have a closure component, defects are skin covered and not exposed to the external environment (Fig. 6A). Closed NTDs range from the asymptomatic spina bifida occulta (Fig. 6B) to the more severe closed spinal dysraphism (Fig. 6C), in which the distal spinal cord is tethered to surrounding non-neural tissues (Copp et al., 2015). Closed spinal dysraphism is compatible with life but associated to lower-limb motor and sensory deficits and a neuropathic bladder. The severity of symptoms increases with age and surgical untethering of the cord may provide some relief from disability. Closed NTDs are also associated to anorectal anomalies, lipoma, absent neural arches in the vertebrae and spinal cord abnormalities such as hydromyelia –a dilatation of the central canal- and diastematomyelia – a longitudinal duplication or splitting of the cord's caudal end (Greene and Copp, 2014).

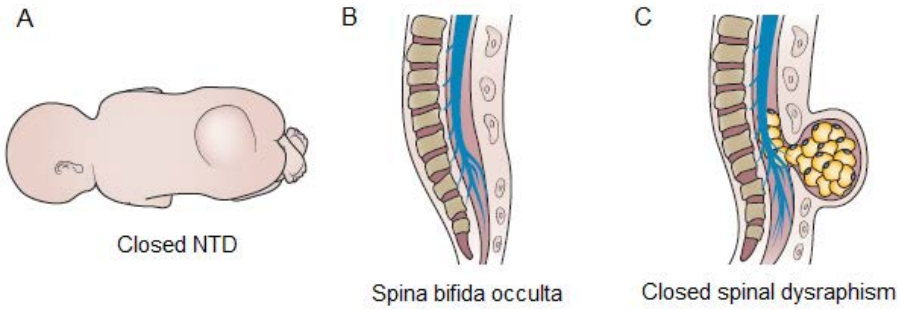

Figure 6. Closed neural tube defects (NTDs). Schematic representation of closed NTDs, which arise from faulty SN. **(A)** Closed NTDs occur at the level of the prospective caudal spinal cord and are skin covered. **(B)** Spina bifida occulta is an asymptomatic NTD in which some of the vertebrae are not completely closed, here with mild diastematomyelia – a longitudinal duplication or splitting of the cord's caudal end. **(C)** Closed spinal dysraphism is a severe closed NTD in which at least two vertebral arches are deficient, here with severe diastematomyelia and covered with a lipoma. Adapted from (Copp et al., 2015).

Causation of NTDs

NTDs have a multifactorial etiology, involving not only multiple genes but also several environmental factors. Genetic factors account for 70% of the variance in NTD prevalence (Leck, 1974). Indeed, the recurrence risk for siblings increases to 2-5% compared to the 0.1% risk in the general population, and gradually decreases in more distant relatives. However, NTDs are rarely present in multiple pregnancies or generations in the same family and the pattern of occurrence seems to be rather sporadic. This together with the high frequency of NTDs worldwide led to the present view of a multifactorial polygenic or oligogenic pattern of inheritance, rather than a model based on single dominant or recessive genes, and an important role of non-genetic factors (Greene et al., 2009). The best-known non-genetic factor is diminished folate one-carbon metabolism or availability and the risk for derived NTDs is prevented by exogenous folic acid supply during pregnancy (Burren et al., 2008). Other environmental risk factors are maternal obesity, diabetes mellitus and hyperthermia (Copp and Greene, 2013). Yet, it seems likely that non-genetic factors generate NTDs only when combined with a predisposing genotype.

The majority of NTDs are non-syndromic, meaning that the only primary defect is the defect in NT formation, and explained by this multifactorial model (Juriloff and Harris, 2018). However, several rare human syndromes of multiple unrelated defects also include NTDs. These syndromic forms are fewer than 10% of NTDs and result from chromosomal defects or Mendelian mutations (Lynch, 2005).

Almost 300 genetic models of NTDs have been described in mice that mimic the range of human NTDs. Many of the mutations causing NTDs in mice implicate genes involved in signalling (such as components of the SHH, BMP, TGF-β and WNT pathways), cell cycle maintenance, cytoskeletal regulation, cell polarity, cell-ECM interaction, transcriptional regulation and chromatin organization, among others (Harris and Juriloff, 2007; Harris and Juriloff, 2010). Human orthologues of some of the mouse genes have been examined as candidates for NTDs, but apart from studies that associated craniorachischisis to mutations in Planar Cell Polarity (PCP) pathway components (Robinson et al., 2012), no major NTD genes have been established in humans (Greene et al., 2009). Finally, although studies have identified numerous risk factors, these may account for less than half of NTDs, suggesting that the majority of genetic and non-genetic factors still remain elusive (Agopian et al., 2013).

Neuromesodermal progenitors, the cells contributing to the caudal NT

Body axis elongation, including the caudal elongation of the NT, is operated by a population of bipotent progenitors located at the caudal end of the embryo. These progenitors are termed neuromesodermal progenitors (NMPs) because they produce both the neural tissue that makes the caudal spinal cord and paraxial mesodermal tissues such as muscle and bone (Cambray and Wilson, 2007; Henrique et al., 2015; Tzouanacou et al., 2009). The co-expression of the early mesodermal marker Brachyury (T/Bra) and the neural progenitor marker Sox2 identifies NMPs, as unique molecular markers are currently lacking (Fig. 7A-F) (Wymeersch et al., 2016). In this way, NMPs have been found in zebrafish, chick, mouse, and human embryos (Martin and Kimelman, 2012; Olivera-Martinez et al., 2012; Row et al., 2016; Wymeersch et al., 2016). NMPs have gain much recent attention since protocols for generating

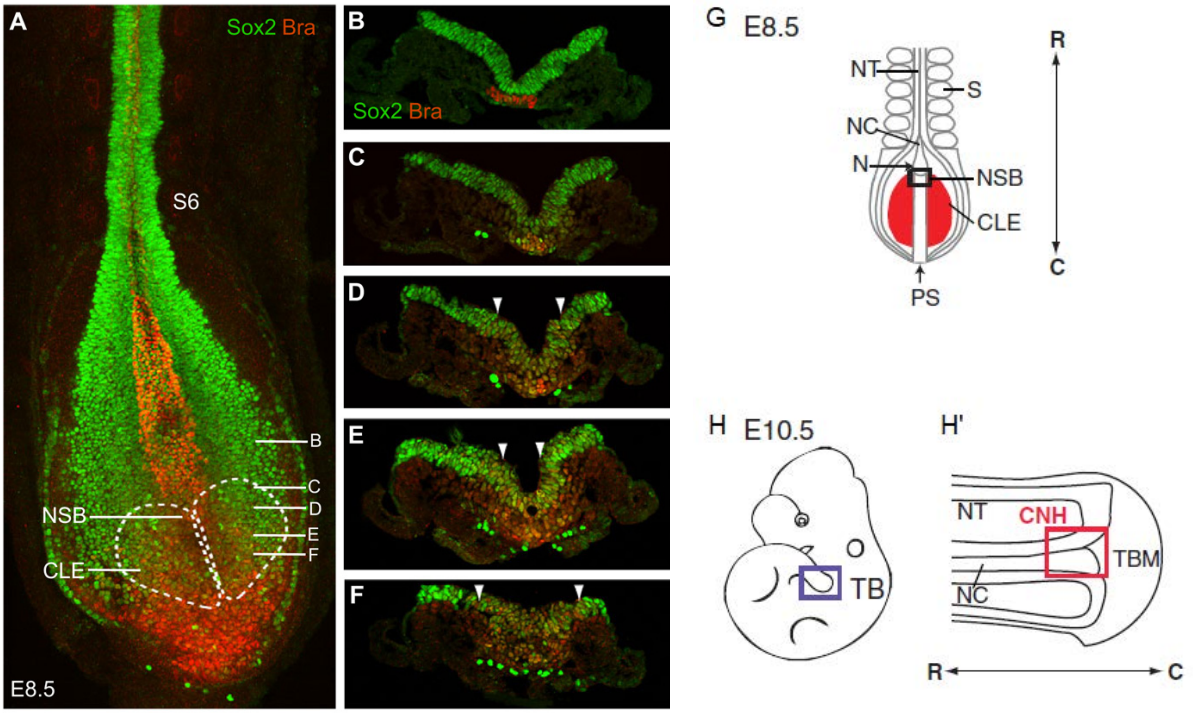

Figure 7. Location of neuromesodermal progenitors (NMPs) in mouse embryos. (A) Confocal maximum intensity projection of the posterior end of an E8.5 (6 somites, S6) mouse embryo stained with antibodies against Sox2 (green) and Brachyury (Bra, red). NMPs are the double-labelled cells located in the node-streak border (NSB) and caudal lateral epiblast (CLE). **(B-F)** Transverse sections at the levels indicated in A. Note the double-labelled cells between the arrowheads. Sox2 is also detected in large, ventrally located migrating germ cells. **(G)** Schematic representation of an early mouse embryo (S6, E8.5), from a dorsal view. At the S6 stage, NMPs locate at the NSB (black box) and CLE (red). **(H)** Schematic representation of a late mouse embryo (S35, E10.5). H' represents a longitudinal section through the tail bud. At later stages, NMPs are found in the chordo-neural hinge (CNH, red box). The CNH is located in the tail bud (TB, blue box), at the junction of the notochord (NC) and neural tube (NT), and rostral to the tail bud mesoderm (TBM). C, caudal; R, rostral; E, embryonic day. **(A-F)** are images from (Henrique et al., 2015). **(G-H)** are adapted from (Wilson et al., 2009).

them from human pluripotent stem cells *in vitro* were established (Gouti et al., 2014; Tsakiridis et al., 2014; Turner et al., 2014). This not only allowed to decipher the gene regulatory networks that determined NMPs fate specification and lineage restriction (Gouti et al., 2017; Koch et al., 2017), but also opened a new experimental paradigm for studying the cellular and molecular basis of caudal spinal cord generation and for advancing tissue engineering for therapeutic purposes.

The discovery of NMPs clearly challenges the classical notions of the formation of three separated germ layers during gastrulation (endoderm, mesoderm and ectoderm) and the subsequent neural cell fate assignment from within the ectoderm (Fig. 2,3). Fate-mapping studies in early mouse and chick embryos allocated NMPs in and near the PS, in both the Node-Streak Border (NSB) and in the Caudal Lateral Epiblast (CLE) (Fig. 7A,G) (Brown and Storey, 2000; Cambray and Wilson, 2007; Iimura et al., 2007; Wymeersch et al., 2016). The NSB will also give rise to the chordo-neural hinge (CNH), a dual fated structure responsible for body axis elongation at later stages (Fig. 7H) (Cambray and Wilson, 2002; Cambray and Wilson, 2007). Homotipic and heterotipic grafting of NMPs in the NSB and CLE regions showed that NMPs choose between retention as progenitors and differentiation as

either neurectoderm or mesoderm based on their location, suggesting the existence of a single NMP identity whose fate is instructed by positional cues (Wymeersch et al., 2016).

WNT3A signalling from the elongating tail, together with FGF8, are required for NMP maintenance and expansion (Garriock et al., 2015; Wymeersch et al., 2016). When WNT activity is inhibited in the epiblast, embryos fail to increase NMP numbers, raising the possibility that the shortened body axis in *Wnt3a* mouse mutants (Greco et al., 1996; Takada et al., 1994) results from the incapability of maintaining NMPs. On the contrary, the somites synthetize retinoic acid (RA), which opposes WNT/FGF signalling and promotes, at least in part, the exit from the NMP state towards the neural identity (Gouti et al., 2017; Olivera-Martinez et al., 2014). As the body axis elongates, NMPs are exposed to diminishing levels of WNT/FGF signalling and to increasing levels of RA, thus differentiating into neural tissue.

The choice of NMPs to form mesoderm also relies on WNT signalling, as in its absence cells differentiate to neural derivatives (Martin and Kimelman, 2012; Nowotschin et al., 2012; Yoshikawa et al., 1997). While moderate levels of WNT3A are needed to maintain the self-renewing NMPs, high WNT3A levels induce the exit from the progenitor state to differentiate into paraxial mesoderm (Jurberg et al., 2014). However, high WNT activity is not sufficient to commit NMPs to a mesodermal fate, suggesting the interplay with other signalling pathways (Gouti et al., 2017; Jurberg et al., 2014).

All these environmental cues ultimately result in different Sox2 and T/Bra levels in NMPs. Sox2 and T/Bra antagonistically control NMPs fate-choice as they activate neural or mesodermal gene expression profiles, respectively (Koch et al., 2017). In the neural lineage, the transition from NMPs to neural progenitor cells (NPCs) of the primary NT goes through an intermediate pre-neural tube (PNT) cell state, which can be reverted back to a multipotent NMP state by FGF signalling (Diez del Corral et al., 2002; Gouti et al., 2017). PNT cells are the early neural progenitors that undergo the morphogenetic movements that close the primary NT (Olivera-Martinez et al., 2014).

NMPs that will undergo SN in the future and differentiate into NPCs of the SNT have been identified in HH8 chick embryos (Shimokita and Takahashi, 2011). At this stage, these cells occupy an area of the epiblast located caudo-medially to the Hensen's Node, the presumptive SN (preSN) region. The preSN region includes both the NSB and the medial portion of the CLE (Fig. 8) (Catala et al., 1995; Catala et al., 1996; Le Douarin, 2001; Le Douarin et al., 1998). This area is discernible at following stages (HH9-11) but gradually shrinks until it disappears at caudal neuropore closure (HH12). When NMPs from the preSN region are traced, only the cells forming the NT are labelled at

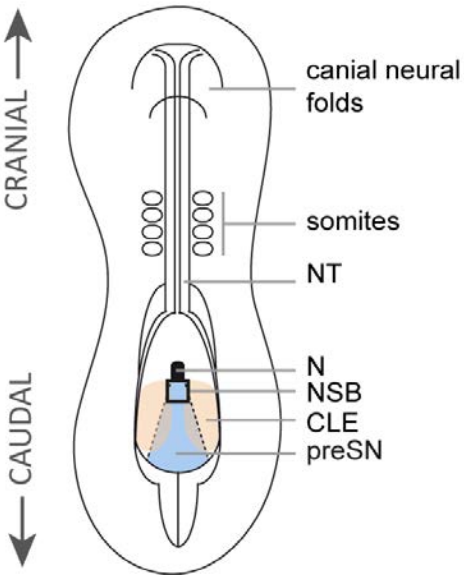

Figure 8. The preSN region in early chick embryos. Schematic representation of an HH8 chick embryo showing the presumptive SN (preSN) region (light blue). The preSN area is located caudo-medially to the Hensen's node and includes both the NSB (black box) and the medial portion of the CLE (overlapping blue and orange). NT, neural tube; N, node; NSB, node-streak border; CLE, caudal lateral epiblast; preSN, presumptive SN region; HH, Hamburger and Hamilton stage. Adapted from (Shimokita and Takahashi, 2011).

later stages, while the cells forming the notochord or the surrounding mesodermal tissues are not (Shimokita and Takahashi, 2011). The identification of the preSN region in the chick embryo allows any cells undergoing SN to be manipulated *in vivo* by *in ovo* electroporation (see Appendix II).

Mesenchymal-to-epithelial transition and *de novo* lumen formation

During embryonic development, many cells are born far from their final destination and must travel long distances to form tissues and organs. Cells in the embryonic epiblast undergo epithelial-to-mesenchymal transition (EMT) in order to ingress and acquire a migratory phenotype (Fig. 2). Once embryonic cells reach their destination, they undergo the reverse process, the mesenchymal-to-epithelial transition (MET), to settle, proliferate and generate multiple tissues (Nieto, 2013). This is the case of the mesenchymal NMPs participating in body axis elongation, which ingress from the epiblast by EMT and later convert into an apico-basally polarised epithelium (the SNT) by MET.

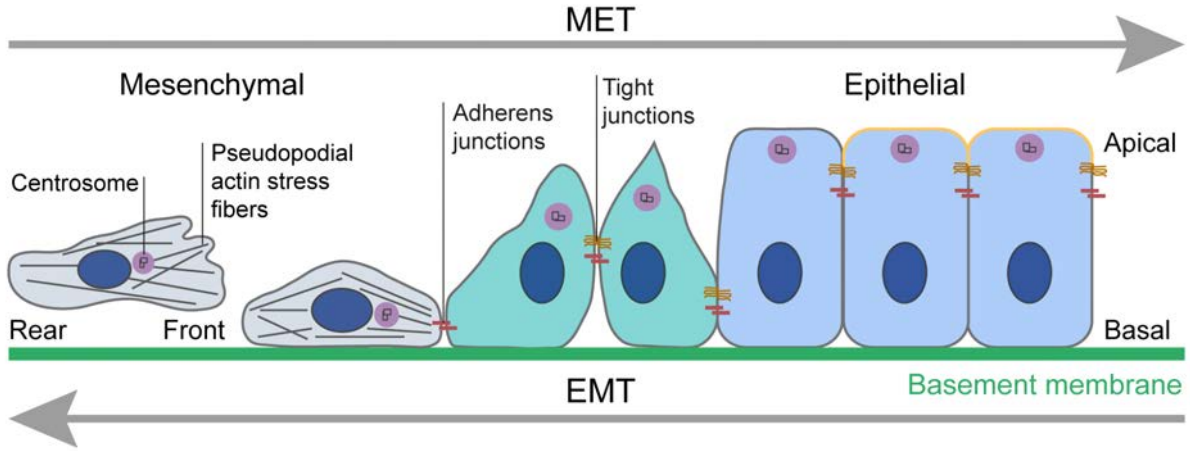

Figure 9. MET and EMT are reversible cellular programs. Mesenchymal cells (grey) display front-rear polarity, high protrusive activity, high motility and invasive properties. Induction of mesenchymal-to-epithelial transition (MET) leads to the repression of genes associated with the mesenchymal state and the concomitant activation of genes associated with the epithelial state. These changes in gene expression result in cellular changes that include the assembly of epithelial cell-cell junctions, the establishment of apico-basal cell polarity and the repositioning of the centrosome. The loss of mesenchymal features is progressive and intermediate states can be maintained. Epithelial cells (light blue) display apico-basal polarity (the apical surface appears in orange), are held together by tight and adherens junctions and are tethered to an underlying basement membrane (green). The reverse process is the epithelial-to-mesenchymal transition (EMT). Adapted from (Dongre and Weinberg, 2019).

EMT and MET are highly conserved and completely reversible cellular programs (Fig. 9). Mesenchymal cells exhibit front-rear polarity, extend pseudopodia, show high motility and invasive properties and only form transient contacts with its neighbours. On the other hand, epithelial cells present an aligned apico-basal polarity, associate to a basement membrane (BM), and are tightly connected by cell-cell junctions. Thus, the program of MET is defined by the acquisition of apico-basal polarity, the loss of migratory protrusions and invasive properties and the establishment of cell-cell junctions (Hay and Zuk, 1995; Yang and Weinberg, 2008). One of the best-studied MET events during embryogenesis is the formation of the nephron epithelium in the developing kidney. During this process, nephric

mesenchymal cells aggregate, begin to express laminin, apico-basally polarise, develop cell-cell adhesions and differentiate into epithelial cells that form kidney tubules (Davies, 1996). Frequently, such as in this later case, the MET is accompanied by the opening of a lumen in between the epithelial cells, the whole process being termed *de novo* lumen formation.

Extensive research using 3D epithelial culture systems (Debnath and Brugge, 2005; O'Brien et al., 2002), together with studies in early mouse and human embryos (Shahbazi and Zernicka-Goetz, 2018; Shahbazi et al., 2019) and in *in vivo* models such as the zebrafish gut (Alvers et al., 2014; Bagnat et al., 2007; Rodriguez-Fraticelli et al., 2015), have deciphered the common principles and conserved molecular networks behind *de novo* lumen morphogenesis. In general, three basic steps can summarize this process: (i) the sensing of both the extracellular matrix (ECM) and the neighbouring cells to set the directionality of cell polarisation; (ii) the coordinated MET of neighbouring cells and the initiation of the luminal space; and (iii) the final expansion and resolution of the lumen (Datta et al., 2011).

Setting the directionality of epithelial polarisation

Mesenchymal cells converging to form a lumen *de novo* first need to define the position where the new space will develop and the directionality of polarisation. In general, lumens are allocated in a shared site between neighbouring cells and oriented perpendicular to the ECM-contacting surface. The precise site at which the lumen will be generated is fixed through interactions with the ECM and/or between neighbouring cells. During neurulation in the zebrafish embryo, cells in the neural rod integrate basal signals from the ECM and cell-cell interactions to determine the localisation of the apical pole (Buckley et al., 2013).

The ECM is sensed through receptors of the integrin family, which bind to collagen, laminin and fibronectin. In Madin-Darby canine kidney (MDCK) cells grown in 3D culture, blocking the function of β1 integrin results in apico-basal inverted polarity, with the apical pole positioned towards the cyst periphery (Bryant et al., 2014; Yu et al., 2005). Integrin binding to the ECM activates in turn cytoskeletal modulators (small GTPases such as Rac1 or Cdc42) that induce apico-basal cell polarity by regulating actin dynamics and laminin assembly (Bayless and Davis, 2002; Davis and Bayless, 2003; Davis and Camarillo, 1996; O'Brien et al., 2001). In mouse embryos developing both *in vivo* and *in vitro*, ECM cues are transmitted through β1 integrin receptors to direct the polarisation of the early epiblast, which forms a rosette-like structure and opens a lumen in the centre (Bedzhov and Zernicka-Goetz, 2014). Notably, cells not only perceive molecular cues from the ECM but also sense its physical conditions, such as matrix stiffness, water tension and cell confinement (Burute et al., 2017; Chlasta et al., 2017; Rodriguez-Fraticelli et al., 2012). High cell confinement promotes epithelial polarisation and central lumen formation in MDCK cells cultured in 3D-micropatterns, by preventing cell spreading, reducing peripheral actomyosin contractility and allowing centrosome repositioning (Rodriguez-Fraticelli et al., 2012). Interestingly, ECMs rich in laminin improve lumen formation, as they create conditions of high cell confinement.

Besides the ECM, neighbouring cell-cell interactions, which occur through cadherins and other adhesion receptors, also play a role in lumen positioning. Apico-basal polarity is initiated in this context when nascent adhesions form in between contacting mesenchymal cells that will be incorporated into the epithelium. The cytoplasmic domains of molecules at nascent adhesions then act as scaffolds to

recruit polarity-signalling molecules that lead to cytoskeletal rearrangements and MET (Baum and Georgiou, 2011; Vaezi et al., 2002; Vasioukhin et al., 2000; Yamada and Nelson, 2007).

MET and lumen initiation

Once mesenchymal cells have recognized the ECM and neighbouring cells, the MET program is triggered. The MET includes the establishment of apico-basal polarity, the formation of cell-cell junctions and the loss of migratory properties (Fig. 9). The acquisition of apico-basal polarity depends on the asymmetric segregation of proteins and lipids to the apical and basolateral cell surfaces, which face the lumen or contact adjacent cells and the underlying ECM, respectively (Bryant et al., 2010; Gassama-Diagne et al., 2006; Martin-Belmonte et al., 2007). Polarity complexes, such as the PAR/aPKC complex, regulate epithelial polarisation, direct polarised membrane transport to define the two surfaces and assemble cellular junctions (Bilder et al., 2003; Bryant et al., 2010; Munro, 2006; Ooshio et al., 2007; Tanentzapf and Tepass, 2003). The centrosome, the main microtubule-organizing centre (MTOC) in animal cells, reorients from the cell front of migrating cells towards the apical pole, to orientate microtubules along the apico-basal axis (Burute et al., 2017; Hebert et al., 2012). Components of the vesicular trafficking pathway are repositioned together with the centrosome, to direct polarised intracellular transport. In this way, proteins destined for either surface are processed along the biosynthetic pathway and transported in vesicles from the trans-Golgi network or recycled through endosomes (Eaton and Martin-Belmonte, 2014; Rodriguez-Boulan et al., 2005; Roman-Fernandez and Bryant, 2016). Tight and adherens junctions are assembled not only to provide cohesion between cells but also to prevent the mixing of proteins and lipids between the apical and basolateral surfaces (Roignot et al., 2013; Shin and Margolis, 2006). Adherens junctions also associate to the actin cytoskeleton, which rearranges from the actin stress fibres forming mesenchymal pseudopodia to a cortical meshwork that provides mechanical stability to the epithelium (Morris and Machesky, 2015). Concomitantly to apical polarisation, the BM is assembled. The BM is a specialized ECM that underlines epithelial cells at their basal surfaces and separates the epithelial layer from other tissues. It is composed of a network of fibrous proteins, such as different types of laminins or fibronectins (Yurchenco, 2011).

The initiation of the new lumen occurs simultaneously to the MET. Two models of *de novo* lumen formation have been proposed from *in vitro* studies in MDCK cells: hollowing and cavitation (Fig. 10).

Hollowing

In the hollowing model, the apical lumen forms when neighbouring cells coordinate the delivery of apical membrane components and proteins to a common site, including anti-adhesins such as podocalyxin (Fig. 10A) (Bryant et al., 2010; Galvez-Santisteban et al., 2012; Martin-Belmonte and Mostov, 2008). These proteins are extensively glycosylated and/or syalylated, resulting in highly negatively charged domains, and open the new luminal space by electrostatic repulsion (Nielsen and McNagny, 2008; Strilic et al., 2010; Takeda et al., 2000; Wesseling et al., 1996). *In vivo,* hollowing drives lumen formation in the zebrafish gut (Bagnat et al., 2007; Horne-Badovinac et al., 2001; Ng et al., 2005; Rodriguez-Fraticelli et al., 2015) and in both mouse and human embryos at implantation stages (Bedzhov and Zernicka-Goetz, 2014; Shahbazi et al., 2016; Shahbazi et al., 2017).

Cavitation

Alternatively, the cavitation model explains the creation of a luminal space involving cell death (Fig. 10B). When a cluster of cells is present, cells in the cluster periphery receive ECM-derived polarisation and survival signals, while those in the interior do not and die by apoptosis (Debnath and Brugge, 2005; Debnath et al., 2002). Lumen formation by cavitation is the predominant mechanism during mammary duct morphogenesis and salivary gland development (Humphreys et al., 1996; Jaskoll and Melnick, 1999).

Both the hollowing and cavitation models provide viable mechanisms of *de novo* lumen formation *in vitro* and *in vivo*. Notably, MDCK cysts change from hollowing to cavitation when rapid polarisation is disrupted (Martin-Belmonte et al., 2008), so the two mechanisms could have a compensatory role to ensure that a lumen is always opened. Furthermore, the lumen in some tissues could emerge because of both mechanisms. While hollowing may initially establish the apical lumen, apoptosis may be used to remove any cells that invade the luminal space during lumen expansion (Blasky et al., 2015).

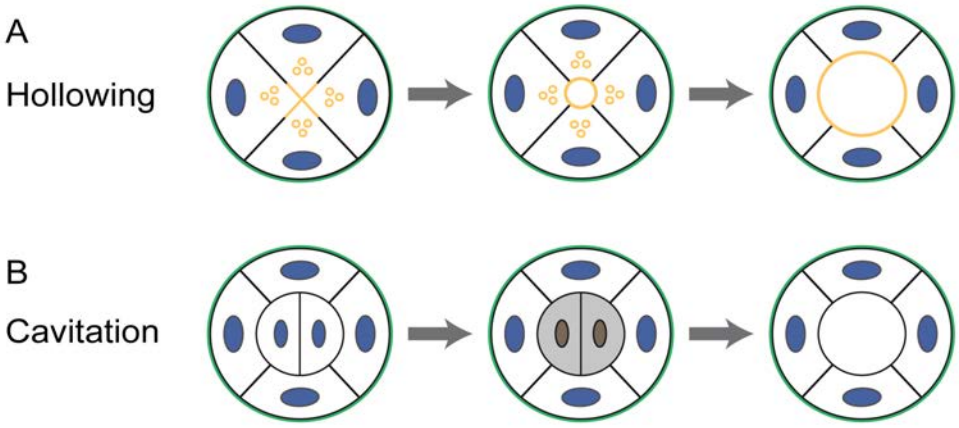

Figure 10. Models of *de novo* lumen formation. Schematic drawing of the two models for opening a lumen de *novo* in between cells, proposed from studies in 3D cultured MDCK cells. **(A)** In the hollowing model, clusters of cells contacting the ECM (green) exocytose vesicles containing luminal components (orange) in a coordinated manner, resulting in apico-basal polarisation and lumen formation in the centre. **(B)** In the cavitation model, the inner cells in the cluster that are not contacting the ECM die by apoptosis (grey), which results in the generation of luminal space. Cell nuclei are drawn in blue. Adapted from (Datta et al., 2011).

Lumen expansion and resolution

Once lumens are opened, they must grow and expand to their functional size. In several systems, multiple small lumen foci form and later coalesce to form a single lumen (Fig. 11). Some vertebrate examples of these events are the formation of the gut in zebrafish and mouse (Alvers et al., 2014; Bagnat et al., 2007; Saotome et al., 2004), the development of the mouse pancreas (Kesavan et al., 2009) and the lumenogenesis of the zebrafish inner ear (Hoijman et al., 2015). Lumen expansion and coalescence is mediated by fluid accumulation in the newly formed lumen, which increases hydrostatic pressure and generates a turgor force (Fig. 11C). This is achieved by the apical delivery and activation of pumps and channels (Bagnat et al., 2007; Bagnat et al., 2010; Krupinski and Beitel, 2009; Li and Naren, 2010; Lowery and Sive, 2005) together with the regulation of the paracellular permeability through claudins, which are tight junctions components (Moriwaki et al., 2007; Nelson et al., 2010;

Zhang et al., 2010). However, fluid accumulation is not the only mechanism driving lumen resolution. In the zebrafish gut, the lumen initially expands by fluid accumulation but final fusion occurs through the breaking of basolateral cell contacts in between the nascent lumens and the expansion of the apical membrane (Fig. 11D) (Alvers et al., 2014). This process requires the simultaneous targeted delivery and fusion of apical endosomes and the removal of basolateral membrane by endocytosis.

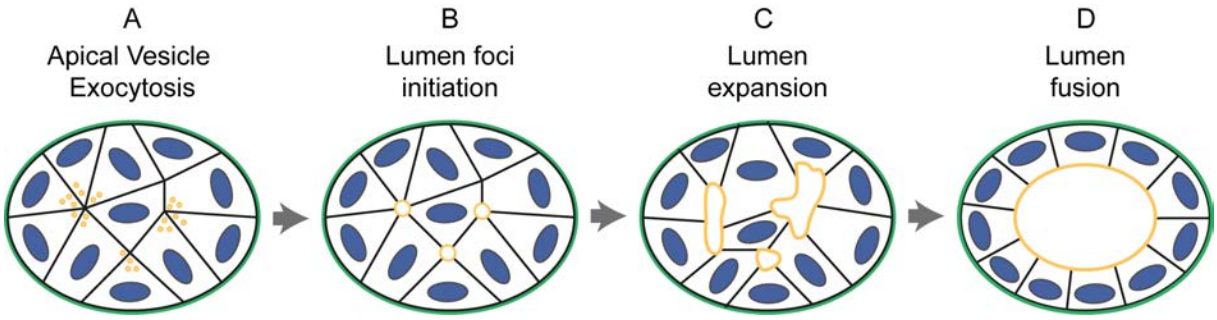

Figure 11. Lumen foci initiation and resolution in multicellular tissues. Schematic drawing of the process of lumen formation in multicellular tissues. **(A)** In multicellular tissues, neighbouring cells coordinate the delivery of apical components (orange) to a common site, which establishes apico-basal cell polarity within single cells. **(B)** As a consequence, small lumen foci open up in between cells. **(C)** The small lumen foci then expand by fluid accumulation, achieved by the action of pumps and channels and the regulation of paracellular permeability through claudins. **(D)** Lumens finally fuse, which requires the simultaneous exocytosis of apical vesicles and the endocytosis of basolateral membranes. The BM appears in green, cell nuclei are depicted in blue and the nascent apical surfaces are in orange. Adapted from (Kesavan et al., 2009).

Finally, the division of cells in the wall of the epithelium also have a role in lumen expansion: if mitosis orient perpendicular to the apico-basal axis and divide in the plane of the monolayer, the walls of the epithelium enlarge (Datta et al., 2011). Moreover, a recent study showed a new role of mitotic rounding, an event occurring at the onset of mitosis, in mechanically pulling the wall of the epithelium to shorten its apico-basal axis, thus contributing to the expansion of the lumen (Hoijman et al., 2015).

The cell biology of NPCs

The NT, regardless of its formation by PN or SN, is composed of neural progenitor cells (NPCs) arranged in a pseudo-stratified epithelium enclosing a single lumen in the centre (Fig. 12A). Each cell extends a basal process to the BM and an apical process to the lumen of the NT, and their nuclei adopt distinct positions along the apico-basal cell axis, according to the progression of the cell cycle. Nuclei of progenitor cells born at the apical surface of the neuroepithelium move toward the basal side during G1 phase of the cell cycle. After completing S-phase contacting the basal portion of the neuroepithelium, the nuclei return to the apical surface, where they undergo mitoses as their parent cells did (Fig.12B). Collectively, these oscillatory nuclear movements are referred to as interkinetic nuclear migration (INM) (Langman et al., 1966; Saade et al., 2018; Sauer, 1935; Taverna and Huttner, 2010).

NPCs in the NT are fully apico-basally polarised epithelial cells (Fig. 12D), that is why they are also termed neuroepithelial cells. NPCs present an apically localised centrosome, located at the base of a solitary primary cilium, which has important functions in sensing environmental cues. NPCs assemble

Apical Junctional Complexes (AJCs) composed by discrete micro-domains where N-Cadherin/β-catenin (adherens junction proteins) and the ZO-1/occludin complex (tight junction proteins) occupy internal positions, while the PAR6/aPKC complex concentrates at the most apical domain (Aaku-Saraste et al., 1996; Afonso and Henrique, 2006; Chenn et al., 1998; Marthiens and Ffrench-Constant, 2009). On the other hand, integrins are basally localised, so to contact the BM, the last being composed of laminin and fibronectin, among other proteins (Fig. 12C).

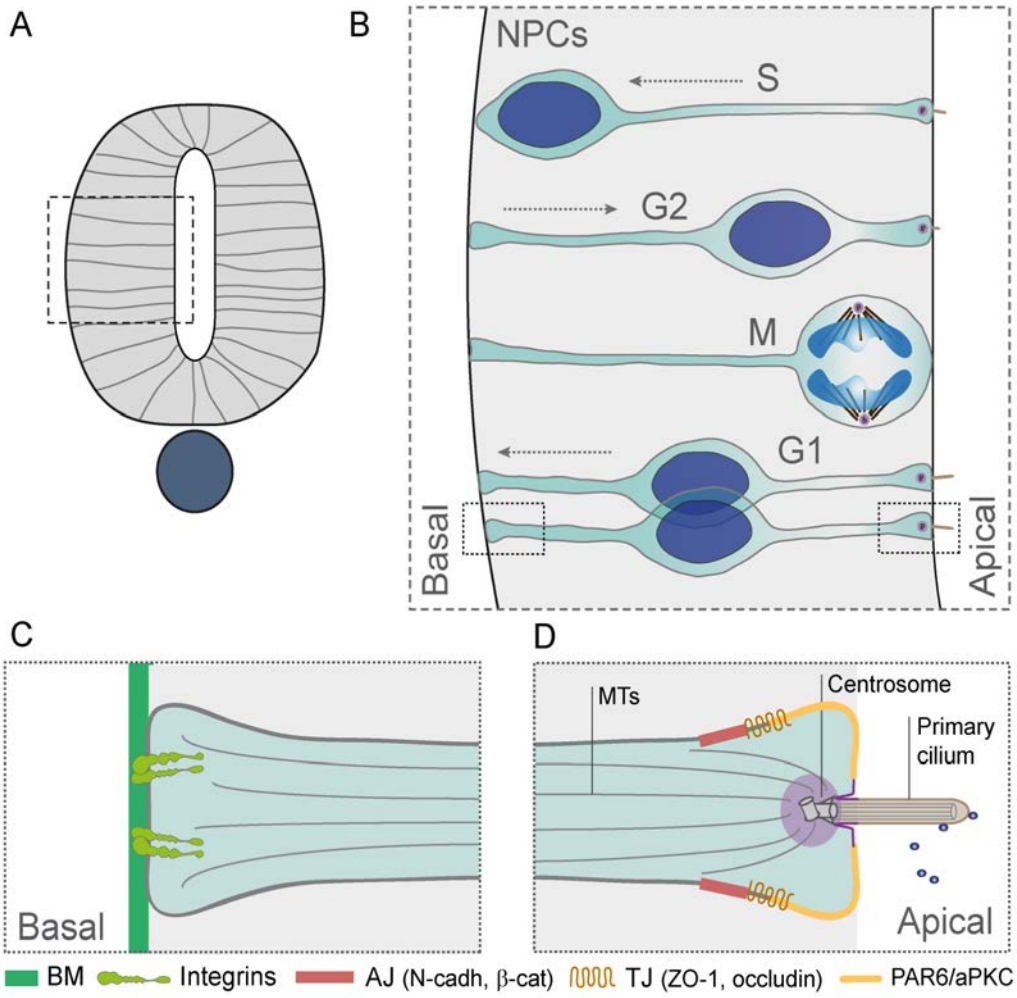

Figure 12. NPCs are epithelial cells that undergo INM. (A) Schematic representation of a transverse section through the neural tube. **(B)** Schematic representation of the interkinetic nuclear migration (INM) of NPCs. The nuclei of dividing NPCs occupy different apico-basal positions depending on the phase of the cell cycle (S, G2, M, G1). Dashed arrows indicate the direction of nuclear migration. **(C-D)** Diagrams of the basal and apical poles of an NPC in the G1 phase of the cell cycle. The primary cilium points to the NT lumen. The centrosome at the cilium base arranges microtubules (MTs). NPCs organize an apical junctional complex in micro-domains, where adherens (AJ) and tight junctions (TJ) occupy internal positions, while the PAR6/aPKC complex concentrates at the most apical domain. Integrin receptors locate to the basal pole to contact the BM. Adapted from (Saade et al., 2018) and after (Afonso and Henrique, 2006).

The TGF-β superfamily of secreted signalling molecules

TGF-β signalling

The transforming growth factor-beta (TGF-β) superfamily is a large family of growth factors named after its first member, TGF-β1. This superfamily includes the TGF-β proteins, Bone Morphogenetic Proteins (BMPs), Growth Differentiation Factors (GDFs), Glial-derived Neurotrophic Factors (GDNFs), Activins, Inhibins, Nodal, Lefty, and Mülllerian Inhibiting Substance (MIS) (Feng and Derynck, 2005; Shi and Massagué, 2003). All these secreted proteins signal through the same linear pathway (Fig. 13). Dimers of ligands induce the formation of a stable serine/threonine kinase receptor complex, consisting of two Type-1 and two Type-2 receptors. Constitutively active Type-2 receptors phosphorylate and thereby activate Type-1 receptors, which in turn propagate the signal by phosphorylating intracellular receptor-regulated SMAD factors (R-SMADs) on three serine residues located at the carboxy-terminal end (Le Dreau and Marti, 2013; Wu and Hill, 2009). Within the R-SMADs, SMAD1/5/8 are specific to BMP signalling (Fig. 13A), while SMAD2/3 are phosphorylated upon TGF-β pathway activation (Fig. 13B). Once phosphorylated, R-SMADs form a trimeric complex with SMAD4, consisting of two R-SMAD molecules and one SMAD4. This trimeric complex favours its stability into the nucleus where, with additional co-factors, SMADs regulate the transcription of their target genes. In absence of ligands, SMAD transcription factors undergo a nuclear-cytoplasmic shuttling, favouring their cytoplasmic localisation and thus avoiding them to modulate transcription. Although this canonical pathway is relatively simple, there is a high combinatorial mixing at the level of ligands, receptors and SMADs, which produces a large diversity in transcriptional outputs (Feng and Derynck, 2005).

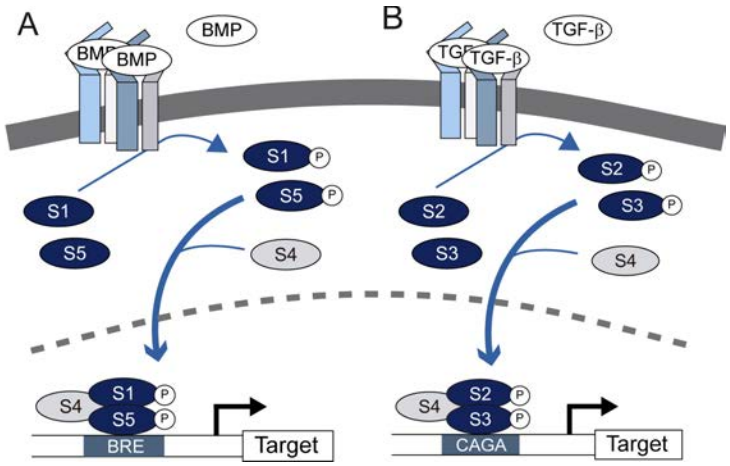

Figure 13. The BMP and TGF-β signalling pathways. (A-B) Schemes representing the basics of the canonical BMP **(A)** and TGF-β **(B)** pathways. Dimers of ligands promote the formation of a complex of transmembrane serine/threonine kinases, in which Type-2 receptors (blue) phosphorylate and thereby activate Type-1 receptors (grey). Type-1 receptors in turn phosphorylate the R-SMADs, which are pathway specific. Thus, SMAD1 (S1) and SMAD5 (S5) are phosphorylated upon BMP ligand stimulation, and SMAD2 (S2) and SMAD3 (S3) upon TGF-β. R-SMAD phosphorylation facilitates their interaction with SMAD4 (S4) that results in the formation of a trimeric complex of two R-SMADs and one SMAD4. This complex presents enhanced nuclear stability and binds to BMP-responsive elements (BRE) or TGF-β-responsive elements (CAGA) found in target gene promoters and, in cooperation with transcriptional co-factors, modulate the expression of target genes. Adapted from (Le Dreau and Marti, 2012).

The TGF-β superfamily, instructive signals for EMT and MET

Members of the TGF-β superfamily have been implicated as major instructive signals of EMT in many morphogenetic processes. In vertebrates, Nodal induces gastrulation and mesendodermal ingression from the embryonic epiblast (Luxardi et al., 2010). Later in development, the entire vertebrate peripheral nervous system is formed from migratory neural crest cells, which delaminated from the developing neural tube through the EMT (Theveneau and Mayor, 2012), a process in which the BMP members of the TGF-β superfamily play a role (Correia et al., 2007; Marchant et al., 1998; Raible, 2006). Furthermore, TGF-β signals trigger the EMT program during both cardiac valve formation and secondary oral palate fusion, two other well-studied physiological EMT events (Yang and Weinberg, 2008). Antibody-blocking experiments using chicken atrioventricular explants showed that TGF-β2 is essential to induce the EMT program in endothelial cells, while TGF-β3 is required for their migration along the ECM (Boyer et al., 1999). Studies in *TGF-β1* and *TGF-β2* knockout mice further confirmed the role of these ligands in inducing the EMT in the context of the embryonic heart (Mercado-Pimentel and Runyan, 2007). Additionally, *TGF-β3* knockout mice present a cleft palate phenotype as this variant initiates the EMT that enables palate fusion (Ahmed et al., 2007).

Various studies have explored the roles of SMAD2 and SMAD3, the TGF-β-activated SMADs, in EMT (Xu et al., 2009). The increased expression of *Smad2* or *Smad3* induces EMT in cultured mouse mammary epithelial cells (Piek et al., 1999; Valcourt et al., 2005). Renal tubule epithelial cells deficient in SMAD3 fail to undergo EMT in response to TGF-β or mechanical stress (Sato et al., 2003) and keratinocytes derived from *Smad3-/-* mice show a reduced migration in response to TGF-β (Ashcroft et al., 1999). SMAD2, however, may play an antagonistic role in the EMT process in some *in vivo* contexts. For example, loss of SMAD2 in keratinocytes promotes EMT (Hoot et al., 2008) and *Smad2-/-* hepatocytes appear mesenchymal and migrate faster than wild-type cells, while *Smad3-/-* hepatocytes retain their epithelial characteristics (Ju et al., 2006).

All these signalling molecules trigger EMT by the activation of transcription factors known as EMT-inducers, and the subsequent repression of epithelial marker gene expression together with the transcriptional activation of mesenchymal genes (Peinado et al., 2007; Vandewalle et al., 2005; Yang and Weinberg, 2008). Moreover, non-canonical signalling pathways, independent of SMAD transcriptional regulation, can also contribute to the EMT. In cultured mammary epithelial cells, TGF-β receptors localise to tight junctions and directly interact with PAR6 and Occludin (Barrios-Rodiles et al., 2005; Ozdamar et al., 2005). Upon ligand activation, the TGF-β Type-2 receptor (TβRII) phosphorylates PAR6 and results in a loss of tight junctions and cytoskeleton rearrangements (Ozdamar et al., 2005).

Although many signalling pathways regulating EMT have been identified, the signals controlling MET during embryonic development have not been well characterised. So far, the best-known epithelializing agent is also a member of the TGF-β superfamily: the bone morphogenetic protein 7 (BMP7). BMP7 has been found to counteract TGF-β signalling and induce MET both *in vivo* and *in vitro*, as seen in kidney development (Dudley et al., 1995) and in the reprogramming of fibroblasts into induced pluripotent stem cells (iPSCs) (Samavarchi-Tehrani et al., 2010).

Primary cilia and TGF-β signalling

Primary cilia are solitary, non-motile sensory organelles that project from the cell surface to detect changes in their extracellular environment, integrate and transmit signalling information to the cell and regulate various cellular, developmental and physiological processes (Christensen et al., 2017; Pedersen et al., 2016). Primary cilia are microtubule-based organelles that extend from a basal body, which derives from the mother centriole (Kobayashi and Dynlacht, 2011; Paintrand et al., 1992), and are enclosed by a bilayer lipid membrane, which is continuous to the cell membrane but differs in its composition (Fig. 14). Defects in primary cilia structure or function are associated with multiple human disorders called ciliopathies (Hildebrandt et al., 2011). Ciliopathies are associated to defects in ciliary formation or maintenance, and range from completely absent cilia to shortened or lengthened conditions (Keeling et al., 2016).

The regulation of the TGF-β superfamily signalling has recently been associated to the primary cilia compartment. TGF-β receptors localize to the primary cilia membrane in various stem cell lines (Fig. 14) and phospho-SMAD2/3 activation relies on TGF-β receptor endocytosis at the base of the cilia (Clement et al., 2013; Zhang et al., 2009). Indeed, primary cilia formation is required for proper TGF-β signalling, as reported in the developing zebrafish embryo (Monnich et al., 2018). However, much less is known about the role of this pathway in ciliary development and differentiation. A unique study in *Xenopus* embryos revealed that TGF-β signalling controls the length of motile cilia. In this context, SMAD2 depletion resulted in shortened motile cilia, likely by affecting the structure and/or function of the transition zone (TZ) of the cilium (Tözser et al., 2015). The TZ is the region between the basal body and cilium proper and acts as a selective fence to regulate the passage of proteins and lipids in and out of the cilium (Christensen et al., 2017; Garcia-Gonzalo et al., 2011; Jensen et al., 2015) (Fig. 14). Importantly, a large number of genes that are mutated in ciliopathies code for proteins that localise to the TZ (Reiter et al., 2012; Takao and Verhey, 2016).

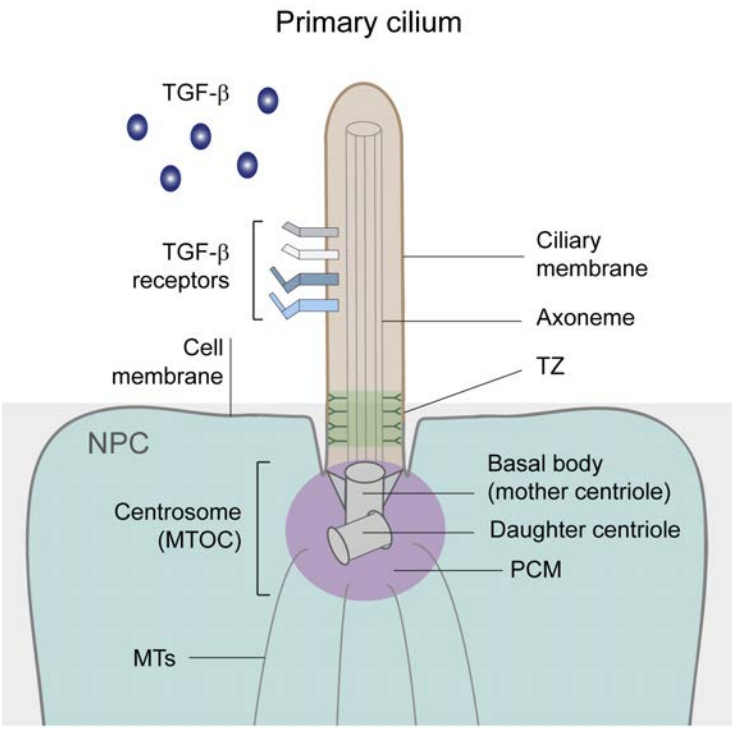

Figure 14. The primary cilium harbours TGF-β signalling receptors. Scheme representing the primary cilium of a NPC. The primary cilium has a microtubule-based axoneme that emerges from a centriolar structure termed the "basal body". The basal body derives from the mother centriole after division and together with the daughter centriole and pericentriolar material (PCM, purple) constitute the centrosome, the main microtubule organising centre (MTOC) in animal cells. The ciliary membrane is continuous with the cell membrane and the transition zone (TZ, green) selectively regulates the passage of proteins and lipids in and out of the cilium. TGF-β receptors locate at the ciliary membrane, where they will be activated by TGF-β ligands. Drawing after (Christensen et al., 2017) and (Joukov and De Nicolo, 2019).

OBJECTIVES

The aim of this thesis is to unravel the cellular events and molecular networks driving secondary neurulation in the chick embryo, as a model to understand human secondary neurulation and associated neural tube defects.

My main objectives are:

- To study the acquisition of neural identity, the establishment of apico-basal polarity and the formation of a single lumen during secondary neurulation.
- To determine the mechanism by which central cells are cleared from the luminal space during secondary lumen resolution.
- To investigate the role of BMP and TGF-β signalling, and specifically of SMAD3 activity, in the morphogenesis of the secondary neural tube, as potential candidates for the generation of neural tube defects.

MATERIALS & METHODS

Chick embryos

Fertilized eggs from the White-Leghorn strain of chickens were incubated horizontally at 38.5°C in an atmosphere of 70% humidity. Embryos were staged following morphological criteria (Hamburger and Hamilton, 1992).

DNA constructs

The pCS2:H2B-GFP, pCS2:H2B-RFP and pCAGGS:_ires_GFP (PCIG) vectors were used at a concentration of 0.5 µg/µl as controls for electroporation (Le Dréau et al., 2014; Megason and McMahon, 2002) (Table 1).

The endogenous activities of the canonical BMP and TGF-β pathways were assessed using reporter constructs producing EGFP under the control of specific promoters at a concentration of 2 µg/µl. The BRE:EGFP reporter consists of an artificial promoter containing two copies of two distinct highly conserved BRE encompassing the genomic regions −1,032/−1,052 (SBE-3, SBE-2, and GC'-5) and −1,080/−1,105 (CAGC-2, CAGC-1, and GC'-3,4) of the natural human Id1 promoter (Korchynskyi and ten Dijke, 2002), which has been cloned upstream of the herpes simplex virus thymidine kinase minimal promoter in a vector carrying EGFP (Le Dreau et al., 2012). The CAGA12:EGFP contains 12 synthetic SMAD3-specific response elements (-$CAGA_{12}$-) cloned in a vector carrying EGFP as a reporter gene (Dennler et al., 1998; Miguez et al., 2013).

Inhibition of endogenous SMAD activity was induced by electroporation of pSUPER or pSHIN vectors (2 µg/µl), which produce sh-RNAs that specifically target chick *SMAD1, SMAD2, SMAD3* and *SMAD5* and reduce to ~50% of their endogenous *mRNA* levels (Brummelkamp et al., 2002; Garcia-Campmany and Marti, 2007; Le Dreau et al., 2012; Miguez et al., 2013) (Table 2). The SMAD3-3S/D mutant was used at 0.25 µg/µl to rescue endogenous SMAD3 activity. As previously described (Garcia-Campmany and Marti, 2007), this pseudophosphorylated mutant version of SMAD3 was generated by PCR-mediated site-directed mutagenesis, replacing the three serines at the C-terminal end by aspartic acid, and cloned into PCIG.

The pCS2:membrane-GFP (Attardo et al., 2008) and the Sox2p:GFP reporter (Saade et al., 2013; Uchikawa et al., 2003) were used to follow cells *in vivo* by time-lapse imaging. The Sox2p:GFP reporter consists of an EGFP cassette from the ptk2:EGFP plasmid under the control of a fragment of the chicken Sox2 promoter covering the 7.6–14 kb of the Sox2 locus. This fragment (provided by M. Uchikawa, Osaka University, Osaka, Japan) has already been shown to specifically reproduce endogenous Sox2 promoter activity in the developing spinal cord (Le Dréau et al., 2014; Saade et al., 2013).

The CEP152-GFP vector (Origene, Clinisciences), encoding a centriolar component required for centriole duplication (Dzhindzhev et al., 2010; Saade et al., 2017), was electroporated at low concentration (200 ng/µl) to label the centrosomes. Alternatively, the ARL13B-RFP vector was electroporated at 50 ng/µl to follow primary cilia localisation and length (Caspary et al., 2007; Saade et al., 2017).

Table 1. Used DNA constructs

Recombinant DNA	Reference/Source
ARL13B-RFP	(Caspary et al., 2007; Saade et al., 2017)
BRE:GFP	(Korchynskyi and ten Dijke, 2002; Le Dreau et al., 2012)
CAGA12:GFP	(Dennler et al., 1998; Miguez et al., 2013)
CEP152-GFP	(Dzhindzhev et al., 2010; Saade et al., 2017)
pCAGGS:_ires_GFP	(Megason and McMahon, 2002)
pCS2:H2B-GFP	(Le Dréau et al., 2014)
pCS2:H2B-RFP	(Le Dréau et al., 2014)
pCS2:membrane-GFP	(Attardo et al., 2008)
pSHIN	(Kojima et al., 2004)
pSUPER	Oligoengine (cat# VEC-pBS-0002)
SMAD3-3S/D	(Garcia-Campmany and Marti, 2007)
Sox2p:GFP	(Saade et al., 2013; Uchikawa et al., 2003)

Table 2. Used sh-RNAs

sh-RNA	References and primer sequences
sh-SMAD1	(Le Dreau and Marti, 2012) F: CTGTGTCACAATTCCTCGG R: CCGAGGATTGTGACACAG
sh-SMAD5	(Le Dreau and Marti, 2012) F: TGCGACATTTCCAGATTCC R: GGAATCTGGAAATGTCGCA
sh-SMAD2	(Miguez et al., 2013) F:GATCCCCGGATTGAACCACAAAGCAATTCAAGAGATTGCTTTGTGGTTCAATCCTTTTTA R:AGCTTAAAAAGGATTGAACCACAAAGCAATCTCTTGAATTGCTTTGTGGTTCAATCCGGG
sh-SMAD3	(Garcia-Campmany and Marti, 2007) F:GATCCCCCGCTTCTGCCTTGGTCTGCTTCAAGAGAGCAGACCAAGCAGAAGCGTT TTTGGAAA R:AGCTTTTCCAAAAACGCTTCTGCTCTGGTCTGCTCTCTTGAAGCAGACCAAGGCAGAAGCGGGG

Chick *in ovo* electroporation

An Intracel Dual Pulse (TSS-20 Ovodyne) electroporator equipped with a footswitch was used to generate electric pulses. We separated a pair of platinum commercial electrodes (CUY610P1.5-1, Nepagene) and only used one side as the positive electrode. We incorporated a sharpened and bent 90º tungsten needle (Fine Science Tools) into a holder and used it as the negative "microelectrode" (Momose et al., 1999; Yasuda et al., 2000) (see Fig. 2C in Appendix II).

Eggs were horizontally incubated at 38.5°C in an atmosphere of 70% humidity until HH9 stage. DNA plasmids were diluted at 0.05-2µg/µl in 60% sucrose in sigma H2O (Sigma-Aldrich, W4502) with 50 ng/ml of Fast Green FCF (Sigma-Aldrich, F7258). Before manipulation, 5ml of albumen was removed from the egg with a syringe and a window was opened at the top of the shell to visualize the embryo (Selleck, 1996). Thin forceps were used to open a small hole in the posterior region of the area opaca, just outside of the area pellucida (see Fig. 2A in Appendix II). 200ml of 1% Penicillin/ Streptomycin (P/S) (Gibco, 15070063) were poured on top of the embryo to improve electrode conductivity. DNA solution was then injected onto the epiblast with a glass capillary by blowing air through an aspirator tube (Sigma-Aldrich, A5177-5EA). DNA was introduced with a glass capillary needle (GD-1, Narishige; made with Narishige PC-10 glass capillary puller) into the small concave region at their posterior end of the stage HH9 embryo, where the neural tube is still open (see Fig. 2A,B in Appendix II). The platinum electrode connected to the positive lead (+) was carefully inserted below the embryo through the hole made previously, parallel to its cranio-caudal axis (see Fig. 2A in Appendix II). The tungsten microelectrode connected to the negative lead (-) was then positioned on top of the embryo, also in parallel to its cranio-caudal axis. Five square pulses of 5V at intervals of 50 ms were delivered. The window in the shell was finally sealed with plastic tape and embryos were incubated until the desired stage.

Immunohistochemistry

Whole-mount immunohistochemistry

In toto embryo immunostaining procedure was carried out as follows:

- Chick embryos were removed from the egg at stage HH15 and fixed in 5ml 4% paraformaldehyde (PFA) (Sigma-Aldrich, 16005) in 1xPhosphate Buffered Saline (PBS) for 2 hours at room temperature (RT) or overnight at 4°C.
- Embryos were transferred to a 2ml tube, using a Pasteur pipette with the end cut off.
- Embryos were washed 3 x 30 min in 0.5% Triton-X-100 (Sigma-Aldrich, X100) in PBS (PBT).
- Embryos were incubated in blocking solution consisting of 0.5% PBT + 1% Albumin from Bovine Serum (BSA, Sigma-Aldrich, 9048-46-8), 0.2% sodium azide (Sigma-Aldrich, S2002) for 1h at RT.
- Embryos were incubated in blocking solution with primary antibody for 2 to 3 days at 4°C with gentle shaking.
- Following incubation, embryos were washed 3 x 1h in 0.5% PBT.
- Embryos were then incubated in blocking solution with secondary antibodies for 2 days at 4°C with gentle shaking.
- Embryos were washed 3 x 10 min in 0.5% PBT
- After washing, embryos were incubated overnight at 4oC with DAPI (1:1000) (Sigma) in 0.5% PBT.
- Finally, embryos were initially washed 3 x 10 min in PBT, followed by 3 longer 30 min washes, transferred to PBS and stocked at 4°C.

Various primary antibodies were used (Table 3) in combination with Alexa® Fluor (488, 555, 633) conjugated secondary antibodies (1:1000, Invitrogen).

Table 3. Used Primary Antibodies

Antibody	Source	Cat. Number	RRID	Host Sp	Conc
Acetylated Tubulin	Sigma	T6793	AB_477585	Mouse	1:1000
aPKC	Santa Cruz	SC-17781	AB_628148	Mouse	1:500
c-Caspase3	BD Biosciences	559565	AB_397274	Rabbit	1:500
Fibronectin	DSHB	B3/D6	AB_2105970	Mouse	1:1000
FOP (FGFR1OP)	Olivier Rosnet	Gift		Rabbit	1:1000
GM130	BD Biosciences	610822	AB_398141	Mouse	1:1000
Integrina6	DSHB	P2C62C4	AB_528301	Mouse	1:500
Integrinb1	DSHB	V2E9	AB_2128055	Mouse	1:1000
N-cadherin	ZYMED	13-2100	AB_2533007	Rat	1:500
Laminin-111	Sigma	L9393	AB_477163	Rabbit	1:1000
phospho-Histone3	Upstate	06-570	AB_310177	Rabbit	1:500
phospho-Histone3	Sigma	H9908	AB_260096	Rat	1:500
phospho-SMAD2/3	Santa Cruz	sc-11769-R	AB_2193189	Rabbit	1:100
Polyglutamilated Tubulin	Adipogen	AG20B-0020	AB_2490210	Mouse	1:1000
SMAD2	Cell signalling	D43B4	AB_10626777	Rabbit	1:250
SMAD3	Abcam	ab28379	AB_2192903	Rabbit	1:100
Sox2	Abcam	ab97959	AB_2341193	Rabbit	1:500
T/Bra	R&D	AF2085	AB_2200235	Goat	1:500
ZO-1	Invitrogen	339111	AB_2533147	Mouse	1:500

Free-floating sections immunohistochemistry

Immunostaining of transversal vibratome sections was carried out as follows:

- Chick embryos were removed from the egg at stage HH15 and fixed in 4% PFA in 1xPBS for 2 hours at RT or 4 h at 4°C.
- Embryos were embedded in plastic moulds with a warm 5% agarose - 10% sucrose matrix and cooled down to solidify.
- Agarose embryo-blocks were sectioned at 50-100μm thickness in a Leica Vibratome (VT1000S), obtaining free-floating transversal sections.
- Sections were washed 3 x 5 min in PBT (PBS + 0.1% Triton-X-100).
- Sections were incubated in blocking solution (10% BSA in PBT) for at least 30min at RT.
- Sections were incubated in antibody solution (1% BSA in PBT) with primary antibody overnight at 4ºC with gentle shaking.
- Following incubation, sections were washed 3 x 10 min in PBT.
- Sections were then incubated in secondary antibodies in antibody solution for 2 hours at room temperature.
- Finally, embryos were initially washed 3 x 10 min in PBT washes and transferred to water for glass-slide mounting, and covered by Mowiol (Sigma-Aldrich, 81381) and a glass-coverslip.

Various primary antibodies were used (Table 3) in combination with Alexa® Fluor (488, 555, 633) conjugated secondary antibodies (1:1000, Invitrogen).

Counter-stains

Counter-stains were added during incubation with the secondary antibody. DAPI (1:5000) was used to visualise nuclei (Sigma-Aldrich, D9542). TRITC conjugated phalloidin (1:1000) was used to visualize F-actin/tissue structure (Sigma-Aldrich, P1951).

In situ hybridisation

Embryos were removed from the egg at stage HH15 and fixed overnight at 4ºC in 4% PFA diluted in 1xPBS. The next day embryos were dehydrated with a series of increasing methanol concentration solutions (25%, 50%, 75% and 100% methanol). Embryos were then stored at -20 ºC for at least overnight. Whole-mount i*n situ* hybridisation was performed following standard procedures with the InsituPro VSi robot (Intavis). Each condition was replicated in two wells with 3-4 embryos each. Probes from the chicken EST project (http://www.chick.manchester.ac.uk/) were used at 1:200 (Table 4). Sonic hedgehog probe was always used as positive control. Hybridised embryos were post-fixed in 4% PFA, rinsed in PBT and embedded in plastic moulds with a warm 5% agarose - 10% sucrose matrix and cooled down to solidify. Agarose embryo-blocks were sectioned at 50µm thickness in a Leica Vibratome, obtaining free-floating transversal sections. Finally, sections were transferred to water for glass-slide mounting, and covered by Mowiol and a glass-coverslip.

Table 4. Used Probes

Symbol	EST/Source
α-*laminin*	ChEST869C13
BMP2	(Francis et al., 1994)
BMP4	(Francis et al., 1994)
BMP5	Randy Johnson
BMP6	Brian Houston
BMP7	Brian Houston
SMAD1	ChEST899n18
SMAD5	Marian Ros
SMAD8	ChEST222h17
TGF-β1	ChEST82G11
TGF-β2	ChEST852A23
TGF-β3	ChEST844B6
SMAD2	ChEST404C19
SMAD3	Juan Hurle
FGF2	Marian Ros
FGF4	Lee Niswander
FGF8	Scott M.K. Lee
NOTCH1	ChEST966G22
NOTCH2	ChEST1007G3

NOTCH4	Jill McMahon
DLL1	ChEST818o9
SHH	Bob Riddle & Cliff Tabin
WNT1	Jill McMahon
WNT3	ChEST441K4
WNT3A	ChEST1005M7
WNT4	ChEST934g18
WNT5A	ChEST2K9
WNT5B	ChEST178o13
WNT6	ChEST415K15
WNT7A	L. Burrus
WNT7B	Jill McMahon
WNT8A	Cliff Hume
WNT9A	ChEST482f1
WNT11	Jill McMahon

TUNEL staining in free-floating sections

The deoxynucleotidyl transferase–mediated deoxyuridinetriphosphate nick end labelling (TUNEL) assay was used to detect programmed cell death by apoptosis (Zakeri and Ahuja, 1994; Zakeri et al., 1993). The TUNEL assay was performed using the *In situ* cell death detection kit POD (Roche, 11 684 817 910) following the manufacturer instructions with some modifications. Embryos were removed from the egg at stage HH15 and fixed overnight at 4°C in 4% PFA diluted in 1xPBS. The next day embryos were dehydrated with a series of solutions with increasing methanol concentration (25%, 50%, 75% and 100% methanol). Embryos were stored at -20 °C for at least overnight and up to six months. Embryos were rehydrated and embedded in plastic moulds with a warm 5% agarose - 10% sucrose matrix and cooled down to solidify. Agarose embryo-blocks were sectioned at 50µm thickness in a Leica Vibratome, obtaining free-floating transversal sections. TUNEL staining was then performed and the most posterior sections were used as positive controls (Hirata and Hall, 2000). Colou r was developed using DAB substrate in a solution containing 0.3% H_2O_2, prepared following the manufacturer instructions (Sigma-Aldrich, 7411-49-6). DAB reaction was stopped by washing a few times in PBS pH=7. Finally, TUNEL stained sections were transferred to water for glass-slide mounting, and covered by Mowiol and a glass-coverslip.

Chick embryo *in vivo* time-lapse imaging

Mounting

Filter paper rings were prepared f rom 2 x 2 cm squares of Whatman grade 1 filter paper (Sigma-Aldrich, WHA1001325) in which a clover-leaf shaped hole was made in the centre with a paper punch, cutting the corners so that they fit in the round imaging plates (see Fig. 3A in Appendix II) (Chapman et al., 2001). Imaging plates were also prepared in advanced by bedding several Millicell cell culture plate

inserts (0.4 mm: Millipore, PICMORG50) with an Agar/Albumen mix (see Fig. 3C in Appendix II).

The tape-sealed window in the egg was reopened and the thick albumen surrounding and covering the embryo carefully removed with a soft tissue (Kimtech Science Kimwipes, 34155). A paper ring was placed on top of the vitelline membrane so that the embryo located in the center of the clover-shaped hole (see Fig. 3B in Appendix II), the vitelline membrane was cut through and around the whole perimeter of the filter paper ring and finally the filter with the embryo attached was pulled away from the yolk. Embryos with the best overall morphology and the greatest level of transgene expression were selected for imaging and transferred ventral side up to the imaging plates.

Imaging was performed inside a culture chamber created from a Corning ® Costar ® polystyrene 6-well plate (Sigma, CLS3736) (Benazeraf et al., 2010; Rupp et al., 2003). To favour the optics, the plastic in the lid was replaced with glass (see Fig. 3D in Appendix II). Each well of the culture chamber was filled with 1.5 mL of a solution of 5 ml thin albumen and 5 ml of 123 mM NaCl, the embryos in the imaging plates were transferred to the wells of the culture chamber and 1xPBS was added in between wells to maintain a moist environment inside the culture chamber. The culture chamber was finally sealed with electrical insulation tape (see Fig. 3E in Appendix II).

In vivo time-lapse imaging

Embryos were visualised under an upright wide-field microscope Axio Imager 2 (Zeiss) equipped with a motorized stage and an incubation chamber. The temperature was set to 39.5 °C so that the temperature at the level of the embryo was around 37.5 °C. The Experiment designer module of version 2.3 blue edition of the ZEN software (Zeiss) (RRID: SCR_013672) was used to set up the acquisition. For 5x objective, 10 z images every 10 minutes for 100 loops were acquired with a resolution of 1024x1024 binning 4x4 (see Fig. 4 in Appendix II). For 20x objective, 10 z images every 6 minutes for 150 loops were acquired with a resolution of 1024x1024 binning 4x4 (see Fig. 5 in Appendix II). The images of each embryo acquired were first time-stitched with the ZEN software (Zeiss) and then exported to Image J/Fiji software for image processing and analysis (see Appendix II).

Microscopy for fixed samples

Bright-field microscopy

In situ hybridisation and TUNEL processed sections were photographed under a Leica DMR microscope. The objectives used were a Leica HC Plan Fluotar 20X infinity (NA 0.5) or a Leica HC Plan Fluotar 40X infinity (NA 1.0), without any immersion medium. Images were improved with Adobe Photoshop CS5 (RRID: SCR_014199).

Confocal microscopy

Embryos were imaged on an inverted Zeiss LSM-780 confocal microscope, equipped with an Argon multiline gas laser at 488 nm, a DPSS laser at 561 nm and a HeNe laser at 633nm.

Whole-mount imaging

Two square 40x40mm coverslips were glued on top of a glass slide so that a narrow channel formed in the middle. Whole-mount immunostained stage HH15 chick embryos were then introduced in the narrow channel, and finally covered by Mowiol and a glass-coverslip. The objective used was a 25X (NA 0.75), glycerol immersion. Images were acquired from 25–80 optical sections spaced 2μM apart using ZEN software (Zeiss).

Imaging free-floating sections

Free-floating transversal sections were mounted on a glass-slide and covered by Mowiol and a glass-coverslip for imaging. The objectives used were a 40X (NA 1.3) or a 63X (NA 1.4), both oil immersion. Images were acquired from 5-20 optical sections spaced 0.5-1 μM apart using ZEN software (Zeiss). When intensity had to be quantified, confocal images were acquired maintaining the same laser and gain parameters.

3D lumen reconstruction

Raw whole-mount confocal data was exported to the Imaris software (Bitplane) (RRID:SCR_007370). The secondary forming lumen was reconstructed using the Contour Surface tool. The 3D structure was extracted by manually drawing the lumen contour, visible with ZO-1 immunostaining, on consecutive 2D z-slices.

Image analysis and quantifications

General Image Analysis

Raw confocal data was exported to ImageJ/FiJi (http://rsbweb.nih.gov/ij/)(RRID: SCR_003070) to be processed and analysed (Rueden et al., 2017; Schindelin et al., 2012). Projections of z-stacks are maximum projections unless otherwise indicated. Figures and schemes were generated using Adobe Illustrator CS5 (RRID: SCR_014199).

Quantifications in transversal sections

Nuclear SMAD3 intensity

Sh-SMAD3 and pSUPER control vectors were co-electroporated with H2B-RFP and stained with an antibody against endogenous SMAD3. Images from both conditions were acquired with the same laser and gain parameters. The polygon selection tool of ImageJ was used to delineate H2B-RFP+ cell nuclei and the integrated density was measured. Results are presented in GraphPad Prism 6 box & whisker plots.

Cell death

Cleaved-Caspase3 (c-Caspase3) antibody was used to detect apoptosis in fixed transversal sections of stage HH15 chick embryos. For WT quantifications, we counted both the number of c-Capase3+

cells and the number of total DAPI cells. For electroporated embryos, we counted c-Caspase3+ cells, H2B-RFP+ cells and total cells (DAPI). Percentages were then calculated and presented in GraphPad Prism 6 bar graphs.

Proliferation

Phospho-histone 3 (pH3) antibody was used to detect mitotic cells in fixed transversal sections of stage HH15 chick embryos. For WT quantifications, we counted both the number of pH3+ cells and the number of total DAPI cells. For electroporated embryos, we counted pH3+ cells, H2B-RFP+ cells and total cells (DAPI). Percentages were then calculated and presented in GraphPad Prism 6 bar graphs.

Sox2 and T/Bra nuclear intensities

Images from fixed transversal sections of stage HH15 chick embryos stained for Sox2 and T/Bra antibodies were acquired with the same gain and laser parameters. The area, integrated density and mean grey value were measured for each nucleus and for three neighbouring selections with no fluorescence (background measurements). The level of fluorescence in the nucleus was then determined with the corrected total cell fluorescence (CTCF). CTCF is calculated with the formula CTCF= Integrated nuclear density – (Area of selected nucleus x Mean fluorescence of background readings). Log10 (CTCF) was finally calculated and represented in GraphPad Prism 6 box & whisker plots.

Images from fixed stage HH15 transversal sections stained for Sox2, T/Bra and Fibronectin were used to correlate nuclear intensities (CTCF) with cell distance from the basement membrane (BM). A straight line was drawn with the ImageJ command from the centre of the nucleus to the closest Fibronectin staining and distance was measured. Results are presented in GraphPad Prism 6 linear regression plots. We considered peripheral cells those in contact with the BM and central cells those located further than 40µM from BM.

Sh-SMAD3 and H2B-RFP control vectors were electroporated and stained with an antibody against Sox2. Images were acquired with the same parameters and analysed. The polygon selection tool of ImageJ was used to delineate electroporated cell nuclei and the integrated density of Sox2 nuclear staining was measured. For each selected H2B-RFP+ positive nucleus, three nucleus of non-electroporated neighbouring cells (negative for H2B-RFP) were also delimited and their Sox2 integrated density measured. The following ratio was then calculated: integrated density of nuclear Sox2 H2B-RFP + cell/mean integrated density of three H2B-RFP- neighbouring cells. Results are presented in GraphPad Prism 6 box & whisker plots.

Cell shape

Actin staining (Phalloidin) was used to visualize cell shape in WT, pSUPER control and sh-SMAD3 transversal sections. Cells were delimited with the polygon selection tool and cell shape was quantified by measuring cell circularity, a parameter included in ImageJ Shape descriptors. Circularity is calculated with the formula $4\pi\times[\text{Area}]/[\text{Perimeter}]^2$, with a value of 1.0 indicating a perfect circle. As the value approaches 0.0, it indicates an increasingly elongated shape. Results are presented in GraphPad Prism 6 box & whisker plots.

Centrosome positioning

The centrosomes were visualized with FOP antibody and DAPI was used to stain the nucleus in WT, pSUPER control and sh-SMAD3 transversal sections. The straight-line tool of ImageJ was used to draw a line from the centrosomes to the edge of the nucleus and the distance was measured. Results are presented in GraphPad Prism 6 box & whisker plots.

Golgi measurements

Basal-most Golgi

The centrosomes and the Golgi apparatus were visualized with FOP and GM130 antibodies, respectively, in HH15 WT transversal sections. The straight-line tool of ImageJ was used to draw a line from the centrosomes to the distal end of GM130 staining and the distance was measured. Results are presented in GraphPad Prism 6 box & whisker plots showing all points, median and interquartile range.

Golgi extension

The Golgi apparatus was visualized with GM130 antibody in pSUPER control and sh-SMAD3 transversal sections. The straight-line tool of ImageJ was used to draw a line from the apical to the basal limit of GM130 staining and its length was measured. Results are presented in GraphPad Prism 6 box & whisker plots.

Sequence of protein polarisation

Fixed transversal confocal images of FOP, N-cadherin, ZO-1, aPKC and β1 Integrin in the polarising medullary cord were used to define the sequence of epithelial polarity acquisition. Co-stainings were used to analyse the presence or absence of the mentioned components in each cell. We calculated the percentage of cells with: i. only the centrosome localised apically; ii. apically localised centrosome and apical N-cadherin; iii. apical centrosome, apical N-cadherin and apical ZO-1; iv. apical centrosome, apical N-cadherin and apical aPKC; v. apical centrosome and basal β1 integrin and vi. apical centrosome, basal β1 integrin and apical N-cadherin. Results are represented in GraphPad Prism 6 stacked bar graphs.

Cell length and distance from lumen foci to basement membrane

Actin staining (phalloidin) and DAPI were used to visualize cell shape and cell nuclei in transversal control sections at the lumen initiation stage. The straight-line tool of ImageJ was used to draw a line along the length of the cell and its distance was measured. aPKC and Laminin were used to visualise the small lumen foci and the basal lamina, respectively, in control and sh-SMAD3 transversal sections at the lumen initiation stage. A straight line was drawn from the lumen foci to the closest laminin staining with the ImageJ command. Results are presented in GraphPad Prism 6 box & whisker plots.

SMAD apico-basal intensity profiles

CEP152-GFP was electroporated in order to detect the two centrioles in chick neuroepithelial cells. CEP152-GFP electroporated embryos were co-stained with polyglutamilated tubulin, to visualize the primary cilium, and SMAD3, phSMAD2/3 and SMAD2 antibodies to study their localisation. Intensity profiles were generated with the Plot profile ImageJ command by drawing a straight line from

the apical tip of the primary cilium to the basal daughter centriole. Intensity for the stained proteins was then measured along the drawn line.

Ciliary SMAD3 intensity

Sh-SMAD3 and pSUPER control vectors were co-electroporated with PCIG and stained with antibodies against endogenous SMAD3 and Polyglutamilated Tubulin, the last for visualizing primary cilia. Images from both conditions were acquired with the same laser and gain parameters. The polygon selection tool of ImageJ was used to delineate the accumulated SMAD3 at the cilia base and integrated density was measured. Results are presented in GraphPad Prism 6 box & whisker plots.

Ciliary length

The length of primary cilia was quantified in ARL13B-RFP electroporated embryos, in combination with control pSUPER+PCIG, sh-SMAD3+PCIG, sh-SMAD2, SMAD3-3S/D or sh-SMAD3+SMAD3-3S/D. A straight or segmented line was drawn onto the ARL13B-RFP staining of each cell and length was measured with the ImageJ command. Results are represented in GraphPad Prism 6 box & whisker plots.

Quantifications in time-lapse movies

Distance to last pair of somites

The distance to the last pair of somites was measured in the generated movies (membrane-GFP or sh-SMAD3 and pSUPER control co-electroporated with Sox2p:GFP). Cell divisions of mesenchymal cells in the centre of the tissue were spotted and the first time point where mitotic rounding was detected was analysed. A straight line was drawn from the mitosis to the level of the last pair of somites, visible in bright-field images, with the ImageJ straight-line tool. Distance was measured and presented in GraphPad Prism 6 box & whisker plots.

Distance from centre

A straight line was drawn in the centre of the neural tube by following the lumen in all movie time points. membrane-GFP+, sh-SMAD3 Sox2p:GFP + or pSUPER control Sox2p:GFP + mitosis were spotted and tracked back until the beginning of the movie. The distance from the drawn midline to the analysed cell and their daughter cells was measured in each time point with the ImageJ straight-line tool. Results along time are presented in GraphPad Prism 6 linear regression graphs.

Circularity

membrane-GFP+, sh-SMAD3 Sox2p:GFP + or pSUPER control Sox2p:GFP+ cell divisions were spotted in time-lapse movies and tracked back until the beginning of the movie. Cells were delimited with the polygon selection tool of Image J and cell shape was quantified by measuring cell circularity in each time point. Circularity is calculated with the formula $4\pi\times[\text{Area}]/[\text{Perimeter}]^2$, with a value of 1.0 indicating a perfect circle. As the value approaches 0.0, it indicates an increasingly elongated shape. Results along time are presented in GraphPad Prism 6 linear regression graphs.

Statistical analysis

Quantitative data is expressed as mean±sem/SD or as median±IQR. Statistical analysis was performed using the GraphPad Prism 6 (RRID: SCR_002798). Significance was assessed by performing the Mann-Whitney test when comparing two populations or the Kruskal-Wallis when comparing more than two. In this later case, Dunn's multiple comparisons test was also run. In the few cases were data followed a normal distribution, assessed with the D'Agostino Pearson omnibus normality test, one-way ANOVA was performed. In this later case, Tukey's multiple comparisons test was also run *(*$p<0.05$, **$p<0.01$*, and ***$p<0.001$*).

RESULTS

Secondary neural tube (SNT) formation in the chick embryo

During vertebrate development, neuromesodermal progenitors (NMPs) are recruited to elongate the caudal body axis and drive the caudal elongation of the neural tube (NT). These bipotential progenitor cells converge onto the dorsal midline and generate neural progenitor cells (NPCs) by undergoing mesenchymal-to-epithelial transition (MET). The MET is the central event of secondary neurulation (SN), along with the formation of a compact medullary cord and the opening of the secondary neural tube (SNT) lumen. The complete process can be followed in stage HH15 chick embryos (Hamburger and Hamilton, 1992), as different degrees of polarisation exist along the cranio-caudal axis (Fig. 15A-G). In the caudal most region, NMPs drive body axis elongation, while in more cranial regions these cells become confined around the dorsal tissue midline (Fig. 15C,D), undergo MET and initiate lumens (Fig. 15E). The first cells to epithelialize locate at the periphery of the medullary cord, while central cells remain mesenchymal until the very end of the process. It is between these two cell populations that small cavities of varied size and shape form and later resolve to form the single central lumen of the secondary neural tube (SNT) (Fig. 15F,G).

Morphogenesis of the SNT requires SMAD3 mediated TGF-β activity

To search for the extrinsic signals instructing SNT formation, we *in vivo* assessed the endogenous activity of the BMP/TGF-β pathways, which are known to play key roles in anterior NT formation (Le Dreau and Marti, 2012; Ulloa and Briscoe, 2007). BMP/TGF-β canonical signalling is substantially linear; dimers of ligands bind to a defined receptor complex composed of transmembrane serine/threonine kinases, which propagate the signal through the SMAD family of transcription factors (Fig. 16A,B). Electroporation of a BMP- (BRE:GFP) (Le Dreau et al., 2012) or a TGF-β-responsive (CAGA12:GFP) (Miguez et al., 2013) fluorescent reporter, together with a control H2B-RFP vector at stage HH9 showed 24hours post-electroporation (hpe) (Fig. 16C) that both pathways are active in the developing chick embryo SNT (Fig. 16D,E).

In order to test for the contribution of canonical BMP and TGF-β signalling in SNT formation, we analysed the consequences of SMAD inhibition, following electroporation of short-hairpin RNA targeting specific chick *SMAD mRNAs* - which are expressed at different levels in the forming SNT (Fig. 17A-H). BMP signalling appeared to be dispensable for the correct morphogenesis of the SNT, since inhibition of SMAD1/5 resulted in the formation of a normal SNT (Fig. 16H-J). Electroporation of sh-SMAD2, although efficiently inhibited endogenous SMAD2 expression (Miguez et al., 2013), was not sufficient to perturb SNT formation (Fig. 16K). However, inhibition of the TGF-β effector SMAD3 resulted in an aberrant SNT, exhibiting multiple small lumens along the cranio-caudal (Fig. 16F,G) and the dorso-ventral axes (Fig. 16L).

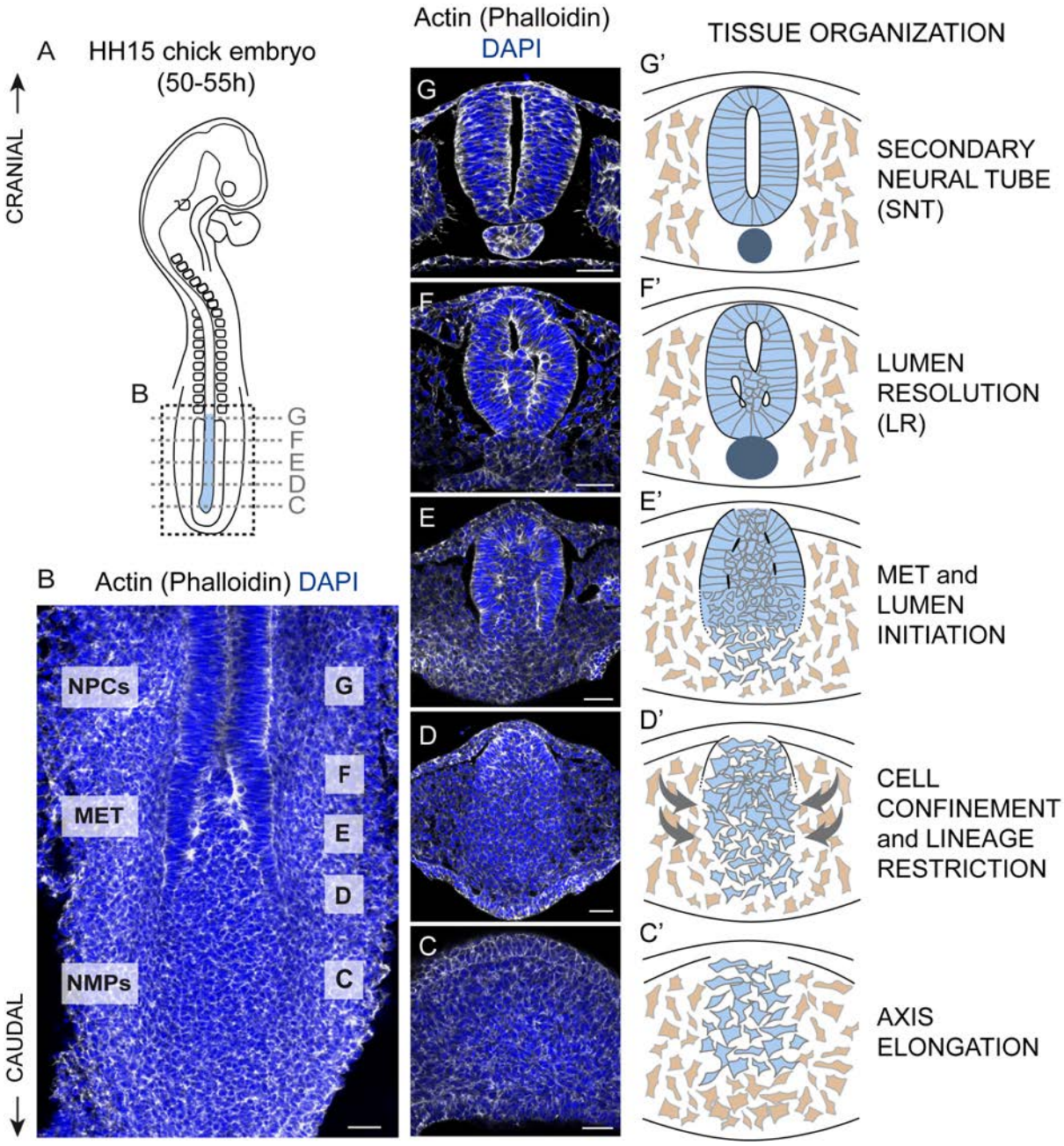

Figure 15. Chick secondary neurulation (SN). (A) Drawing of a stage HH15 chick embryo showing the caudal region where SN is taking place. The progression of SN can be followed along the cranio-caudal axis of the same embryo. **(B)** Dorsal view of the boxed region in A showing the distribution of actin (Phalloidin, white). DAPI (blue) stains cell nuclei. The cells in posterior regions are mesenchymal neuromesodermal progenitors (NMPs), those in the intermediate regions are undergoing the mesenchymal-to-epithelial transition (MET) and the anterior cells are epithelial neural progenitor cells (NPCs). The transverse sections in C-G correspond to different levels along the cranio-caudal axis. Scale bar = 40 μm. **(C-G)** Transverse sections at different cranio-caudal levels showing the distribution of actin (white). DAPI (blue) stains cell nuclei. Scale bars = 40 μm. **(C'-G')** Schematic representation of chick SN showing major tissue rearrangements. SN undergoing cells are shown in light blue, the surrounding mesoderm is in brown and the notochord appears in dark blue. **(C'-D')** Chick SN starts with the condensation and confinement of NMPs in the centre of the tissue and the formation of a solid medullary chord (grey arrows). **(E')** Cells located dorsally and at the periphery of the medullary chord are the first to undergo the MET. Epithelialization propagates ventrally, although the cells in the centre of the tissue remain mesenchymal and small lumens open up between the peripheral epithelial and central mesenchymal cell populations. **(F')** The small cavities formed coalesce to form a single central lumen. **(G')** The result of this process is that a hollow secondary neural tube (SNT) is formed that is surrounded by NPCs.

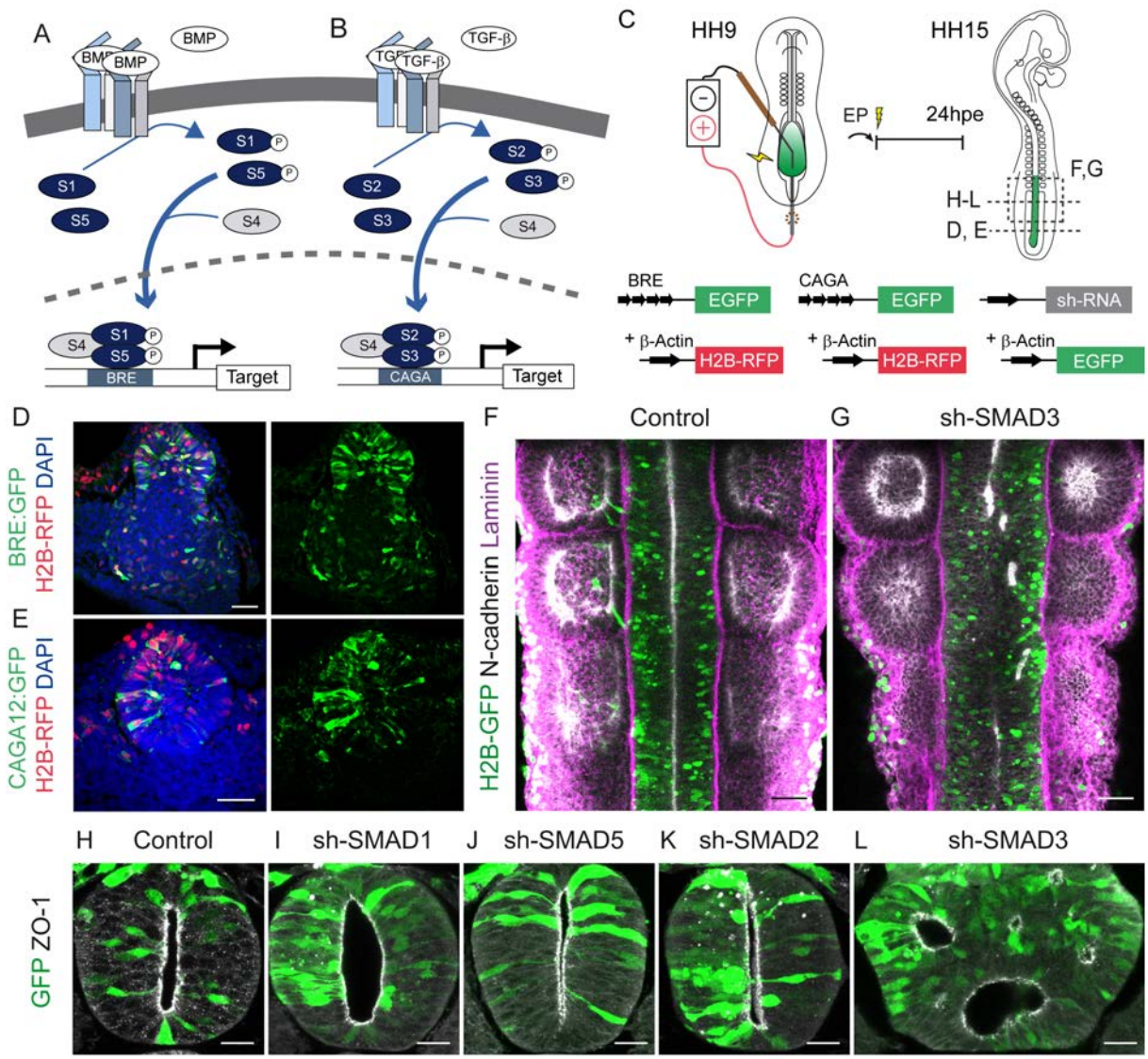

Figure 16. SNT formation in the chick embryo requires SMAD3 activity. (A,B) Scheme summarizing the BMP and TGF-β signalling components. **(C)** Scheme showing the method and timing of the co-electroporation in chick embryos and the electroporated DNAs (EP, electroporation; hpe, hours post-electroporation). **(D)** The BMP reporter is active in NMPs, 24hpe of BRE:GFP (green) and control H2B-RFP (red). DAPI (blue) stains nuclei. Scale bar = 40 μm. **(E)** The TGF-β reporter is active in NMPs, 24hpe of CAGA12:GFP (green) and control H2B-RFP (red). DAPI (blue) stains nuclei. Scale bar = 40 μm. **(F,G)** Dorsal views of control H2B-GFP (green, F) or sh-SMAD3 (green, G) electroporated NTs. N-cadherin (white) lines the NT lumen and laminin (pink) stains the basement membrane and somites. Scale bars = 40 μm. **(H-L)** Selected images of transverse sections 24hpe of the indicated DNAs (green), ZO-1 staining (white) lines the NT lumen. sh-SMAD3 electroporation results in multiple lumens (L). Scale bar = 20 μm.

Interestingly, SMAD3 appeared highly expressed in polarizing NMPs at the dorsal periphery of the chord and then spread to the whole developing SNT (Fig. 17H). Additionally, electroporation of the TGF-β-responsive CAGA12:GFP fluorescent reporter, which is indeed specific to SMAD3 activity (Miguez et al., 2013), together with a control H2B-RFP vector showed 24hpe high caudal activity and within the SN region, while control H2B-RFP+ cells were found along the whole cranio-caudal axis (Fig. 18A). Finally, while sh-SMAD3 electroporation efficiently decreased endogenous SMAD3 levels (median±IQR integrated density control=543.1±486.7 vs sh-SMAD3=148.6±113.5: Fig. 18B,C), it did not compromise tissue or NMPs viability, as assessed by the rate of apoptosis and proliferation of total cells (mean±SD %c-Casp3+ cells control=1.9±1.0 vs sh-SMAD3=3.0±1.8: Fig. 18D,E; mean±SD %pH3+ cells control=4.7±1.5 vs sh-SMAD3=3.8±1.1: Fig. 18D,F) and electroporated cells (mean±SD %c-Casp3 H2B-RFP+ cells control=3.1±3.3 vs sh-SMAD3=4.0±1.9: Fig. 18D,G; mean±SD %pH3+ H2B-RFP+ cells control=3.4±2.5 vs sh-SMAD3=3.4±2.1: Fig. 18D,H), respectively. All these observations prompted us to search for the precise cellular events regulated by TGF-β/SMAD3 signalling, that might be instructive for SNT formation.

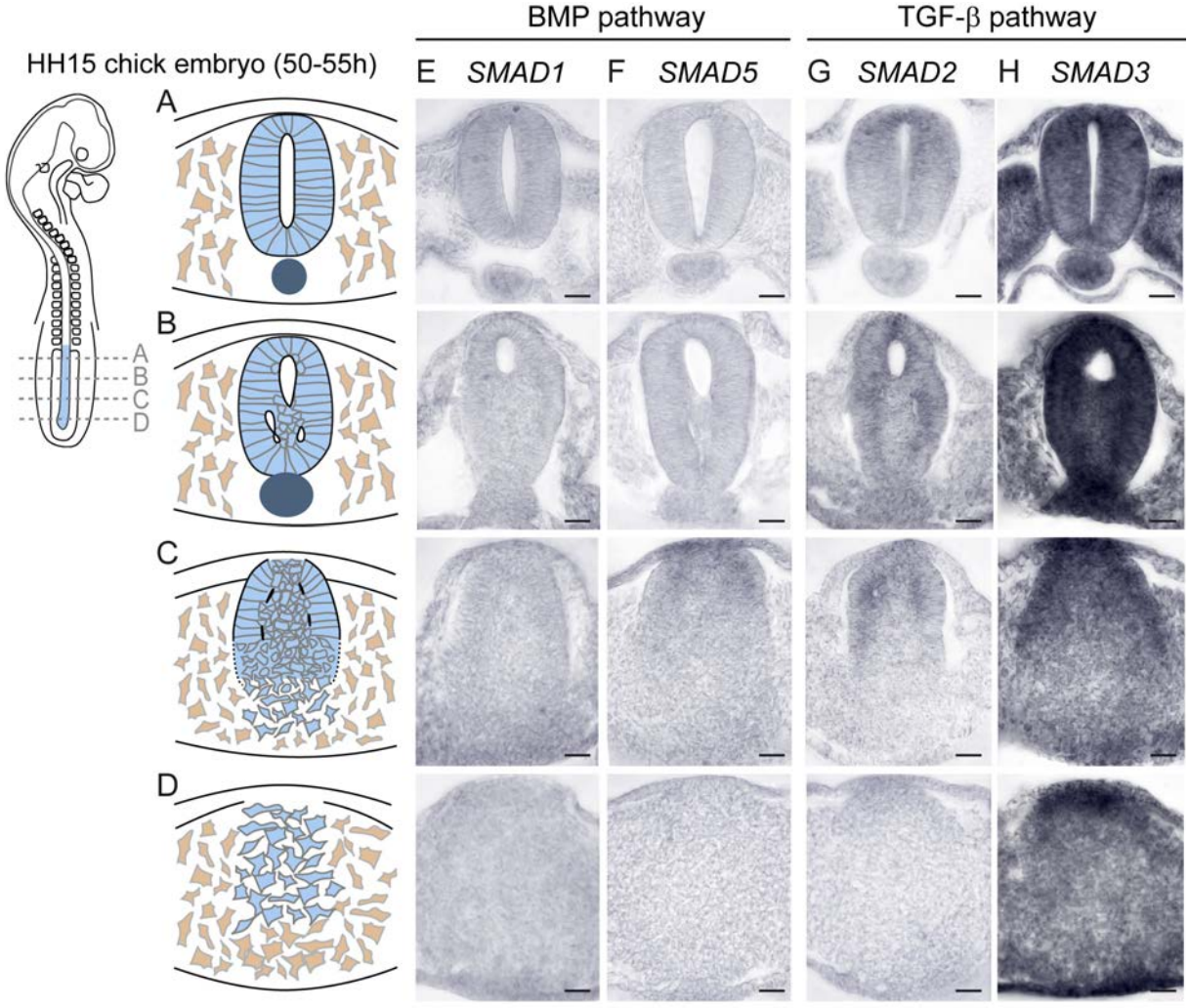

Figure 17. Expression analysis of the BMP and TGF-β SMADs in the developing SNT. (A-D) Drawing of a stage HH15 chick embryo and the cellular processes occurring along the cranio-caudal axis during SNT formation. **(E-I)** Selected images of transverse sections at A-D cranio-caudal levels hybridised with probes for the indicated ***mRNAs***. Scale bars = 20 μm.

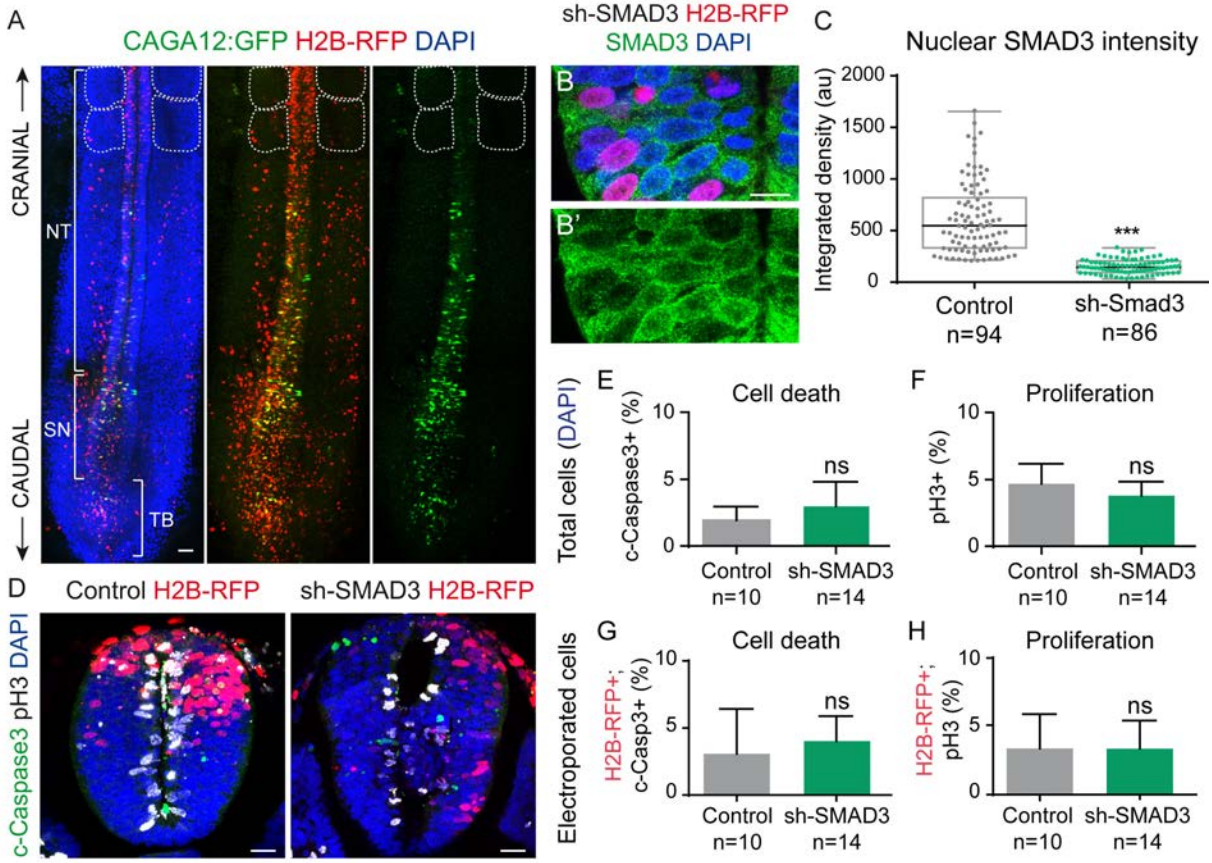

Figure 18. SMAD3 activity in the forming SNT. (A) Dorsal view of CAGA12:GFP (green) and control H2B-RFP (red) 24hpe co-electroporation. DAPI (blue) stains nuclei. Dotted lines delineate somites. NT, neural tube; SN, secondary neurulation region; TB, tail bud. Scale bar = 40 μm. **(B)** Selected image of transverse sections 24hpe of sh-SMAD3 and control H2B-RFP (red) co-electroporation. DAPI (blue) stains cell nuclei. Anti-SMAD3 (green) stains endogenous SMAD3, for protein quantification plotted in C. Scale bars = 40 μm. **(C)** Plots fluorescence nuclear intensity in control and sh-SMAD3 electroporated cells (horizontal bold lines show the median; n=94, 86 cells from 10 embryos/condition; ***p<0.001 Mann-Whitney test). **(D)** Selected images of transverse sections 24hpe of control or sh-SMAD3, electroporated together with control H2B-RFP (red). DAPI (blue) stains cell nuclei, pH3 (white) stains dividing cells, c-Caspase3 (green) stains apoptotic cells. Scale bars = 20 μm. **(E)** Plots the percentage of c-Caspase3+ cells/total cell number (DAPI) in control and sh-SMAD3 electroporated embryos (plot shows the mean±SD; n=10-14 embryos/condition; p>0.05 Mann-Whitney test). **(F)** Plots the percentage of mitotic pH3+ cells/total cell number (DAPI) in control and sh-SMAD3 electroporated embryos (plot shows the mean±SD; n=10-14 embryos/condition; p>0.05 Mann-Whitney test). **(G)** Plots the percentage of c-Caspase3+ H2B-RFP+ cells/total H2B-RFP+ cells in control and sh-SMAD3 electroporated embryos (plot shows the mean±SD; n=10-14 embryos/condition; p>0.05 Mann-Whitney test). **(H)** Plots the percentage of mitotic pH3+ H2B-RFP+ cells/total H2B-RFP+ cells in control and sh-SMAD3 electroporated embryos (plot shows the mean±SD; n=10-14 embryos/condition; p>0.05 Mann-Whitney test).

Cell confinement of NMPs and restriction into NPCs are independent of SMAD3 activity

Tail bud NMPs will generate NPCs of the SNT and trunk mesodermal tissues. The co-expression of the transcription factors T/Brachyury (T/Bra) and Sox2 characterize NMPs, and NPCs emerging from dual fated NMPs downregulate T/Bra but maintain high Sox2 expression (Gouti et al., 2014; Kondoh and Takemoto, 2012; Olivera-Martinez et al., 2012; Tsakiridis and Wilson, 2015; Wymeersch et al., 2016). The complete neural lineage restriction process can be followed in the same stage HH15 chick embryo, by analyzing endogenous T/Bra and Sox2 at several axial levels, from the caudal tail bud

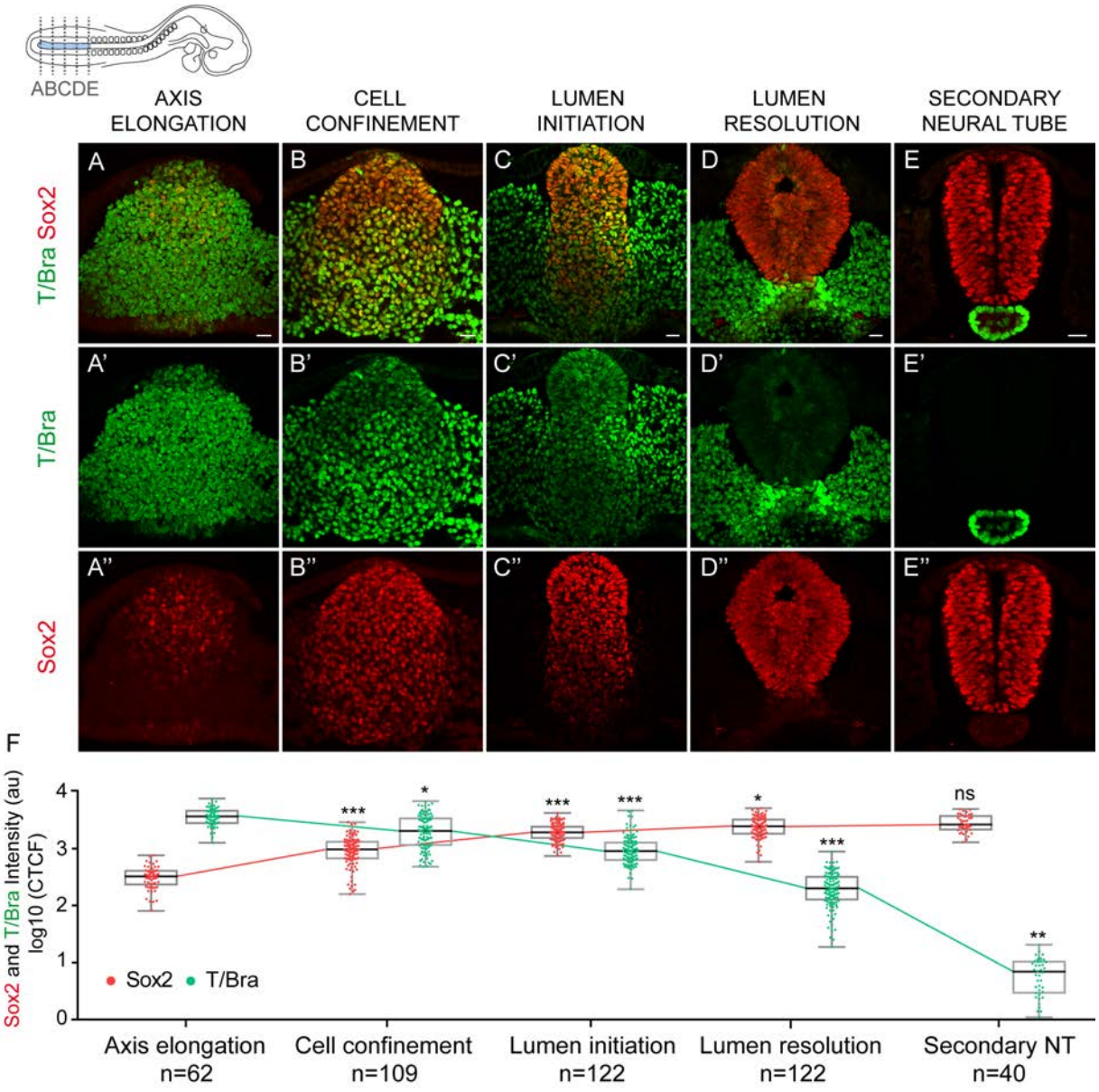

Figure 19. Lineage restriction of NMPs into NPCs is characterised by T/Bra downregulation and Sox2 upregulation. (A-E) Selected images of transverse sections at the indicated cranio-caudal levels, stained for T/Bra (green) and Sox2 (red). Scale bars = 20 μm. **(F)** Plots fluorescence nuclear intensity of T/Bra and Sox2 at the indicated tissue remodeling events (horizontal bold lines show the median; n=62, 109, 122, 122, 40 cells from 10 embryos; *p<0.05, **p<0.01, ***p<0.001 Kruskal-Wallis test).

to the cranial SNT (Fig. 19A-E). At initial stages, T/Bra is broadly expressed in the tailbud, including in the lateral mesoderm here excluded from quantifications, downregulated along SN and finally restricted to the notochord (Fig. 19A'-E'). Low levels of Sox2 expression already appeared in the early tailbud, in a dorsal and central area (Fig. 19A''), from where Sox2 expression propagated ventrally (Fig. 19B''), suggesting that the differentiation of NPCs in the medullary cord advances in a dorso-ventral direction. Sox2 expression was finally confined to the SNT (Fig. 19E'').

Quantification of endogenous T/Bra and Sox2 within the SN-undergoing region not only revealed a strong decrease of T/Bra expression along SN (median±IQR log10 of T/Bra CTCF axis elongation=3.6±0.2; cell confinement=3.3±0.5; lumen initiation=3.0±0.3; lumen resolution=2.3±0.4; SNT=0.8±0.5: Fig. 19A'-E',F), but also an increase of Sox2 levels (median±IQR log10 of Sox2 CTCF axis elongation=2.5±0.2; cell confinement=3.0±0.3; lumen initiation=3.3±0.2; lumen resolution=3.4±0.2; SNT=3.4±0.2: Fig. 19A''-E'',F), consequent with the progressive generation of NPCs. The expression of T/Bra and Sox2 gradually changed over time in the developing SNT, suggesting the existence of a transitional state in the path from NMPs to NPCs. We have termed the transiting cells as pre-secondary neural tube (PSNT) cells, in concordance to the pre-neural tube (PNT) cell state found in primary development (Olivera-Martinez et al., 2014). PSNT cells with increasing Sox2 levels and decreasing T/Bra levels are present at the cell confinement and MET/lumen initiation stages, but by the time the lumen resolves, cells present very low levels of T/Bra (Fig. 19D') and Sox2 levels already reached those of the SNT (Fig. 19F). Thus, we have considered here that NMPs have restricted to NPCs by the lumen resolution stage.

The developing SNT becomes gradually confined by a basement membrane (BM), which is also assembled in a dorso-ventral fashion, as shown by the analysis of laminin and fibronectin localisation along the cranio-caudal axis in stage HH15 chick embryos (Fig. 20A-D). At tail bud stages, a BM underlies the dorsal ectoderm and separates it from internal tissues (Fig. 20A). Eventually, a new BM starts growing at each side of the prospective medullary cord, from the dorsal ectodermal BM towards ventral regions. PSNT cells are gradually confined to central regions of the tissue and segregated from the lateral mesoderm, in a dorso-ventral direction (Fig. 20B). The examination of α-*laminin RNA* expression by *in situ* hybridisation revealed that it is synthesized by the NMPs at the onset of SN, upregulated in PSNT cells and maintained all along the process (Fig. 20G). The result of this process is a SNT enclosed by a BM composed of both laminin and fibronectin (Fig. 20D). Integrin receptors are also expressed in NMPs and co-localise with BM components, suggesting a possible instructive role for the BM-integrin signalling axis in the SN process (Fig. 20E-F).

Indeed, we found a positive correlation between T/Bra expression and distance to the BM, and a converse negative correlation between Sox2 expression and distance to the BM (Fig. 21A,B). Moreover, during cell confinement, lumen initiation and lumen resolution, the expression levels of T/Bra are high in central cells as compared to peripheral cells (median±IQR log10 of T/Bra CTCF peripheral cells at cell confinement=3.1±0.3; lumen initiation=2.9±0.3; lumen resolution=2.2±0.4 vs central cells at cell confinement=3.5±0.3; lumen initiation=3.1±0.3; lumen resolution=2.4±0.3: Fig. 21D). Conversely, the levels of expression of Sox2 are high in peripheral cells, as compared to central cells (median±IQR log10 of Sox2 CTCF peripheral cells at cell confinement=3.1±0.2; lumen initiation =3.3±0.2; lumen resolution=3.5±0.2 vs central cells at cell confinement=2.9±0.4; lumen initiation=3.2±0.2; lumen resolution=3.3±0.2: Fig. 21E). In summary, T/Bra+ and Sox2+ NMPs

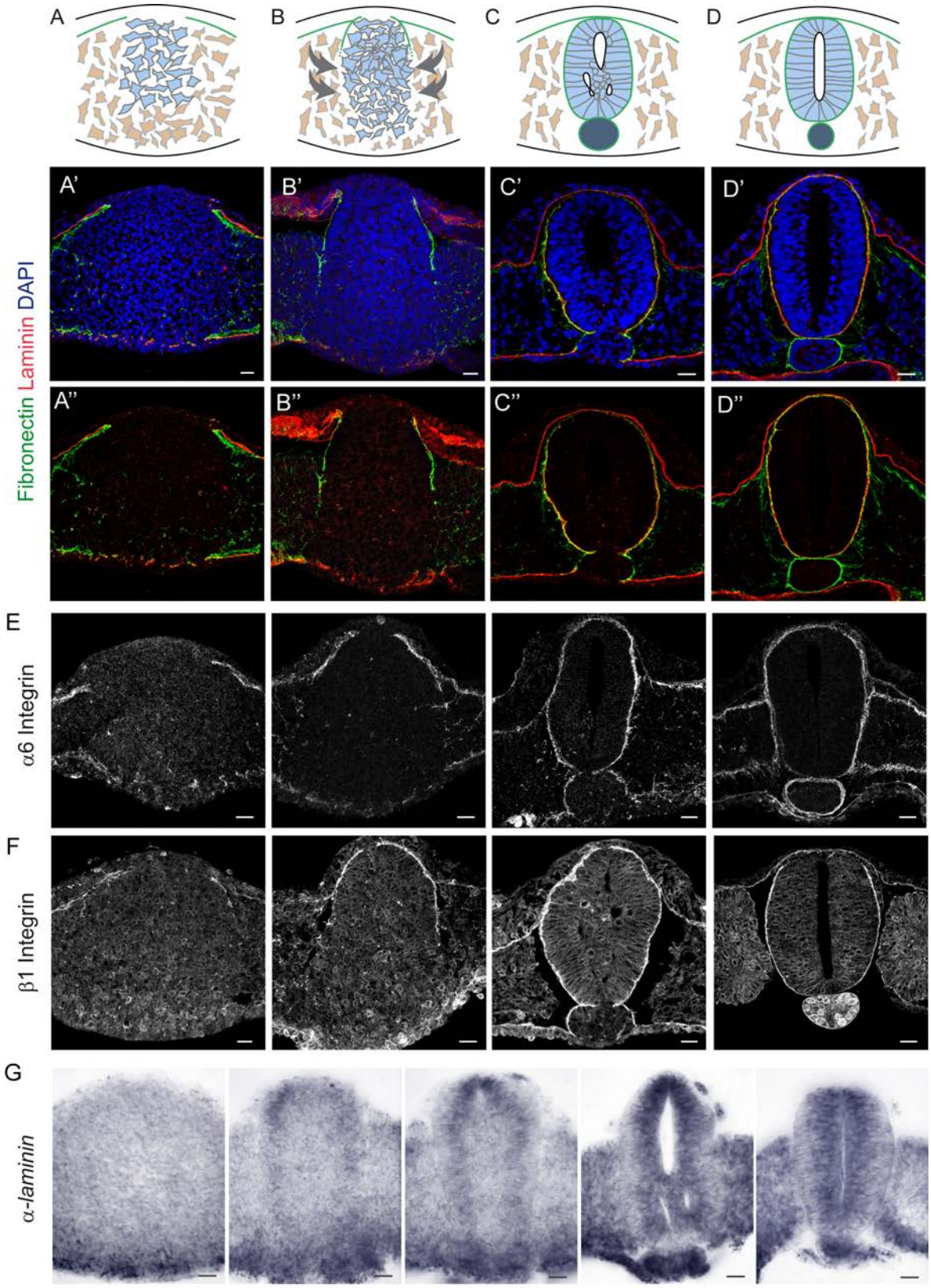

Figure 20. The basement membrane (BM) assembles in a dorso-ventral direction. (A-D) Schemes showing the cellular processes occurring during SN and selected images of transverse sections at the indicated cranio-caudal levels, co-stained for the BM proteins fibronectin (green) and laminin (red). DAPI (blue) stains cell nuclei. The developing BM is depicted in green in schemes. Scale bars = 20 μm. **(E-F)** Selected images of transverse sections of the developing SNT stained for α6 and β1 integrin (grey). Scale bars = 20 μm. (**G)** Selected images of transverse sections hybridised with α-*laminin mRNA* probe. Scale bars = 20 μm.

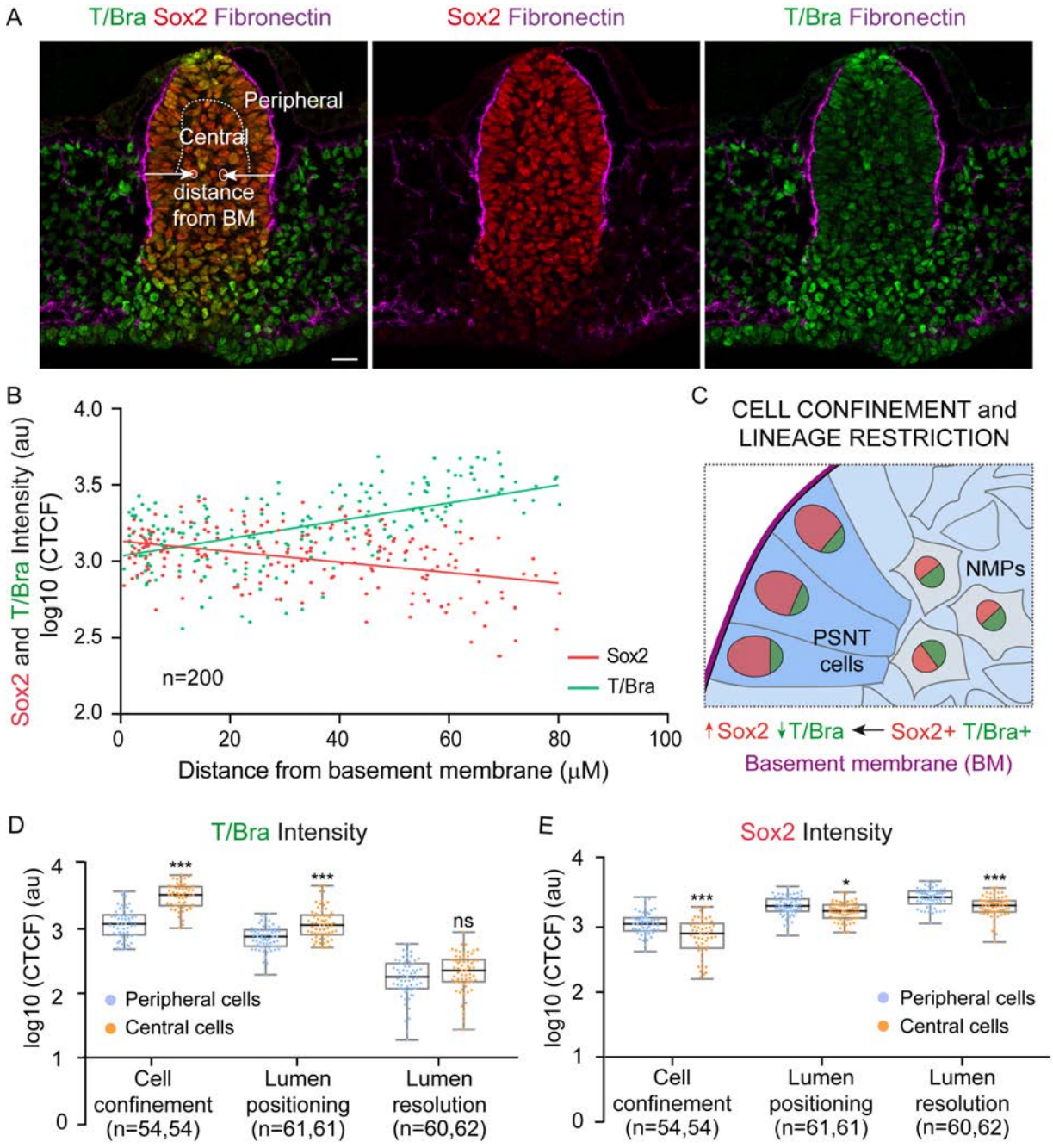

Figure 21. Lineage restriction of NMPs in association to the BM. (A) Selected image of transverse sections, stained for T/Bra (green), Sox2 (red) and Fibronectin (purple). Dotted white line separates peripheral and central cell populations. The method for measuring cell nucleus distance from the basement membrane (BM) plotted in B is also shown. Scale bar = 20 μm. **(B)** Plots fluorescence nuclear intensity of T/Bra and Sox2, at the indicated distance from the BM. **(C)** Scheme showing SNT developing section and the lineage restriction of NMPs into PSNT cells. Cells contacting the BM (purple) are the first to convert to PSNT cells, this transition being characterised by T/Bra downregulation and Sox2 upregulation. **(D)** Plots T/Bra fluorescence nuclear intensity in central and peripheral NPCs, at the indicated tissue remodelling events (horizontal bold lines show the median; n=54,54; 61, 61; 60,62 cells from 10 embryos; ***p<0.001 Kruskal-Wallis test). **(E)** Plots Sox2 fluorescence nuclear intensity in central and peripheral NPCs, at the indicated tissue remodelling events (horizontal bold lines show the median; n=54,54; 61, 61; 60,62 cells from 10 embryos; *p<0.05, ***p<0.001 Kruskal-Wallis test).

convert to NPCs by downregulating T/Bra and upregulating Sox2 and this event first occurs in peripheral cells contacting the BM, which transit through an intermediate PSNT state to generate NPCs (Fig. 21C). Altogether, these observations place the BM as a possible instructor for neural lineage restriction in the developing SNT.

In order to test for a possible role of canonical TGF-β signalling in NMPs lineage restriction, we analysed endogenous T/Bra and Sox2 levels, 24hpe of sh-SMAD3 electroporation (Fig. 22A). Results showed that T/Bra is progressively downregulated in NMPs electroporated with sh-SMAD3, although it remained high in the surrounding lateral mesodermal cells, as well as in axial notochord cells (Fig. 22B). Sox2 levels in sh-SMAD3 electroporated NPCs were comparable to surrounding non-electroporated cells (median±IQR Sox2 intensity ratio control=0.7±0.3 vs sh-SMAD3=0.8±0.4: Fig. 22B,C) and Sox2+ cells were progressively restricted to the SNT (Fig. 22E). Moreover, a BM properly confines the SNT 24hpe of sh-SMAD3 electroporation (Fig. 16G). All these observations indicate that SMAD3 activity does not affect cell confinement and is dispensable for neural lineage restriction.

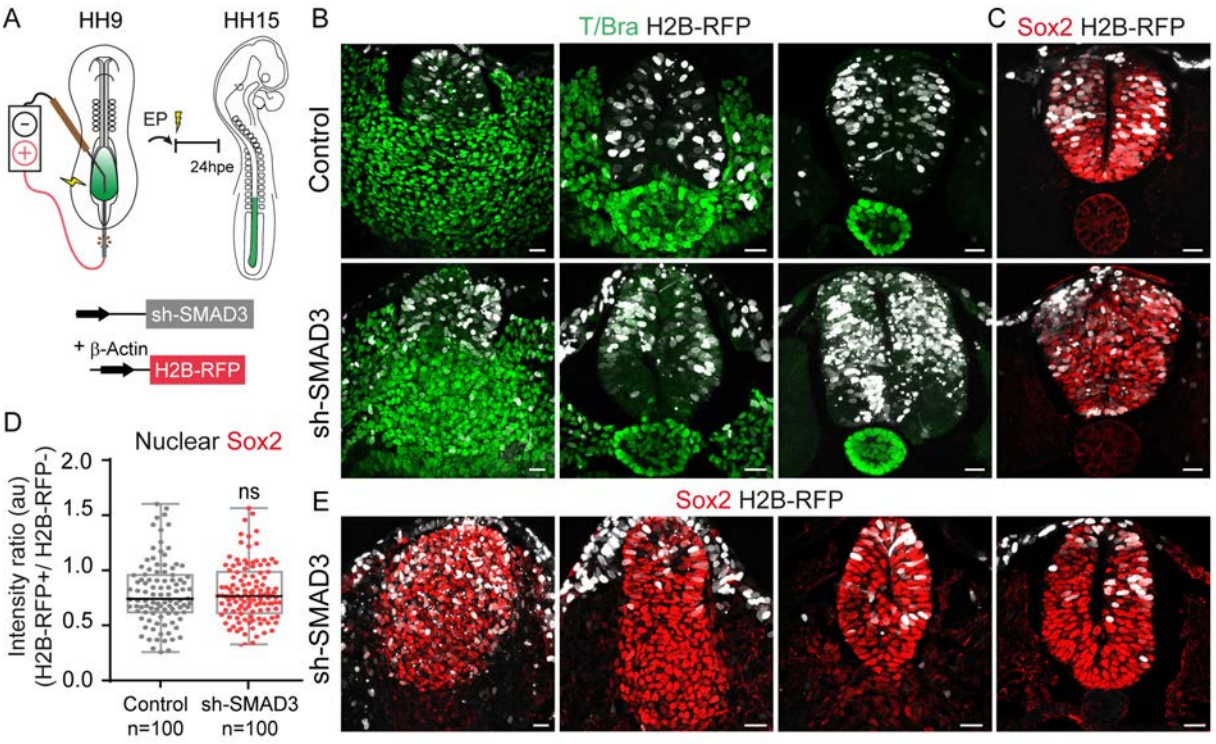

Figure 22. Lineage restriction of NMPs is independent of SMAD3 activity. (A) Scheme showing the method and timing of the co-electroporation in chick embryos and the electroporated DNAs (EP, electroporation; hpe, hours post-electroporation). **(B)** Selected images of transverse sections of control and sh-SMAD3 electroporated embryos (white), showing the developing SNT stained for T/Bra (green). Scale bars = 20 μm. **(C)** Selected images of transverse sections of control and sh-SMAD3 electroporated embryos (white), showing the formed SNT stained for Sox2 (red). Scale bars = 20 μm. **(D)** Plots ratio of Sox2 fluorescence intensity in control and sh-SMAD3 electroporated cells (horizontal bold lines show the median; n=100, 100 cells from 10 embryos/condition; p>0.05 Mann-Whitney test). **(E)** Selected images of transverse sections of control and sh-SMAD3 electroporated embryos (white), showing the developing SNT stained for Sox2 (red). Scale bars = 20 μm.

The triggering of MET and the initiation of multiple lumen foci are not controlled by SMAD3 activity

The morphogenesis of the SNT includes the mesenchymal-to-epithelial transition (MET) of transiting PSNT to generate epithelial NPCs, a process that can be followed along the cranio-caudal axis in stage HH15 chick embryos (Fig. 23). The orientation of epithelial polarity in MDCK cells growing in 3D culture (Bryant et al., 2014; Martin-Belmonte et al., 2008), and in the early mouse embryo (Bedzhov and Zernicka-Goetz, 2014), depends on the interaction of the cells with the ECM. Similarly, in the developing SNT, the first cells to acquire epithelial polarity are those in contact with the forming BM, the ones located dorsally and in the periphery of the cord (Fig. 23A-B). To characterize the subcellular events accompanying cell epithelialization, we analysed cell shape, centrosome positioning, Golgi distribution, and polarity protein localisation at early MET stages (Fig. 23C-O). During MET in the SNT, cells change their shape from polygonal to elongated (median±IQR circularity central cells=0.8±0.1 vs peripheral cells=0.3±0.2: Fig. 23C,D,M), which occurs concomitantly to basal nuclear positioning (Fig. 23E-H). The perinuclear centrosome becomes apically localised, as determined by the distance from FOP+ labelled centrosomes (Yan et al., 2006) to the nucleus (median±IQR distance central cells=0.9±0.5µm vs peripheral cells=9.7±10.3µm: Fig. 23E,F,N). The high variability found in peripheral cell centrosome-to-nucleus distance associates to the onset of interkinetic nuclear migration (INM), which separates or brings together the centrosome and the nucleus depending on the phase of the cell cycle. Additionally, the Golgi elongates and it is confined to the apical cellular process, as determined by labelling with the cis-Golgi matrix protein GM130 (Nakamura et al., 1995) (median±IQR distance central cells=3.3±1.6µm vs peripheral cells=9.9±6.8µm: Fig. 23G,H,O), similar to that observed for NPCs in the developing cerebral cortex (Taverna et al., 2016). Finally, cell epithelialization includes the apical organization of the apical membrane in discrete micro-domains where N-cadherin and the ZO-1/occludin complex occupy internal positions, while aPKC concentrates at the most apical domain (Aaku-Saraste et al., 1996; Afonso and Henrique, 2006; Chenn et al., 1998; Marthiens and ffrench-Constant, 2009). Thus, apical proteins such as N-cadherin or ZO-1 are progressively accumulated in the apical pole of the cell (Fig. 23I-L).

To establish the sequence of apical polarisation, we analysed the subcellular localisation of FOP, N-cadherin and aPKC at the initial stages of MET (Fig. 24A,B,E). While all the analysed cells already showed an apically localised centrosome, several also presented apical N-cadherin, and only a few apical aPKC. Neither N-cadherin nor aPKC were found before apical centrosome positioning and, furthermore, apical aPKC was never found before N-cadherin apical accumulation (mean±sem % of peripheral cells with apical FOP=73.7±5.1 vs apical FOP and N-cadherin=26.3±5.1; apical FOP=73.8±8.0 vs apical FOP and N-cadherin=6.6±1.3 vs apical FOP, N-cadherin and aPKC=19.6±8.9: Fig. 24A,B,E). Moreover, co-staining of FOP, N-cadherin and ZO-1 revealed N-cadherin and ZO-1 co-localisation, being always apically found at the same time and, again, never before FOP (mean±sem % of peripheral cells with apical FOP=72.6±9.9 vs apical FOP, N-cadherin and ZO-1=27.4±9.9: Fig. 24C,E). Finally, peripheral cells with apical FOP already showed basal β1 Integrin, and no cells were found with only one of these components apico-basally polarised, which suggest that apical and basal polarities are organised concomitantly (mean±sem % of peripheral cells with apical FOP and β1 integrin=64.5±6.6 vs apical FOP, β1 integrin and N-cadherin=35.5±6.6: Fig. 24D,F). In summary, we found the subcellular events of apico-basal polarisation to be sequential

in PSNT cells, as such apical centrosome positioning and basal β1 integrin localisation is followed by N-cadherin/ZO-1 apical membrane accumulation, and last, aPKC apical-most membrane localization (Fig. 24G).

As NMPs transformed into fully epithelialized NPCs, we observed multiple small lumens emerging at the interface between the peripheral epithelial and central mesenchymal cell populations (Fig. 24H). These small lumen foci (LF) always formed at one-cell distance from the BM, as the distance from LF to the BM was comparable to that of cell length (median±IQR cell length=26.5±9.2μm vs LF to BM distance=26.8±6.4μm: Fig. 24H,I,J,K). We next tested for a possible role of canonical TGF-β signalling in triggering MET and lumen initiation. 24hpe, sh-SMAD3 cells properly locate N-cadherin and aPKC to their apical pole (Fig. 24J) and multiple small lumens still open up at one-cell distance from the BM (median±IQR LF to BM distance control=26.8±6.4μm vs sh-SMAD3=28.0±5.5μm: Fig. 24J,K). Altogether, results show that SMAD3 activity is dispensable for the subcellular processes involved in MET triggering and lumen foci initiation, which prompted us to search for defects in late stages of MET and in SNT lumen resolution.

Figure 23. MET in association to the basement membrane (BM). (A,B) Schemes showing the cellular processes occurring during MET in the SNT (TB, tail bud; MET, mesenchymal-to-epithelial transition). The developing BM appears in green. In B', central PSNT cells are shown in grey and peripheral PSNT cells are in light blue. **(C,D)** Selected images of transverse sections stained for the actin cytoskeleton (white). Higher magnifications of the boxed regions are shown in C', D'. Dotted lines in D' delineate central (orange) and peripheral (blue) cell shape. Scale bars = 20 μm. **(E,F)** Selected images of transverse sections showing fibronectin deposition (green) and centrosome positioning (purple). Higher magnifications of the boxed regions are shown in E', F'. Scale bars = 20 μm. **(G,H)** Selected images of transverse sections showing laminin deposition (red) and Golgi polarisation (green). Higher magnifications of the boxed regions are shown in G', H'. Scale bars = 20 μm. **(I-L)** Selected images of transverse sections stained for the indicated apical and basal polarity proteins. Higher magnifications of the boxed regions are shown in I'-L'. Scale bars = 20 μm. **(M)** Plots circularity in central and peripheral chord cells (horizontal bold lines show the median; n=100, 100 cells from 10 embryos; ***p<0.001 Mann-Whitney test). **(N)** Plots the distance from FOP staining to the nucleus in central and peripheral chord cells (horizontal bold lines show the median; n=70, 70 cells from 10 embryos; ***p<0.001 Mann-Whitney test). **(O)** Plots the distance from FOP to the basal-most Golgi (distal GM130) in central and peripheral chord cells (horizontal bold lines show the median; n=102, 90 cells from 10 embryos; ***p<0.001 Mann-Whitney test). **(N'-O')** Schemes showing the measurements performed in N,O. Cell nuclei are depicted in blue, centrosomwes in purple and the cis-Golgi in green.

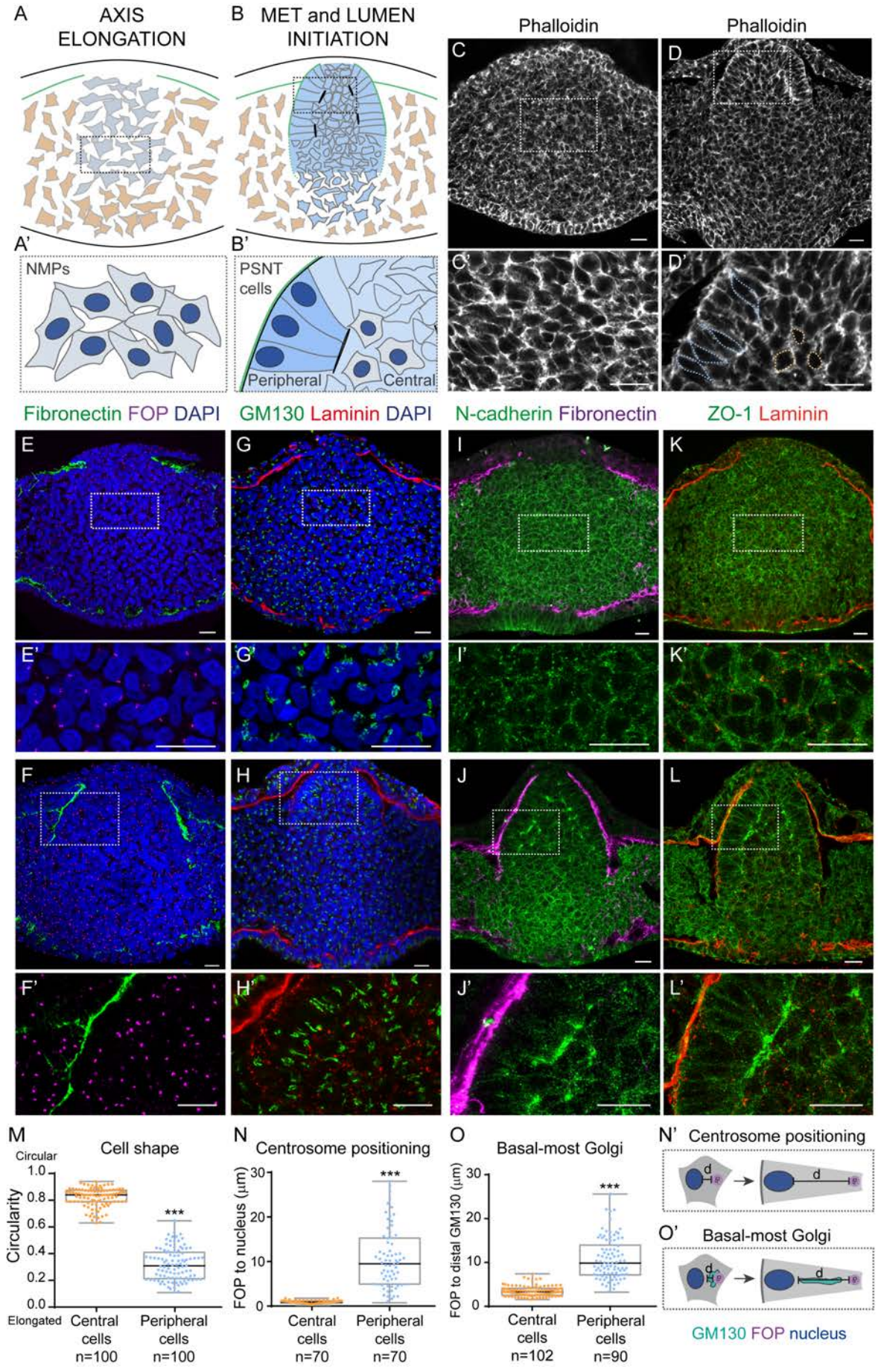
A
AXIS ELONGATION
B
MET and LUMEN INITIATION
Phalloidin
Phalloidin
C
D
A'
B'
NMPs
PSNT cells
Peripheral
Central
C'
D'
Fibronectin FOP DAPI
GM130 Laminin DAPI
N-cadherin Fibronectin
ZO-1 Laminin
E
G
I
K
E'
G'
I'
K'
F
H
J
L
F'
H'
J'
L'
M
Cell shape
Circular
Elongated
Circularity
1.0
0.8
0.6
0.4
0.2
0.0
***
Central cells n=100
Peripheral cells n=100
N
Centrosome positioning
FOP to nucleus (µm)
30
20
10
0
***
Central cells n=70
Peripheral cells n=70
O
Basal-most Golgi
FOP to distal GM130 (µm)
30
20
10
0
***
Central cells n=102
Peripheral cells n=90
N'
Centrosome positioning
d
d
O'
Basal-most Golgi
d
d
GM130 FOP nucleus

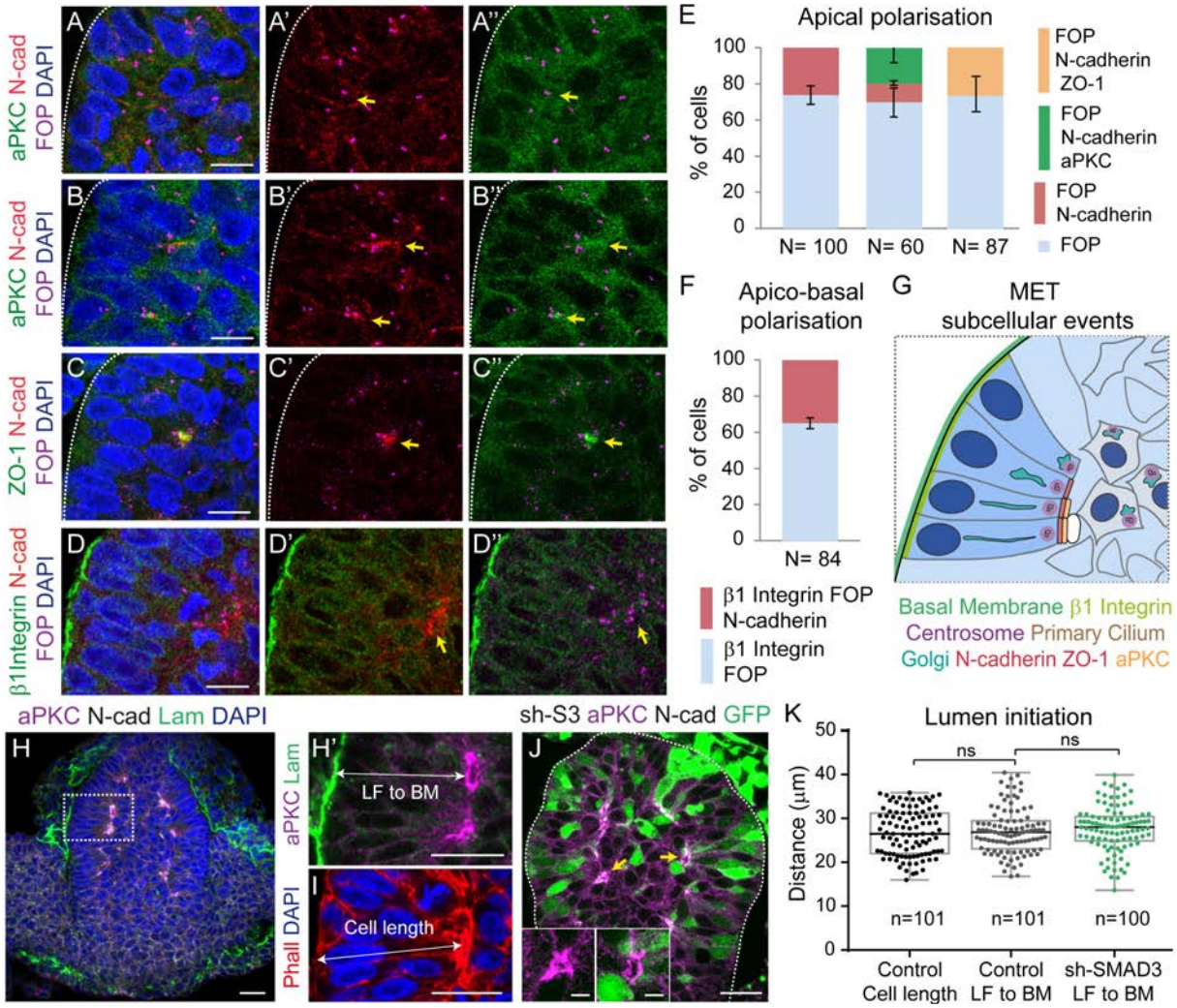

Figure 24. Lumen initiation occurs at a one-cell distance from the BM, and it is independent of SMAD3 activity. **(A-C)** Selected image of transverse sections stained for the centrosomes (purple), N-cadherin (red) and aPKC or ZO-1 (green) at the first steps of peripheral cell polarisation. The yellow arrows points to apically localized centrosomes with or without apical protein accumulation. Scale bars = 10 μm. **(D)** Selected images of transverse sections stained for the centrosomes (purple), the basal protein β1 integrin (green) and the apical protein N-cadherin (red). β1 integrin is basally localised in all cells with apically localised centrosomes. The yellow arrow points to apically localized centrosomes with apical N-cadherin accumulation and without aPKC. Scale bars = 10 μm. **(E)** Plots the percentage of polarizing peripheral chord cells presenting only apical centrosome (FOP); apical centrosome and N-cadherin; apical centrosome, N-cadherin and aPKC; or apical centrosome, N-cadherin and ZO-1 (plot shows the mean±sem; n=100, 60, 87 cells from 10 embryos). **(F)** Plots the percentage of polarizing peripheral chord cells presenting apical centrosome (FOP) and basal β1 integrin or apical centrosome, basal β1 integrin and N-cadherin (plot shows the mean±sem; n=84 cells from 10 embryos). **(G)** Scheme of polarising PSNT cells. The centrosome is the first organelle to be apically localised and then the Golgi, N-cadherin/ZO-1 and finally aPKC follow it. The BM and β1 integrins basally line the MET undergoing cells. **(H)** Selected image of transverse sections at the lumen initiation stage stained for aPKC (green), N-cadherin (red) and laminin (purple). A higher magnification of the boxed region appears in H' showing the distance from lumen foci (LF) to the basement membrane (BM). Scale bars = 20 μm. **(I)** Selected image of transverse sections at the lumen initiation stage where cell length is visualised by staining the actin cytoskeleton (red) and nucleus (DAPI, blue). Scale bar = 20 μm. **(J)** Selected image of transverse sections 24hpe of sh-SMAD3 electroporation (green) at the lumen initiation stage showing N-cadherin (white) and aPKC localisation (purple). Higher magnifications of the lumen foci pointed by the yellow arrows are shown. Scale bars = 20 μm, 5 μm. **(K)** Plots control embryos cell length and control and sh-SMAD3 embryos distance from lumen foci (LF) to basement membrane (BM) at the lumen initiation stage (horizontal bold lines show the median; n=101, 101, 100 cells from 10 embryos/condition; p>0.05 Kruskal-Wallis test).

SMAD3 activity is dispensable for the complete epithelialization of NPCs but necessary for single lumen formation

Formation of a single and continuous lumen in the SNT requires distinct luminal rearrangements and cellular events of 3D tissue remodelling. We used Imaris reconstruction to generate 3D images of the lumen size and shape from ZO-1 *in toto* immunostained HH15 chick embryos (Fig. 25A-F). Analysis revealed that the caudal small lumen foci tend to coalesce first into three enlarged lumens (one dorsal-central and two ventral-lateral) which will finally fuse into a single central cavity in cranial regions (Fig. 25A-F). We also found a population of cells that remain in between the resolving lumens until the end of lumen coalescence (Fig. 25C,E,F).

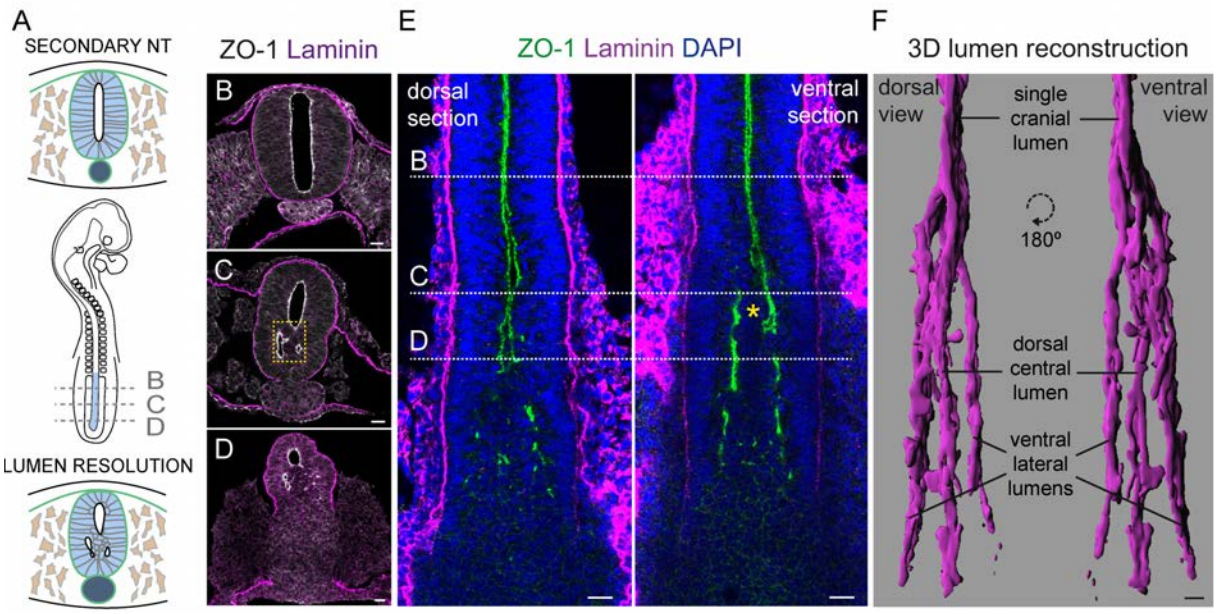

Figure 25. The clearance of central cells from the lumen is necessary for its resolution. **(A)** Drawing of a HH15 chick embryo and the cellular processes occurring during secondary lumen resolution that give rise to a SNT with a single central lumen. **(B-D)** Selected images of transverse sections at the indicated cranio-caudal levels in A, showing the localisation of ZO-1 (white) and the BM (laminin, purple). The dotted yellow square encloses central cells. Scale bars = 20 μm. **(E)** Dorsal views at two different dorso-ventral levels of the SN region in a HH15 chick embryo stained for ZO-1 (green) and laminin (purple). DAPI (blue) stains cell nuclei. Dotted lines show the cranio-caudal levels for B-D. The yellow star marks central cells. Scale bars = 20 μm. **(F)** Dorsal and ventral views of the 3D reconstruction of a stage HH15 chick embryo secondary lumen. The single cranial lumen caudally splits into one dorsal-central lumen and two ventral-lateral lumens (n=5 embryos). Scale bar = 20 μm.

Lumen resolution (LR) requires the clearance of this central cell population to generate the SNT composed of NPCs arranged around a single central cavity (Fig. 26A,I). Analysis of central cells at the LR stage revealed that even though they have already lost T/Bra expression (Fig. 26B), that is why we call them here central NPCs, they retain mesenchymal characteristics (Fig. 26C-H). Central NPCs maintain a circular cell shape, while peripheral NPCs at the stage of LR have already lost circularity, heading towards the fully elongation of NPCs in the formed SNT (median±IQR circularity central NPCs (LR)=0.8±0.1, peripheral NPCs (LR)=0.2±0.1, NPCs (SNT)=0.1±0.03: Fig. 26C,F,J). Central NPCs also present the centrosome close to their nucleus (median±IQR FOP to nucleus distance central NPCs (LR)=1.1±0.6μm, peripheral NPCs (LR)=14.3±11.0μm, NPCs

(SNT)=27.7±21.2µm: Fig. 26D,E,G,L), a pericentrosomal Golgi (median±IQR FOP to distal GM130 distance central NPCs (LR)=4.8±2.8µm, peripheral NPCs (LR)=16.8±10.3µm, NPCs (SNT)=22.2±20.3µm: Fig. 26D,H,K) and disorganised apical polarity (Fig. 26E).

We next tested for a possible role of canonical TGF-β signalling in final NPCs epithelialization. To that end, we analyzed cell shape, centrosome positioning, Golgi elongation and polarity protein localization in sh-SMAD3 electroporated cells of the SNT, at cranio-caudal levels where the morphogenesis of the neighbouring somites and underlying notochord was completed. 24hpe, sh-SMAD3 cells of the SNT properly elongate (median±IQR circularity control=0.1±0.1 vs sh-SMAD3=0.2±0.1: Fig. 27A,B), and apically localize their centrosomes, as control electroporated cells (median±IQR FOP to nucleus distance control=16.6±10.6µm vs sh-SMAD3=19.3±13.0µm: Fig. 27C,D). Although sh-SMAD3 electroporated cells fail to elongate their Golgi (median±IQR GM130 length control=13.3±6.9µm vs sh-SMAD3=6.3±3.7µm: Fig. 27E,F), these cells organize apical membrane micro-domains containing N-cadherin, ZO-1, and aPKC (Fig. 27G, H), similar to control electroporated cells. Although the apico-basal polarity is properly organized in NPCs, sh-SMAD3 electroporated embryos present a multiple lumen phenotype of the SNT in which small lumens are correctly initiated (Fig. 24K,L) but fail to coalesce into a single central cavity (Fig. 27H). Altogether, results suggest that SMAD3 activity is dispensable for the subcellular processes involved in cell epithelialization; however, it appeares to be required for the resolution of a centrally positioned single lumen during SNT formation.

Figure 26. Central NPCs at the stage of lumen resolution maintain mesenchymal characteristics. (A) Scheme of the cellular events occurring in secondary lumen resolution (LR). The BM appears in green. The two populations of peripheral and central NPCs are shown in A'. **(B)** Selected image of transverse sections at the LR phase stained for Sox2 (red) and T/Bra (green). Both central and peripheral NPCs are Sox2+ and T/Bra- at this stage. Dotted white line delineates central NPCs and a higher magnification is shown in B', B''. Scale bars = 20 µm. **(C)** Selected image of transverse sections stained for the actin cytoskeleton (white). A higher magnification of the boxed region is shown in C', where blue dotted lines delineate cell shape of peripheral and central NPCs. Scale bars = 20 µm. **(D)** Selected image of transverse sections stained for the centrosomes (purple) and the cis-Golgi (green). DAPI (blue) stains cell nuclei. A higher magnification of the boxed region is shown in D'. Scale bars = 20 µm. **(E)** Selected image of transverse sections stained for the centrosomes (purple) and the polarity protein aPKC (green). DAPI (blue) stains cell nuclei. A higher magnification of the boxed region is shown E'. Scale bars = 20 µm. **(F)** Plots cells shape/circularity of central and peripheral NPCs at the stage of lumen resolution (LR) and of NPCs once the secondary neural tube (SNT) is fully formed (horizontal bold lines show the median; n=100, 100, 100 cells from 10 embryos; ***p<0.001 Kruskal-Wallis test). **(G)** Plots the distance from apical FOP to the nucleus in central and peripheral NPCs at the stage of LR and in NPCs of the formed SNT (horizontal bold lines show the median; n=100, 100, 100 cells from 10 embryos; ***p<0.001 Kruskal-

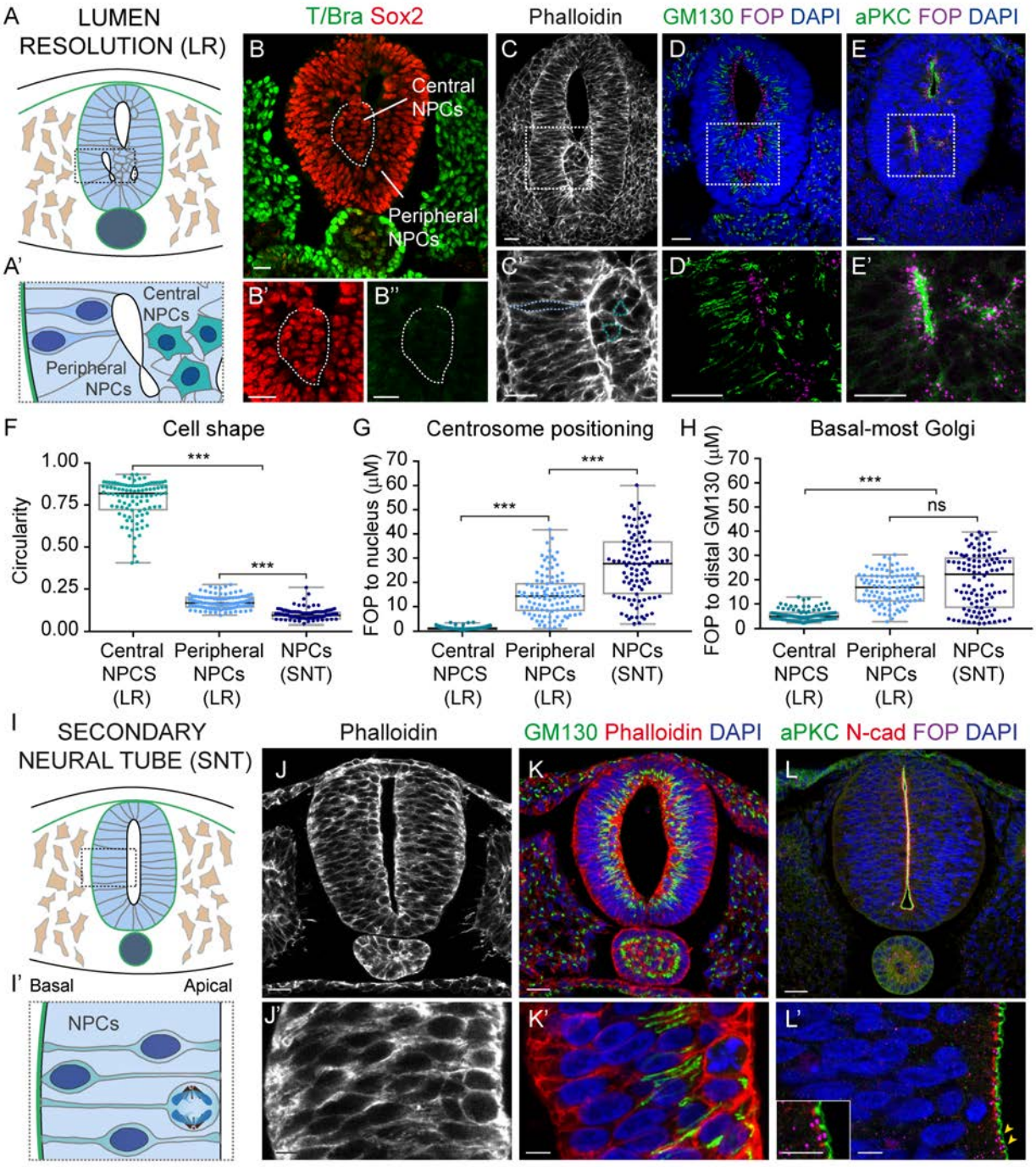

Wallis test). **(H)** Plots the distance from FOP to the basal-most Golgi (distal GM130) in central and peripheral NPCs at the stage of LR and in NPCs of the formed SNT (horizontal bold lines show the median; n=100, 100, 110 cells from 10 embryos; ***p<0.001 Kruskal-Wallis test). **(I)** Scheme of the formed secondary neural tube (SNT). SN results in a SNT with a single lumen in its centre surrounded by dividing epithelial NPCs as shown in I'. Apical and basal surfaces are indicated. The BM appears in green. **(J)** Selected image of transverse sections of the formed SNT stained for the actin cytoskeleton (white). A higher magnification is shown in J'. Scale bars = 20 µm, 5 µm. **(K)** Selected image of transverse sections of the formed SNT stained for the actin cytoskeleton (red) and the cis-Golgi (green). DAPI (blue) stains cell nuclei. A higher magnification is shown in K'. Scale bars = 20 µm, 5 µm. **(L)** Selected image of transverse sections stained for the centrosomes (purple), the polarity protein aPKC (green) and the junctional protein N-cadherin (red). DAPI (blue) stains cell nuclei. A higher magnification is shown in L', where the yellow arrows point to the two apical complexes shown at the bottom left. Scale bars = 20 µm, 5 µm.

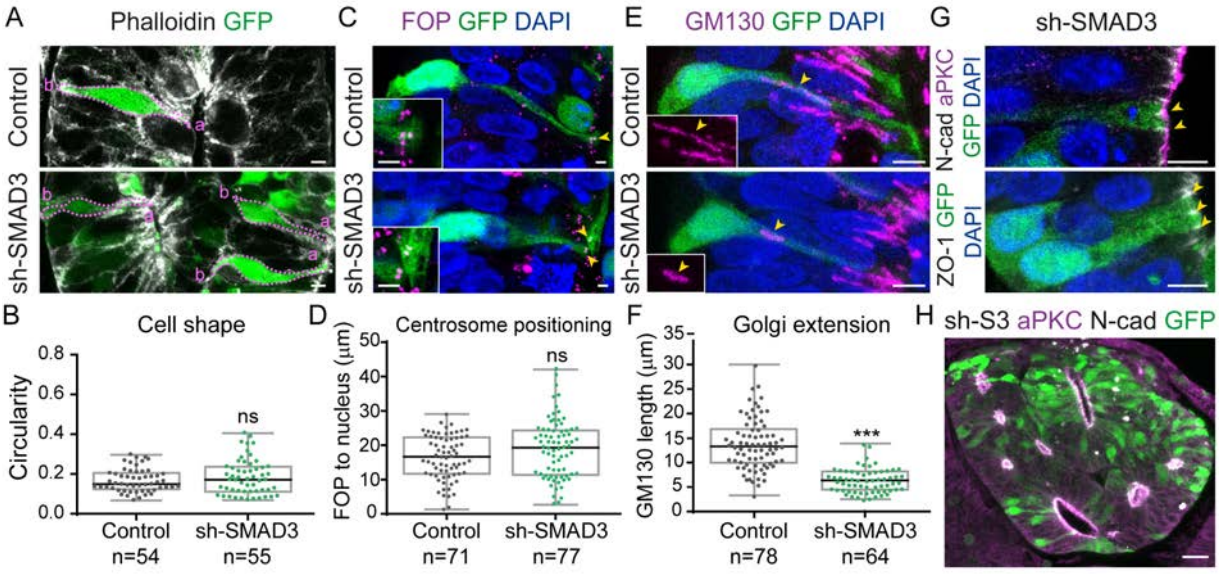

Figure 27. SMAD3 activity is dispensable for complete NPCs epithelialization but required for single lumen formation. (A) Selected images of 24hpe control and sh-SMAD3 electroporated cells (green) showing the actin cytoskeleton (white). Dotted pink lines delineate cell shape. Apical (a) and basal (b) surfaces are indicated for each cell. Scale bars = 5 µm. **(B)** Plots cell shape/circularity in 24hpe control and sh-SMAD3 electroporated embryos (horizontal bold lines show the median; n=54, 55 cells from 10 embryos/condition; p>0.05 Mann-Whitney test). **(C)** Selected images of 24hpe control and sh-SMAD3 electroporated cells (green) showing the apically localised centrosomes (purple; yellow arrows). Higher magnifications are shown on the bottom left. Scale bars = 2.5 µm. **(D)** Plots distance from apical FOP to the nucleus, in 24hpe control and sh-SMAD3 electroporated embryos (horizontal bold lines show the median; n=71, 77 cells from 10 embryos/condition; p>0.05 Mann-Whitney test). **(E)** Selected images of 24hpe control and sh-SMAD3 electroporated cells (green) showing cis-Golgi organisation (purple; yellow arrows). Scale bars = 5 µm. **(F)** Plots Golgi extension, determined by GM130 length, in 24hpe control and sh-SMAD3 electroporated embryos (horizontal bold lines show the median; n=71, 77 cells from 10 embryos/condition; ***p<0.001 Mann-Whitney test). **(G)** Selected images of sh-SMAD3 electroporated cells (green) stained for the indicated apical polarity proteins (yellow arrows). Scale bars = 5µm. **(H)** Selected image of transverse sections 24hpe of sh-SMAD3 electroporation (green). N-cadherin (white) and aPKC (purple) apically line the small multiple lumens. Scale bar = 20 µm. DAPI (blue) stains cell nuclei.

Programmed Cell Death of central NPCs is not required for the morphogenesis of the SNT lumen

Resolution into a single continuous lumen in the developing SNT requires the clearing of central mesenchymal NPCs. To test whether cavitation participates in lumen resolution, we examined sections of stage HH15 chick embryos at various cranio-caudal levels for cleaved caspase-3-positive or TUNEL-positive cells. Whereas there were variable numbers of apoptotic cells in the dorsal NT and dorsal non-neural ectoderm, such cells were almost absent from the forming SNT (mean±sem %c-Caspase3 NPCs (LR)=0.6±0.1), or even from the inner cell mass surrounded by forming lumens (mean±sem %c-Caspase3 central NPCs (LR)=0.3±0.2), indicating that cavitation does not contribute to lumen resolution in the SNT (Fig. 28A-C). However, the population of centrally located NPCs appeared to intercalate among epithelialized NPCs of the forming SNT, as observed in transverse sections stained for actin cytoskeleton (Phalloidin) (Fig. 28D). 24hpe of sh-SMAD3 electroporation showed the presence of centrally located NPCs at LR stages (Fig. 28E), which do not die by apoptosis either, as assessed in previous quantifications (Fig. 18D-H). However, central NPCs remained at cranial levels, where the notochord and somites have formed (Fig. 28F). This suggests a possible failure in the clearance of cells from the luminal space, which drove us to investigate this largely unknown event.

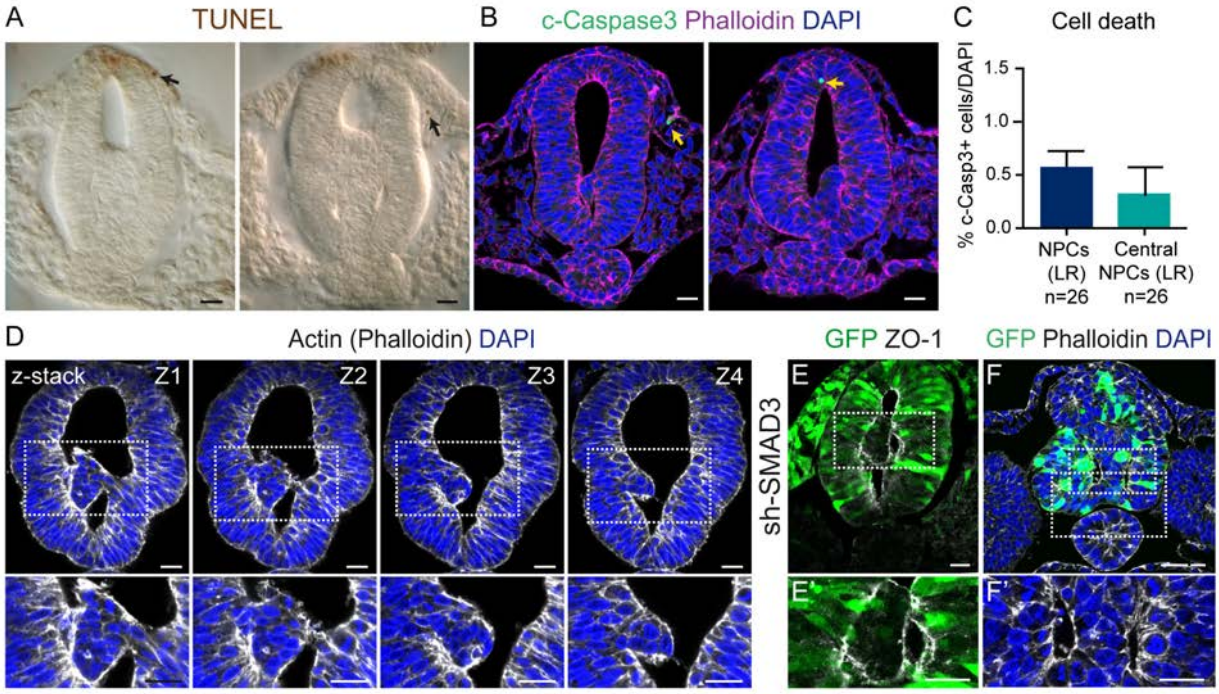

Figure 28. Apoptosis is not required for secondary lumen formation. (A) Selected image of transverse sections stained with the TUNEL method. Black arrows indicate TUNEL+ cells. Scale bars = 20 μm. **(B)** Selected image of transverse sections stained for cleaved Caspase3 (c-Caspase3, green) and the actin cytoskeleton (purple). DAPI (blue) stains cell nuclei. Yellow arrows indicate c-Caspase3+ cells. Scale bars = 20 μm. **(C)** Plots the percentage of c-Caspase3+ cells in the whole SNT and in the central cell mass of NPCs (plot shows the mean±sem; n=26 sections from 10 embryos). **(D)** Consecutive sections of a transverse z-stack (Z1-Z4) at the lumen resolution phase, stained for actin cytoskeleton (white) and nuclei (DAPI, blue). Higher magnifications of the boxed regions are shown. Scale bars = 20 μm. **(E)** Selected images of transverse sections 24hpe of sh-SMAD3 (green) at the lumen resolution stage, stained for ZO-1 (white). A higher magnification of the boxed region is shown in E'. Scale bars = 20 μm. **(F)** Selected images of transverse sections 24hpe of sh-SMAD3 (green) stained for the actin cytoskeleton (white) and cell nuclei (DAPI, blue). A higher magnification of the boxed region is shown in F'. Scale bars = 20 μm.

Central NPCs intercalate into the lateral walls of the neuroepithelium

The mechanism by which central NPCs are cleared from the secondary forming lumen remains elusive, though our results suggest that cell intercalation might be the driving process (Fig. 28D). To directly test this hypothesis, we set for the *in vivo* analysis of the process by electroporation of stage HH9 chick embryos, which were later cultured and imaged under an upright wide-field microscope. This system allows chick embryos to elongate and to develop at the approximate same rate as they do *in ovo* (Supplementary Movie S1; related to Fig.4 in Appendix II) (Benazeraf et al., 2010; Benazeraf et al., 2017; Rupp et al., 2003). It also permits the tracking over time of electroporated fluorescently labelled cells of the elongating SNT, these cells exhibiting high motility, high rate of cell division, and important cell mixing (Supplementary Movies S2, S3; related to Fig.5 Appendix II).

Analysis of membrane-GFP electroporated cells along time revealed circular mesenchymal cells centrally localized in the elongating SNT (green arrows at t=00:00 in Fig. 29A-C). We consistently observed central cell intercalation into the lateral walls of the neuroepithelium, perceived as a lateral cell movement away from the centre of the tissue accompanied with a cell shape change from circular to elongated (red arrows in Fig. 29A,B; Supplementary Movies S4, S5). Notably, intercalating cells presented high protrusive activity (Fig. 29A,B) and central cell intercalation always occurred just after cell division (dotted circles in Fig. 29A,B). Indeed quantification of dividing cells in fixed sections of stage HH15 embryos showed the proportion of mitotic cells to be significantly higher in the area where the single lumen is resolving, as compared to the formed SNT or to the caudal tail bud (mean±SD %pH3 cells SNT=4.4±1.0µm vs LR=7.0±2.5µm vs Tail bud=3.3±1.1µm: Fig.29D,E).

We next quantified cell distance from the centre, circularity and cranio-caudal location along time, the last analysed as the distance to the last pair of formed somites, in spotted membrane-GFP+ central mitosis and generated daughter cells (Fig. 29F; Fig. 30A-I). Results showed that the outcome of central cell division varies along the cranio-caudal axis (Fig. 29E,F). At the anterior SNT (median±IQR distance to the last pair of somites=494.8±464.0µm), central cells divide symmetrically before both daughter cells elongate and migrate laterally to intercalate among epithelialized NPCs (Fig. 29A,F; Fig. 30A-C; Supplementary Movie S4). We termed this mode of division as II, as it produces two intercalating daughter cells (IDCs) (Fig. 29A'). At intermediate regions (median±IQR distance to the last pair of somites=803.2±163.2µm), central cells divide asymmetrically, such that one daughter cell remains mesenchymal and centrally located, while the other daughter cell elongates and migrates laterally to intercalate among epithelialized NPCs forming the SNT (Fig. 29B,F; Fig. 30D-F; Supplementary Movie S5). We termed this mode of division as IC, as it gives rise to one intercalating (IDC) and one central daughter cell (CDC) (Fig. 29B'). At the caudal tail bud (median±IQR distance to the last pair of somites=1040.0±193.1µm) mesenchymal central cells divide symmetrically, such that both daughter cells remain rounded and centrally located (Fig. 29C,F; Fig. 30G-I; Supplementary Movies S6 and S7). We termed this mode of division as CC, as it generates two central daughter cells (CDCs) (Fig. 29C').

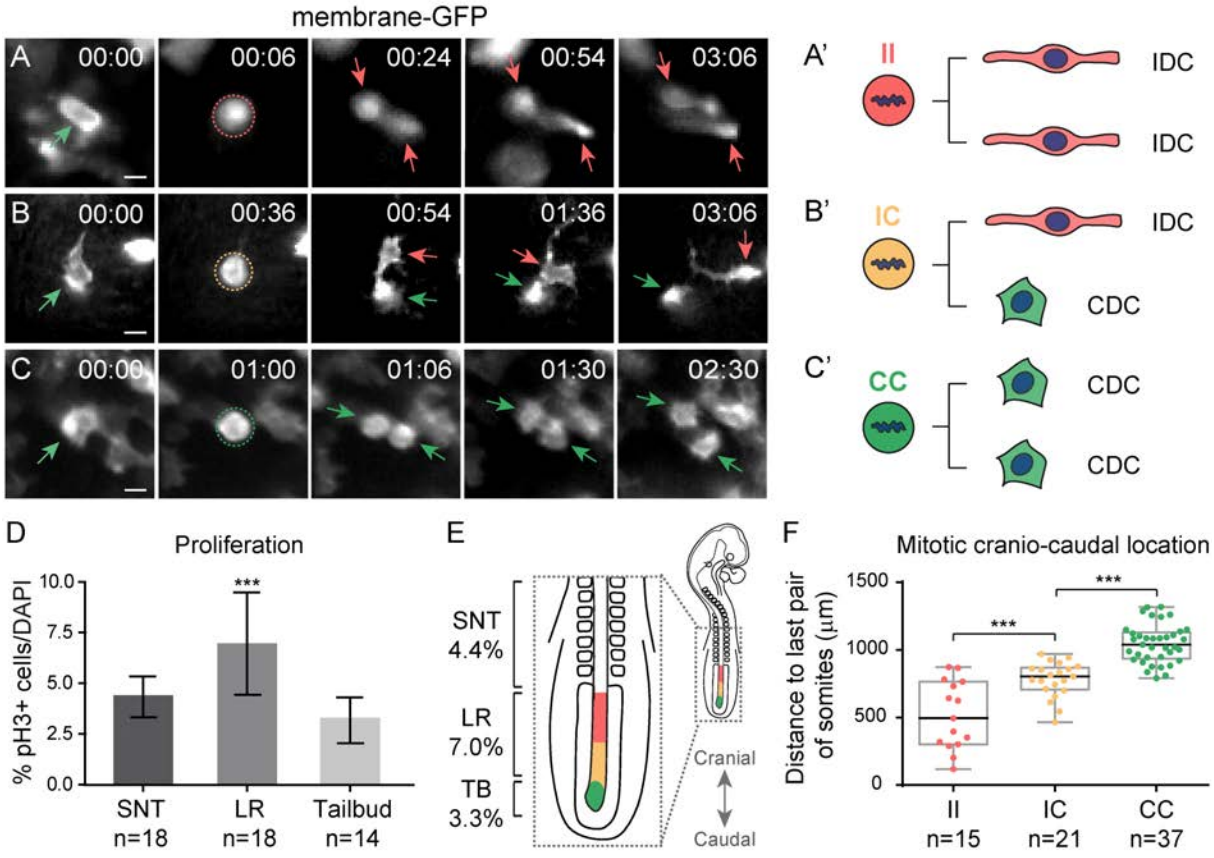

Figure 29. Three modes of division coexist in the developing SNT but localise at different cranio-caudal levels. **(A-C)** Selected frames of membrane-GFP electroporated embryos time-lapse movies showing a representative mitosis for each of the three modes of cell division. The mother central mesenchymal cell (green arrow) generates two intercalating daughter cells (dark and light red arrows) in A; one cell that remains in the center (green arrow) and one intercalating cell (red arrow) in B; and two central daughter cells (dark and light green arrows) in C. Scale bars = 10 µm. **(A'-C')** Schemes of the three modes of division that coexist during SNT formation. A cell undergoing mitosis can generate either two intercalating daughter cells (A', II mode of division, red), one intercalating and one centrally remaining daughter cell (B', IC mode of division, yellow) or two central daughter cells (C', CC mode of division, green). **(D)** Plots the percentage of mitotic pH3+ cells once the SNT is completed, in the lumen resolution stage (LR) and in the early elongating tail bud (TB) (plot shows the mean ±SD n=18, 18, 14 sections from 10 embryos; **p<0.01,***p<0.001 one-way ANOVA). **(E)** Schematic drawing of a stage HH15 chick embryo showing a higher magnification of its caudal region. The mean mitotic indexes in D are indicated for each region (left). The approximate cranio-caudal location for each of the three modes of division is also shown (II, red; IC, yellow; CC, green). **(F)** Plots the cranio-caudal location for each of the three modes of division as the distance from each measured division to the last formed pair of somites (horizontal bold lines show the median; n=15, 21, 37 divisions from 13 time-lapse movies; ***p<0.001 one-way ANOVA).

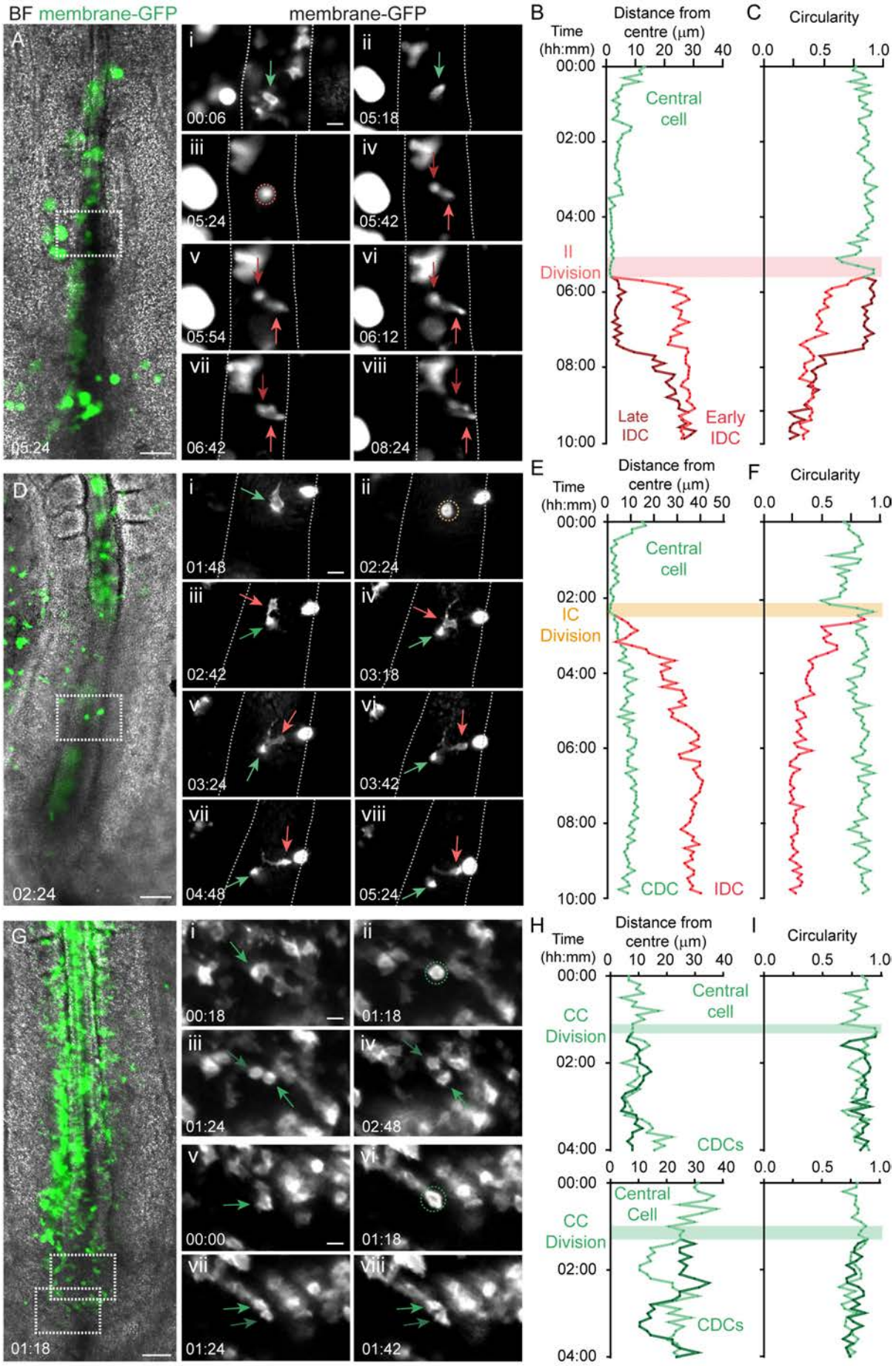
BF membrane-GFP
membrane-GFP
A
i
ii
00:06
05:18
iii
iv
05:24
05:42
v
vi
05:54
06:12
vii
viii
06:42
08:24
05:24
B
Time (hh:mm)
Distance from centre (μm)
0 10 20 30 40
00:00
02:00
04:00
06:00
08:00
10:00
Central cell
II Division
Late IDC
Early IDC
C
Circularity
0.0 0.5 1.0
D
i
ii
01:48
02:24
iii
iv
02:42
03:18
v
vi
03:24
03:42
vii
viii
04:48
05:24
02:24
E
Time (hh:mm)
Distance from centre (μm)
0 10 20 30 40 50
00:00
02:00
04:00
06:00
08:00
10:00
Central cell
IC Division
CDC
IDC
F
Circularity
0.0 0.5 1.0
G
i
ii
00:18
01:18
iii
iv
01:24
02:48
v
vi
00:00
01:18
vii
viii
01:24
01:42
01:18
H
Time (hh:mm)
Distance from centre (μm)
0 10 20 30 40
00:00
02:00
04:00
Central cell
CC Division
CDCs
Central Cell
CC Division
CDCs
I
Circularity
0.0 0.5 1.0

Figure 30. Daughter cells that result from II or IC divisions intercalate into the lateral walls of the neuroepithelium. **(A)** Selected frames of membrane-GFP electroporated embryos time-lapse movies showing a representative II mitosis. A central mesenchymal cell (i-ii, green arrow), divides (iii, red dotted circle) and generates two intercalating daughter cells (IDC) (iv-viii, dark and light red arrows). Scale bars = 100 μm, 20 μm. **(B)** Plots cell distance from the centre of the cells in A along the time-lapse movie (10h). The two daughter cells leave the centre of the tissue as they intercalate into the SNT lateral wall (dark and light red). **(C)** Plots circularity of the cells in A along the time-lapse movie (10h). The two daughter cells elongate and lose circularity as they intercalate into the SNT lateral wall (dark and light red). **(D)** Selected frames of membrane-GFP electroporated embryos time-lapse movies showing a representative IC mitosis. A central mesenchymal cell (i, green arrow), divides (ii, orange dotted circle) and generates one intercalating daughter cell (IDCs) (iii-viii, red arrow) and one central daughter cell (CDC) (iii-viii, green arrow). Scale bars = 100 μm, 20 μm. **(E)** Plots cell distance from the centre of the cells in D along the time-lapse movie (10h). One daughter cell remains in the centre (green) while the other moves away and intercalates into the SNT lateral wall (red). **(F)** Plots circularity of the cells in D along the time-lapse movie (10h). One daughter cell maintains the high circularity of the mother cell (green) while the other elongates (red). **(G)** Selected frames of membrane-GFP electroporated embryos time-lapse movies showing two representative CC mitosis. A central mesenchymal cell (i,v, green arrows), divides (ii, vi, green dotted circles) and generates two central daughter cells (CDCs) (iii-iv, vii-viii, dark and light green arrows). Scale bars =100 μm, 20 μm. (**H)** Plots cell distance from the centre of the cells in G along 4h of the time-lapse movie. Both daughter cells remain in the centre of the tissue or in the same position as the mother cell (dark and light green). **(I)** Plots circularity of the cells in G along 4h of the time-lapse movie. Both daughter cells maintain high circularity (dark and light green). CDC, central daughter cell; IDC, intercalating daughter cell.

SMAD3 activity is crucial for central cell intercalation

In order to test for a possible role of canonical TGF-β signalling in cell intercalation and single lumen resolution during SNT formation, stage HH9 chick embryos were electroporated with sh-SMAD3 or control Sox2p:GFP vector (Saade et al., 2013; Uchikawa et al., 2003) and imaged for tracking of fluorescently labelled cells over time (Fig. 31A-I). sh-SMAD3 electroporated central cells were able to divide in a similar ratio to control electroporated cells (Fig. 18F,H; Fig. 31F). However, sh-SMAD3 electroporated daughter cells remained centrally located after mitosis and failed to intercalate into the lateral epithelialized SNT (Fig. 31B-I; Fig. 32D-F; Supplementary Movies S8, S9, S10), regardless of the mitotic cranio-caudal location (median±IQR distance to the last pair of somites control II=732±378.8mm, IC=843±123mm, CC=1008±163mm vs sh-SMAD3 CI=718.8±503.5mm, CC=831.9±445.8mm: Fig. 31F). On the contrary, Sox2p:GFP control cells intercalated normally (Fig. 32A-C; Supplementary Movie S11). Faulty cell intercalation in sh-SMAD3 electroporated embryos resulted in an abnormal persistence of central cells at cranial levels (Fig. 31B-D), that eventually elongated at central positions (last time points in Fig. 31G-I). This disturbed the resolution of the developing lumen and ultimately led to the NTDs with a multilumen phenotype.

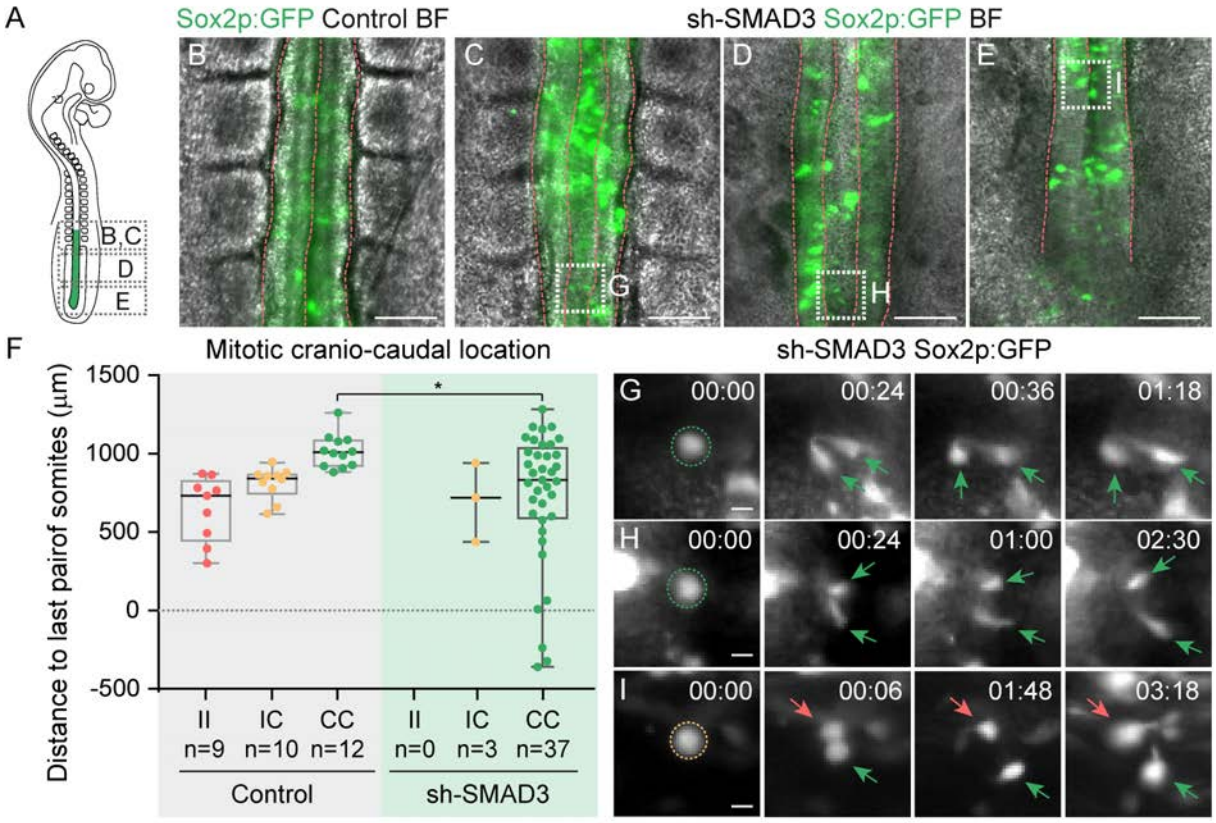

Figure 31. The majority of sh-SMAD3 divisions generate two daughter central cells. (A) Drawing of an electroporated HH15 chick embryo showing the cranio-caudal levels of B-E. **(B)** Selected frame of Sox2p:GFP electroporated control embryos time-lapse movies at the cranio-caudal level indicated in A. Red dotted lines delineate the apico-basal surfaces of the SNT. Scale bar = 100 µm. **(C-E)** Selected frames of sh-SMAD3 Sox2p:GFP electroporated control embryos time-lapse movies at the cranio-caudal levels indicated in A. Frames are the last time points of G,H,I mitotic sequences, as indicated by the boxed regions. Red dotted lines delineate the apico-basal surfaces of the SNT. Note the abnormal accumulation of cells in the centre of the SNT in C and D. Scale bars = 100µm. **(F)** Plots the cranio-caudal location for each of the three modes of division as the distance from each measured division to the last formed pair of somites in both Sox2p:GFP control and sh-SMAD3 electroporated embryos. Mostly all sh-SMAD3 divisions generate two central daughter cells (CC divisions), regardless of the cranio-caudal position (horizontal bold lines show the median; n=9,10,12 divisions from 5 Sox2p:GFP control and n=0,3,37 divisions from 6 sh-SMAD3 time-lapse movies; *p<0.05 Kruskal-Wallis test). **(G-I)** Selected frames of sh-SMAD3 Sox2p:GFP movies showing three different cell divisions at the indicated cranio-caudal positions in C,D,E. The dotted circles indicate the mitosis (CC divisions, green; IC division, yellow), the green arrows point to central daughter cells and the red arrow to an intercalating daughter cell. Scale bars = 10µm.

Figure 32. sh-SMAD3 electroporated cells fail to intercalate into the lateral walls of the forming SNT. (A) Selected frame of Sox2p:GFP control time-lapse movies. The boxed region refers to the last time point (v) of the sequence in B. Scale bar = 100µm. **(B)** Selected frames of HH15 Sox2p:GFP time-lapse movies showing a representative IC mitosis. A mesenchymal cell (i, green arrow), divides (ii, orange dotted circle) and generates a daughter cell which remains in the centre (iii-v, green arrow) and another which intercalates into the SNT lateral wall (iii-v, red arrow). Scale bars = 10µm. **(C)** Plots cell distance from the centre of the cells in B along the time-lapse movie. One daughter cell remains in the centre (green) while the other moves away and intercalates into the SNT lateral wall (red). **(D-F)** Plots cell distance from the centre along the time-lapse movie of shSMAD3 Sox2p:GFP cells in Fig. 31G,H,I. All daughter cells remain close to the centre (both dark and light green). CDC, central daughter cell; IDC, intercalating daughter cell.

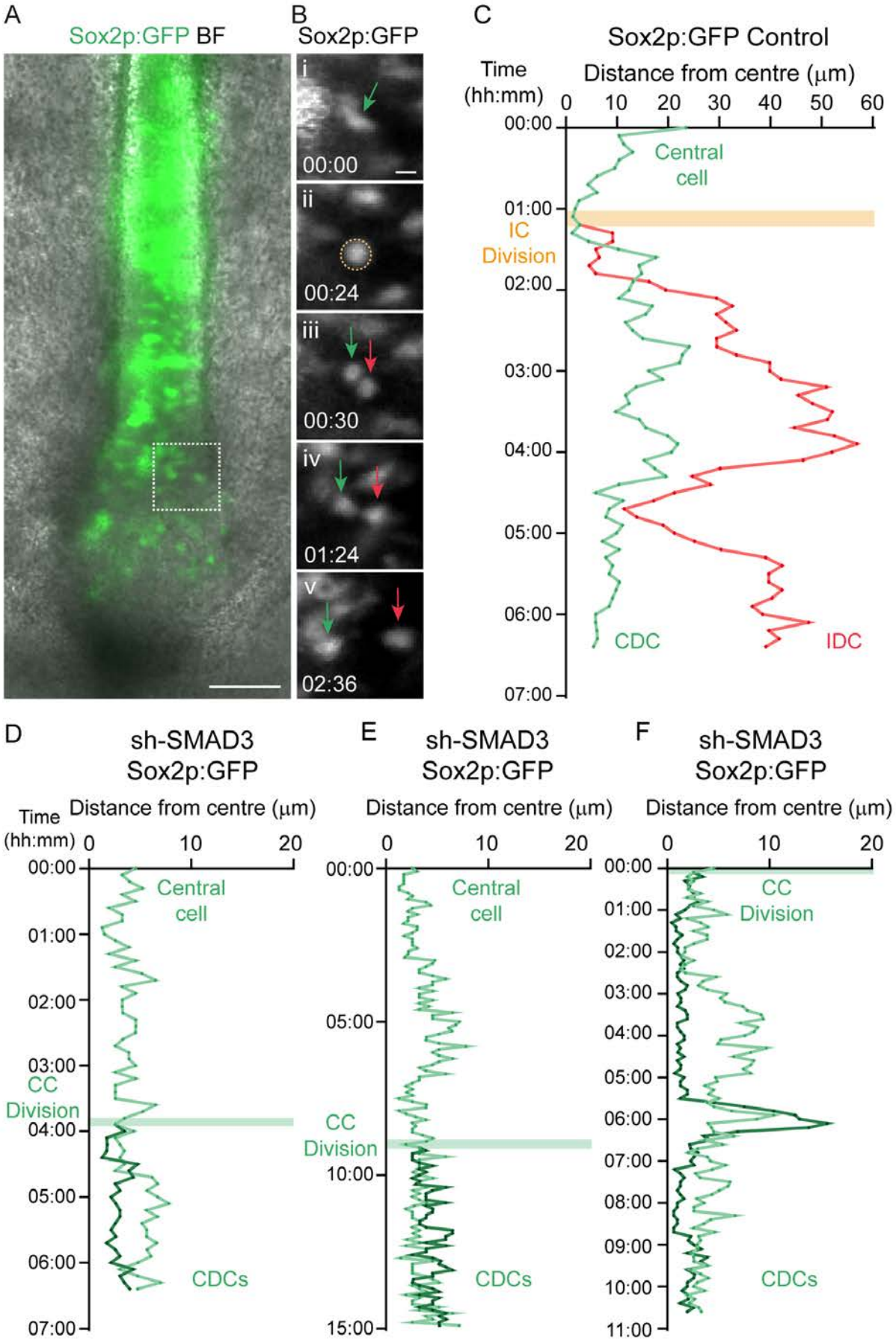
A
Sox2p:GFP BF
B
Sox2p:GFP
i
00:00
ii
00:24
iii
00:30
iv
01:24
v
02:36
C
Sox2p:GFP Control
Time (hh:mm)
Distance from centre (μm)
0 10 20 30 40 50 60
00:00
01:00
02:00
03:00
04:00
05:00
06:00
07:00
Central cell
IC Division
CDC
IDC
D
sh-SMAD3 Sox2p:GFP
Time (hh:mm)
Distance from centre (μm)
0 10 20
00:00
01:00
02:00
03:00
04:00
05:00
06:00
07:00
Central cell
CC Division
CDCs
E
sh-SMAD3 Sox2p:GFP
Distance from centre (μm)
0 10 20
00:00
05:00
10:00
15:00
Central cell
CC Division
CDCs
F
sh-SMAD3 Sox2p:GFP
Distance from centre (μm)
0 10 20
00:00
01:00
02:00
03:00
04:00
05:00
06:00
07:00
08:00
09:00
10:00
11:00
CC Division
CDCs

SMAD3 activity is required in NPCs for primary cilia length control

To start to search for the subcellular mechanisms driving central NPC intercalation, we next investigated primary cilia, since this organelle coordinates multiple activities that are required for directional cell migration. Primary cilia project from the cell surface, acting as antennas to sense and transmit extracellular positional and migratory cues (Veland et al., 2014). We first analysed endogenous SMAD3 subcellular localisation in NPCs of the SNT (Fig. 33A). Co-stainings of SMAD3 or activated phospho-SMAD2/3 with apical (aPKC), junctional (N-cadherin) and ciliary (Polyglutamilated Tubulin) proteins revealed an accumulation of the protein at the base of the primary cilium (Fig. 33B,C), as previously observed *in vitro* (Christensen et al., 2017; Clement et al., 2013; Monnich et al., 2018). Intensity quantifications of SMAD3, phospho-SMAD2/3 and SMAD2 along the cilium-centrosome axis showed that SMAD3 and phospho-SMAD2/3, but not SMAD2, localise between the basal body and the cilium proper (Fig. 33D-F), probably associating to the TZ (Tözser et al., 2015).

To test for a possible role of canonical TGF-β signalling in cilia formation, HH9 embryos were co-electroporated with the ciliary membrane marker ARL13B-RFP at a low concentration (Saade et al., 2017) together with sh-SMAD3 or sh-SMAD2. Control cells showed variable cilia lengths (median±IQR ciliary length control=1.5±0.7μm) in association with cell cycle phase and nuclear positioning. The electroporation of sh-SMAD3, which efficiently decreased endogenous SMAD3 protein at the ciliary base of NPCs (median±IQR ciliary SMAD3 integrated density control=33.2±19.9 vs sh-SMAD3=12.3±10.7: Fig. 33G), resulted in significantly longer primary cilia (median±IQR ciliary length sh-SMAD3=2.0±1.2μm: Fig. 33H,K). On the contrary, the length of primary cilia in sh-SMAD2 electroporated NPCs was not affected, coherent with the absence of SMAD2 at the base of the cilia (median±IQR ciliary length sh-SMAD2=1.7±0.9μm: Fig. 33H,J). While the electroporation at a low concentration of SMAD3-3S/D, a constitutively active SMAD3 mutant (Garcia-Campmany and Marti, 2007), was not sufficient to modulate ciliary length (median±IQR ciliary length SMAD3-3S/D=1.6±0.7μm: Fig. 33D,H), its co-electroporation with sh-SMAD3 rescued ciliopathy (median±IQR ciliary length sh-SMAD3+SMAD3-3S/D=1.5±0.8μm: Fig. 33D,I), confirming the specificity of the reported ciliopathy. Thus, the depletion of SMAD3 activity results in ciliary lengthening, highlighting a new role for SMAD3 in the control of NPCs ciliary length. This ciliopathy in turn might impair the reception of extracellular migratory cues, among others, and contribute to the failure of central cell intercalation.

Figure 33. SMAD3 is essential for the control of ciliary length in NPCs. (A) Selected image of transverse sections stained with SMAD3 antibody (red). DAPI (blue) stains cell nuclei. A higher magnification of the boxed region is shown in A'. SMAD3 apically accumulates in NPCs (red dots in A'). Scale bars = 10 μm. **(B)** Selected image of transverse sections stained with SMAD3 antibody (S3, red), aPKC (green) and junctional N-cadherin (white). DAPI (blue) stains cell nuclei. The yellow arrow points to apical SMAD3 accumulation. Scale bar = 5 μm. **(C)** Selected image of transverse sections stained with endogenous phospho-SMAD2/3 antibody (phS2/3, red) and Polyglutamilated Tubulin (green), the last showing primary cilia. DAPI (blue) stains cell nuclei. Yellow arrows point to phospho-SMAD2/3 accumulation at the base of the cilia. Scale bar = 5 μm. **(D-F)** Selected images of transverse sections and the related intensity plots of endogenous SMAD3, phospho-SMAD2/3 and SMAD2 (red) and the indicated centrosomal (CEP152-GFP, green) or

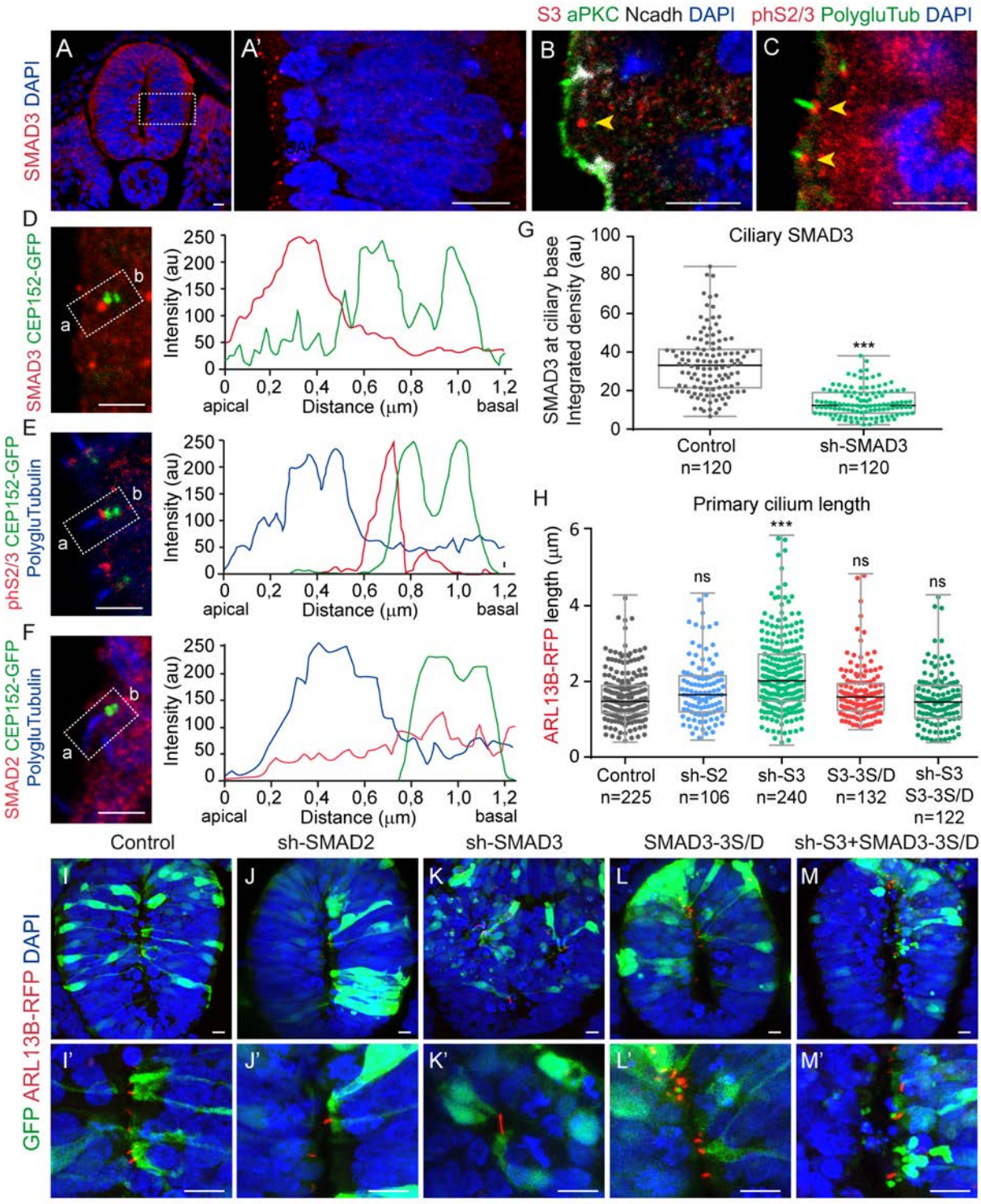

ciliary (Polyglutamilated Tubulin, blue) proteins, from apical (a, left) to basal (b, right). Scale bars = 2.5 µm. **(G)** Plots fluorescence intensity of SMAD3 at the base of the cilia in control and sh-SMAD3 electroporated cells (horizontal bold lines show the median; n=120, 120 cells from 10 embryos/condition; ***p<0.001 Mann-Whitney test). **(H)** Plots primary cilium length in control, sh-SMAD2, sh-SMAD3, SMAD3-3S/D and sh-SMAD3+SMAD3-3S/D (horizontal bold lines show the median; n=225, 106, 240, 132, 122 from 10 embryos/condition; ***p<0.001 Kruskal-Wallis test). **(I-M)** Selected images of transverse sections electroporated with the indicated DNAs (green) and ARL13B-RFP (red) to visualise primary cilia. Selected images of transverse sections at high magnification are shown for each condition in I'-M'. sh-SMAD3 electroporated cells present lengthened cilia **(K')**. Scale bars = 10 µm.

DISCUSSION

The morphogenesis of the SNT is a complex process that requires coordinated cell dynamics, extracellular signalling and tissue rearrangements. In this work, we provide an exhaustive description of the morphogenetic events that built the SNT in the chick embryo. Although this process was studied in the past (Dady et al., 2014; Schoenwolf and Delongo, 1980; Shimokita and Takahashi, 2011), it was never investigated to this extent, even though it is crucial for unravelling the causes of many caudal NTDs. Our findings lead to a revision of the pre-existent model for SN in the chick embryo, the fundamental steps of which we discuss below. Importantly, we have found that the final resolution of the lumen involves central cell intercalation into the lateral walls of the neuroepithelium, a question that remain unsolved for decades (Schoenwolf and Delongo, 1980). We also show that TGF-β/SMAD3 activity is required for the formation of a single central lumen in the chick SNT. Defective TGF-β/SMAD3 activity leads to caudal NTDs characterised by the presence of multiple small lumens. This phenotype is not due to changes in cell viability, cell identity, lumen initiation or apico-basal polarity disruption; but arises from a failure in central cell intercalation during lumen resolution. Finally, we also found lengthened cilia in TGF-β depleted NPCs, suggesting a role of the pathway in the control of ciliary length and a possible mechanism for faulty central cell intercalation.

The basis of SNT formation

How the tail bud transforms into the SNT with a single lumen in its centre is largely a mystery. The commonly accepted model of this process was developed in the 80's and was based on light and scanning electron microscopy studies (Schoenwolf and Delongo, 1980; Schoenwolf and Kelley, 1980). However, the formation of the SNT is a dynamic process that needs to be revisited taking advantage of the knowledge attained in the past few decades and the wide variety of up-to-date available techniques. By studying chick embryos developing *in vivo*, we have been able to decipher the main morphogenetic events driving SNT formation, which lead to the modification of the previously defined model (Schoenwolf and Delongo, 1980). We carefully studied the SN process starting at the mesenchymal NMPs driving caudal body axis elongation, until the complete formation of the caudal SNT, composed of epithelial NPCs enclosing a single central lumen. Based on our findings, we divided the morphogenesis of the SNT into three fundamental steps: (i) cell confinement of NMPs and neural lineage restriction, (ii) MET and initiation of multiple lumens, (iii) lumen resolution into a single central cavity. Our model proposes that SNT formation involves two related cell transformations: first, a change in cell identity from NMPs to NPCs, and second, a switch in cell polarity from mesenchymal (front-rear) to epithelial (apico-basal) (Fig. 34). Both transformations highly associate to the growing BM, which suggests an important role for BM/integrin signalling in the SN process, discussed in following sections. Concomitant to these cellular changes, the SNT lumen is formed *de*

novo in between cells. Small lumens open up at one-cell distance from the BM and isolate a central mesenchymal cell population. The accepted model for SN does not explain how this population of central cells is cleared from the lumen, although it considers the possibility of central cell intercalation into the lateral walls of the neuroepithelium (Schoenwolf and Delongo, 1980). However, even though this hypothesis was posed decades ago, it was never tested. By performing *in vivo* time-lapse imaging in electroporated chick embryos, we were able to follow central NPCs along time. Results show that central cells indeed intercalate into the lateral walls of the neuroepithelium as lumens coalesce. The result of this process is that a hollow SNT composed of epithelial NPCs around a single central lumen arises. Altogether, we have merged studies on cell identity, cell polarity and cell dynamics to extend and complete the pre-existing model of normal SNT development, setting the basis to understand the pathology of caudal NTDs.

The molecular signals driving SN

The molecular signals driving SNT formation remain largely unknown. The Appendix I presents our analysis of the expression of 34 components of the main developmental pathways (BMP, FGF, NOTCH, SONIC HEDGEHOG, TGF-β and WNT) in stage HH15 chick embryos. Whole-mount in situ hybridisation and transverse sections through these same embryos showed interesting patterns of BMP and TGF-β pathway components, such as *BMP2*, *TGF-β1* and *SMAD3*, which lead us to the careful investigation of these two signalling pathways. However, other candidate pathways also emerged from this analysis: WNT, FGF and NOTCH (see *WNT3A, WNT5A, WNT5B, FGF8* and *DLL1* expression patterns in Appendix I). Indeed, WNT and FGF signalling play important roles in the maintenance and expansion of NMPs (Garriock et al., 2015; Takemoto et al., 2006; Wymeersch et al., 2016; Yamaguchi et al., 1999) and in the induction of the mesodermal or neural lineage in NMPs derivatives (Diez del Corral et al., 2002; Gouti et al., 2017; Martin and Kimelman, 2012; Nowotschin et al., 2012; Yoshikawa et al., 1997). On the other hand, the NOTCH pathway has been somewhat explored in *Xenopus* tail bud development. Posterior grafts expressing a constitutively active form of NOTCH-1 induced ectopic tails that contained NT but not somites, suggesting a role for NOTCH in the control of tail bud outgrowth and somitogenesis (Beck and Slack, 1999). Indeed, NOTCH signalling has been demonstrated to be a key player in the regulation of somite formation and segmentation (Conlon et al., 1995; Dale et al., 2003; Evrard et al., 1998; Jiang et al., 2000; Zhang and Gridley, 1998). Yet, it still needs to be elucidated if this pathway has any implications in SNT formation.

The BMP and TGF-β pathways remain largely unexplored in the context of SNT morphogenesis. Members of the TGF-β superfamily have been implicated as major induction signals of EMT and MET (Polyak and Weinberg, 2009; Yang and Weinberg, 2008) and TGF-β pathway components have been found to interact with the apico-basal polarity pathway during MHP formation in the primary NT (Amarnath and Agarwala, 2017) and with the actin cytoskeleton during epithelial lumen expansion (Denker et al., 2015). Moreover, mouse mutants for the BMP and TGF-β pathway components present closed spina bifida phenotypes (Harris and Juriloff, 2007; Sanford et al., 1997; Stottmann et al., 2006), raising the possibility of a key function in SN.

In this work, we show that both TGF-β and BMP signalling pathways are active during the process of SN, supporting the results obtained from the analysis of gene expression. While the inhibition of BMP SMADs results in normal SNTs, the depletion of TGF-β SMAD3, but not SMAD2, generates

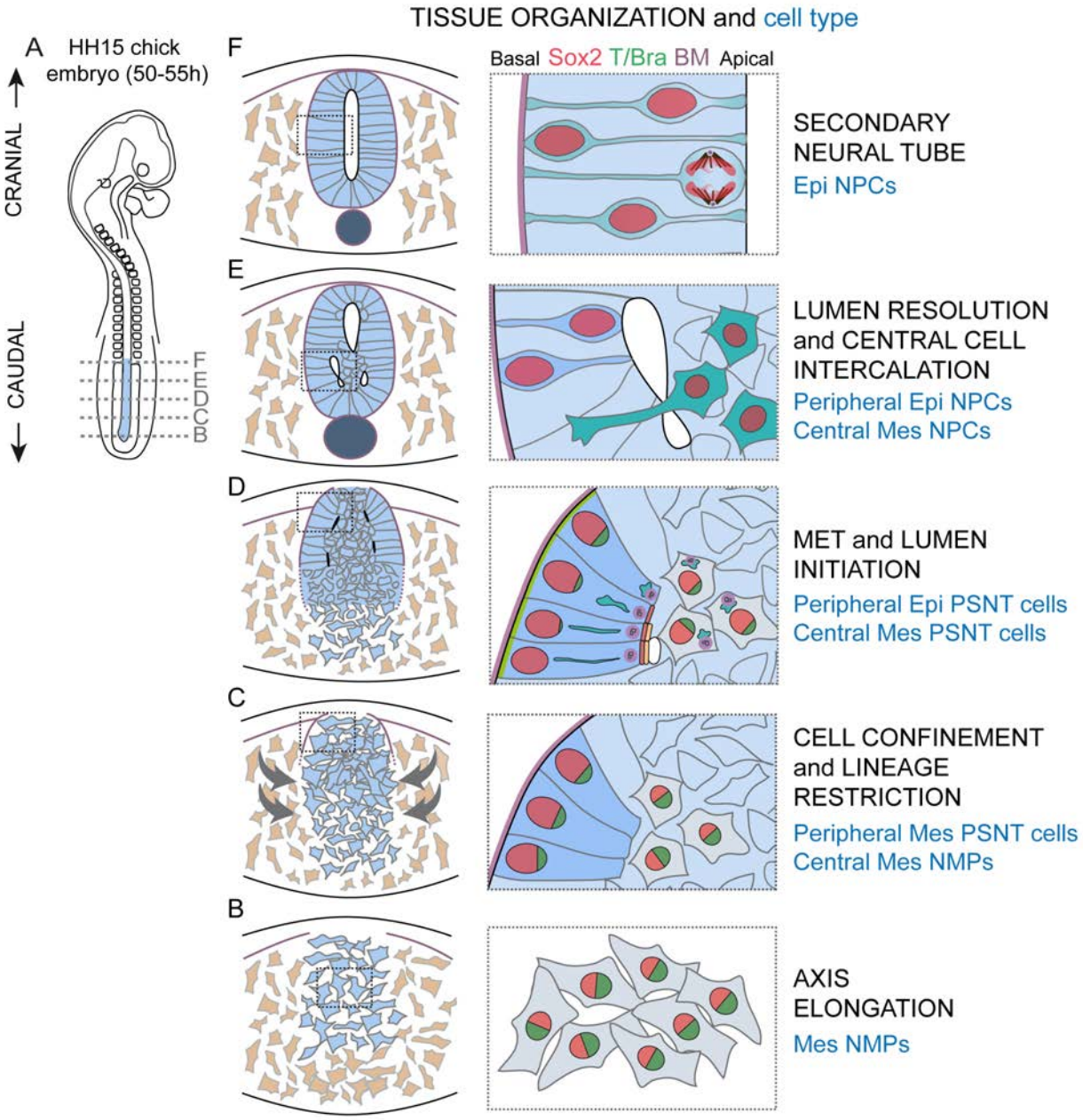

Figure 34. Extension of the model of chick SN. (A) Drawing of a HH15 chick embryo showing the caudal region where SN is taking place. The progression of SN can be followed along the cranio-caudal axis of the same embryo. **(B-F)** Schematic representation of chick SN showing major tissue and cellular rearrangements. SN undergoing cells are shown in light blue, the surrounding mesoderm is in brown, the notochord appears in dark blue and the basement membrane (BM) in purple. During the SN process, Sox2 expression (red) is upregulated and T/Bra (green) downregulated. **(B-C)** Chick SN starts with the condensation and confinement of mesenchymal Sox2+ T/Bra+ neuromesodermal progenitors (NMPs) in the centre of the tissue and the formation of a solid medullary chord (grey arrows). The BM (purple) starts growing ventrally at each side of the medullary cord and cells in its contact downregulate T/Bra and upregulate Sox2, exiting from the NMP state towards the pre-secondary neural tube (PSNT) cell identity. **(D)** Peripheral PSNT cells in contact with the BM are the first to undergo the mesenchymal-to-epithelial transition (MET) Cells in the centre of the tissue remain mesenchymal although they have already started to downregulate T/Bra and upregulate Sox2. Small lumens initiate between the peripheral epithelial and central mesenchymal PSNT cell populations**. (E)** The small cavities formed coalesce into a single central lumen. Both peripheral and central cells are Sox2+ T/Bra- neural progenitor cells (NPCs) by this stage. NPCs in the centre of the developing SNT remain mesenchymal until they eventually intercalate in between the peripheral epithelial NPCs. **(F)** The result of this process is that a hollow secondary neural tube is formed that is surrounded by Sox2+ T/Bra- epithelial NPCs. Mes, mesenchymal; Epi, epithelial.

a NTD characterised by a multilumen phenotype. We cannot completely rule out a possible role for BMP in the process, as the negative results obtained with BMP sh-SMADs electroporation could still be explained if the inhibition of the BMP pathway is normally required for SNT formation. Experiments with constitutively active forms of the BMP SMADs will answer this question (Le Dréau et al., 2014).

The different outcome of the two TGF-β SMADs inhibition resides in the fact that SMAD3 and SMAD2 can either cooperate or antagonize to regulate their transcriptional targets (Miguez et al., 2013). Phosphorylated R-SMAD proteins form heterotrimeric complexes with SMAD4 that enter the nuclei, recruit various co-factors and bind to DNA in order to regulate target gene expression (Moustakas and Heldin, 2002; Moustakas et al., 2001). These complexes can contain two SMAD2 and one SMAD4; two SMAD3 and one SMAD4; or even one SMAD2, one SMAD3 and one SMAD4 molecules (Shi and Massagué, 2003). As SMAD2 and SMAD3 recruit different co-factors and target different regulatory sequences (Brown et al., 2007), the balance between the heterotrimeric complexes formed upon ligand stimulation dictates the set of genes that ultimately will be activated. SMAD2 targets are exclusively activated by the SMAD2-SMAD2-SMAD4 trimer; whereas both the SMAD2-SMAD3-SMAD4 and the SMAD3-SMAD3-SMAD4 complexes activate SMAD3 targets (Miguez et al., 2013). Our results therefore suggest that the activation of SMAD3 targets, but not of SMAD2 targets, is crucial for SNT morphogenesis.

The transition from NMPs to NPCs during SNT formation

Our study has identified the NMPs of the medullary cord in chick embryos, and has followed along development their transformation into NPCs of the SNT (Fig. 34B-F). Our analysis show that NPCs emerge from dual fated NMPs by downregulating T/Bra and upregulating Sox2 expression, consistent with previous studies (Gouti et al., 2017; Koch et al., 2017; Olivera-Martinez et al., 2012). The loss of T/Bra expression and the increase in Sox2 results in the repression of mesodermal genes and in the induction of neural genes (Faial et al., 2015; Sharov et al., 2008). Mesodermal genes are tightly associated to the mesenchymal cell polarity, indeed T/Bra has been found to promote EMT in human cells (Fernando et al., 2010). On the contrary, neural genes reinforce neuroepithelial cell polarity (Sharov et al., 2008). Interestingly, T/Bra not only activates mesodermal control genes but also represses neural control genes, including *Sox2* (Koch et al., 2017). This is reflected in our results as every decrease of nuclear T/Bra intensity is accompanied with an increased in nuclear Sox2 intensity. For all this, once NMPs change their gene expression profile towards the NPC signature, the MET is triggered. The lineage restriction of NMPs into NPCs in the medullary cord of chick embryos is gradual rather than abrupt and the reversibility of the process in this context remains largely unknown. In the anterior NT, PNT cells coming from NMPs can revert back to the multipotent NMP state (Olivera-Martinez et al., 2012). PSNT cells in the cell confinement/lineage restriction and MET/lumen initiation stages could represent this transitional population in the SNT. By the stage of lumen resolution, the majority of cells seem to have acquired the NPC state. However, further studies need to be performed in order to define the precise lineage identity and to unravel the potential reversibility of SN undergoing cells.

In this work, we have also observed a correlation between the BM and increasing Sox2 and decreasing T/Bra levels. The BM assembles following a dorso-ventral direction, which also correlates with

the direction of neural lineage acquisition. Notably, the first cells to exit the NMP state are those contacting the BM. These evidences suggest a possible role for the confining BM in cell identity specification. If this is the case, an unknown initiating signal for BM assemblage still exists, and BM-integrin signalling must be either cooperating or promoted by the well-known molecular networks of neural lineage specification. However, it is also possible that the exit from the NMP state, induced by other extracellular signals, is what initiates BM deposition. Our results only correlate the acquisition of neural identity with the proximity to the BM, but we have not investigated the causal relationship between these two events. Functional experiments are required to answer these open questions.

Finally, our results show that interfering with TGF-β signalling does not affect cell confinement or lineage acquisition in the SNT. The BM is intact 24hpe of sh-SMAD3 electroporation and all SNT cells are Sox2+ and T/Bra-. The extracellular signals involved in NMPs transition to NPCs have been already identified *in vivo* (Gouti et al., 2017; Koch et al., 2017; Olivera-Martinez et al., 2012; Wymeersch et al., 2016) and are highly conserved in vertebrates, despite the large variations in the cellular behaviours that drive body axis elongation (Steventon and Martinez Arias, 2017; Steventon et al., 2016). Interestingly, what differs between vertebrate species is NMPs growth dynamics and timing of decision making, which associate to different strategies of embryo development (external or internal, speed of development, physical constraints, etc.) (Attardi et al., 2018). However, the majority of investigations were performed in mouse and chick embryos from earlier developmental stages, in which the tail bud was not yet present. This is not trivial, as recent investigations indicate that several molecular networks differ between trunk (early PS derived) and tail (late CNH derived) development (Aires et al., 2016; Aires et al., 2019; Gouti et al., 2017; Jurberg et al., 2013: Wymeersch et al., 2019). In one of these studies, GDF11, a member of the TGF-β superfamily that also signals through SMAD2/3, was found to be a key regulator of tail bud NMPs. *Gdf11-/-* mouse embryos showed an expansion of the NMP pool and a bias towards the production of neural derivatives, which resulted in larger NTs with increased rates of cell division (Aires et al., 2019). Although we did not find any specific increase on proliferation in the SNT of sh-Smad3 electroporated chick embryos, increased production of neural progenitors could also be deregulating lumenogenesis and contributing to the multilumen phenotype. Further quantifications of Sox2+ cell number in control and sh-SMAD3 embryos will help to rule out this possibility.

The BM dictates the directionality of cell epithelialization and induces MET in the developing SNT

The interaction of cells with the surrounding ECM sets the directionality of apico-basal cell polarisation *in vitro* (Bedzhov and Zernicka-Goetz, 2014; Bryant et al., 2014; Martin-Belmonte et al., 2008) and *in vivo* (Buckley et al., 2013). The results that we present here point to the importance of the growing BM in providing spatial information for PSNT cell polarisation. As the BM grows ventrally, cell confinement and epithelialization propagate in the same direction. The BM instructs the position of the basal pole, so that BM-contacting cells localise their centrosomes to the opposite side and start elongating (Fig. 34D). That is why we have never observed any sign of apical polarity before BM deposition or integrin basal localisation. As for the study of lineage acquisition, only functional experiments targeting BM assemblage or BM-integrin signalling will determine their role in PSNT epithelial polarity orientation. Moreover, the exact pathways downstream of BM-integrin signalling

operating in the polarisation of the SNT are as yet elusive. As the molecular networks behind epithelial polarity acquisition are highly conserved, we believe that integrin binding to the growing BM of the SNT produces a similar cellular response to that observed *in vitro*, that is through the activation of small GTPases (Bayless and Davis, 2002; Davis and Bayless, 2003; Davis and Camarillo, 1996; O'Brien et al., 2001). In fact, the only previous study of *in vivo* SN manipulation investigated Rac1 and Cdc42 activity in SN-undergoing cells (Shimokita and Takahashi, 2011). This study found that the overactivation of Cdc42 and both the inhibition and overactivation of Rac1 resulted in a mesenchymal cell mass of electroporated cells in the centre of the lumen. These results suggest that both proteins are critical for the MET during SN, as observed in MDCK cysts (Bryant and Mostov, 2008; Martin-Belmonte et al., 2007).

As the BM grows ventrally at each side of the medullary cord, the tissue is increasingly composed of a peripheral apico-basal polarising population and a central population that does not receive BM epithelializing cues and remains mesenchymal (Fig. 34D). Apically localised centrosomes are the first sign of apical polarisation we have detected in peripheral cells, which subsequently drag the Golgi to the apical process and are then followed by the apical localisation of N-cadherin/ZO-1 and aPKC. This sequence of polarisation first localises and builds the machinery (apico-basal oriented MTs and Golgi trafficking) needed for the proper localisation of proteins towards the nascent apical pole. However, previous studies showed that apical proteins, such as PAR3, are necessary for determining centrosome positioning in various cell types (Cai et al., 2003; Feldman and Priess, 2012; Grill et al., 2001; Kemphues et al., 1988; Schmoranzer et al., 2009) and, more interestingly, for apical centrosomal localisation during zebrafish neurulation (Buckley et al., 2013; Hong et al., 2010). In fact, PAR3 is apically localised in the polarised chick NT and its overexpression results in the formation of ectopic rosettes in basal regions of the neuroepithelium (Afonso and Henrique, 2006). All this evidence suggests that PAR3 is also acting upstream of centrosome localisation in the MET of peripheral PSNT cells.

Multiple lumen initiation

Subsequently to apico-basal polarity acquisition, multiple small lumens emerge *de novo* in between the BM-contacting cells and the BM-non-contacting cells. The formation of multiple small lumens is a frequent event *in vivo* (Alvers et al., 2014; Bagnat et al., 2007; Hoijman et al., 2015; Kesavan et al., 2009; Saotome et al., 2004). We believe that this phenomenon is highly associated to cell number: the more cells participating in *de novo* lumen formation, the more lumen foci tend to emerge. This of course promotes a faster lumen development and growth in multicellular tissues. Interestingly, the small lumen foci of the developing SNT could be implicated in luminal signalling, a newly described signalling mechanism (Durdu et al., 2014). Luminal signalling establishes that multicellular tissues use emerging lumen foci to locally concentrate secreted signalling molecules and ensure coordinated signalling responses within the cells sharing the lumen. The developing SNT could also exploit this mechanism, as the multiple lumen foci could be acting as hubs to coordinate cellular behaviours in the medullary cord. They could be concentrating extracellular cues secreted by peripheral cells and constraining its signalling activity, such as BMP2 or TGF-β1 (see Fig. 37 and 39 in Appendix I), and ensure that they reach to the inner cell mass of centrally located cells in the proper time, in order to promote cell polarisation or cell intercalation.

SMAD3 activity does not affect the MET or the initiation of multiple lumens

A role of TGF-β signalling in the disruption of epithelial organisation and EMT is well established (Yang and Weinberg, 2008). However, we show here that SMAD3 depletion does not affect the capability of cells to apico-basally polarise and initiate multiple lumen foci in the developing SNT. As we observe a laminin-stained BM properly confining the SNT in sh-SMAD3 embryos, we hypothesise that the instructive role of the BM for the MET remains intact. Indeed, sh-SMAD3 cells normally elongate and correctly localise their centrosomes to the apical pole. The Golgi apparatus is the only organelle that we have found altered in sh-SMAD3 electroporated NPCs, as it fails to extend as control cells. Although the Golgi is abnormally short, it is still confined to the apical process of NPCs, between the nucleus and the apical surface. It is important to denote that we only studied the cis-Golgi, through the staining of GM130, and left the trans-Golgi unexplored. Nevertheless, the Golgi apparatus in NPCs of the developing neocortex is oriented with their cis-to-trans axis perpendicular to the apico-basal axis of the cell (Taverna et al., 2016). If this is conserved in spinal cord NPCs, which is highly probable, then the extension of the Golgi will not affect apico-basal trafficking to a large extent but other Golgi cisternae functionalities. Indeed, junctional and apical markers such as N-cadherin, ZO-1 and aPKC present a normal subcellular distribution and completely line the multiple luminal surfaces, suggesting that apical intracellular trafficking occurs normally. The fact that TGF-β activity depletion results in a multilumen phenotype with proper apico-basal polarity, rather than in the absence of polarisation and the complete inexistence of a lumen, points to a possible role of the pathway in the last steps of SNT lumen formation.

The three modes of division during SN

A crucial step in late *de novo* lumen morphogenesis is the resolution of a single lumen, which requires coordinated tissue remodelling and luminal expansion. In the SNT, the initiation of multiple lumens is followed by a transient triple lumen stage (one dorsal-central and two ventral-lateral). As lumens coalesce, a population of cord cells remain centrally located; therefore, the clearance of these cells from the centre of the lumen becomes essential for single lumen formation. Our results show that these cells maintain mesenchymal features, even though they had lost T/Bra expression, and that they do not die by apoptosis. Instead, they withdraw from the luminal space by intercalating into the lateral walls of the neuroepithelium. We also report that a cell division always takes place shortly before cell intercalation and that three modes of division occur in the developing SNT, according to their outcome. II are symmetric divisions that generate two intercalating daughter cells (Fig. 35B,B'). IC are asymmetric divisions in which one daughter cell intercalates while the other remains centrally located (Fig. 35C,C'). In this mode, the asymmetric inheritance during mitosis of yet unknown determinants could dictate which cell remains as a central cell and which cell intercalates into the lateral wall during the next cell cycle (Saade et al., 2017; Saade et al., 2018). CC are symmetric divisions that produce two centrally remaining daughter cells (Fig. 35D,D'). Interestingly, although the three modes of division occur simultaneously, they are associated to different cranio-caudal levels of the embryo, which represent different developmental stages. Caudal regions represent earlier stages of the SN process and cells undergo CC divisions to increase the pool of NMPs elongating the body axis. As we move towards cranial regions, the mode of division switches to IC and then to II. This transition through the

different modes of division increasingly promotes cell intercalation and gradually consumes the pool of centrally located cells, which ultimately clears the luminal space.

The extracellular signals that dictate the mode of division in the developing SNT have not yet been identified, mostly because this is the first study that describes these events. Although TGF-β depletion biases mitosis towards the CC mode, we do not think that the pathway has a role in the control of the mode of cell division. The basis of this assumption is the fact that mitosis are *per se* asymmetric, due to the built-in asymmetry of the two centrosomes that are passed on to the daughter cells (mother and daughter) (Saade et al., 2018). Extracellular signals act to overcome these intrinsic asymmetries and promote the expansion of progenitors through symmetric divisions, as observed for SHH and BMP in the anterior NT (Le Dréau et al., 2014; Saade et al., 2013; Saade et al., 2017). Decreasing SHH or BMP signalling in the anterior NT biases NPCs mode of division towards the default asymmetric type, contrary to what results from TGF-β depletion.

A novel role for TGF-β/SMAD3 signalling in central cell intercalation

Our results show that the majority of sh-SMAD3 electroporated NPCs coming from central mitosis are unable to intercalate into the lateral walls of the neuroepithelium, and remain in the centre of the tissue (Fig. 35B''-D''). Central NPCs at the time of lumen resolution maintain the mesenchymal features of the NMPs of the early tail bud. As discussed in previous sections, T/Bra promotes the mesenchymal phenotype in NMPs; however, by the stage of lumen resolution, all cells are mostly T/Bra-, including the central population. Therefore, other molecular factors must account for the maintenance of mesenchymal features in central NPCs.

A role of TGF-β signalling in promoting mesenchymal characteristics is well recognised (Yang and Weinberg, 2008). We found that the TGF-β pathway is active and SMAD3 highly expressed in central cells at the lumen resolution stage. We hypothesize that TGF-β signalling, through SMAD3, could be replacing the lost T/Bra activity in central NPCs and ensure that they retain the mesenchymal features. The maintained mesenchymal capabilities confer high cell motility and invasive protrusions to central cells and permit their intercalation into the lateral walls of the developing neuroepithelium. Indeed, TGF-β activity controls actin polymerisation and actomyosin contractility during the lumen expansion of the *Ciona intestinallis* notochord (Denker et al., 2015). Both actin polymerisation and actomyosin contractility are essential for mesenchymal cell migration (Chi et al., 2014; Ridley et al., 2003). On one hand, actin polymerisation drives protrusion formation at the leading edge of the cell, in the direction of migration. These protrusions can be large lamellipodia, which push along a broad length of plasma membrane, or spike-like filopodia, that serve as sensors to explore the local environment. Indeed, intercalating membrane-GFP+ cells in our time-lapse movies present both types of protrusions. On the other hand, actomyosin contractility is crucial to retract the rear regions during cell migration. In case of SMAD3 depletion, TGF-β signalling is lost too early, central cells loose motility and protrusive activity too soon and they become unable to intercalate (Fig. 35B''-D''). In the end, sh-SMAD3 cells properly elongate and polarise at central locations around the closest initiated lumen, as apico-basal polarisation is not affected, which leads to the multilumen phenotype. To verify this hypothesis, we plan to quantify cell motion in the generated movies and to investigate the protrusive activity of control and sh-SMAD3 electroporated cells.

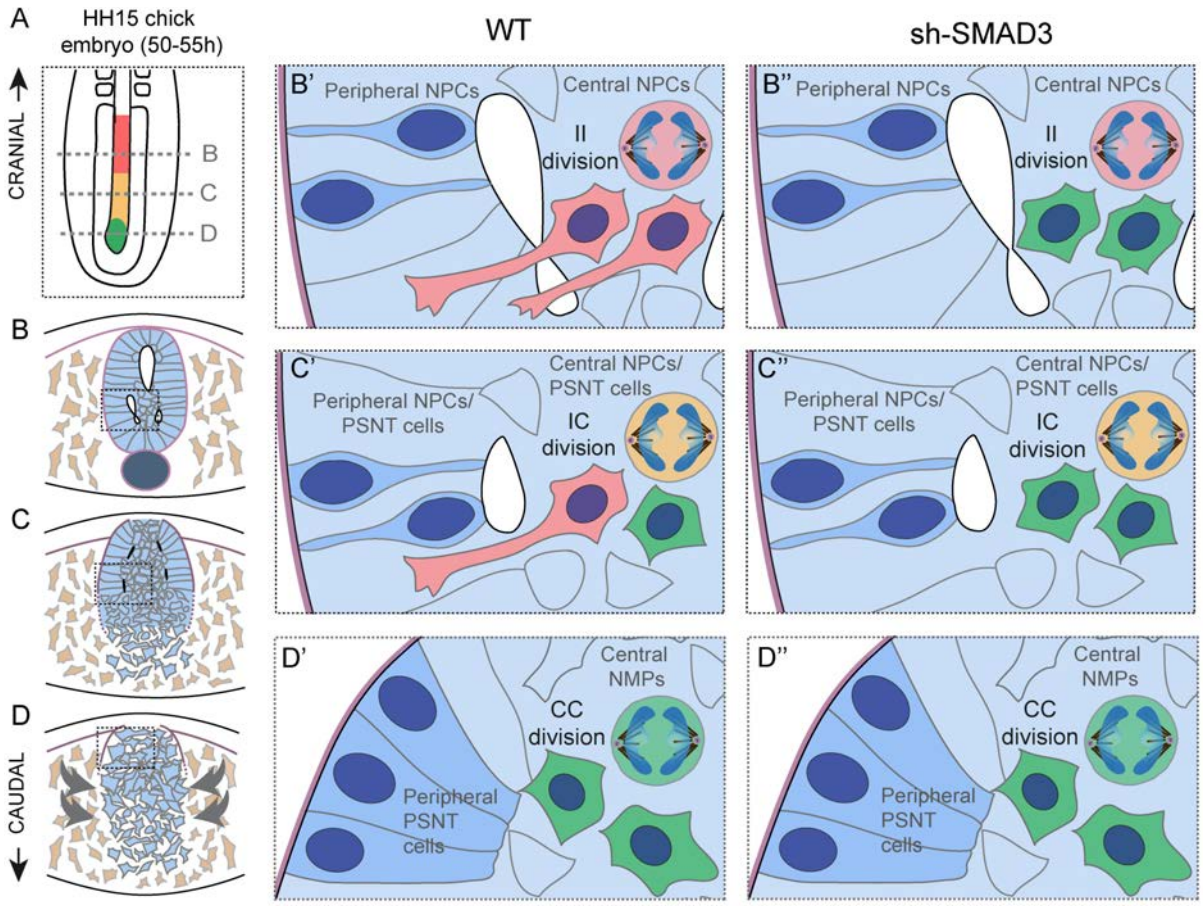

Figure 35. The three modes of division in WT and sh-SMAD3 embryos. (A) Schematic drawing of the caudal region of an HH15 chick embryo. The approximate cranio-caudal location for each of the three modes of division is shown (II, red; IC, yellow; CC, green). **(B-D)** Schematic representation of chick SN showing major tissue and cellular rearrangements. SN undergoing cells are shown in light blue, the surrounding mesoderm is in brown, the notochord appears in dark blue and the basement membrane in purple. **(B'-D')** Schematic representation of the SN cellular rearrangements in chick WT embryos. The three modes of division are represented. **(B')** II division (red) produces two intercalating daughter cells (red). **(C')** IC division (yellow) generates one intercalating daughter cell (red) and one cell that remains in the centre (green). **(D')** CC division (green) produces two centrally located daughter cells (green). **(B''-D'')** Schematic representation of the SN cellular rearrangements in chick sh-SMAD3 embryos. Central cells likely undergo the three modes of division (red, yellow and green) but all of them generate two centrally located cells (green), in spite of the cranio-caudal level at which they occur. NMPs, neuromesodermal progenitors; PSNT cells, pre-secondary neural tube cells; NPCs, neural progenitor cells.

The SMAD3-associated ciliopathy: causation and link to central cell intercalation failure

In this study, we report that TGF-β signalling, through SMAD3, affects the ciliary length in NPCs of the SNT. Previous research performed in *Xenopus* embryos, showed that TGF-β signalling influences the ciliary length of motile cilia (Tözser et al., 2015). In this context, blocking SMAD2 activity resulted in shortened motile cilia, whereas non-motile primary cilia were not disturbed. In the SNT, SMAD3 depletion results in a ciliopathy characterised by abnormally lengthened cilia, while sh-SMAD2 electroporated cells present normal ciliary length. This suggests that the control of ciliary length by TGF-β depends both on the context and on the SMAD-specific regulation of transcription. SMAD2

depletion in *Xenopus* resulted in the absence of several TZ proteins from cilia (Tözser et al., 2015). In line with this, our results show that SMAD3, but not SMAD2, localises to the base of the primary cilia in NPCs of the SNT, likely associating to the TZ (Fig. 36C). The TZ plays an essential role in the control of ciliary length by regulating the selective passage of proteins and lipids into and out of the cilium (Garcia-Gonzalo et al., 2011; Jensen et al., 2015; Reiter et al., 2012; Takao and Verhey, 2016). Altogether, our data indicates that TGF-β signalling affects the regulation of ciliary length in NPCS of the SNT through SMAD3 activity, likely by affecting TZ structure and function (Fig. 36D). Further investigation on the TZ in control and sh-SMAD3 conditions will answer this question.

In addition to the TZ, the control of the length of assembled cilia also requires a tight regulation of the processes that shorten and lengthen the cilia (Keeling et al., 2016). These processes involve both the general vesicular transport system through the Golgi and recycling endosomes and a highly conserved transport system specialised for the transport of proteins in and out of the cilium - the microtubule based intraflagellar transport (IFT) system. The coordinated action of both systems not only provides the necessary components at the tips of the cilia (exocytosis and anterograde transport) but also recycles ciliary products (retrograde transport and endocytosis) (Fig. 36C). To maintain the proper length of the cilia, subunits being added must always match subunits coming off, thus achieving a state of "dynamic stability" (Marshall and Rosenbaum, 2001; Stephens, 1997). Indeed, disorders on ciliary and cellular transport systems produce shortened or lengthened cilia (Besschetnova et al., 2010; Palmer et al., 2011). In this study, we report a failure in Golgi extension in sh-SMAD3 electroporated cells. Although it did not affect apico-basal polarisation, it remains to be seen whether this defect can have an impact on NPCs ciliary length. If so, increased exocytosis and/or ciliary anterograde transport or decreased endocytosis and/or ciliary retrograde transport could result in the lengthened cilia phenotype (Fig. 36D).

Compelling evidence suggests that primary cilia also coordinate multiple events that are required for cell migration, which, when aberrantly regulated, lead to morphogenetic defects (Veland et al., 2014). The ECM provides positional information and guidance to cells in motion through chemical and mechanical cues, such as soluble morphogens and variations in ECM composition, confinement and stiffness. Importantly, primary cilia harbour receptors for several signalling pathways, such as SHH, WNT/PCP or TGF-β, and for the ECM (Christensen et al., 2008; Christensen et al., 2017; McGlashan et al., 2006; Satir et al., 2010) and in migratory cells orient to the direction of migration (Albrecht-Buehler, 1977). Thus, the cilium could function both as a sensor and as a cellular GPS for the navigation of cells (Fig. 36B,C), integrating spatiotemporal information and modulating cytoskeletal changes to yield a cell behaviour, directionality, and speed that, together, constitute the migratory response (Christensen et al., 2008; Jones et al., 2012; Veland et al., 2014). Indeed, ciliopathies are also associated to defective cell migration and neurodevelopmental migration-related disorders in mice (Baudoin et al., 2012; Higginbotham et al., 2012; Tobin et al., 2008). In summary, we hypothesize that SMAD3-associated ciliopathy impairs primary cilia in central NPCs, avoiding the proper sensing and integration of environmental migratory cues (Fig. 36D). This ultimately contributes to the failure of central cell intercalation and to the generation of NTDs. Further investigations on ciliary function in control and sh-SMAD3 electroporated cells will enlighten this issue.

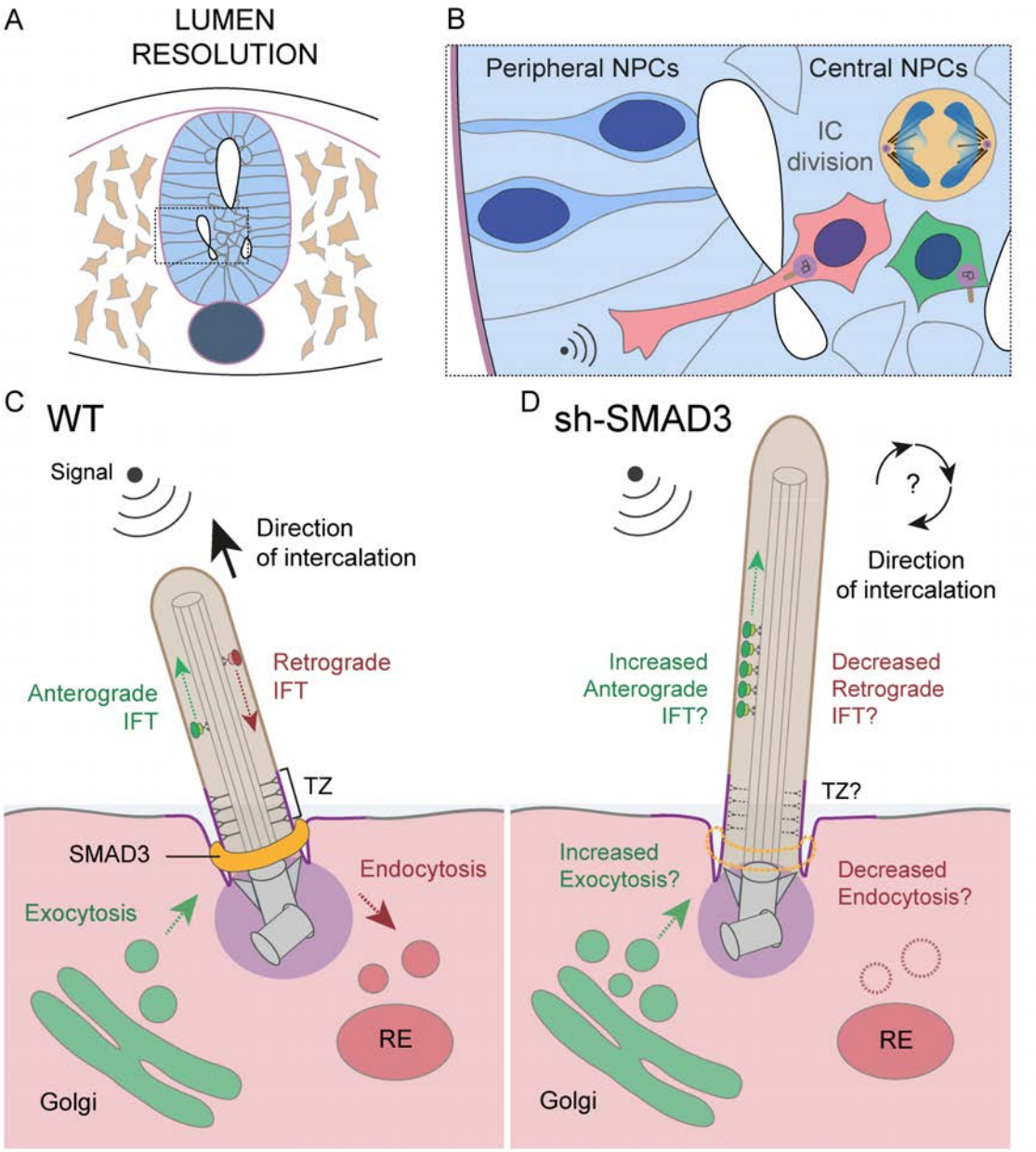

Figure 36. The possible causes of SMAD3-associated ciliopathy and link to central NPC intercalation failure. **(A-B)** Schematic representation of chick SN at the lumen resolution stage showing major tissue and cellular rearrangements. SN undergoing cells are shown in light blue, the surrounding mesoderm is in brown, the notochord appears in dark blue and the basement membrane in purple. An IC division (yellow) is represented, giving rise to an intercalating daughter cell (red) and a centrally located daughter cell (green). **(C)** Schematic representation of the primary cilium of an intercalating cell in WT embryos. Soluble signalling molecules or mechanical cues are sensed by the primary cilium and direct cell intercalation. The length of the primary cilium is determined by the correct gating of ciliary proteins and lipids in the transition zone (TZ) and by the balance of added and extracted subunits. Exocytosis from the Golgi and anterograde IFT lengthen the cilium (green), while endocytosis at the ciliary base and retrograde IFT shorten it (red). SMAD3 (orange) localises to the base of the cilium in NPCs and likely associates to the TZ. **(D)** Schematic representation of the primary cilium of an intercalating cell in sh-SMAD3 embryos. The lengthened cilia of sh-SMAD3 electroporated cells probably avoids the correct sensing of soluble signalling molecules or mechanical cues and results in faulty cell intercalation. The lengthened cilia phenotype could be a consequence of: (i) incorrect gating of proteins and lipids in the TZ, (ii) increased exocytosis and/or anterograde IFT (green), or (iii) decrease endocytosis and/or retrograde IFT (red). SMAD3 no longer localises at the ciliary base. NPCs, neural progenitor cells; RE, recycling endosome; TZ, transition zone; IFT, intraflagellar transport system.

The chick as a model for human SN and associated NTDs

In this thesis, we have focused in the study of the SN in the chick embryo and posed it as an ideal model to gain understanding in human NTDs. Yet, it remains unclear to what extent chick SN represents that of humans. Nevertheless, the formation of the vertebrate body plan during embryonic development is similar across species and is tightly controlled by common developmental regulatory networks (Wolpert, 1997). Scientists such as Karl von Baer, Charles Darwin and Ernst Haeckel observed the astonishing similarity in the appearance of embryos from different vertebrate species as far back as the 19th century (Darwin, 1859; Haeckel, 1874; von Baer, 1828).

In terms of neural development, all vertebrates undergo neurulation to generate a hollow dorsal NT. What varies among vertebrate species is the mode of neurulation chosen to do so, which seem to directly correlate with the method of reproduction (Harrington et al., 2009). Only amniotes (reptiles, birds and mammals) undergo both PN and SN, at least those studied so far. As caudal NTDs emerge from a failure of the process of SN, the most direct approach to study human caudal NTDs is the study of amniote SN. The limited availability of human tissue to perform histological analyses at different developmental stages (Abbott, 2011) reinforces the need to use animal models to understand the events shaping the SNT. While manipulating and imaging mammalian embryos is still problematic, the chick embryo provides an easily accessible model in which the stages of development can be readily identified (Hamburger and Hamilton, 1992). At early stages of development the avian body plan is very similar to that of mammals and these embryos have excellent optical properties as they are thin and planar (Rupp et al., 2003). Furthermore, the SN region in the chick embryo extends up to the lumbar region (Criley, 1969; Dady et al., 2014), closely resembling human development (O'Rahilly and Muller, 1994; O'Rahilly and Muller, 2002), whereas SN only occurs at the tail level in mice (Nievelstein et al., 1993; Shum et al., 2010).

In this study, we have unravelled the dynamics of central NPCs intercalation and found that a failure in the process generates caudal NTDs. Human embryos also present an inner cell mass in between coalescing lumens of the SNT (Saitsu et al., 2004), which is completely absent from mouse SN (Schoenwolf, 1984). Thus, caudal NTDs in human embryos could also arise from a failure in the intercalation and clearance of the inner cell mass from the lumen and, as for chick, TGF-β/SMAD3 activity could be playing an important role in the human process. Then, the one remaining challenge is to determine the extent of conservation of our presented results. Not only investigations across other amniotes will shed light on this subject, but advantage could be also taken from the study of non-amniote animal models, even though they only undergo PN (Harrington et al., 2009; Harrington et al., 2010). Zebrafish and *Xenopus* neurulation shows an active process of radial intercalation, as a superficial layer of neural plate cells extends membrane protrusions and inserts between deep cells to create a single-layered NT (Davidson and Keller, 1999; Hong and Brewster, 2006). This radial intercalation process may share many common features with central cell intercalation in the developing SNT. Thus, combining the study of both amniote and non-amniote animal models could answer the remaining questions on the cellular behaviours that shape the caudal SNT, the failure of which generates caudal NTDs.

CONCLUSIONS

1. Morphogenesis of the secondary neural tube (SNT) requires SMAD3 mediated TGF-β activity, as its depletion results in a multilumen phenotype.

2. Cell confinement and lineage restriction of neuromesodermal progenitors (NMPs) occur in a dorso-ventral fashion and are independent of SMAD3 activity.

3. The triggering of mesenchymal-to-epithelial transition (MET) in cells contacting the basal membrane (BM) and the initiation of several lumen foci at a one-cell distance from the BM are not controlled by SMAD3 activity.

4. SMAD3 activity is dispensable for the complete epithelialization of neural progenitor cells (NPCs) but necessary for single lumen formation.

5. Programmed cell death of central NPCs is not required for the morphogenesis of the SNT lumen.

6. Central NPCs intercalate into the lateral walls of the neuroepithelium as the lumen resolves and SMAD3 activity is essential for this event.

7. Central cells undergo symmetric II (intercalating+intercalating) or asymmetric IC (intercalating+central) modes of cell division to coordinate lumen resolution, while caudal CC (central+central) divisions increase the pool of NMPs contributing to tail bud elongation.

8. SMAD3 activity is required for the control of primary cilia length in NPCs.

REFERENCES

Aaku-Saraste, E., Hellwig, A. and Huttner, W. B. (1996). Loss of occludin and functional tight junctions, but not ZO-1, during neural tube closure--remodeling of the neuroepithelium prior to neurogenesis. *Dev. Biol.* **180**, 664–679.

Abbott, A. (2011). Tissue-bank shortage: Brain child. *Nature* **478**, 442–443.

Afonso, C. and Henrique, D. (2006). PAR3 acts as a molecular organizer to define the apical domain of chick neuroepithelial cells. *J Cell Sci* **119**, 4293–4304.

Agopian, A. J., Tinker, S. C., Lupo, P. J., Canfield, M. A. and Mitchell, L. E. (2013). Proportion of neural tube defects attributable to known risk factors. *Birth Defects Res. A. Clin. Mol. Teratol.* **97**, 42–46.

Ahmed, S., Liu, C.-C. and Nawshad, A. (2007). Mechanisms of palatal epithelial seam disintegration by transforming growth factor (TGF) beta3. *Dev. Biol.* **309**, 193–207.

Aires, R., Jurberg, A. D., Leal, F., Novoa, A., Cohn, M. J. and Mallo, M. (2016). Oct4 Is a Key Regulator of Vertebrate Trunk Length Diversity. *Dev Cell* **38,** 262–274.

Aires, R., Dias, A. and Mallo, M. (2018). Deconstructing the molecular mechanisms shaping the vertebrate body plan. *Curr. Opin. Cell Biol.* **55,** 81–86.

Aires, R., de Lemos, L., Novoa, A., Jurberg, A. D., Mascrez, B., Duboule, D. and Mallo, M. (2019). Tail Bud Progenitor Activity Relies on a Network Comprising Gdf11, Lin28, and Hox13 Genes. *Dev. Cell* **48,** 383-395.e8**.**

Albrecht-Buehler, G. (1977). Phagokinetic tracks of 3T3 cells: parallels between the orientation of track segments and of cellular structures which contain actin or tubulin. *Cell* **12**, 333–339.

Alvers, A. L., Ryan, S., Scherz, P. J., Huisken, J. and Bagnat, M. (2014). Single continuous lumen formation in the zebrafish gut is mediated by smoothened-dependent tissue remodeling. *Development* **141**, 1110–1119.

Amarnath, S. and Agarwala, S. (2017). Cell-cycle-dependent TGFbeta-BMP antagonism regulates neural tube closure by modulating tight junctions. *J Cell Sci* **130**, 119–131.

Ashcroft, G. S., Yang, X., Glick, A. B., Weinstein, M., Letterio, J. L., Mizel, D. E., Anzano, M., Greenwell-Wild, T., Wahl, S. M., Deng, C., et al. (1999). Mice lacking Smad3 show accelerated wound healing and an impaired local inflammatory response. *Nat. Cell Biol.* **1**, 260–266.

Attardi, A., Fulton, T., Florescu, M., Shah, G., Muresan, L., Lenz, M. O., Lancaster, C., Huisken, J., van Oudenaarden, A. and Steventon, B. (2018). Neuromesodermal progenitors are a conserved source of spinal cord with divergent growth dynamics. *Development* **145**,.

Attardo, A., Calegari, F., Haubensak, W., Wilsch-Brauninger, M. and Huttner, W. B. (2008). Live imaging at the onset of cortical neurogenesis reveals differential appearance of the neuronal phenotype in apical versus basal progenitor progeny. *PLoS One* **3**, e2388.

Bagnat, M., Cheung, I. D., Mostov, K. E. and Stainier, D. Y. (2007). Genetic control of single lumen formation in the zebrafish gut. *Nat Cell Biol* **9**, 954–960.

Bagnat, M., Navis, A., Herbstreith, S., Brand-Arzamendi, K., Curado, S., Gabriel, S., Mostov, K., Huisken, J. and Stainier, D. Y. R. (2010). Cse1l is a negative regulator of CFTR-dependent fluid secretion. *Curr. Biol.* **20**, 1840–1845.

Barrios-Rodiles, M., Brown, K. R., Ozdamar, B., Bose, R., Liu, Z., Donovan, R. S., Shinjo, F., Liu, Y., Dembowy, J., Taylor, I. W., et al. (2005). High-throughput mapping of a dynamic signaling network in mammalian cells. *Science* **307**, 1621–1625.

Baudoin, J.-P., Viou, L., Launay, P.-S., Luccardini, C., Espeso Gil, S., Kiyasova, V., Irinopoulou, T., Alvarez, C., Rio, J.-P., Boudier, T., et al. (2012). Tangentially migrating neurons assemble a primary cilium that promotes their reorientation to the cortical plate. *Neuron* **76**, 1108–1122.

Baum, B. and Georgiou, M. (2011). Dynamics of adherens junctions in epithelial establishment, maintenance, and remodeling. *J. Cell Biol.* **192**, 907–917.

Bayless, K. J. and Davis, G. E. (2002). The Cdc42 and Rac1 GTPases are required for capillary lumen formation in three-dimensional extracellular matrices. *J. Cell Sci.* **115**, 1123–1136.

Beck, C. W. and Slack, J. M. (1999). A developmental pathway controlling outgrowth of the Xenopus tail bud. *Development* **126**, 1611–1620.

Bedzhov, I. and Zernicka-Goetz, M. (2014). Self-organizing properties of mouse pluripotent cells initiate morphogenesis upon implantation. *Cell* **156**, 1032–1044.

Benazeraf, B. and Pourquie, O. (2013). Formation and segmentation of the vertebrate body axis. *Annu Rev Cell Dev Biol* **29**, 1–26.

Benazeraf, B., Francois, P., Baker, R. E., Denans, N., Little, C. D. and Pourquie, O. (2010). A random cell motility gradient downstream of FGF controls elongation of an amniote embryo. *Nature* **466**, 248–252.

Benazeraf, B., Beaupeux, M., Tchernookov, M., Wallingford, A., Salisbury, T., Shirtz, A., Shirtz, A., Huss, D., Pourquie, O., Francois, P., et al. (2017). Multi-scale quantification of tissue behavior during amniote embryo axis elongation. *Development*.

Besschetnova, T. Y., Kolpakova-Hart, E., Guan, Y., Zhou, J., Olsen, B. R. and Shah, J. V (2010). Identification of signaling pathways regulating primary cilium length and flow-mediated adaptation. *Curr. Biol.* **20**, 182–187.

Bilder, D., Schober, M. and Perrimon, N. (2003). Integrated activity of PDZ protein complexes regulates epithelial polarity. *Nat. Cell Biol.* **5**, 53–58.

Blasky, A. J., Mangan, A. and Prekeris, R. (2015). Polarised protein transport and lumen formation during epithelial tissue morphogenesis. *Annu Rev Cell Dev Biol* **31**, 575–591.

Boyer, A. S., Ayerinskas, I. I., Vincent, E. B., McKinney, L. A., Weeks, D. L. and Runyan, R. B. (1999). TGFbeta2 and TGFbeta3 have separate and sequential activities during epithelial-mesenchymal cell transformation in the embryonic heart. *Dev. Biol.* **208**, 530–545.

Brown, J. M. and Storey, K. G. (2000). A region of the vertebrate neural plate in which neighbouring cells can adopt neural or epidermal fates. *Curr. Biol.* **10**, 869–872.

Brown, K. A., Pietenpol, J. A. and Moses, H. L. (2007). A tale of two proteins: differential roles and regulation of Smad2 and Smad3 in TGF-beta signaling. *J. Cell. Biochem.* **101**, 9–33.

Brummelkamp, T. R., Bernards, R. and Agami, R. (2002). A system for stable expression of short interfering RNAs in mammalian cells. *Science* **296**, 550–553.

Bryant, D. M. and Mostov, K. E. (2008). From cells to organs: building polarised tissue. *Nat. Rev. Mol. Cell Biol.* **9**, 887.

Bryant, D. M., Datta, A., Rodriguez-Fraticelli, A. E., Peranen, J., Martin-Belmonte, F. and Mostov, K. E. (2010). A molecular network for de novo generation of the apical surface and lumen. *Nat Cell Biol* **12**, 1035–1045.

Bryant, D. M., Roignot, J., Datta, A., Overeem, A. W., Kim, M., Yu, W., Peng, X., Eastburn, D. J., Ewald, A. J., Werb, Z., et al. (2014). A molecular switch for the orientation of epithelial cell polarization. *Dev Cell* **31**, 171–187.

Buckley, C. E., Ren, X., Ward, L. C., Girdler, G. C., Araya, C., Green, M. J., Clark, B. S., Link, B. A. and Clarke, J. D. (2013). Mirror-symmetric microtubule assembly and cell interactions drive lumen formation in the zebrafish neural rod. *EMBO J* **32**, 30–44.

Burren, K. A., Savery, D., Massa, V., Kok, R. M., Scott, J. M., Blom, H. J., Copp, A. J. and Greene, N. D. E. (2008). Gene-environment interactions in the causation of neural tube defects: folate deficiency increases susceptibility conferred by loss of Pax3 function. *Hum. Mol. Genet.* **17**, 3675–3685.

Burute, M., Prioux, M., Blin, G., Truchet, S., Letort, G., Tseng, Q., Bessy, T., Lowell, S., Young, J., Filhol, O., et al. (2017). Polarity Reversal by Centrosome Repositioning Primes Cell Scattering during Epithelial-to-Mesenchymal Transition. *Dev Cell* **40**, 168–184.

Cai, Y., Yu, F., Lin, S., Chia, W. and Yang, X. (2003). Apical complex genes control mitotic spindle geometry and relative size of daughter cells in Drosophila neuroblast and pI asymmetric divisions. *Cell* **112**, 51–62.

Cambray, N. and Wilson, V. (2002). Axial progenitors with extensive potency are localised to the mouse chordoneural hinge. *Development* **129**, 4855–4866.

Cambray, N. and Wilson, V. (2007). Two distinct sources for a population of maturing axial progenitors. *Development* **134**, 2829–2840.

Caspary, T., Larkins, C. E. and Anderson, K. V (2007). The graded response to Sonic Hedgehog depends on cilia architecture. *Dev. Cell* **12**, 767–778.

Catala, M., Teillet, M. A. and Le Douarin, N. M. (1995). Organization and development of the tail bud analyzed with the quail-chick chimaera system. *Mech Dev* **51**, 51–65.

Catala, M., Teillet, M. A., De Robertis, E. M. and Le Douarin, M. L. (1996). A spinal cord fate map in the avian embryo: while regressing, Hensen's node lays down the notochord and floor plate thus joining the spinal cord lateral walls. *Development* **122**, 2599–2610.

Cearns, M. D., Escuin, S., Alexandre, P., Greene, N. D. and Copp, A. J. (2016). Microtubules, polarity and vertebrate neural tube morphogenesis. *J Anat* **229**, 63–74.

Chapman, S. C., Collignon, J., Schoenwolf, G. C. and Lumsden, A. (2001). Improved method for chick whole-embryo culture using a filter paper carrier. *Dev Dyn* **220**, 284–289.

Chenn, A., Zhang, Y. A., Chang, B. T. and McConnell, S. K. (1998). Intrinsic polarity of mammalian neuroepithelial cells. *Mol. Cell. Neurosci.* **11**, 183–193.

Chi, Q., Yin, T., Gregersen, H., Deng, X., Fan, Y., Zhao, J., Liao, D. and Wang, G. (2014). Rear actomyosin contractility-driven directional cell migration in three-dimensional matrices: a mechano-chemical coupling mechanism. *J. R. Soc. Interface* **11**, 20131072.

Chlasta, J., Milani, P., Runel, G., Duteyrat, J. L., Arias, L., Lamiré, L. A., Boudaoud, A. and Grammont, M. (2017). Variations in basement membrane mechanics are linked to epithelial morphogenesis. *Dev.* **144**, 4350–4362.

Christensen, S. T., Pedersen, S. F., Satir, P., Veland, I. R. and Schneider, L. (2008). The primary cilium coordinates signaling pathways in cell cycle control and migration during development and tissue repair. *Curr. Top. Dev. Biol.* **85**, 261–301.

Christensen, S. T., Morthorst, S. K., Mogensen, J. B. and Pedersen, L. B. (2017). Primary Cilia and Coordination of Receptor Tyrosine Kinase (RTK) and Transforming Growth Factor beta (TGF-beta) Signaling. *Cold Spring Harb Perspect Biol* **9**,.

Clement, C. A., Ajbro, K. D., Koefoed, K., Vestergaard, M. L., Veland, I. R., Henriques de Jesus, M. P. R., Pedersen, L. B., Benmerah, A., Andersen, C. Y., Larsen, L. A., et al. (2013). TGF-β Signaling Is Associated with Endocytosis at the Pocket Region of the Primary Cilium. *Cell Rep.* **3**, 1806–1814.

Colas, J. F. and Schoenwolf, G. C. (2001). Towards a cellular and molecular understanding of neurulation. *Dev Dyn* **221**, 117–145.

Conlon, R. A., Reaume, A. G. and Rossant, J. (1995). Notch1 is required for the coordinate segmentation of somites. *Development* **121**, 1533–1545.

Copp, A. J. and Greene, N. D. E. (2013). Neural tube defects--disorders of neurulation and related embryonic processes. *Wiley Interdiscip. Rev. Dev. Biol.* **2**, 213–227.

Copp, A. J., Greene, N. D. and Murdoch, J. N. (2003). The genetic basis of mammalian neurulation. *Nat Rev Genet* **4**, 784–793.

Copp, A. J., Adzick, N. S., Chitty, L. S., Fletcher, J. M., Holmbeck, G. N. and Shaw, G. M. (2015). Spina bifida. *Nat Rev Dis Prim.* **1**, 15007.

Correia, A. C., Costa, M., Moraes, F., Bom, J., Novoa, A. and Mallo, M. (2007). Bmp2 is required for migration but not for induction of neural crest cells in the mouse. *Dev Dyn* **236**, 2493–2501.

Costanzo, R., Watterson, R. L. and Schoenwolf, G. C. (1982). Evidence that secondary neurulation occurs autonomously in the chick embryo. *J Exp Zool* **219**, 233–240.

Creasy, M. R. and Alberman, E. D. (1976). Congenital malformations of the central nervous system in spontaneous abortions. *J. Med. Genet.* **13**, 9–16.

Criley, B. B. (1969). Analysis of embryonic sources and mechanims of development of posterior levels of chick neural tubes. *J Morphol* **128**, 465–501.

Dady, A., Havis, E., Escriou, V., Catala, M. and Duband, J. L. (2014). Junctional neurulation: a unique developmental program shaping a discrete region of the spinal cord highly susceptible to neural tube defects. *J Neurosci* **34**, 13208–13221.

Dale, J. K., Maroto, M., Dequeant, M.-L., Malapert, P., McGrew, M. and Pourquie, O. (2003). Periodic notch inhibition by lunatic fringe underlies the chick segmentation clock. *Nature* **421**, 275–278.

Darwin, C. R. (1859). *On the origin of species by means of natural selection, or the preservation of favoured races in the struggle for life*. London: John Murray.

Datta, A., Bryant, D. M. and Mostov, K. E. (2011). Molecular regulation of lumen morphogenesis. *Curr Biol* **21**, R126-36.

Davidson, L. A. and Keller, R. E. (1999). Neural tube closure in Xenopus laevis involves medial migration, directed protrusive activity, cell intercalation and convergent extension. *Development* **126**, 4547–4556.

Davies, J. A. (1996). Mesenchyme to epithelium transition during development of the mammalian kidney tubule. *Acta Anat. (Basel).* **156**, 187–201.

Davis, G. E. and Bayless, K. J. (2003). An integrin and Rho GTPase-dependent pinocytic vacuole mechanism controls capillary lumen formation in collagen and fibrin matrices. *Microcirculation* **10**, 27–44.

Davis, G. E. and Camarillo, C. W. (1996). An alpha 2 beta 1 integrin-dependent pinocytic mechanism involving intracellular vacuole formation and coalescence regulates capillary lumen and tube formation in three-dimensional collagen matrix. *Exp. Cell Res.* **224**, 39–51.

Debnath, J. and Brugge, J. S. (2005). Modelling glandular epithelial cancers in three-dimensional cultures. *Nat. Rev. Cancer* **5**, 675–688.

Debnath, J., Mills, K. R., Collins, N. L., Reginato, M. J., Muthuswamy, S. K. and Brugge, J. S. (2002). The role of apoptosis in creating and maintaining luminal space within normal and oncogene-expressing mammary acini. *Cell* **111**, 29–40.

Denker, E., Sehring, I. M., Dong, B., Audisso, J., Mathiesen, B. and Jiang, D. (2015). Regulation by a TGFbeta-ROCK-actomyosin axis secures a non-linear lumen expansion that is essential for tubulogenesis. *Development* **142**, 1639–1650.

Dennler, S., Itoh, S., Vivien, D., ten Dijke, P., Huet, S. and Gauthier, J. M. (1998). Direct binding of Smad3 and Smad4 to critical TGF beta-inducible elements in the promoter of human plasminogen activator inhibitor-type 1 gene. *EMBO J.* **17**, 3091–3100.

Diez del Corral, R., Breitkreuz, D. N. and Storey, K. G. (2002). Onset of neuronal differentiation is regulated by paraxial mesoderm and requires attenuation of FGF signalling. *Development* **129**, 1681–1691.

Dolk, H., Loane, M. and Garne, E. (2010). The prevalence of congenital anomalies in Europe. *Adv. Exp. Med. Biol.* **686**, 349–364.

Dongre, A. and Weinberg, R. A. (2019). New insights into the mechanisms of epithelial–mesenchymal transition and implications for cancer. *Nat. Rev. Mol. Cell Biol.* **20**, 69–84.

Downs, K. M. (2009). The enigmatic primitive streak: prevailing notions and challenges concerning the body axis of mammals. *Bioessays* **31**, 892–902.

Duband, J.-L. (2010). Diversity in the molecular and cellular strategies of epithelium-to-mesenchyme transitions: Insights from the neural crest. *Cell Adh. Migr.* **4**, 458–482.

Dudley, A. T., Lyons, K. M. and Robertson, E. J. (1995). A requirement for bone morphogenetic protein-7 during development of the mammalian kidney and eye. *Genes Dev.* **9**, 2795–2807.

Durdu, S., Iskar, M., Revenu, C., Schieber, N., Kunze, A., Bork, P., Schwab, Y. and Gilmour, D. (2014). Luminal signalling links cell communication to tissue architecture during organogenesis. *Nature* **515**, 120–124.

Dzhindzhev, N. S., Yu, Q. D., Weiskopf, K., Tzolovsky, G., Cunha-Ferreira, I., Riparbelli, M., Rodrigues-Martins, A., Bettencourt-Dias, M., Callaini, G. and Glover, D. M. (2010). Asterless is a scaffold for the onset of centriole assembly. *Nature* **467**, 714–718.

Eaton, S. and Martin-Belmonte, F. (2014). Cargo sorting in the endocytic pathway: a key regulator of cell polarity and tissue dynamics. *Cold Spring Harb. Perspect. Biol.* **6**, a016899.

Eom, D. S., Amarnath, S., Fogel, J. L. and Agarwala, S. (2012). Bone morphogenetic proteins regulate hinge point formation during neural tube closure by dynamic modulation of apicobasal polarity. *Birth Defects Res A Clin Mol Teratol* **94**, 804–816.

Evrard, Y. A., Lun, Y., Aulehla, A., Gan, L. and Johnson, R. L. (1998). lunatic fringe is an essential mediator of somite segmentation and patterning. *Nature* **394**, 377–381.

Eyal-Giladi, H. and Kochav, S. (1976). From cleavage to primitive streak formation: a complementary normal table and a new look at the first stages of the development of the chick. I. General morphology. *Dev. Biol.* **49**, 321–337.

Faial, T., Bernardo, A. S., Mendjan, S., Diamanti, E., Ortmann, D., Gentsch, G. E., Mascetti, V. L., Trotter, M. W., Smith, J. C. and Pedersen, R. A. (2015). Brachyury and SMAD signalling collaboratively orchestrate distinct mesoderm and endoderm gene regulatory networks in differentiating human embryonic stem cells. *Development* **142**, 2121–2135.

Feldman, J. L. and Priess, J. R. (2012). A role for the centrosome and PAR-3 in the hand-off of MTOC function during epithelial polarization. *Curr. Biol.* **22**, 575–582.

Feng, X.-H. and Derynck, R. (2005). Specificity and versatility in tgf-beta signaling through Smads. *Annu. Rev. Cell Dev. Biol.* **21**, 659–693.

Fernando, R. I., Litzinger, M., Trono, P., Hamilton, D. H., Schlom, J. and Palena, C. (2010). The T-box transcription factor Brachyury promotes epithelial-mesenchymal transition in human tumor cells. *J. Clin. Invest.* **120**, 533–544.

Francis, P. H., Richardson, M. K., Brickell, P. M. and Tickle, C. (1994). Bone morphogenetic proteins and a signalling pathway that controls patterning in the developing chick limb. *Development* **120**, 209–218.

Galvez-Santisteban, M., Rodriguez-Fraticelli, A. E., Bryant, D. M., Vergarajauregui, S., Yasuda, T., Banon-Rodriguez, I., Bernascone, I., Datta, A., Spivak, N., Young, K., et al. (2012). Synaptotagmin-like proteins control the formation of a single apical membrane domain in epithelial cells. *Nat Cell Biol* **14**, 838–849.

Garcia-Campmany, L. and Marti, E. (2007). The TGFbeta intracellular effector Smad3 regulates neuronal differentiation and cell fate specification in the developing spinal cord. *Development* **134**, 65–75.

Garcia-Gonzalo, F. R., Corbit, K. C., Sirerol-Piquer, M. S., Ramaswami, G., Otto, E. A., Noriega, T. R., Seol, A. D., Robinson, J. F., Bennett, C. L., Josifova, D. J., et al. (2011). A transition zone complex regulates mammalian ciliogenesis and ciliary membrane composition. *Nat. Genet.* **43**, 776–784.

Garriock, R. J., Chalamalasetty, R. B., Kennedy, M. W., Canizales, L. C., Lewandoski, M. and Yamaguchi, T. P. (2015). Lineage tracing of neuromesodermal progenitors reveals novel Wnt-dependent roles in trunk progenitor cell maintenance and differentiation. *Development* **142**, 1628–1638.

Gassama-Diagne, A., Yu, W., ter Beest, M., Martin-Belmonte, F., Kierbel, A., Engel, J. and Mostov, K. (2006). Phosphatidylinositol-3,4,5-trisphosphate regulates the formation of the basolateral plasma membrane in epithelial cells. *Nat. Cell Biol.* **8**, 963–970.

Gilbert SF. (2000). *Developmental Biology*. 6th editio. Sunderland (MA): Sinauer Associates.

Gouti, M., Tsakiridis, A., Wymeersch, F. J., Huang, Y., Kleinjung, J., Wilson, V. and Briscoe, J. (2014). In vitro generation of neuromesodermal progenitors reveals distinct roles for wnt signalling in the specification of spinal cord and paraxial mesoderm identity. *PLoS Biol* **12**, e1001937.

Gouti, M., Delile, J., Stamataki, D., Wymeersch, F. J., Huang, Y., Kleinjung, J., Wilson, V. and Briscoe, J. (2017). A Gene Regulatory Network Balances Neural and Mesoderm Specification during Vertebrate Trunk Development. *Dev Cell* **41**, 243-261 e7.

Greco, T. L., Takada, S., Newhouse, M. M., McMahon, J. A., McMahon, A. P. and Camper, S. A. (1996). Analysis of the vestigial tail mutation demonstrates that Wnt-3a gene dosage regulates mouse axial development. *Genes Dev.* **10**, 313–324.

Greene, N. D. and Copp, A. J. (2014). Neural tube defects. *Annu Rev Neurosci* **37**, 221–242.

Greene, N. D. E., Stanier, P. and Copp, A. J. (2009). Genetics of human neural tube defects. *Hum. Mol. Genet.* **18**, R113-29.

Griffith, C. M., Wiley, M. J. and Sanders, E. J. (1992). The vertebrate tail bud: three germ layers from one tissue. *Anat. Embryol. (Berl).* **185**, 101–113.

Grill, S. W., Gonczy, P., Stelzer, E. H. and Hyman, A. A. (2001). Polarity controls forces governing asymmetric spindle positioning in the Caenorhabditis elegans embryo. *Nature* **409**, 630–633.

Haeckel, E. (1874). *Anthropogenie oder Entwickelungsgeschichte des Menschen.* Engelmann: Leipzig.

Hamburger, V. and Hamilton, H. L. (1992). A series of normal stages in the development of the chick embryo. 1951. *Dev Dyn* **195**, 231–272.

Harrington, M. J., Hong, E. and Brewster, R. (2009). Comparative analysis of neurulation: first impressions do not count. *Mol Reprod Dev* **76**, 954–965.

Harrington, M. J., Chalasani, K. and Brewster, R. (2010). Cellular mechanisms of posterior neural tube morphogenesis in the zebrafish. *Dev Dyn* **239**, 747–762.

Harris, M. J. and Juriloff, D. M. (2007). Mouse mutants with neural tube closure defects and their role in understanding human neural tube defects. *Birth Defects Res A Clin Mol Teratol* **79**, 187–210.

Harris, M. J. and Juriloff, D. M. (2010). An update to the list of mouse mutants with neural tube closure defects and advances toward a complete genetic perspective of neural tube closure. *Birth Defects Res A Clin Mol Teratol* **88**, 653–669.

Hay, E. D. and Zuk, A. (1995). Transformations between epithelium and mesenchyme: normal, pathological, and experimentally induced. *Am. J. Kidney Dis.* **26**, 678–690.

Hebert, A. M., DuBoff, B., Casaletto, J. B., Gladden, A. B. and McClatchey, A. I. (2012). Merlin/ERM proteins establish cortical asymmetry and centrosome position. *Genes Dev.* **26**, 2709–2723.

Henrique, D., Abranches, E., Verrier, L. and Storey, K. G. (2015). Neuromesodermal progenitors and the making of the spinal cord. *Development* **142**, 2864–2875.

Higginbotham, H., Eom, T.-Y., Mariani, L. E., Bachleda, A., Hirt, J., Gukassyan, V., Cusack, C. L., Lai, C., Caspary, T. and Anton, E. S. (2012). Arl13b in primary cilia regulates the migration and placement of interneurons in the developing cerebral cortex. *Dev. Cell* **23**, 925–938.

Hildebrandt, F., Benzing, T. and Katsanis, N. (2011). Ciliopathies. *N Engl J Med* **364**, 1533–1543.

Hirata, M. and Hall, B. K. (2000). Temporospatial patterns of apoptosis in chick embryos during the morphogenetic period of development. *Int J Dev Biol* **44**, 757–768.

Hoijman, E., Rubbini, D., Colombelli, J. and Alsina, B. (2015). Mitotic cell rounding and epithelial thinning regulate lumen growth and shape. *Nat Commun* **6**, 7355.

Holmdahl, D. (1925). Experimentelle Untersuchungen uber die Lage der Grenze primarer und sekundarer Korperentwicklung beim Huhn. *Anat Anz* 393–396.

Hong, E. and Brewster, R. (2006). N-cadherin is required for the polarised cell behaviors that drive neurulation in the zebrafish. *Development* **133**, 3895–3905.

Hong, E., Jayachandran, P. and Brewster, R. (2010). The polarity protein Pard3 is required for centrosome positioning during neurulation. *Dev. Biol.* **341**, 335–345.

Hoot, K. E., Lighthall, J., Han, G., Lu, S.-L., Li, A., Ju, W., Kulesz-Martin, M., Bottinger, E. and Wang, X.-J. (2008). Keratinocyte-specific Smad2 ablation results in increased epithelial-mesenchymal transition during skin cancer formation and progression. *J. Clin. Invest.* **118**, 2722–2732.

Horne-Badovinac, S., Lin, D., Waldron, S., Schwarz, M., Mbamalu, G., Pawson, T., Jan, Y., Stainier, D. Y. and Abdelilah-Seyfried, S. (2001). Positional cloning of heart and soul reveals multiple roles for PKC lambda in zebrafish organogenesis. *Curr. Biol.* **11**, 1492–1502.

Huang, X. and Saint-Jeannet, J.-P. (2004). Induction of the neural crest and the opportunities of life on the edge. *Dev. Biol.* **275**, 1–11.

Hughes, A. F. and Freeman, R. B. (1974). Comparative remarks on the development of the tail cord among higher vertebrates. *J. Embryol. Exp. Morphol.* **32**, 355–363.

Humphreys, R. C., Krajewska, M., Krnacik, S., Jaeger, R., Weiher, H., Krajewski, S., Reed, J. C. and Rosen, J. M. (1996). Apoptosis in the terminal endbud of the murine mammary gland: a mechanism of ductal morphogenesis. *Development* **122**, 4013–4022.

Huss, D., Benazeraf, B., Wallingford, A., Filla, M., Yang, J., Fraser, S. E. and Lansford, R. (2015). A transgenic quail model that enables dynamic imaging of amniote embryogenesis. *Development* **142**, 2850–2859.

Iimura, T., Yang, X., Weijer, C. J. and Pourquie, O. (2007). Dual mode of paraxial mesoderm formation during chick gastrulation. *Proc. Natl. Acad. Sci. U. S. A.* **104**, 2744–2749.

Jaskoll, T. and Melnick, M. (1999). Submandibular gland morphogenesis: stage-specific expression of TGF-alpha/EGF, IGF, TGF-beta, TNF, and IL-6 signal transduction in normal embryonic mice and the phenotypic effects of TGF-beta2, TGF-beta3, and EGF-r null mutations. *Anat. Rec.* **256**, 252–268.

Jelinek, R., Seichert, V. and Klika, E. (1969). Mechanism of morphogenesis of caudal neural tube in the chick embryo. *Folia Morphol. (Warsz).* **17**, 355–367.

Jensen, V. L., Li, C., Bowie, R. V, Clarke, L., Mohan, S., Blacque, O. E. and Leroux, M. R. (2015). Formation of the transition zone by Mks5/Rpgrip1L establishes a ciliary zone of exclusion (CIZE) that compartmentalises ciliary signalling proteins and controls PIP2 ciliary abundance. *EMBO J.* **34**, 2537–2556.

Jiang, Y. J., Aerne, B. L., Smithers, L., Haddon, C., Ish-Horowicz, D. and Lewis, J. (2000). Notch signalling and the synchronization of the somite segmentation clock. *Nature* **408**, 475–479.

Jones, T. J., Adapala, R. K., Geldenhuys, W. J., Bursley, C., AbouAlaiwi, W. A., Nauli, S. M. and Thodeti, C. K. (2012). Primary cilia regulates the directional migration and barrier integrity of endothelial cells through the modulation of hsp27 dependent actin cytoskeletal organization. *J. Cell. Physiol.* **227**, 70–76.

Joukov, V. and De Nicolo, A. (2019). The Centrosome and the Primary Cilium: The Yin and Yang of a Hybrid Organelle. *Cells* **8**,.

Ju, W., Ogawa, A., Heyer, J., Nierhof, D., Yu, L., Kucherlapati, R., Shafritz, D. A. and Bottinger, E. P. (2006). Deletion of Smad2 in mouse liver reveals novel functions in hepatocyte growth and differentiation. *Mol. Cell. Biol.* **26**, 654–667.

Jurberg, A. D., Aires, R., Varela-Lasheras, I., Novoa, A. and Mallo, M. (2013). Switching axial progenitors from producing trunk to tail tissues in vertebrate embryos. *Dev Cell* **25,** 451–462.

Jurberg, A. D., Aires, R., Novoa, A., Rowland, J. E. and Mallo, M. (2014). Compartment-dependent activities of Wnt3a/beta-catenin signaling during vertebrate axial extension. *Dev Biol* **394,** 253–263.

Juriloff, D. M. and Harris, M. J. (2018). Insights into the Etiology of Mammalian Neural Tube Closure Defects from Developmental, Genetic and Evolutionary Studies. *J. Dev. Biol.* **6**,.

Karfunkel, P. (1974). The mechanisms of neural tube formation. *Int. Rev. Cytol.* **38**, 245–271.

Keeling, J., Tsiokas, L. and Maskey, D. (2016). Cellular Mechanisms of Ciliary Length Control. *Cells* **5**.

Keller, R., Shih, J., Sater, A. K. and Moreno, C. (1992). Planar induction of convergence and extension of the neural plate by the organizer of Xenopus. *Dev. Dyn.* **193**, 218–234.

Keller, R., Shook, D. and Skoglund, P. (2008). The forces that shape embryos: physical aspects of convergent extension by cell intercalation. *Phys. Biol.* **5**, 15007.

Kemphues, K. J., Priess, J. R., Morton, D. G. and Cheng, N. S. (1988). Identification of genes required for cytoplasmic localization in early C. elegans embryos. *Cell* **52**, 311–320.

Kesavan, G., Sand, F. W., Greiner, T. U., Johansson, J. K., Kobberup, S., Wu, X., Brakebusch, C. and Semb, H. (2009). Cdc42-mediated tubulogenesis controls cell specification. *Cell* **139**, 791–801.

Kimelman, D. (2016). Tales of Tails (and Trunks): Forming the Posterior Body in Vertebrate Embryos. *Curr. Top. Dev. Biol.* **116**, 517–536.

Klika, E. and Jelinek, R. (1969). The structure of the end and tail bud of the chick embryo. *Folia Morphol. (Warsz).* **17**, 29–40.

Kobayashi, T. and Dynlacht, B. D. (2011). Regulating the transition from centriole to basal body. *J. Cell Biol.* **193**, 435–444.

Koch, F., Scholze, M., Wittler, L., Schifferl, D., Sudheer, S., Grote, P., Timmermann, B., Macura, K. and Herrmann, B. G. (2017). Antagonistic Activities of Sox2 and Brachyury Control the Fate Choice of Neuro-Mesodermal Progenitors. *Dev Cell* **42**, 514-526 e7.

Kochav, S., Ginsburg, M. and Eyal-Giladi, H. (1980). From cleavage to primitive streak formation: a complementary normal table and a new look at the first stages of the development of the chick. II. Microscopic anatomy and cell population dynamics. *Dev. Biol.* **79**, 296–308.

Kojima, S., Vignjevic, D. and Borisy, G. G. (2004). Improved silencing vector co-expressing GFP and small hairpin RNA. *Biotechniques* **36**, 74–79.

Kondoh, H. and Takemoto, T. (2012). Axial stem cells deriving both posterior neural and mesodermal tissues during gastrulation. *Curr Opin Genet Dev* **22**, 374–380.

Korchynskyi, O. and ten Dijke, P. (2002). Identification and functional characterization of distinct critically important bone morphogenetic protein-specific response elements in the Id1 promoter. *J. Biol. Chem.* **277**, 4883–4891.

Krupinski, T. and Beitel, G. J. (2009). Unexpected roles of the Na-K-ATPase and other ion transporters in cell junctions and tubulogenesis. *Physiology (Bethesda).* **24**, 192–201.

Langman, J., Guerrant, R. L. and Freeman, B. G. (1966). Behavior of neuro-epithelial cells during closure of the neural tube. *J Comp Neurol* **127**, 399–411.

Le Douarin, N. M. (2001). Early neurogenesis in Amniote vertebrates. *Int J Dev Biol* **45**, 373–378.

Le Douarin, N. M., Teillet, M. A. and Catala, M. (1998). Neurulation in amniote vertebrates: a novel view deduced from the use of quail-chick chimeras. *Int J Dev Biol* **42**, 909–916.

Le Dreau, G. and Marti, E. (2012). Dorsal-ventral patterning of the neural tube: a tale of three signals. *Dev Neurobiol* **72**, 1471–1481.

Le Dreau, G. and Marti, E. (2013). The multiple activities of BMPs during spinal cord development. *Cell. Mol. Life Sci.* **70**, 4293–4305.

Le Dreau, G., Garcia-Campmany, L., Rabadan, M. A., Ferronha, T., Tozer, S., Briscoe, J. and Marti, E. (2012). Canonical BMP7 activity is required for the generation of discrete neuronal populations in the dorsal spinal cord. *Development* **139**, 259–268.

Le Dreau, G., Saade, M., Gutierrez-Vallejo, I. and Marti, E. (2014). The strength of SMAD1/5 activity determines the mode of stem cell division in the developing spinal cord. *J Cell Biol* **204**, 591–605.

Le Dréau, G., Saade, M., Gutiérrez-Vallejo, I. and Martí, E. (2014). The strength of SMAD1/5 activity determines the mode of stem cell division in the developing spinal cord. *J. Cell Biol.*

Leck, I. (1974). Causation of neural tube defects: clues from epidemiology. *Br. Med. Bull.* **30**, 158–163.

Li, C. and Naren, A. P. (2010). CFTR chloride channel in the apical compartments: spatiotemporal coupling to its interacting partners. *Integr. Biol. (Camb).* **2**, 161–177.

Lowery, L. A. and Sive, H. (2004). Strategies of vertebrate neurulation and a re-evaluation of teleost neural tube formation. *Mech Dev* **121**, 1189–1197.

Lowery, L. A. and Sive, H. (2005). Initial formation of zebrafish brain ventricles occurs independently of circulation and requires the nagie oko and snakehead/atp1a1a.1 gene products. *Development* **132**, 2057–2067.

Luxardi, G., Marchal, L., Thome, V. and Kodjabachian, L. (2010). Distinct Xenopus Nodal ligands sequentially induce mesendoderm and control gastrulation movements in parallel to the Wnt/PCP pathway. *Development* **137**, 417–426.

Lynch, S. A. (2005). Non-multifactorial neural tube defects. *Am. J. Med. Genet. C. Semin. Med. Genet.* **135C**, 69–76.

Malcoe, L. H., Shaw, G. M., Lammer, E. J. and Herman, A. A. (1999). The effect of congenital anomalies on mortality risk in white and black infants. *Am. J. Public Health* **89**, 887–892.

Marchant, L., Linker, C., Ruiz, P., Guerrero, N. and Mayor, R. (1998). The inductive properties of mesoderm suggest that the neural crest cells are specified by a BMP gradient. *Dev. Biol.* **198**, 319–329.

Marshall, W. F. and Rosenbaum, J. L. (2001). Intraflagellar transport balances continuous turnover of outer doublet microtubules: implications for flagellar length control. *J. Cell Biol.* **155**, 405–414.

Marthiens, V. and ffrench-Constant, C. (2009). Adherens junction domains are split by asymmetric division of embryonic neural stem cells. *EMBO Rep* **10**, 515–520.

Martin-Belmonte, F. and Mostov, K. (2008). Regulation of cell polarity during epithelial morphogenesis. *Curr. Opin. Cell Biol.* **20**, 227–234.

Martin-Belmonte, F., Gassama, A., Datta, A., Yu, W., Rescher, U., Gerke, V. and Mostov, K. (2007). PTEN-mediated apical segregation of phosphoinositides controls epithelial morphogenesis through Cdc42. *Cell* **128**, 383–397.

Martin-Belmonte, F., Yu, W., Rodriguez-Fraticelli, A. E., Ewald, A. J., Werb, Z., Alonso, M. A. and Mostov, K. (2008). Cell-polarity dynamics controls the mechanism of lumen formation in epithelial morphogenesis. *Curr Biol* **18**, 507–513.

Martin, B. L. and Kimelman, D. (2012). Canonical Wnt signaling dynamically controls multiple stem cell fate decisions during vertebrate body formation. *Dev. Cell* **22**, 223–232.

Mayor, R. and Theveneau, E. (2013). The neural crest. *Development* **140**, 2247–2251.

McGlashan, S. R., Jensen, C. G. and Poole, C. A. (2006). Localization of extracellular matrix receptors on the chondrocyte primary cilium. *J. Histochem. Cytochem.* **54**, 1005–1014.

Megason, S. G. and McMahon, A. P. (2002). A mitogen gradient of dorsal midline Wnts organizes growth in the CNS. *Development* **129**, 2087–2098.

Mercado-Pimentel, M. E. and Runyan, R. B. (2007). Multiple transforming growth factor-beta isoforms and receptors function during epithelial-mesenchymal cell transformation in the embryonic heart. *Cells. Tissues. Organs* **185**, 146–156.

Miguez, D. G., Gil-Guinon, E., Pons, S. and Marti, E. (2013). Smad2 and Smad3 cooperate and antagonize simultaneously in vertebrate neurogenesis. *J Cell Sci* **126**, 5335–5343.

Mikawa, T., Poh, A. M., Kelly, K. A., Ishii, Y. and Reese, D. E. (2004). Induction and patterning of the primitive streak, an organizing center of gastrulation in the amniote. *Dev. Dyn.* **229**, 422–432.

Momose, T., Tonegawa, A., Takeuchi, J., Ogawa, H., Umesono, K. and Yasuda, K. (1999). Efficient targeting of gene expression in chick embryos by microelectroporation. *Dev Growth Differ* **41**, 335–344.

Monnich, M., Borgeskov, L., Breslin, L., Jakobsen, L., Rogowski, M., Doganli, C., Schroder, J. M., Mogensen, J. B., Blinkenkjaer, L., Harder, L. M., et al. (2018). CEP128 Localizes to the Subdistal Appendages of the Mother Centriole and Regulates TGF-beta/BMP Signaling at the Primary Cilium. *Cell Rep* **22**, 2584–2592.

Moriwaki, K., Tsukita, S. and Furuse, M. (2007). Tight junctions containing claudin 4 and 6 are essential for blastocyst formation in preimplantation mouse embryos. *Dev. Biol.* **312**, 509–522.

Morris, H. T. and Machesky, L. M. (2015). Actin cytoskeletal control during epithelial to mesenchymal transition: focus on the pancreas and intestinal tract. *Br. J. Cancer* **112**, 613–620.

Morris, J. K., Rankin, J., Draper, E. S., Kurinczuk, J. J., Springett, A., Tucker, D., Wellesley, D., Wreyford, B. and Wald, N. J. (2016). Prevention of neural tube defects in the UK: a missed opportunity. *Arch Dis Child* **101**, 604–607.

Morriss-Kay, G., Wood, H. and Chen, W. H. (1994). Normal neurulation in mammals. *Ciba Found. Symp.* **181**, 51–59.

Moustakas, A. and Heldin, C.-H. (2002). From mono- to oligo-Smads: the heart of the matter in TGF-beta signal transduction. *Genes Dev.* **16**, 1867–1871.

Moustakas, A., Souchelnytskyi, S. and Heldin, C. H. (2001). Smad regulation in TGF-beta signal transduction. *J. Cell Sci.* **114**, 4359–4369.

Muller, F. and O'Rahilly, R. (1987). The development of the human brain, the closure of the caudal neuropore, and the beginning of secondary neurulation at stage 12. *Anat. Embryol. (Berl).* **176**, 413–430.

Munro, E. M. (2006). PAR proteins and the cytoskeleton: a marriage of equals. *Curr. Opin. Cell Biol.* **18**, 86–94.

Nakamura, N., Rabouille, C., Watson, R., Nilsson, T., Hui, N., Slusarewicz, P., Kreis, T. E. and Warren, G. (1995). Characterization of a cis-Golgi matrix protein, GM130. *J. Cell Biol.* **131**, 1715–1726.

Nakatsu, T., Uwabe, C. and Shiota, K. (2000). Neural tube closure in humans initiates at multiple sites: evidence from human embryos and implications for the pathogenesis of neural tube defects. *Anat. Embryol. (Berl).* **201**, 455–466.

Nelson, K. S., Furuse, M. and Beitel, G. J. (2010). The Drosophila Claudin Kune-kune is required for septate junction organization and tracheal tube size control. *Genetics* **185**, 831–839.

Ng, A. N. Y., de Jong-Curtain, T. A., Mawdsley, D. J., White, S. J., Shin, J., Appel, B., Dong, P. D. S., Stainier, D. Y. R. and Heath, J. K. (2005). Formation of the digestive system in zebrafish: III. Intestinal epithelium morphogenesis. *Dev. Biol.* **286**, 114–135.

Nielsen, J. S. and McNagny, K. M. (2008). Novel functions of the CD34 family. *J. Cell Sci.* **121**, 3683–3692.

Nieto, M. A. (2013). Epithelial Plasticity: A Common Theme in Embryonic and Cancer Cells. *Science (80-.).* **342**, 1234850.

Nievelstein, R. A., Hartwig, N. G., Vermeij-Keers, C. and Valk, J. (1993). Embryonic development of the mammalian caudal neural tube. *Teratology* **48**, 21–31.

Nikolopoulou, E., Galea, G. L., Rolo, A., Greene, N. D. and Copp, A. J. (2017). Neural tube closure: cellular, molecular and biomechanical mechanisms. *Development* **144**, 552–566.

Nowotschin, S., Ferrer-Vaquer, A., Concepcion, D., Papaioannou, V. E. and Hadjantonakis, A. K. (2012). Interaction of Wnt3a, Msgn1 and Tbx6 in neural versus paraxial mesoderm lineage commitment and paraxial mesoderm differentiation in the mouse embryo. *Dev Biol* **367**, 1–14.

O'Brien, L. E., Jou, T. S., Pollack, A. L., Zhang, Q., Hansen, S. H., Yurchenco, P. and Mostov, K. E. (2001). Rac1 orientates epithelial apical polarity through effects on basolateral laminin assembly. *Nat Cell Biol* **3**, 831–838.

O'Brien, L. E., Zegers, M. M. P. and Mostov, K. E. (2002). Opinion: Building epithelial architecture: insights from three-dimensional culture models. *Nat. Rev. Mol. Cell Biol.* **3**, 531–537.

O'Rahilly, R. and Muller, F. (1994). Neurulation in the normal human embryo. *Ciba Found Symp* **181**, 70–82; discussion 82-9.

O'Rahilly, R. and Muller, F. (2002). The two sites of fusion of the neural folds and the two neuropores in the human embryo. *Teratology* **65**, 162–170.

Olivera-Martinez, I., Harada, H., Halley, P. A. and Storey, K. G. (2012). Loss of FGF-dependent mesoderm identity and rise of endogenous retinoid signalling determine cessation of body axis elongation. *PLoS Biol* **10**, e1001415.

Olivera-Martinez, I., Schurch, N., Li, R. A., Song, J., Halley, P. A., Das, R. M., Burt, D. W., Barton, G. J. and Storey, K. G. (2014). Major transcriptome re-organisation and abrupt changes in signalling, cell cycle and chromatin regulation at neural differentiation in vivo. *Development* **141**, 3266–3276.

Ooshio, T., Fujita, N., Yamada, A., Sato, T., Kitagawa, Y., Okamoto, R., Nakata, S., Miki, A., Irie, K. and Takai, Y. (2007). Cooperative roles of Par-3 and afadin in the formation of adherens and tight junctions. *J. Cell Sci.* **120**, 2352–2365.

Ozdamar, B., Bose, R., Barrios-Rodiles, M., Wang, H.-R., Zhang, Y. and Wrana, J. L. (2005). Regulation of the polarity protein Par6 by TGFbeta receptors controls epithelial cell plasticity. *Science* **307**, 1603–1609.

Pai, Y.-J., Abdullah, N. L., Mohd-Zin, S. W., Mohammed, R. S., Rolo, A., Greene, N. D. E., Abdul-Aziz, N. M. and Copp, A. J. (2012). Epithelial fusion during neural tube morphogenesis. *Birth Defects Res. A. Clin. Mol. Teratol.* **94**, 817–823.

Paintrand, M., Moudjou, M., Delacroix, H. and Bornens, M. (1992). Centrosome organization and centriole architecture: their sensitivity to divalent cations. *J. Struct. Biol.* **108**, 107–128.

Palmer, K. J., MacCarthy-Morrogh, L., Smyllie, N. and Stephens, D. J. (2011). A role for Tctex-1 (DYNLT1) in controlling primary cilium length. *Eur. J. Cell Biol.* **90**, 865–871.

Pedersen, L. B., Mogensen, J. B. and Christensen, S. T. (2016). Endocytic Control of Cellular Signaling at the Primary Cilium. *Trends Biochem. Sci.* **41**, 784–797.

Peeters, M. C., Viebahn, C., Hekking, J. W. and van Straaten, H. W. (1998). Neurulation in the rabbit embryo. *Anat. Embryol. (Berl).* **197**, 167–175.

Peinado, H., Olmeda, D. and Cano, A. (2007). Snail, Zeb and bHLH factors in tumour progression: an alliance against the epithelial phenotype? *Nat. Rev. Cancer* **7**, 415.

Piek, E., Moustakas, A., Kurisaki, A., Heldin, C. H. and ten Dijke, P. (1999). TGF-(beta) type I receptor/ALK-5 and Smad proteins mediate epithelial to mesenchymal transdifferentiation in NMuMG breast epithelial cells. *J. Cell Sci.* **112 (Pt 2**, 4557–4568.

Polyak, K. and Weinberg, R. A. (2009). Transitions between epithelial and mesenchymal states: acquisition of malignant and stem cell traits. *Nat Rev Cancer* **9**, 265–273.

Pytel, A., Bruska, M. and Wozniak, W. (2007). Evidence that the caudal portion of the neural tube develops by cavitation of a neural cord in the caudal eminence of human embryos. *Folia Morphol (Warsz)* **66**, 104–108.

Raible, D. W. (2006). Development of the neural crest: achieving specificity in regulatory pathways. *Curr. Opin. Cell Biol.* **18**, 698–703.

Reiter, J. F., Blacque, O. E. and Leroux, M. R. (2012). The base of the cilium: roles for transition fibres and the transition zone in ciliary formation, maintenance and compartmentalization. *EMBO Rep.* **13**, 608–618.

Ridley, A. J., Schwartz, M. A., Burridge, K., Firtel, R. A., Ginsberg, M. H., Borisy, G., Parsons, J. T. and Horwitz, A. R. (2003). Cell migration: integrating signals from front to back. *Science* **302**, 1704–1709.

Robinson, A., Escuin, S., Doudney, K., Vekemans, M., Stevenson, R. E., Greene, N. D. E., Copp, A. J. and Stanier, P. (2012). Mutations in the planar cell polarity genes CELSR1 and SCRIB are associated with the severe neural tube defect craniorachischisis. *Hum. Mutat.* **33**, 440–447.

Rodriguez-Boulan, E., Kreitzer, G. and Müsch, A. (2005). Organization of vesicular trafficking in epithelia. *Nat. Rev. Mol. Cell Biol.* **6**, 233–247.

Rodriguez-Fraticelli, A. E., Auzan, M., Alonso, M. A., Bornens, M. and Martin-Belmonte, F. (2012). Cell confinement controls centrosome positioning and lumen initiation during epithelial morphogenesis. *J Cell Biol* **198**, 1011–1023.

Rodriguez-Fraticelli, A. E., Bagwell, J., Bosch-Fortea, M., Boncompain, G., Reglero-Real, N., Garcia-Leon, M. J., Andres, G., Toribio, M. L., Alonso, M. A., Millan, J., et al. (2015). Developmental regulation of apical endocytosis controls epithelial patterning in vertebrate tubular organs. *Nat. Cell Biol.* **17**, 241–250.

Roignot, J., Peng, X. and Mostov, K. (2013). Polarity in mammalian epithelial morphogenesis. *Cold Spring Harb Perspect Biol* **5**,.

Roman-Fernandez, A. and Bryant, D. M. (2016). Complex Polarity: Building Multicellular Tissues Through Apical Membrane Traffic. *Traffic* **17**, 1244–1261.

Row, R. H., Tsotras, S. R., Goto, H. and Martin, B. L. (2016). The zebrafish tail bud contains two independent populations of midline progenitor cells that maintain long-term germ layer plasticity and differentiate in response to local signaling cues. *Development* **143**, 244–254.

Rueden, C. T., Schindelin, J., Hiner, M. C., DeZonia, B. E., Walter, A. E., Arena, E. T. and Eliceiri, K. W. (2017). ImageJ2: ImageJ for the next generation of scientific image data. *BMC Bioinformatics* **18**, 529.

Rupp, P. A., Rongish, B. J., Czirok, A. and Little, C. D. (2003). Culturing of avian embryos for time-lapse imaging. *Biotechniques* **34**, 274–278.

Saade, M., Gutierrez-Vallejo, I., Le Dreau, G., Rabadan, M. A., Miguez, D. G., Buceta, J. and Marti, E. (2013). Sonic hedgehog signaling switches the mode of division in the developing nervous system. *Cell Rep* **4**, 492–503.

Saade, M., Gonzalez-Gobartt, E., Escalona, R., Usieto, S. and Marti, E. (2017a). Shh-mediated centrosomal recruitment of PKA promotes symmetric proliferative neuroepithelial cell division. *Nat Cell Biol* **19**, 493–503.

Saade, M., Gonzalez-Gobartt, E., Escalona, R., Usieto, S. and Martí, E. (2017b). Shh-mediated centrosomal recruitment of PKA promotes symmetric proliferative neuroepithelial cell division. *Nat. Cell Biol.* **19**, 493–503.

Saade, M., Blanco-Ameijeiras, J., Gonzalez-Gobartt, E. and Martí, E. (2018). A centrosomal view of CNS growth. *Development* **145**,.

Saitsu, H. and Shiota, K. (2008). Involvement of the axially condensed tail bud mesenchyme in normal and abnormal human posterior neural tube development. *Congenit Anom* **48**, 1–6.

Saitsu, H., Yamada, S., Uwabe, C., Ishibashi, M. and Shiota, K. (2004). Development of the posterior neural tube in human embryos. *Anat Embryol* **209**, 107–117.

Samavarchi-Tehrani, P., Golipour, A., David, L., Sung, H.-K., Beyer, T. A., Datti, A., Woltjen, K., Nagy, A. and Wrana, J. L. (2010). Functional genomics reveals a BMP-driven mesenchymal-to-epithelial transition in the initiation of somatic cell reprogramming. *Cell Stem Cell* **7**, 64–77.

Sanford, L. P., Ormsby, I., Gittenberger-de Groot, A. C., Sariola, H., Friedman, R., Boivin, G. P., Cardell, E. L. and Doetschman, T. (1997). TGFbeta2 knockout mice have multiple developmental defects that are non-overlapping with other TGFbeta knockout phenotypes. *Development* **124**, 2659–2670.

Saotome, I., Curto, M. and McClatchey, A. I. (2004). Ezrin is essential for epithelial organization and villus morphogenesis in the developing intestine. *Dev. Cell* **6**, 855–864.

Saraga-Babic, M., Sapunar, D. and Wartiovaara, J. (1995). Variations in the formation of the human caudal spinal cord. *J. Hirnforsch.* **36**, 341–347.

Satir, P., Pedersen, L. B. and Christensen, S. T. (2010). The primary cilium at a glance. *J. Cell Sci.* **123**, 499–503.

Sauer, F. C. (1935). Mitosis in the neural tube. *J. Comp. Neurol.* **62**, 377–405.

Schindelin, J., Arganda-Carreras, I., Frise, E., Kaynig, V., Longair, M., Pietzsch, T., Preibisch, S., Rueden, C., Saalfeld, S., Schmid, B., et al. (2012). Fiji: an open-source platform for biological-image analysis. *Nat Methods* **9**, 676–682.

Schmoranzer, J., Fawcett, J. P., Segura, M., Tan, S., Vallee, R. B., Pawson, T. and Gundersen, G. G. (2009). Par3 and dynein associate to regulate local microtubule dynamics and centrosome orientation during migration. *Curr. Biol.* **19**, 1065–1074.

Schoenwolf, G. C. (1984). Histological and ultrastructural studies of secondary neurulation in mouse embryos. *Am J Anat* **169**, 361–376.

Schoenwolf, G. C. and Delongo, J. (1980). Ultrastructure of secondary neurulation in the chick embryo. *Am J Anat* **158**, 43–63.

Schoenwolf, G. C. and Kelley, R. O. (1980). Characterization of intercellular junctions in the caudal portion of the developing neural tube of the chick embryo. *Am J Anat* **158**, 29–41.

Selleck, M. A. (1996). Culture and microsurgical manipulation of the early avian embryo. *Methods Cell Biol.* **51**, 1–21.

Shahbazi, M. N. and Zernicka-Goetz, M. (2018). Deconstructing and reconstructing the mouse and human early embryo. *Nat. Cell Biol.* **20**, 878–887.

Shahbazi, M. N., Jedrusik, A., Vuoristo, S., Recher, G., Hupalowska, A., Bolton, V., Fogarty, N. N. M., Campbell, A., Devito, L., Ilic, D., et al. (2016). Self-organization of the human embryo in the absence of maternal tissues. *Nat Cell Biol* **18**, 700–708.

Shahbazi, M. N., Scialdone, A., Skorupska, N., Weberling, A., Recher, G., Zhu, M., Jedrusik, A., Devito, L. G., Noli, L., Macaulay, I. C., et al. (2017). Pluripotent state transitions coordinate morphogenesis in mouse and human embryos. *Nature* **552**, 239.

Shahbazi, M. N., Siggia, E. D. and Zernicka-Goetz, M. (2019). Self-organization of stem cells into embryos: A window on early mammalian development. *Science* **364**, 948–951.

Sharov, A. A., Masui, S., Sharova, L. V, Piao, Y., Aiba, K., Matoba, R., Xin, L., Niwa, H. and Ko, M. S. (2008). Identification of Pou5f1, Sox2, and Nanog downstream target genes with statistical confidence by applying a novel algorithm to time course microarray and genome-wide chromatin immunoprecipitation data. *BMC Genomics* **9**, 269.

Shi, Y. and Massagué, J. (2003). Mechanisms of TGF-beta signaling from cell membrane to the nucleus. *Cell* **113**, 685–700.

Shimokita, E. and Takahashi, Y. (2011). Secondary neurulation: Fate-mapping and gene manipulation of the neural tube in tail bud. *Dev Growth Differ* **53**, 401–410.

Shin, K. and Margolis, B. (2006). ZOning out tight junctions. *Cell* **126**, 647–649.

Shum, A. S. and Copp, A. J. (1996). Regional differences in morphogenesis of the neuroepithelium suggest multiple mechanisms of spinal neurulation in the mouse. *Anat. Embryol. (Berl).* **194**, 65–73.

Shum, A. S., Tang, L. S., Copp, A. J. and Roelink, H. (2010). Lack of motor neuron differentiation is an intrinsic property of the mouse secondary neural tube. *Dev Dyn* **239**, 3192–3203.

Smith, J. L. and Schoenwolf, G. C. (1987). Cell cycle and neuroepithelial cell shape during bending of the chick neural plate. *Anat Rec* **218**, 196–206.

Smith, J. L. and Schoenwolf, G. C. (1989). Notochordal induction of cell wedging in the chick neural plate and its role in neural tube formation. *J. Exp. Zool.* **250**, 49–62.

Smith, J. L. and Schoenwolf, G. C. (1991). Further evidence of extrinsic forces in bending of the neural plate. *J. Comp. Neurol.* **307**, 225–236.

Smith, J. L. and Schoenwolf, G. C. (1997). Neurulation: coming to closure. *Trends Neurosci.* **20**, 510–517.

Stephens, R. E. (1997). Synthesis and turnover of embryonic sea urchin ciliary proteins during selective inhibition of tubulin synthesis and assembly. *Mol. Biol. Cell* **8**, 2187–2198.

Steventon, B. and Martinez Arias, A. (2017). Evo-engineering and the cellular and molecular origins of the vertebrate spinal cord. *Dev Biol* **432**, 3–13.

Steventon, B., Duarte, F., Lagadec, R., Mazan, S., Nicolas, J.-F. and Hirsinger, E. (2016). Species-specific contribution of volumetric growth and tissue convergence to posterior body elongation in vertebrates. *Development* **143**, 1732 LP – 1741.

Stottmann, R. W., Berrong, M., Matta, K., Choi, M. and Klingensmith, J. (2006). The BMP antagonist Noggin promotes cranial and spinal neurulation by distinct mechanisms. *Dev. Biol.* **295**, 647–663.

Strilic, B., Eglinger, J., Krieg, M., Zeeb, M., Axnick, J., Babal, P., Muller, D. J. and Lammert, E. (2010). Electrostatic cell-surface repulsion initiates lumen formation in developing blood vessels. *Curr. Biol.* **20**, 2003–2009.

Takada, S., Stark, K. L., Shea, M. J., Vassileva, G., McMahon, J. A. and McMahon, A. P. (1994). Wnt-3a regulates somite and tail bud formation in the mouse embryo. *Genes Dev.* **8**, 174–189.

Takao, D. and Verhey, K. J. (2016). Gated entry into the ciliary compartment. *Cell. Mol. Life Sci.* **73**, 119–127.

Takeda, T., Go, W. Y., Orlando, R. A. and Farquhar, M. G. (2000). Expression of podocalyxin inhibits cell-cell adhesion and modifies junctional properties in Madin-Darby canine kidney cells. *Mol. Biol. Cell* **11**, 3219–3232.

Takemoto, T., Uchikawa, M., Kamachi, Y. and Kondoh, H. (2006). Convergence of Wnt and FGF signals in the genesis of posterior neural plate through activation of the Sox2 enhancer N-1. *Development* **133**, 297–306.

Tanentzapf, G. and Tepass, U. (2003). Interactions between the crumbs, lethal giant larvae and bazooka pathways in epithelial polarization. *Nat. Cell Biol.* **5**, 46–52.

Taverna, E. and Huttner, W. B. (2010). Neural progenitor nuclei IN motion. *Neuron* **67**, 906–914.

Taverna, E., Mora-Bermudez, F., Strzyz, P. J., Florio, M., Icha, J., Haffner, C., Norden, C., Wilsch-Brauninger, M. and Huttner, W. B. (2016). Non-canonical features of the Golgi apparatus in bipolar epithelial neural stem cells. *Sci Rep* **6**, 21206.

Theveneau, E. and Mayor, R. (2012). Neural crest migration: interplay between chemorepellents, chemoattractants, contact inhibition, epithelial-mesenchymal transition, and collective cell migration. *Wiley Interdiscip Rev Dev Biol* **1**, 435–445.

Tobin, J. L., Di Franco, M., Eichers, E., May-Simera, H., Garcia, M., Yan, J., Quinlan, R., Justice, M. J., Hennekam, R. C., Briscoe, J., et al. (2008). Inhibition of neural crest migration underlies craniofacial dysmorphology and Hirschsprung's disease in Bardet-Biedl syndrome. *Proc. Natl. Acad. Sci. U. S. A.* **105**, 6714–6719.

Tözser, J., Earwood, R., Kato, A., Brown, J., Tanaka, K., Didier, R., Megraw, T. L., Blum, M. and Kato, Y. (2015). TGF-β Signaling Regulates the Differentiation of Motile Cilia. *Cell Rep.* **11**, 1000–1007.

Tsakiridis, A. and Wilson, V. (2015). Assessing the bipotency of in vitro-derived neuromesodermal progenitors. *F1000Research* **4**, 100.

Tsakiridis, A., Huang, Y., Blin, G., Skylaki, S., Wymeersch, F., Osorno, R., Economou, C., Karagianni, E., Zhao, S., Lowell, S., et al. (2014). Distinct Wnt-driven primitive streak-like populations reflect in vivo lineage precursors. *Development* **141**, 1209–1221.

Turner, D. A., Rue, P., Mackenzie, J. P., Davies, E. and Martinez Arias, A. (2014). Brachyury cooperates with Wnt/beta-catenin signalling to elicit primitive-streak-like behaviour in differentiating mouse embryonic stem cells. *BMC Biol* **12**, 63.

Tzouanacou, E., Wegener, A., Wymeersch, F. J., Wilson, V. and Nicolas, J. F. (2009). Redefining the progression of lineage segregations during mammalian embryogenesis by clonal analysis. *Dev Cell* **17**, 365–376.

Uchikawa, M., Ishida, Y., Takemoto, T., Kamachi, Y. and Kondoh, H. (2003). Functional analysis of chicken Sox2 enhancers highlights an array of diverse regulatory elements that are conserved in mammals. *Dev Cell* **4**, 509–519.

Ulloa, F. and Briscoe, J. (2007). Morphogens and the control of cell proliferation and patterning in the spinal cord. *Cell Cycle* **6**, 2640–2649.

Vaezi, A., Bauer, C., Vasioukhin, V. and Fuchs, E. (2002). Actin cable dynamics and Rho/Rock orchestrate a polarised cytoskeletal architecture in the early steps of assembling a stratified epithelium. *Dev. Cell* **3**, 367–381.

Valcourt, U., Kowanetz, M., Niimi, H., Heldin, C.-H. and Moustakas, A. (2005). TGF-beta and the Smad signaling pathway support transcriptomic reprogramming during epithelial-mesenchymal cell transition. *Mol. Biol. Cell* **16**, 1987–2002.

Vandewalle, C., Comijn, J., De Craene, B., Vermassen, P., Bruyneel, E., Andersen, H., Tulchinsky, E., Van Roy, F. and Berx, G. (2005). SIP1/ZEB2 induces EMT by repressing genes of different epithelial cell-cell junctions. *Nucleic Acids Res.* **33**, 6566–6578.

Vasioukhin, V., Bauer, C., Yin, M. and Fuchs, E. (2000). Directed actin polymerization is the driving force for epithelial cell-cell adhesion. *Cell* **100**, 209–219.

Veland, I. R., Lindbaek, L. and Christensen, S. T. (2014). Linking the Primary Cilium to Cell Migration in Tissue Repair and Brain Development. *Bioscience* **64**, 1115–1125.

von Baer, K. E. (1828). *Über Entwicklungsgeschichte der Thiere: Beobachtung und Reflexión.* (ed. Königsberg) Bornträger.

Wesseling, J., van der Valk, S. W. and Hilkens, J. (1996). A mechanism for inhibition of E-cadherin-mediated cell-cell adhesion by the membrane-associated mucin episialin/MUC1. *Mol. Biol. Cell* **7**, 565–577.

Wilson, V., Olivera-Martinez, I. and Storey, K. G. (2009). Stem cells, signals and vertebrate body axis extension. *Development* **136**, 1591–1604.

Wolpert, L. (1997). *Principles Of Development*. (ed. Oxford University Press).

Wu, M. Y. and Hill, C. S. (2009). Tgf-beta superfamily signaling in embryonic development and homeostasis. *Dev. Cell* **16**, 329–343.

Wymeersch, F. J., Huang, Y., Blin, G., Cambray, N., Wilkie, R., Wong, F. C. K. and Wilson, V. (2016). Position-dependent plasticity of distinct progenitor types in the primitive streak. *Elife* **5**, e10042.

Wymeersch, F. J., Skylaki, S., Huang, Y., Watson, J. A., Economou, C., Marek-Johnston, C., Tomlinson, S. R. and Wilson, V. (2019). Transcriptionally dynamic progenitor populations organised around a stable niche drive axial patterning. *Development* **146,.**

Xu, J., Lamouille, S. and Derynck, R. (2009). TGF-beta-induced epithelial to mesenchymal transition. *Cell Res.* **19**, 156–172.

Yamada, S. and Nelson, W. J. (2007). Localized zones of Rho and Rac activities drive initiation and expansion of epithelial cell-cell adhesion. *J. Cell Biol.* **178**, 517–527.

Yamaguchi, T. P., Bradley, A., McMahon, A. P. and Jones, S. (1999). A Wnt5a pathway underlies outgrowth of multiple structures in the vertebrate embryo. *Development* **126**, 1211–1223.

Yan, X., Habedanck, R. and Nigg, E. A. (2006). A complex of two centrosomal proteins, CAP350 and FOP, cooperates with EB1 in microtubule anchoring. *Mol. Biol. Cell* **17**, 634–644.

Yang, J. and Weinberg, R. A. (2008a). Epithelial-mesenchymal transition: at the crossroads of development and tumor metastasis. *Dev Cell* **14**, 818–829.

Yang, J. and Weinberg, R. A. (2008b). Epithelial-mesenchymal transition: at the crossroads of development and tumor metastasis. *Dev. Cell* **14**, 818–29.

Yang, H. J., Wang, K. C., Chi, J. G., Lee, M. S., Lee, Y. J., Kim, S. K. and Cho, B. K. (2003). Neural differentiation of caudal cell mass (secondary neurulation) in chick embryos: Hamburger and Hamilton Stages 16-45. *Brain Res Dev Brain Res* **142**, 31–36.

Yang, H. J., Lee, D. H., Lee, Y. J., Chi, J. G., Lee, J. Y., Phi, J. H., Kim, S. K., Cho, B. K. and Wang, K. C. (2014). Secondary neurulation of human embryos: morphological changes and the expression of neuronal antigens. *Childs Nerv Syst* **30**, 73–82.

Yasuda, K., Momose, T. and Takahashi, Y. (2000). Applications of microelectroporation for studies of chick embryogenesis. *Dev Growth Differ* **42**, 203–206.

Ybot-Gonzalez, P., Cogram, P., Gerrelli, D. and Copp, A. J. (2002). Sonic hedgehog and the molecular regulation of mouse neural tube closure. *Development* **129**, 2507–2517.

Yoshikawa, Y., Fujimori, T., McMahon, A. P. and Takada, S. (1997). Evidence That Absence of Wnt-3aSignaling Promotes Neuralization Instead of Paraxial Mesoderm Development in the Mouse. *Dev. Biol.* **183**, 234–242.

Yu, W., Datta, A., Leroy, P., O'Brien, L. E., Mak, G., Jou, T.-S., Matlin, K. S., Mostov, K. E. and Zegers, M. M. P. (2005). Beta1-integrin orients epithelial polarity via Rac1 and laminin. *Mol. Biol. Cell* **16**, 433–445.

Yurchenco, P. D. (2011). Basement membranes: cell scaffoldings and signaling platforms. *Cold Spring Harb. Perspect. Biol.* **3**,.

Zakeri, Z. F. and Ahuja, H. S. (1994). Apoptotic cell death in the limb and its relationship to pattern formation. *Biochem. Cell Biol.* **72**, 603–613.

Zakeri, Z. F., Quaglino, D., Latham, T. and Lockshin, R. A. (1993). Delayed internucleosomal DNA fragmentation in programmed cell death. *FASEB J. Off. Publ. Fed. Am. Soc. Exp. Biol.* **7**, 470–478.

Zhang, N. and Gridley, T. (1998). Defects in somite formation in lunatic fringe-deficient mice. *Nature* **394**, 374–377.

Zhang, X., Lei, K., Yuan, X., Wu, X., Zhuang, Y., Xu, T., Xu, R. and Han, M. (2009). SUN1/2 and Syne/Nesprin-1/2 complexes connect centrosome to the nucleus during neurogenesis and neuronal migration in mice. *Neuron* **64**, 173–187.

Zhang, J., Piontek, J., Wolburg, H., Piehl, C., Liss, M., Otten, C., Christ, A., Willnow, T. E., Blasig, I. E. and Abdelilah-Seyfried, S. (2010). Establishment of a neuroepithelial barrier by Claudin5a is essential for zebrafish brain ventricular lumen expansion. *Proc Natl Acad Sci U S A* **107**, 1425–1430.

APPENDIX I

Identification of the morphogenetic signals relevant for chick secondary neurulation (SN)

The main morphogenetic signals driving SN remain largely unknown, even though a failure in this process results in caudal NTDs. Here we have analysed the expression of 34 components of the main developmental pathways (BMP, FGF, NOTCH, SHH, TGF-β and WNT) in the tail bud of stage HH15 chick embryos (Fig. 37-41). Whole mount in situ hybridisation and transverse sections through these same embryos identified a total of 20 genes that presented interesting patterns of expression that potentially associate to the process of SN. Accordingly, we have organized these novel genes into 5 categories:

A. Downregulated genes from neuro mesodermal progenitors (NMPs) to neural progenitor cells (NPCs), which include FGF8, DLL1, WNT3A.

B. Upregulated genes from NMPs to NPCs such as NOTCH1, SMAD2, WNT4, WNT6 and BMP4.

C. Upregulated genes in pre-Secondary Neural Tube (PSNT) cells at intermediate steps of SN as SMAD3, SMAD5 or WNT5B.

D. Genes with maintained dorsal expression along the SN process, that comprise BMP2, BMP7, TGF-b1 and WNT5A.

E. Genes expressed in the ventrally forming notochord, which include NOTCH2, SHH, TGF-b2, TGF-b3 and WNT8A.

Our study indicates several genes that might be driving the process of SN. However, the bona-fide validation of these candidate genes requires functional studies to outline their roles in SNT formation. In this thesis, we have only performed functional experiments concerning the BMP and TGF-β pathways and found an implication of TGF-β, through its transducer SMAD3, in the process of central cell intercalation. Thereby, further experiments choosing other candidate genes will help to decipher the molecular networks involved in each step of SNT formation. Moreover, many other candidate genes from which we have not analysed their expression remain to be identified.

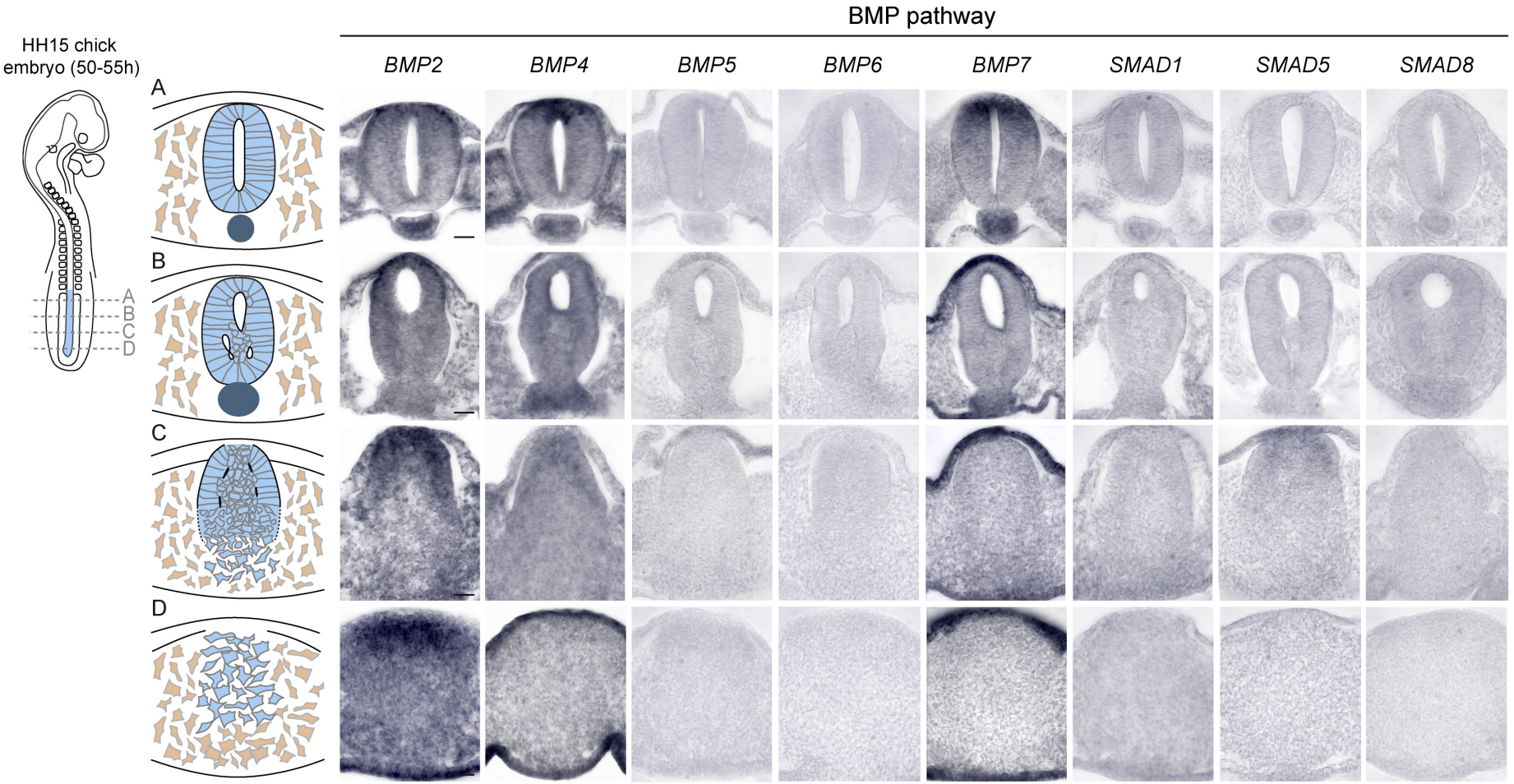

Figure 37. Expression analysis of several components of the BMP pathway. Selected images of transverse sections at A-D cranio-caudal levels hybridised with probes for the indicated ***mRNAs***. Scale bars = 20 μm.

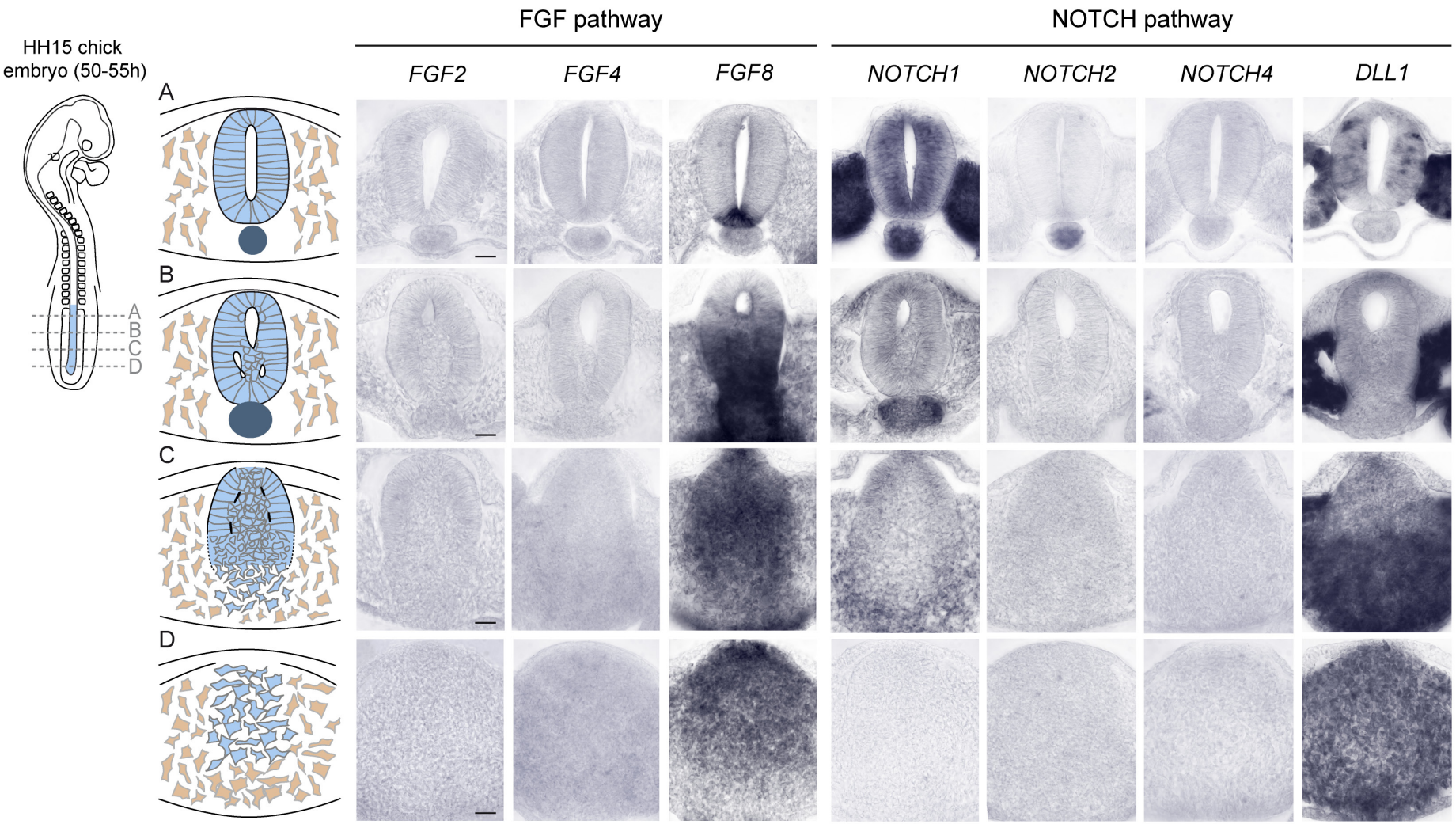

Figure 38. Expression analysis of several components of the FGF and NOTCH pathways. Selected images of transverse sections at A-D cranio-caudal levels hybridised with probes for the indicated ***mRNAs***. Scale bars = 20 μm.

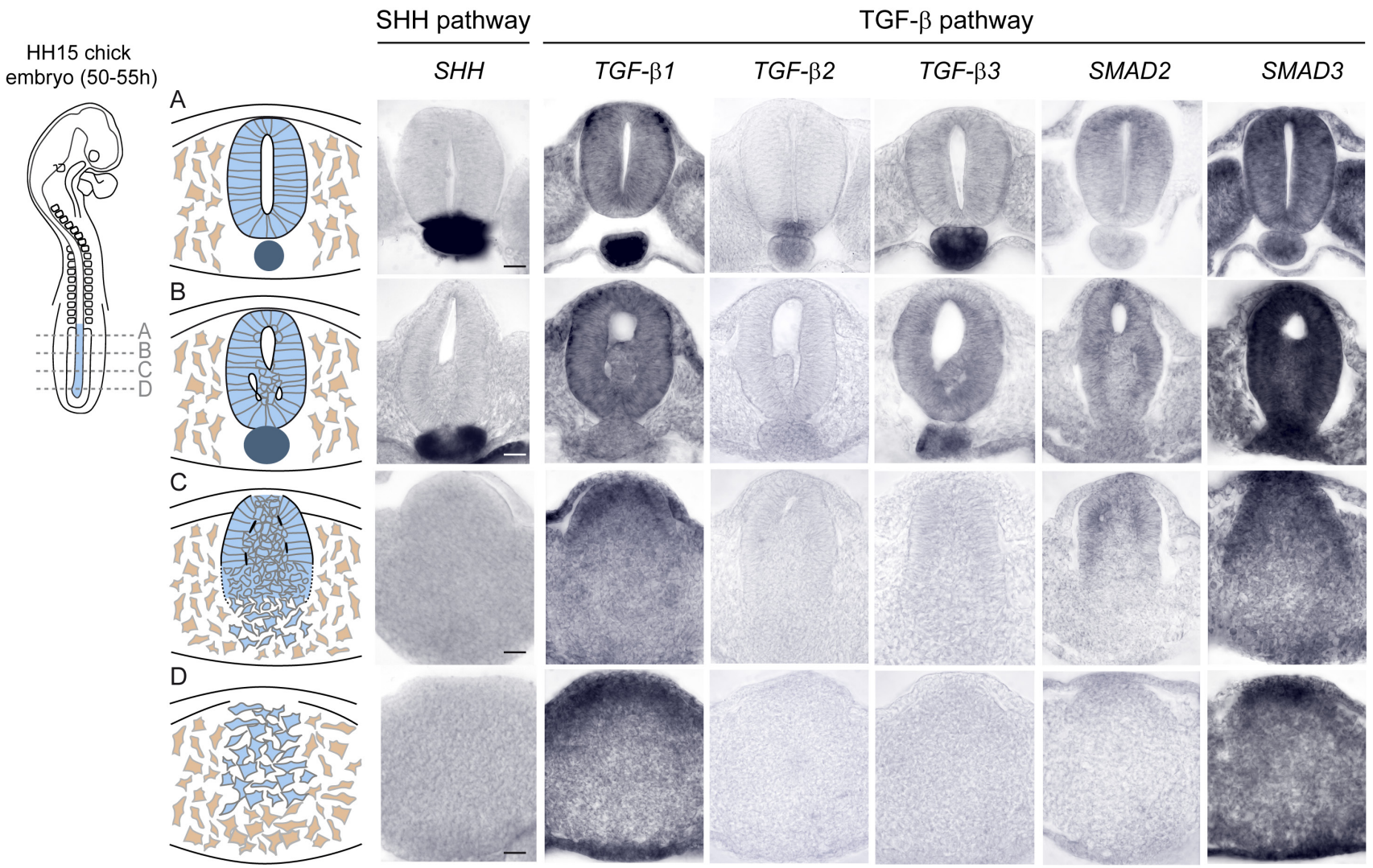

Figure 39. Expression analysis of several components of the SHH and TGF-β pathways. Selected images of transverse sections at A-D cranio-caudal levels hybridised with probes for the indicated ***mRNAs***. Scale bars = 20 μm.

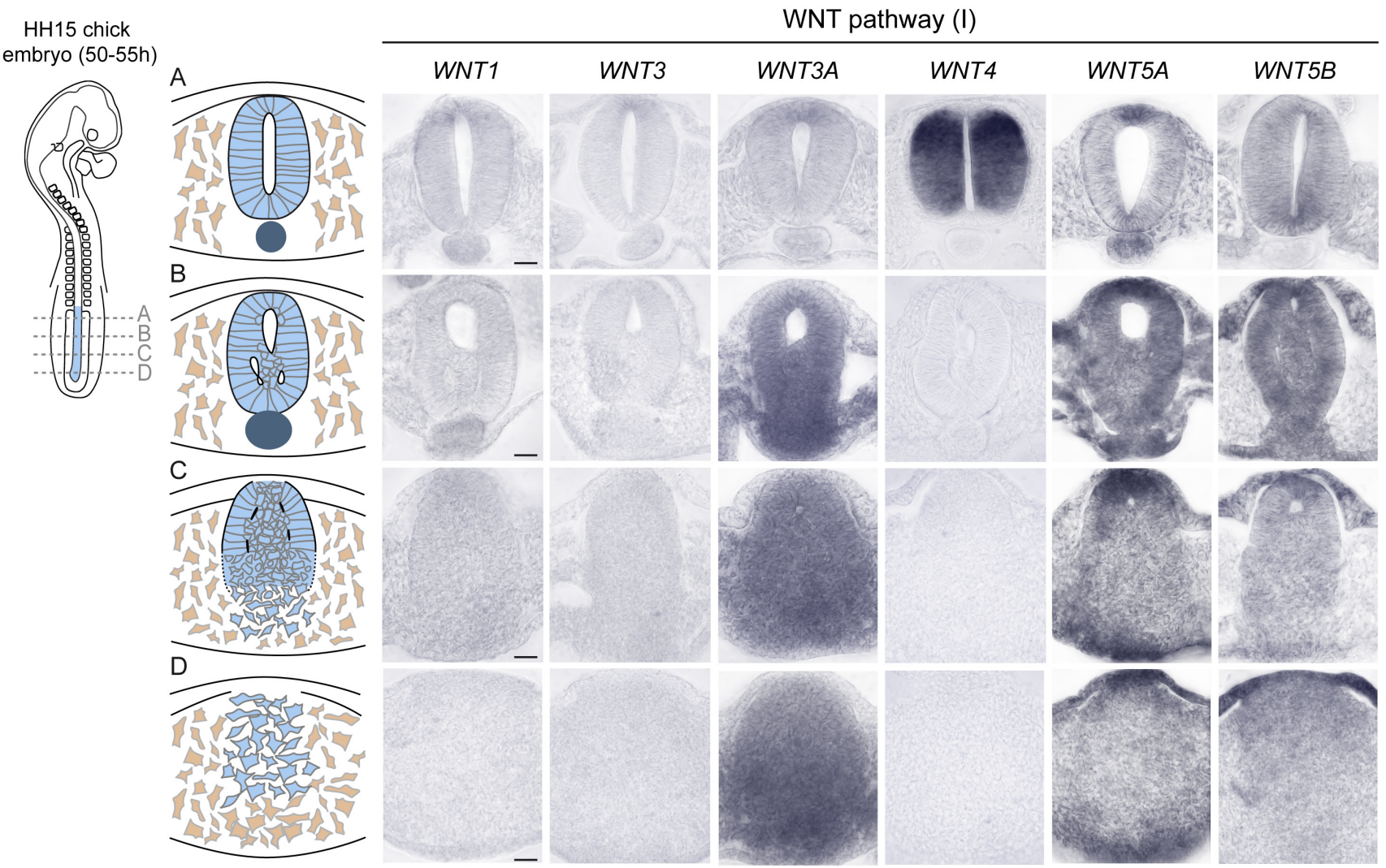

Figure 40. Expression analysis of several components of the WNT pathway (I). Selected images of transverse sections at A-D cranio-caudal levels hybridised with probes for the indicated *mRNAs*. Scale bars = 20 μm.

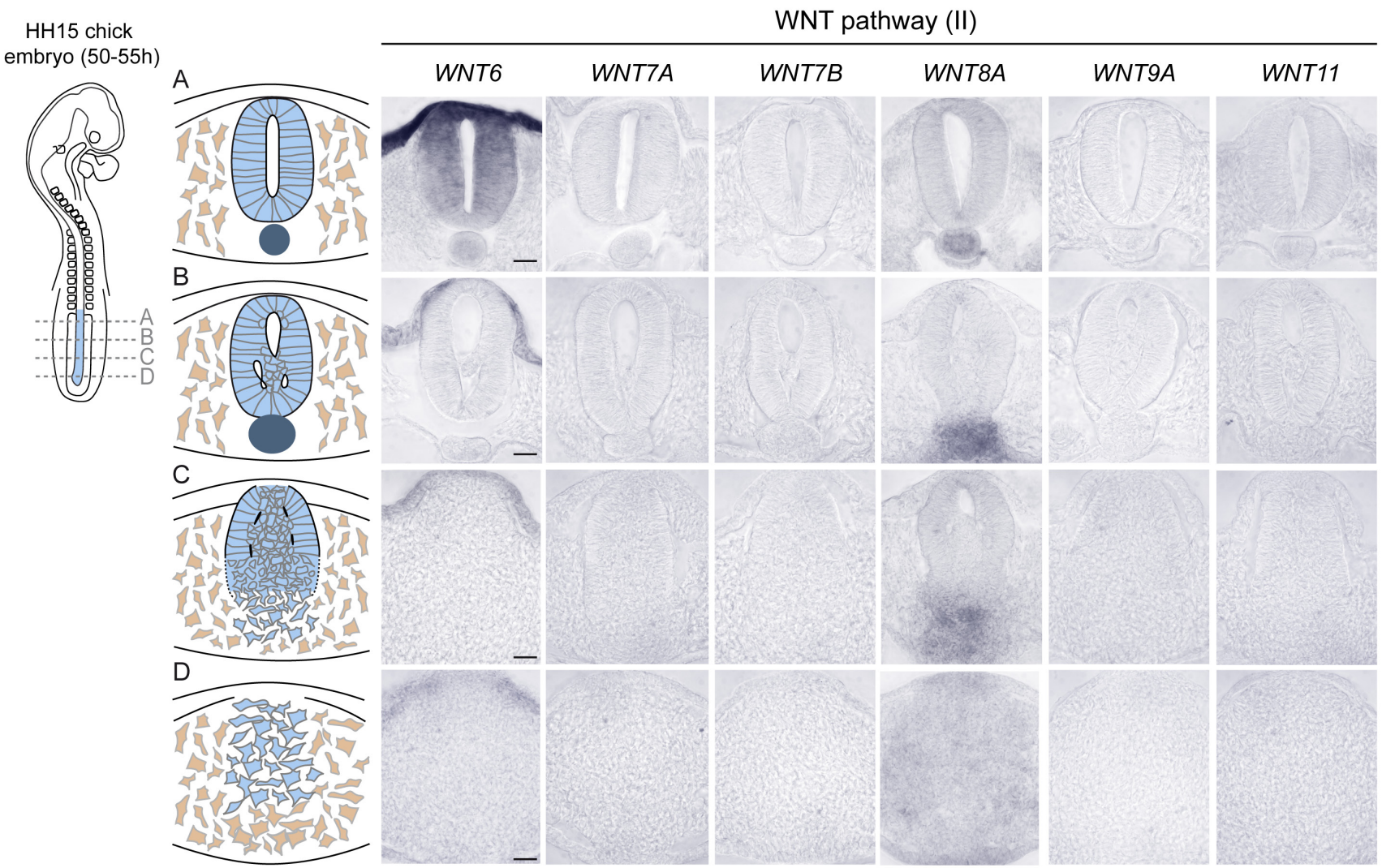

Figure 41. Expression analysis of several components of the WNT pathway (II). Selected images of transverse sections at A-D cranio-caudal levels hybridised with probes for the indicated ***mRNAs***. Scale bars = 20 μm.

APPENDIX II

Book chapter

In vivo analysis of the Mesenchymal-to-Epithelial transition during chick secondary neurulation

Elena Gonzalez-Gobartt, Guillaume Allio, Bertrand Bénazéraf and Elisa Martí

Methods in Molecular Biology. (*In press, to be released in early 2020*)

Summary:

This book chapter aroused from the 3-month visit of the PhD student to the lab of Dr. Bertrand Bénazéraf (Centre de Biologie du Développement, Toulouse). We describe here a new method to follow the MET during SN in the chick embryo, combining early *in ovo* chick electroporation (expertise of the PhD student and Dr. Elisa Marti's lab) with *in vivo* time-lapse imaging (expertise of Dr. Bertrand Bénazéraf lab) (Benazeraf et al., 2010; Benazeraf et al., 2017; Huss et al., 2015). This procedure allows the cells undergoing SN to be manipulated in order to investigate the MET process, permitting their cell dynamics to be followed *in vivo*.

PhD student contribution: The PhD student set up the method, together with Dr. Bertrand Bénazéraf and Guillaume Allio, and wrote the manuscript.

Chapter 28

In vivo analysis of the Mesenchymal-to-Epithelial transition during chick secondary neurulation

Elena Gonzalez-Gobartt[1], Guillaume Allio[2], Bertrand Bénazéraf[2] and Elisa Martí[1]

1-Instituto de Biología Molecular de Barcelona, CSIC, Parc Científic de Barcelona, C/Baldiri i Reixac 20, Barcelona 08028, Spain.

2- Centre de Biologie du Développement (CBD), Centre de Biologie Intégrative (CBI), Université de Toulouse, CNRS, UPS, Toulouse, France.

Abstract

The neural tube in amniote embryos forms as a result of two consecutive events along the antero-posterior axis, referred to as primary and secondary neurulation (PN and SN). While PN involves the invagination of a sheet of epithelial cells, SN shapes the caudal neural tube through the mesenchymal-to-epithelial transition (MET) of neuro-mesodermal progenitor cells, followed by cavitation of the medullary chord. The technical difficulties in studying SN mainly involve the challenge of labelling and manipulating SN cells *in vivo*. Here we describe a new method to follow MET during SN in the chick embryo, combining early *in ovo* chick electroporation with *in vivo* time-lapse imaging. This procedure allows the cells undergoing SN to be manipulated in order to investigate the MET process, permitting their cell dynamics to be followed *in vivo*.

Keywords: Mesenchymal-to-epithelial transition, Secondary neurulation, Neural tube formation, Chick embryo, *In ovo* electroporation, *In vivo* time-lapse imaging, Cell dynamics

1. Introduction

During development, the entire vertebrate peripheral nervous system (PNS) is formed through the epithelial–to-mesenchymal transition (EMT) of neuroepithelial cells, which generates migratory neural crest cells, one of the best studied examples of physiological EMT [1-3]. By contrast, the mesenchymal-to-epithelial transition (MET) is the reverse process and it plays an important role during organogenesis, as well as in the elongation of the caudal nervous system, a process known as secondary neurulation (SN). Indeed, the formation of the vertebrate neural tube (NT) involves two different morphogenetic events, primary (PN) and secondary neurulation (SN) [4,5]. During PN, the lateral ends of the anterior neural plate elevate and the bilateral neural folds fuse with each other to form the anterior NT [6-8]. By contrast, in SN mesenchymal neuro-mesodermal progenitor cells are recruited to elongate the caudal body axis and drive the caudal elongation of the NT. The MET of neuro-mesodermal progenitor cells (NMPCs) is the central event of SN, along with the formation

of a compact nerve cord and its subsequent cavitation to form the caudal NT. In human embryos, the transition from the primary to the secondary NT occurs at the lumbosacral level; therefore the development of the lumbar, sacral, coccygeal and equinal cord largely involves SN [9-12].

Here, we propose that the chick embryo is an ideal model to understand the MET events that occur during amniote SN. While manipulating and imaging mammalian embryos is still problematic, the chick embryo provides an easily accessible model in which the stages of development can be readily identified [13]. At early stages of development the avian body plan is very similar to that of mammals, and these embryos have excellent optical properties as they are thin and planar [14]. Furthermore, the SN region in the chick embryo extends up to the lumbar region [15,16], closely resembling human development, whereas SN only occurs at the tail level in mice [17-19].

In the chick, SN starts when undifferentiated NMPCs converge onto the dorsal midline, adopt a neural cell identity and undergo MET. The complete MET process can be followed in stage HH15 chick embryos, as different degrees of polarisation exist along the anteroposterior axis (FIG. 1). The first cells to undergo MET are located in the periphery of the medullary cord, while the central cells remain mesenchymal until the very end of the process. It is between these two cell populations that small cavities of varied size and shape form, later coalescing to form a single central lumen (FIG. 1C-G) [20,21].

However, the analysis of SN *in vivo* has always been technically difficult. Cell tracing studies have identified the epiblast region occupied by cells that undergo SN in the future (the preSN region), located caudo-medially to Hensen's Node at stage HH9 chick embryos [22-26]. However, the NT is still open in the posterior domains of stage HH9 chick embryos, so for electroporation the DNA must be injected on top of the epiblast and the electrodes positioned above and below the embryo (FIG. 2A-B). Earlier embryonic stages have always been electroporated *ex ovo* in this way [27,28], which facilitates the electroporation of the flat epiblast, although cultured embryos do not grow to stage HH15 with normal body elongation [29].

Here we propose a new method for the *in vivo* analysis of MET during SN that overcomes all these technical difficulties. The method involves combining early *in ovo* chick embryo electroporation with time-lapse imaging in a culture set-up specifically adapted to avian embryos [30,31,14]. This technique allows any cells undergoing SN to be manipulated *in vivo* in order to investigate the MET process, and it permits cell dynamics to be followed *in vivo*. Briefly, stage HH9 chick embryos are electroporated *in ovo* to transform the preSN region, injecting the DNA onto the surface of the concave cavity that exists at the posterior end of the embryo, where the primary NT is still open. The electrodes are then positioned carefully above and below the embryo (FIG. 2A-B), and an electrical current is applied so that the posterior cells incorporate the plasmid DNA. Subsequently, the eggs are sealed and incubated for 24h, until the embryos reach stage HH15 (FIG. 2D-G). The next day the eggs are opened again and the embryos are removed using a filter paper ring (FIG. 3A-B), which not only facilitates their manipulation but also provides the mechanical support essential to generate the correct tensions and deformation that occur during normal embryo elongation [29]. Embryos attached to these rings are then cleaned to avoid any yolk and debris interfering with their visualization, and they are transferred to pre-prepared imaging plates containing Agar/Albumen culture media (FIG. 3C). Finally, the embryos are placed in a culture chamber (FIG. 3D-E) and examined under an upright wide-field

microscope. The system we describe here allows 6 specimens to be visualized simultaneously and they can be analysed over long periods of time, these embryos developing at approximately the same rate as they do *in ovo* (FIG. 4, MOVIE S1). In the videos generated with this system, the cells undergoing MET can be visualised and tracked during the process of SN (FIG. 5, MOVIE S2-S3).

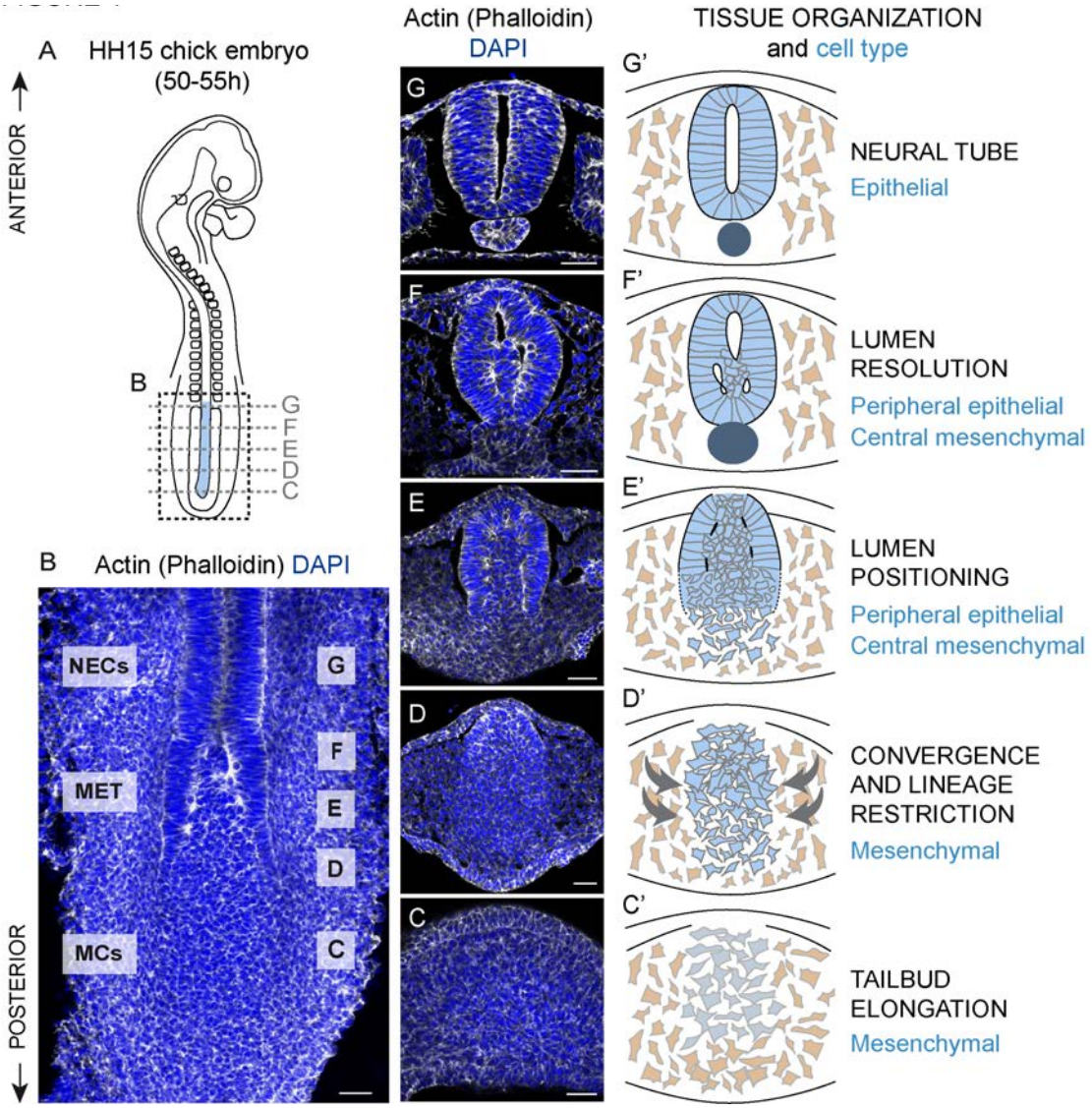

Fig. 1. Chick secondary neurulation (SN). (A) Drawing of a HH15 chick embryo showing the caudal region where SN is taking place. The progression of SN can be followed along the antero-posterior axis of the same embryo. **(B)** Dorsal view of the boxed region in A showing the distribution of actin (Phalloidin) in white. The cells in posterior regions are mesenchymal cells (MCs), those in the intermediate regions are undergoing the mesenchymal-to-epithelial transition (MET) and the anterior cells are neuroepithelial cells (NECs). The transverse sections in C-G correspond to different levels along the antero-posterior axis. Scale bar = 40 μm. **(C-G)** Transverse sections at different antero-posterior levels showing the distribution of actin. Scale bar = 40 μm. **(C'-G')** Schematic representation of chick SN showing major cell and tissue rearrangements. Neural progenitors are shown in light blue, the surrounding mesoderm is in brown and the notochord appears in dark blue. **(C'-D')** Chick SN starts with the convergence of neuro-mesodermal progenitors in the centre of the tissue and the formation of a solid medullary chord (grey arrows). **(E')** Cells located dorsally and at the periphery of the medullary chord are the first to undergo the MET. Epithelialization propagates ventrally, although the cells in the centre of the tissue remain mesenchymal and small lumens open up between the peripheral epithelial and central mesenchymal cell populations. **(F')** The small cavities formed coalesce in a dorsoventral gradient to form a single central lumen and the mesenchymal cells that remain in the centre are finally cleared from the lumen. **(G')** The result of this MET and central clearing process is that a hollow neural tube is formed that is surrounded by neuroepithelial cells.

2. Materials

2.1. Electroporation of chick SN cells *in ovo*

1. Fertilized eggs are obtained from the White-Leghorn chicken strain.

2. Electroporation mixture containing the plasmid DNA. Here we use plasmids containing pSox2:eGFP [32-34] and the TopFlash:d2eGFP [35,36] reporters as examples. Before injection, the DNA plasmids are diluted to 2μg/μl in 60% sucrose prepared in H_2O, adding 1:10 of Fast Green FCF.

3. TSS-20 Ovodyne Electroporator operated by a footswitch or equivalent equipment generating square electrical pulses.

4. Electrodes (FIG. 2C). We separated a pair of commercial platinum electrodes (CUY610P1.5-1, Nepagene or equivalent) and only used one side as the positive electrode. We incorporated a sharpened and bent 90º tungsten needle (Fine Science Tools) into a holder and used it as the negative 'microelectrode' [37,38].

5. Glass capillaries with a filament (GD-1, Narishige or equivalent) are used to make injection needles with a glass capillary puller (PC-10, Narishige or equivalent).

6. Aspirator tube assemblies for calibrated microcapillary pipettes (Sigma-Aldrich, A5177-5EA or equivalent).

7. 1% Penicillin/Streptomycin (P/S) in MilliQ H_2O.

8. Syringe, thin forceps, curved scissors and plastic tape.

2.2. Imaging plate preparation

1. Millicell cell culture plate inserts (0.4 mm: Millipore, PICMORG50).

2. 25 mL of thin albumen from eggs incubated overnight.

3. 10% glucose in MilliQ H2O.

4. 0.6% Granulated Agar (Difco, 0145-17-0) in MilliQ H2O.

5. 5M NaCl in MilliQ H2O.

6. P/S, undiluted.

7. Water bath, 50 mL Falcon tubes and Pasteur pipettes. TSS-20 Ovodyne Electroporator operated by a footswitch or equivalent equipment generating square electrical pulses.

8. Electrodes (FIG. 2C). We separated a pair of commercial platinum electrodes (CUY610P1.5-1, Nepagene or equivalent) and only used one side as the positive electrode. We incorporated a sharpened and bent 90º tungsten needle (Fine Science Tools) into a holder and used it as the negative 'microelectrode' [37,38].

9. Glass capillaries with a filament (GD-1, Narishige or equivalent) are used to make injection needles with a glass capillary puller (PC-10, Narishige or equivalent).

10. Aspirator tube assemblies for calibrated microcapillary pipettes (Sigma-Aldrich, A5177-

5EA or equivalent).

11. 1% Penicillin/Streptomycin (P/S) in MilliQ H_2O.

12. Syringe, thin forceps, curved scissors and plastic tape.

2.3. Mounting and *in vivo* time-lapse imaging

1. Filter paper rings prepared from 2 x 2 cm squares of Whatman grade 1 filter paper in which a clover-leaf shaped hole is made in the centre with a paper punch, cutting the corners so that they fit in the round imaging plates (FIG. 3A).

2. PBS 1× (1 L): 8 g NaCl, 0.2 g KCl, 1.44 g Na2HPO4, 0.24 g KH2PO4, 800 mL of MilliQ H2O, adjusted pH to 7.4 and to 1 L, sterilized by autoclaving and stored at room temperature.

3. 5 mL of thin albumen from eggs incubated overnight.

4. 5 mL of 123 mM NaCl in MilliQ H2O.

5. Soft tissues (Kimtech Science Kimwipes, or equivalent), thin forceps, fine scissors, Pasteur pipettes, electrical insulation tape and 100 mm petri dishes.

6. Culture chamber [14] created from a Corning ® Costar ® polystyrene 6-well plate (Sigma, CLS3736 or equivalent). To favour the optics, the plastic in the lid is replaced with glass. In each well, a 23 mm hole is made in the centre of the lid by pushing a heated cork borer through the plastic, smoothing the rough edges and sealing a 25 mm diameter glass #1 coverslip over the hole using Marine Adhesive (Zolux Silicone "SA 500") (FIG.3D).

2.4. Image processing and analysis

1. ZEN software (Zeiss) Version 2.3 blue edition with the experiment designer option or any equivalent option allowing time-lapse imaging with multiple XYZ positions.

2. Image J/Fiji software [39,40].

3. BioFormat plugin [41] (https://imagej.net/Bio-Formats).

4. Image5D (Joachim Walter - https://imagej.nih.gov/ij/plugins/image5d.html) plugins.

5. Stack focuser (Michael Umorin - https://imagej.nih.gov/ij/plugins/stack-focuser.html) plugin.

6. MultiStackReg plugin (Brad Busse and Kota Miura - http://bradbusse.net/downloads.html).

7. StackReg plugin [42] (http://bigwww.epfl.ch/thevenaz/stackreg/).

8. Grid/Collection stitching plugin [43] (https://imagej.net/Image_Stitching#Grid.2FCollection_Stitching).

9. Manual Tracking plugin (Fabrice P. Cordelières -https://imagej.nih.gov/ij/plugins/track/track.html).

3. Methods

3.1. Electroporation of chick SN cells *in ovo*

1. Incubate eggs horizontally at 38.5 °C in an atmosphere of 70% humidity until stage HH9.
2. Remove 5 mL of albumen from the egg with a syringe.
3. Open a window at the top of the shell with curved scissors to visualize the embryo.
4. Make a small hole with thin forceps in the posterior region of the area opaca, just outside of the area pellucida. Avoid touching the embryo (FIG. 2A).
5. Pour 200 mL of 1% P/S onto the embryo to improve electrode conductivity (see Note 1).
6. Inject the DNA solution onto the epiblast with a glass capillary by blowing air through the aspirator tube. Introduce the DNA into the small concave region at their posterior end of the stage HH9 embryo, where the neural tube is still open (FIG. 2A-B: see Notes 2 & 3).
7. Carefully insert the platinum electrode connected to the positive lead (+) below the embryo through the hole made previously, parallel to its antero-posterior axis (FIG. 2A-B).
8. Position the tungsten microelectrode connected to the negative lead (-) on top of the embryo, also parallel to the embryo's antero-posterior axis (FIG. 2A-B).
9. Deliver five 50 ms square pulses of 5V at intervals of 50 ms with the electroporator (see Note 4).
10. Seal the window in the shell with tape and incubate embryos until they reach stage HH15 (+24h).

3.2. Imaging plate preparation

1. Heat a water bath to 50 ºC. Collect 25 mL of thin albumen from the eggs incubated overnight in a sterile 50 mL tube and stir it for 15 mins at RT (see Note 5).
2. Add 0.75 mL of 10% glucose to the albumen and place the mixture in the water bath.
3. Boil 25 mL of 0.6% BactAgar in MilliQ H2O and add 0.615 mL of 5M NaCl. Transfer this solution into another sterile 50 mL tube and place it into the water bath to equilibrate to 50 ºC.
4. Mix the solutions of Albumen/Glucose and Agar/NaCl in a sterile 50 mL tube and add 100µl of P/S (see Note 6).
5. Use a sterile Pasteur pipette to pour 1.5 mL of the Albumen/Agar mix onto the cell culture inserts on a flat surface (see Note 7), leaving the Albumen/Agar imaging plates at RT to cool until the gel becomes solid and then storing them at 4 ºC (see Note 8).

3.3. Mounting and *in vivo* time-lapse imaging

1. Reopen the tape-sealed window in the egg, and carefully remove the thick albumen surrounding and covering the embryo with a soft tissue (see Note 9).
2. Place a paper ring on top of the vitelline membrane so that the embryo is located in the center of the clover-shaped hole (FIG. 3A-B), and cut through the vitelline membrane and around the

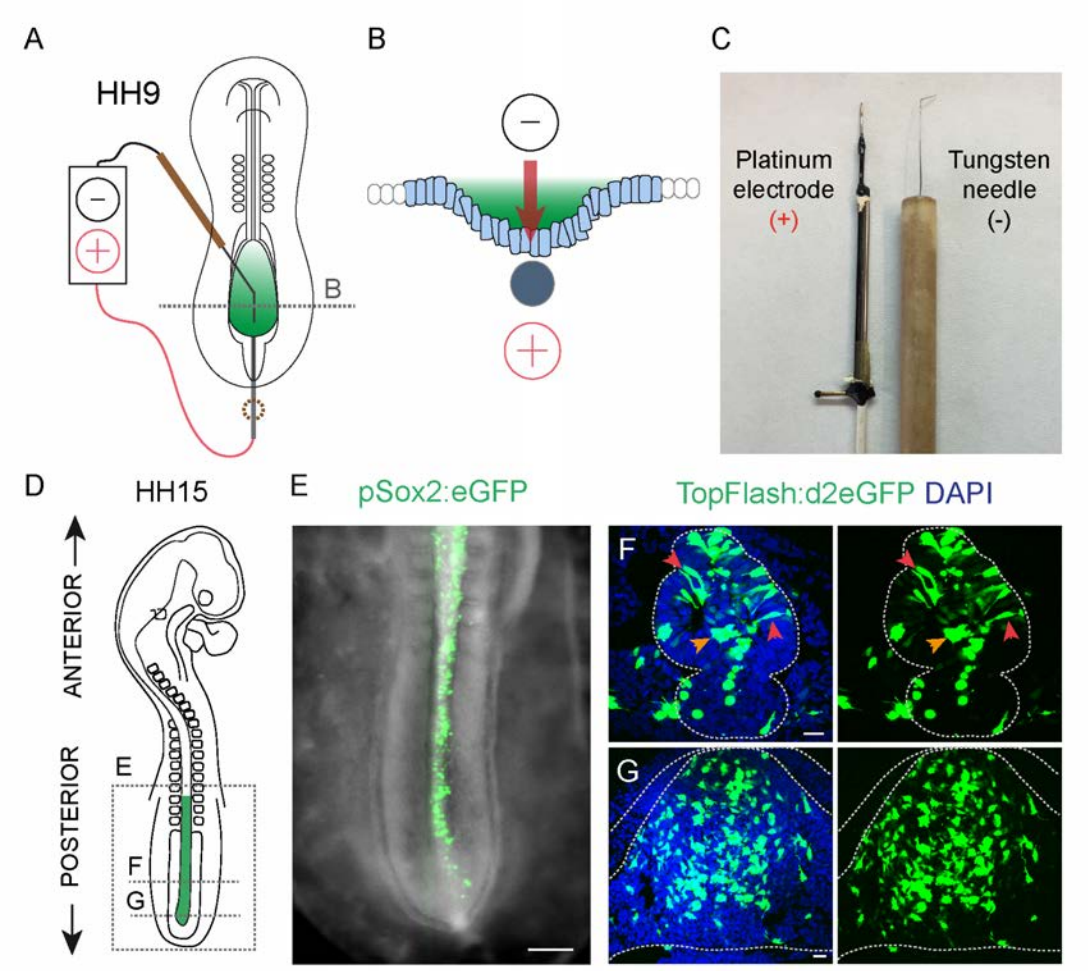

Fig. 2. Chick *in ovo* electroporation of SN cells. (A) The DNA mix (green) is injected into the concave region of the epiblast at the caudal end of a HH9 chick embryo. The positioning of the electrodes is shown, whereby the positive platinum electrode is placed below the embryo through a hole made in the vitelline membrane, while the tungsten needle connected to the negative electrode is positioned on top of the embryo. Both electrodes are positioned parallel to the antero-posterior axis of the embryo. **(B)** Scheme of a transverse section of a chick embryo at the level of the dotted line in A. The epiblast is electroporated by applying the current from top to bottom (red arrow). **(C)** Image of the two electrodes used. **(D)** Schematic representation of a HH15 chick embryo showing the region electroporated using our method 24 hours-post-electroporation (hpe). **(E)** Dorsal view of the boxed region in D following the electroporation of pSox2:eGFP. Both the caudal neural tube and the SN region are efficiently electroporated. Scale bar = 200 μm. **(F-G)** Transverse sections at the two levels indicated in D showing the electroporation of TopFlash:d2eGFP. F is at the level where the lumen is forming, and where both peripheral epithelial (red arrows) and central mesenchymal cells (orange arrow) are labelled. G shows the efficient electroporation of the posterior progenitor cells. Scale bar = 40 μm.

whole perimeter of the filter paper ring with a small pair of scissors, carefully pulling the filter with the embryo attached away from the yolk (see Note 10).

3. Place the embryo ventral side up in a petri dish containing 1x PBS, and clean the remaining yolk and debris by blowing streams of PBS over the embryo with a Pasteur pipette (see Note 11).

4. Select the embryos with the best overall morphology and the greatest level of transgene expression for imaging (see Note 12).

5. Transfer the selected embryos to an Agar/Albumen imaging plate dorsal side up (FIG. 3C), and fill each well of the culture chamber with 1.5 mL of a solution of 5 ml thin albumen and 5 ml of 123 mM NaCl.

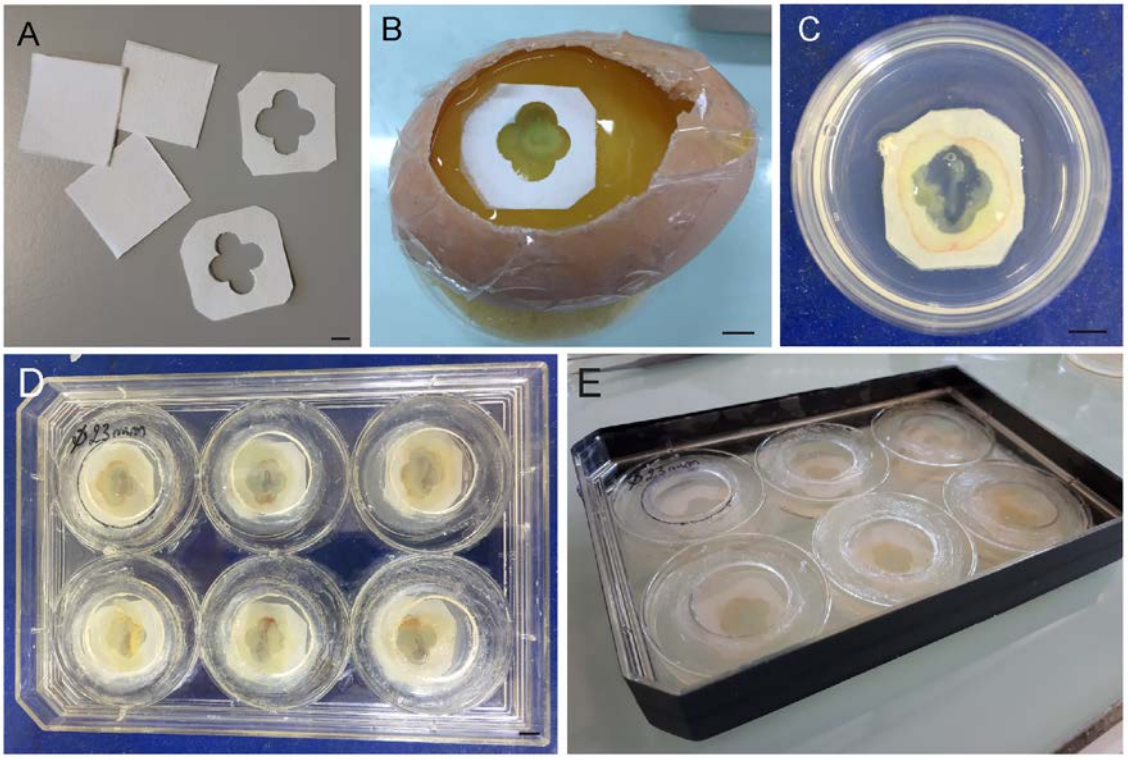

Fig. 3. Embryo culture for *in vivo* time-lapse imaging (A) Paper rings are prepared by making a clover leaf hole in the centre of 2 x 2cm squares of Whatman grade 1 filter paper with a paper punch and cutting off the corners**. (B)** The paper ring is laid over the embryo inside the egg, so that the embryo is positioned in the centre**. (C)** After carefully cutting out the embryo attached to the paper ring, it is then transferred dorsal side up into an imaging plate containing Albumen/Agar. **(D)** Selected embryos (up to 6) are then transferred to the culture chamber for imaging. **(E)** The culture chamber is finally sealed with insulation tape. Scale bar = 0.5 cm.

6. Transfer the embryos in the imaging plates to the wells of the culture chamber (see Note 13) and add 1x PBS between the wells to maintain a moist environment inside the culture chamber. Seal the culture chamber with electrical insulation tape so that up to 6 embryos can be imaged at the same time (FIG. 3D-E: see Note 14).

7. Visualize the embryos under an upright wide-field microscope Axio Imager 2 (Zeiss) equipped with a motorized stage and an incubation chamber. Set the temperature to 39.5 °C so that the temperature at the level of the embryo is around 37.5 °C (see Note 15).

8. Use the Experiment designer module of the ZEN software to set up the acquisition parameters, creating one experimental block for each embryo (i.e.: one 6-well plate = 6 blocks). Define the acquisition parameters for each block after focusing and positioning the embryo in the centre of the field of view (see Note 16).

9. Define a last "blank" block situated in the middle of the imaging plate with the objective in a higher position.

10. Create a "delay block" as the final block and define the delay, which will be the time interval in the time-lapse movie. This delay is synchronised with the preceding blocks and it can be used to pause the process in order to correct drift or loss of focus (see Note 17).

11. Define the number of acquisition loops, which will correspond to the number of time points in the time-lapse video. The motorized stage is now set automatically to move to each previously defined block position, where the given numbers of tiles, channels and slices will be acquired, a process that will be repeated for each loop in every given time interval.

12. With a 5x objective, acquire 10 z images every 10 minutes at a resolution of 1024 x 1024, binning 4 x 4 (FIG. 4, MOVIE S1). With a 20x objective, acquire 10 z images every 6 minutes at a resolution of 1024 x 1024, binning 4 x 4 (FIG. 5: see Note 18).

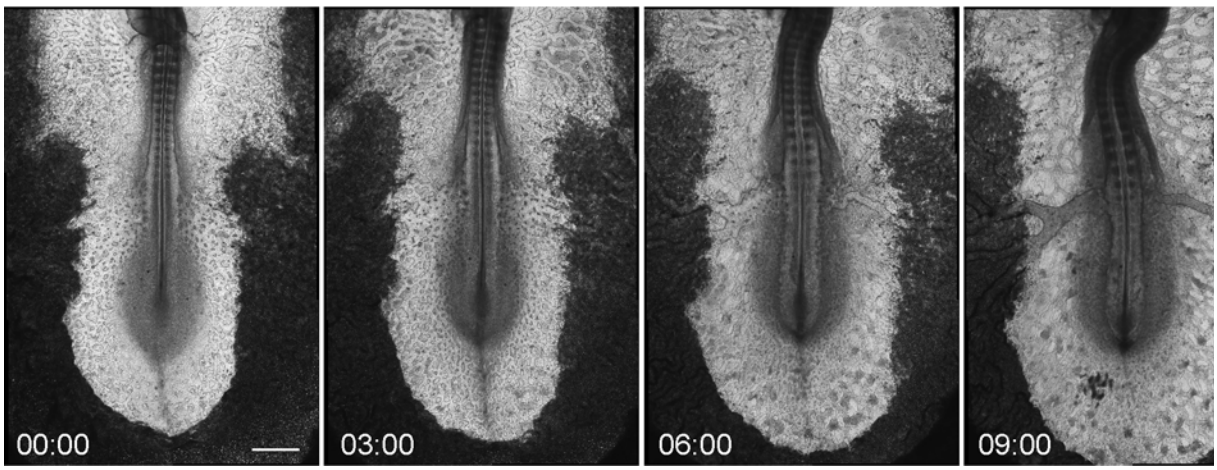

Fig. 4. Normal chick embryo development. Frames from a 5x WT video showing normal chick embryo tail bud elongation and blood vessel formation (hh:mm) (see Movie S1). The embryo was at HH13 when the video begins and it develops to HH16. Scale bar = 500 μm.

3.4. Image processing and analysis

1. Time stitch the images of each embryo acquired with the ZEN software.

2. Open the Tiff file in ImageJ/Fiji using the BioFormat Importer plugin.

3. Convert each tile to the Image5D format (In ImageJ: Plugin tab/Image5D/Stack to Image5D) and apply the Stack focuser plugin, which allows the best focused parts to be selected and projected onto the same plane (see Note 19). Then convert the best focused projection in the Image5D format to the hyperstack format (In ImageJ: Plugin tab/Image5D/Image5D to stack and then Image tab/Hyperstack/Stack to Hyperstack and redefine the dimensions). Repeat the process for each time point of the time-lapse.

4. Stitch together the best focused tiles using the Grid/Collection stitching plugin in order to reconstruct the whole best focused time-lapse movie.

5. Finally, correct the drift along the time-lapse video using the MultiStackReg plugin that is based on the StackReg plugin (see Note 20). The best focused time-lapse movie is now aligned (FIG. 5A-B, MOVIE S2).

6. Individual cells are followed spatiotemporally using the Manual Tracking plugin of the Image J software (FIG. 5C-D, MOVIE S3).

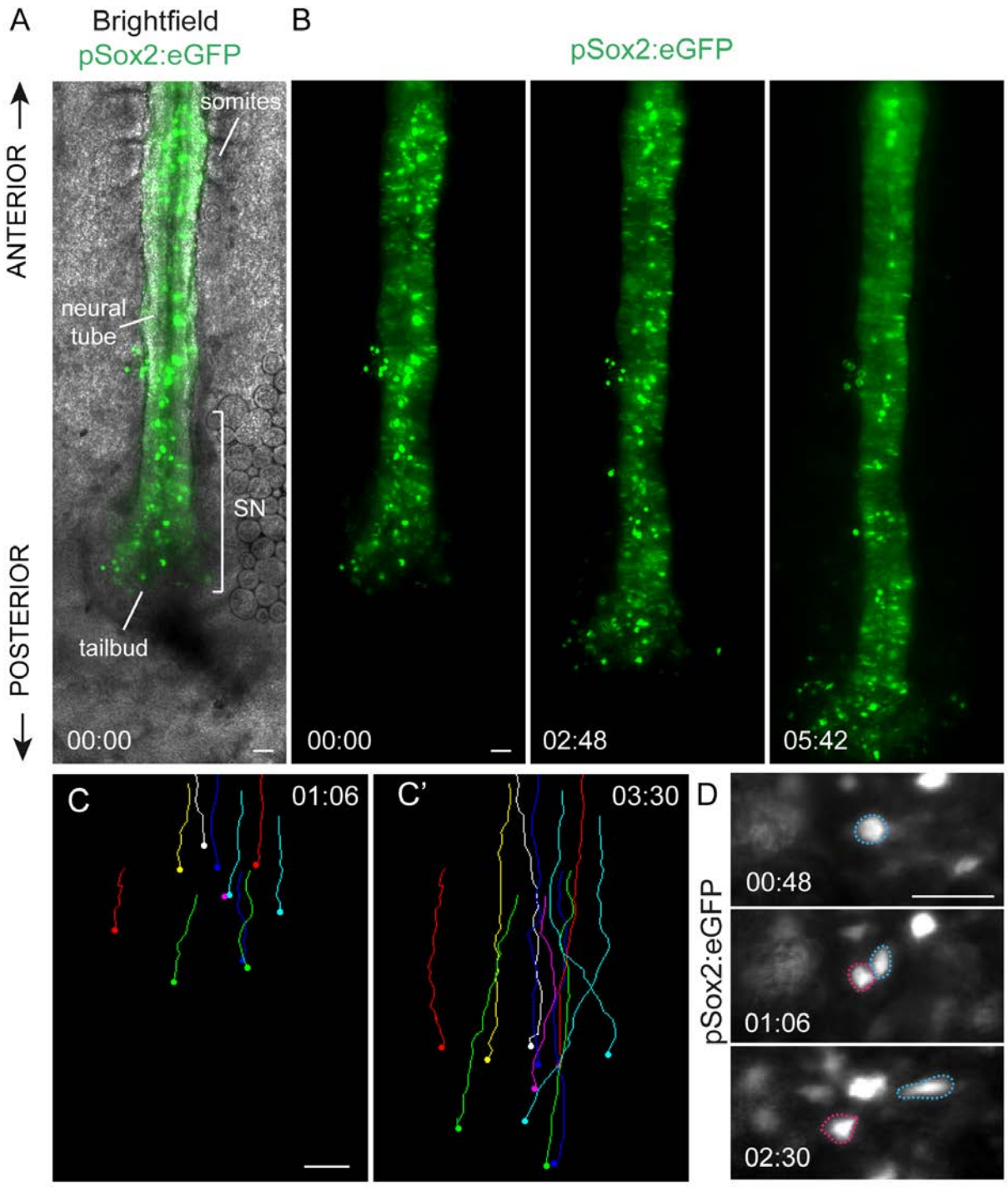

Fig. 5. *In vivo* **analysis of SN cells. (A)** First frame from a 20x video showing a pSox2:eGFP electroporated embryo (see Movie S2). The somites, neural tube, SN region and tail bud are indicated. **(B)** Frames of the same movie as development proceeds, with the tail bud growing caudally and SN advancing. **(C)** Tracks obtained from the embryo in A-B using the Manual Tracking plug-in of the ImageJ software (see Movie S3). **(D)** Frames from the video in A-B at a higher magnification. Single cells are easily followed over time. The cells enclosed by dotted lines correspond to the light blue and magenta tracks in C. The blue cell divides and generates two daughter cells. Scale bars = 50 μm.

4. Notes

1. It is best to perform steps 4 and 5 before placing the electroporation mixture on the epiblast to avoid its diffusion.

2. Repeated injection of DNA through the membranes may block the needle, in which case, clean the tip with a wet tissue or cotton swab.

3. The electroporation mixture can be passed over the top of the epiblast by blowing air through the aspirator tube or with the help of a syringe.

4. Maintain the electrodes moist with 1% of P/S in MilliQ H2O to diminish the resistance between the electrodes.

5. To prepare the imaging plates, collect the thin albumen at the time of electroporation with a syringe, as both procedures are performed on the same day. Thin albumen can also be collected by cracking an egg incubated overnight into a petri dish and recovering it with a Pasteur pipette.

6. Wait for the two solutions to equilibrate to the same temperature as the hot agar could "cook" the thin albumen if they are mixed too early.

7. Try to fill the culture inserts in a way that the culture medium dries as flat as possible, avoiding the introduction of bubbles.

8. Imaging plates should be prepared fresh, no more than 2 days in advance. The plates can be stored at 4 ºC in sterile 35mm petri dishes.

9. The albumen prevents the membranes from attaching to the filter paper so try to remove as much as possible. However, if the embryo is already dry and it is touched again with the tissue, the blastoderm may attach and break and the embryo will be lost.

10. Pull the filter paper with the embryo away from the yolk obliquely. It is best to pull in the direction of the yolk flow produced by the cutting of membranes or along the anteroposterior embryonic axis.

11. Do not blow streams of PBS directly onto the embryo. Clean it by blowing away from the centre where the embryo is located, towards the sides of the filter paper.

12. Electroporated embryos can be screened and selected in the egg, in PBS or in 35mm petri dishes embedded in the Agar/Albumen mix. These can be done when preparing the imaging plates.

13. Dip the bottom of the plates in PBS before transferring them to the culture chamber to avoid forming bubbles under the imaging plates.

14. Before sealing the culture chamber and to avoid any condensation during image acquisition, the coverslip should be sprayed with an antifog solution typically used for scuba diving masks.

15. Place the 6-well plate into the incubation chamber of the microscope but do not start the video recording straight away. Leave the embryos to recover for at least 1h.

16. Define the number of slices, number of tiles, number of channels, laser power and exposure time. Images are acquired in a mosaic format, with different tiles representing each field of view.

17. Frequently check the time-lapse image acquisition during the first hours of imaging as the focus may be lost due to the embryo settling down and due to its elongation. Refocus as often as necessary, during the pausing time.

18. In vivo time-lapse imaging of SN cells can be performed using other systems using some mounting modifications. For example, for confocal imaging we mount the embryos in Lab-Tek® 2-well glass chamber slides.

19. The Stack focuser plugin detects the sharpest details of each image in a z-stack.

20. Registration is calculated on the channel displaying the highest contrast and it is then applied to the other channels.

References

1. Gouignard N, Andrieu C, Theveneau E (2018) Neural crest delamination and migration: Looking forward to the next 150 years. Genesis 56 (6-7):e23107. doi:10.1002/dvg.23107

2. Mayor R, Theveneau E (2013) The neural crest. Development 140 (11):2247-2251. doi:10.1242/dev.091751

3. Theveneau E, Mayor R (2012) Neural crest migration: interplay between chemorepellents, chemoattractants, contact inhibition, epithelial-mesenchymal transition, and collective cell migration. Wiley Interdiscip Rev Dev Biol 1 (3):435-445. doi:10.1002/wdev.28

4. Harrington MJ, Hong E, Brewster R (2009) Comparative analysis of neurulation: first impressions do not count. Mol Reprod Dev 76 (10):954-965. doi:10.1002/mrd.21085

5. Lowery LA, Sive H (2004) Strategies of vertebrate neurulation and a re-evaluation of teleost neural tube formation. Mech Dev 121 (10):1189-1197. doi:10.1016/j.mod.2004.04.022

6. Smith JL, Schoenwolf GC (1987) Cell cycle and neuroepithelial cell shape during bending of the chick neural plate. Anat Rec 218 (2):196-206. doi:10.1002/ar.1092180215

7. Colas JF, Schoenwolf GC (2001) Towards a cellular and molecular understanding of neurulation. Developmental dynamics : an official publication of the American Association of Anatomists 221 (2):117-145. doi:10.1002/dvdy.1144

8. Nikolopoulou E, Galea GL, Rolo A, Greene ND, Copp AJ (2017) Neural tube closure: cellular, molecular and biomechanical mechanisms. Development 144 (4):552-566. doi:10.1242/dev.145904

9. Saitsu H, Shiota K (2008) Involvement of the axially condensed tail bud mesenchyme in normal and abnormal human posterior neural tube development. Congenit Anom (Kyoto) 48 (1):1-6. doi:10.1111/j.1741-4520.2007.00178.x

10. Saitsu H, Yamada S, Uwabe C, Ishibashi M, Shiota K (2004) Development of the posterior neural tube in human embryos. Anat Embryol (Berl) 209 (2):107-117. doi:10.1007/s00429-004-0421-2

11. O'Rahilly R, Muller F (2002) The two sites of fusion of the neural folds and the two neuropores in the human embryo. Teratology 65 (4):162-170. doi:10.1002/tera.10007

12. O'Rahilly R, Muller F (1994) Neurulation in the normal human embryo. Ciba Found Symp 181:70-82; discussion 82-79

13. Hamburger V, Hamilton HL (1992) A series of normal stages in the development of the chick embryo. 1951. Developmental dynamics : an official publication of the American Association of Anatomists 195 (4):231-272. doi:10.1002/aja.1001950404

14. Rupp PA, Rongish BJ, Czirok A, Little CD (2003) Culturing of avian embryos for time-lapse imaging. BioTechniques 34 (2):274-278. doi:10.2144/03342st01

15. Dady A, Havis E, Escriou V, Catala M, Duband JL (2014) Junctional neurulation: a unique developmental program shaping a discrete region of the spinal cord highly susceptible to neural tube defects. J Neurosci 34 (39):13208-13221. doi:10.1523/JNEUROSCI.1850-14.2014

16. Criley BB (1969) Analysis of embryonic sources and mechanims of development of posterior levels of chick neural tubes. J Morphol 128 (4):465-501. doi:10.1002/jmor.1051280406

17. Shum AS, Tang LS, Copp AJ, Roelink H (2010) Lack of motor neuron differentiation is an intrinsic property of the mouse secondary neural tube. Developmental dynamics : an official publication of the American Association of Anatomists 239 (12):3192-3203. doi:10.1002/dvdy.22457

18. Schoenwolf GC (1984) Histological and ultrastructural studies of secondary neurulation in mouse embryos. Am J Anat 169 (4):361-376. doi:10.1002/aja.1001690402

19. Nievelstein RA, Hartwig NG, Vermeij-Keers C, Valk J (1993) Embryonic development of the mammalian caudal neural tube. Teratology 48 (1):21-31. doi:10.1002/tera.1420480106

20. Schoenwolf GC, Delongo J (1980) Ultrastructure of secondary neurulation in the chick embryo. Am J Anat 158 (1):43-63. doi:10.1002/aja.1001580106

21. Schoenwolf GC, Kelley RO (1980) Characterization of intercellular junctions in the caudal portion of the developing neural tube of the chick embryo. Am J Anat 158 (1):29-41. doi:10.1002/aja.1001580105

22. Shimokita E, Takahashi Y (2011) Secondary neurulation: Fate-mapping and gene manipulation of the neural tube in tail bud. Dev Growth Differ 53 (3):401-410. doi:10.1111/j.1440-169X.2011.01260.x

23. Catala M, Teillet MA, De Robertis EM, Le Douarin ML (1996) A spinal cord fate map in the avian embryo: while regressing, Hensen's node lays down the notochord and floor plate thus joining the spinal cord lateral walls. Development 122 (9):2599-2610

24. Catala M, Teillet MA, Le Douarin NM (1995) Organization and development of the tail bud analyzed with the quail-chick chimaera system. Mech Dev 51 (1):51-65

25. Le Douarin NM, Teillet MA, Catala M (1998) Neurulation in amniote vertebrates: a novel view deduced from the use of quail-chick chimeras. Int J Dev Biol 42 (7):909-916

26. Le Douarin NM (2001) Early neurogenesis in Amniote vertebrates. Int J Dev Biol 45 (1):373-378

27. Voiculescu O, Papanayotou C, Stern CD (2008) Spatially and temporally controlled electroporation of early chick embryos. Nat Protoc 3 (3):419-426. doi:10.1038/nprot.2008.10

28. Hatakeyama J, Shimamura K (2008) Method for electroporation for the early chick embryo. Dev Growth Differ 50 (6):449-452. doi:10.1111/j.1440-169X.2008.01040.x

29. Chapman SC, Collignon J, Schoenwolf GC, Lumsden A (2001) Improved method for chick whole-embryo culture using a filter paper carrier. Developmental dynamics : an official publication of the American Association of Anatomists 220 (3):284-289. doi:10.1002/1097-0177(20010301)220:3<284::AID-DVDY1102>3.0.CO;2-5

30. Benazeraf B, Beaupeux M, Tchernookov M, Wallingford A, Salisbury T, Shirtz A, Shirtz A, Huss D, Pourquie O, Francois P, Lansford R (2017) Multi-scale quantification of tissue behavior during amniote embryo axis elongation. Development. doi:10.1242/dev.150557

31. Benazeraf B, Francois P, Baker RE, Denans N, Little CD, Pourquie O (2010) A random cell motility gradient downstream of FGF controls elongation of an amniote embryo. Nature 466 (7303):248-252. doi:10.1038/nature09151

32. Saade M, Gutierrez-Vallejo I, Le Dreau G, Rabadan MA, Miguez DG, Buceta J, Marti E (2013) Sonic hedgehog signaling switches the mode of division in the developing nervous system. Cell Rep 4 (3):492-503. doi:10.1016/j.celrep.2013.06.038

33. Uchikawa M, Ishida Y, Takemoto T, Kamachi Y, Kondoh H (2003) Functional analysis of chicken Sox2 enhancers highlights an array of diverse regulatory elements that are conserved in mammals. Dev Cell 4 (4):509-519

34. Le Dreau G, Saade M, Gutierrez-Vallejo I, Marti E (2014) The strength of SMAD1/5 activity determines the mode of stem cell division in the developing spinal cord. J Cell Biol 204 (4):591-605. doi:10.1083/jcb.201307031

35. Rios AC, Denans N, Marcelle C (2010) Real-time observation of Wnt beta-catenin signaling in the chick embryo. Developmental dynamics : an official publication of the American Association of Anatomists 239 (1):346-353. doi:10.1002/dvdy.22174

36. Serralbo O, Marcelle C (2014) Migrating cells mediate long-range WNT signaling. Development 141 (10):2057-2063. doi:10.1242/dev.107656

37. Momose T, Tonegawa A, Takeuchi J, Ogawa H, Umesono K, Yasuda K (1999) Efficient targeting of gene expression in chick embryos by microelectroporation. Dev Growth Differ 41 (3):335-344

38. Yasuda K, Momose T, Takahashi Y (2000) Applications of microelectroporation for studies of chick embryogenesis. Dev Growth Differ 42 (3):203-206

39. Rueden CT, Schindelin J, Hiner MC, DeZonia BE, Walter AE, Arena ET, Eliceiri KW (2017) ImageJ2: ImageJ for the next generation of scientific image data. BMC bioinformatics 18 (1):529. doi:10.1186/s12859-017-1934-z

40. Schindelin J, Arganda-Carreras I, Frise E, Kaynig V, Longair M, Pietzsch T, Preibisch S, Rueden C, Saalfeld S, Schmid B, Tinevez JY, White DJ, Hartenstein V, Eliceiri K, Tomancak P, Cardona A (2012) Fiji: an open-source platform for biological-image analysis. Nature methods 9 (7):676-682. doi:10.1038/nmeth.2019

41. Linkert M, Rueden CT, Allan C, Burel JM, Moore W, Patterson A, Loranger B, Moore J, Neves C, Macdonald D, Tarkowska A, Sticco C, Hill E, Rossner M, Eliceiri KW, Swedlow JR (2010) Metadata matters: access to image data in the real world. J Cell Biol 189 (5):777-782. doi:10.1083/jcb.201004104

42. Thevenaz P, Ruttimann UE, Unser M (1998) A pyramid approach to subpixel registration based on intensity. IEEE transactions on image processing : a publication of the IEEE Signal Processing Society 7 (1):27-41. doi:10.1109/83.650848

43. Preibisch S, Saalfeld S, Tomancak P (2009) Globally optimal stitching of tiled 3D microscopic image acquisitions. Bioinformatics (Oxford, England) 25 (11):1463-1465. doi:10.1093/bioinformatics/btp184

Supplementary Movie Legends

MOVIE S1. In vivo time-lapse imaging of a WT chick embryo (5x) over 10h showing normal tail bud elongation and blood vessel formation (hh:mm). Related to Figure 4.

MOVIE S2. In vivo time-lapse imaging of a pSox2:eGFP electroporated embryo (20x) over 10h. Related to Figure 5.

MOVIE S3. In vivo time-lapse imaging of a pSox2:eGFP electroporated embryo showing the tracks obtained using the Manual Tracking plug-in of the ImageJ software. Related to Figure 5.

APPENDIX III

Article

Shh-mediated centrosomal recruitment of PKA promotes symmetric proliferative neuroepithelial cell division

Murielle Saade, Elena Gonzalez-Gobartt, Rene Escalona, Susana Usieto and Elisa Martí

Nature Cell Biology (2017)

Summary:

Embryonic growth of the central nervous system (CNS) requires a finely tuned balance between the different modes of divisions that NPCs undergo: self-expanding (symmetric proliferative, PP) divisions that generate two progenitor daughter cells; self-renewing (asymmetric, PN) divisions that generate one progenitor daughter cell and one neuron; and self-consuming (terminal symmetric neurogenic, NN) divisions that generate two neurons. Early proliferative PP divisions are critical for expanding the progenitor pool and the timing of the switch to PN, and later NN, ultimately determines differential rates of growth in different CNS regions and, thus, the overall microstructure and function. Impaired balance between the three division modes can lead to human disorders such as microcephaly, highlighting the relevance of understanding the mechanisms that regulate the temporal production of different cell types. Previous studies demonstrated that BMP (Le Dreau et al., 2014) and SHH signalling (Saade et al., 2013) are required for progenitor pool expansion by maintaining symmetric divisions. The PhD student participated in the continuation of this last work, searching for the intrinsic mechanism that integrates SHH responses into the control of NPCs division mode. In the study presented here, we showed that activation of the SHH pathway leads to an increase in pericentrin expression, a relevant protein for centrosome maturation. High levels of pericentrin facilitate the symmetric recruitment to centrosomes of one component of the SHH signalling pathway, the protein kinase A (PKA). Centrosomal PKA symmetric docking allows positive feedback to SHH signalling and the maintenance of proliferative PP division.

PhD student contribution: The PhD student performed the experiments together with Dr. Murielle Saade, contributed to image acquisition and quantification, carried out the complete statistical analysis and discussed results.

nature cell biology

Shh-mediated centrosomal recruitment of PKA promotes symmetric proliferative neuroepithelial cell division

Murielle Saade[1], Elena Gonzalez-Gobartt[1], Rene Escalona[1,2], Susana Usieto[1] and Elisa Martí[1,3]

Tight control of the balance between self-expanding symmetric and self-renewing asymmetric neural progenitor divisions is crucial to regulate the number of cells in the developing central nervous system. We recently demonstrated that Sonic hedgehog (Shh) signalling is required for the expansion of motor neuron progenitors by maintaining symmetric divisions. Here we show that activation of Shh/Gli signalling in dividing neuroepithelial cells controls the symmetric recruitment of PKA to the centrosomes that nucleate the mitotic spindle, maintaining symmetric proliferative divisions. Notably, Shh signalling upregulates the expression of pericentrin, which is required to dock PKA to the centrosomes, which in turn exerts a positive feedback onto Shh signalling. Thus, by controlling centrosomal protein assembly, we propose that Shh signalling overcomes the intrinsic asymmetry at the centrosome during neuroepithelial cell division, thereby promoting self-expanding symmetric divisions and the expansion of the progenitor pool.

The vertebrate nervous system is an extraordinarily complex assembly of diverse cell types, all of which arise from pluripotent neuroepithelial cells. Neuroepithelial cells form a one-cell-thick pseudostratified epithelium in which mitosis occurs at the apical face[1]. Whereas mitotic division of a single cell generally produces two identical daughter cells, in the developing nervous system the identity of the progeny depends on the mode of division that neuroepithelial cells undergo[2–5]: self-expanding (symmetric proliferative, PP) divisions that expand the progenitor pool by generating two, identical progenitor daughter cells; self-renewing (asymmetric, PN) divisions that generate one progenitor daughter cell and another with a more restricted potential; and self-consuming (terminal symmetric neurogenic, NN) divisions that generate two cells committed to differentiate, thereby depleting the progenitor pool. Premature transition to divisions that generate neurons rapidly exhausts the progenitor reservoir and restricts the number of neurons that can ultimately be produced. Indeed, such alterations are considered a major cause of microcephaly, highlighting the relevance of understanding the mechanisms that regulate the expansion of the progenitor pool.

The intrinsic asymmetry of cell division is driven by the centrosomes that nucleate the mitotic spindle. The centrosome replicates in a semi-conservative manner, resulting in the formation of two centrosomes—the original maternal centrosome and a new daughter centrosome. These maternal and daughter centrioles present notable differences in molecular composition, ultrastructure and function[6,7], an intrinsic asymmetry that influences the fate of the daughter cells[8]. Thus, in the developing mouse neocortex, the centrosome retaining the maternal centriole remains in the ventricular zone (VZ) and it is preferentially inherited by progenitors, whereas the centrosome containing the daughter centriole leaves the VZ to differentiate[9]. The maternal centriole has been further linked to neural progenitors in this tissue, as retention of part of the ciliary membrane by the mother centriole at the onset of mitosis delivers it to only one of the two daughter cells[10]. Interestingly, the loss of a mature centriole-specific protein (ninein) was sufficient to prematurely deplete progenitors from the VZ[9]. Hence, the intrinsic centrosomal asymmetries must be overcome for the progenitor pool to expand through symmetric proliferative (PP) divisions during early neural development.

We recently showed that Sonic hedgehog (Shh) signalling maintains the PP mode of division in motor neuron progenitors (pMNs) in the developing spinal cord[11]. Thus, we set to study whether Shh signalling might be responsible for overcoming the intrinsic asymmetry in dividing neuroepithelial cells. Shh is a growth factor that augments proliferation in stem-cell niches in the adult telencephalon[12,13]. In addition to its principal role in patterning[14], Shh signalling promotes the proliferation and survival of neural progenitors in the developing nervous system[15]. Here we show that, in the developing chick spinal cord, activation of the Shh/Gli pathway is correlated with

[1]Instituto de Biología Molecular de Barcelona, CSIC, ParcCientífic de Barcelona, C/Baldiri i Reixac 20, Barcelona 08028, Spain. [2]Present address: Departamento de Embriologia, Facultad de Medicina, Universidad Nacional Autónoma de México, Ciudad de Mexico CP 04510, Mexico.
[3]Correspondence should be addressed to E.M. (e-mail: emgbmb@ibmb.csic.es)

Received 25 March 2016; accepted 16 March 2017; published online 27 April 2017; DOI: 10.1038/ncb3512

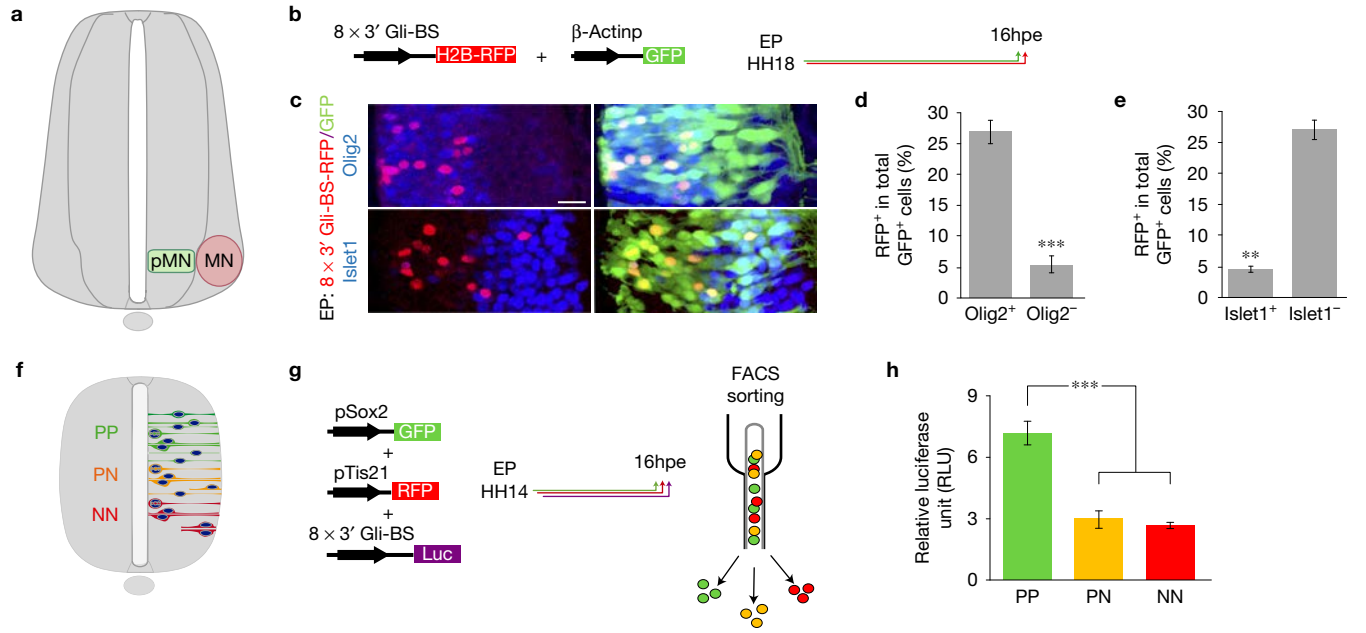

Figure 1 Strong Shh/Gli activity in symmetrically dividing MN progenitors. (**a**) Scheme showing the motor neuron progenitor domain (pMN) and the differentiated motor neurons (MN) in the developing ventral spinal cord. (**b**) Scheme showing the DNAs and timing of the co-electroporation (hpe = hours post-electroporation). (**c**) Selected images of NT sections immunostained for anti-Olig2 (blue) or anti-Islet1 (blue) 16hpe of 8 × 3′ Gli-BS-RFP (red) and control β-Actinp-GFP (green). (**d**) Quantification of the ratio of RFP^+/GFP^+ cells in the $Olig2^+$ domain (27 ± 2 RFP^+/GFP^+ cells versus 5 ± 1 RFP^-/GFP^+ cells; plot shows the mean ± s.e.m., $n=20$ sections of seven embryos; three independent experiments; Mann–Whitney U test; $^{***}P<0.001$). (**e**) Quantification of the RFP^+/GFP^+ cell ratio in the $Islet1^+$ domain (4.3 ± 0.45 RFP^+/GFP^-cells versus 26 ± 1.5 RFP^+/GFP^+ cells; plot shows the mean ± s.e.m., $n=20$ sections of six embryos; Mann–Whitney U test; $^{**}P<0.01$). (**f**) Scheme showing the three modes of division occurring in the developing spinal cord; PP, PN and NN. (**g**) Scheme showing the co-electroporated DNAs and cell sorting experiment. (**h**) Quantification of Luc/Renilla activity 16hpe in each cell pool (PP = 7 ± 0.7, PN = 3 ± 0.5, NN = 2 ± 0.2RLU; plots show the mean ± s.e.m., $n=13$ embryos per condition; three independent experiments; one-way ANOVA; $^{***}P<0.001$). Scale bars, 15 μm. Images are representative of three independent experiments.

symmetric centrosomal recruitment of PKA in pMNs, symmetric inheritance of apical membrane domains, proliferative PP divisions and the inhibition of neurogenesis. The docking of PKA to centrosomes is dependent on the A-kinase anchoring proteins pericentrin (PCNT) and AKAP9[16]. Interestingly, the transcriptional activity of Shh/Gli is sufficient to regulate *PCNT* expression, which is strongly expressed in cells that undergo symmetric PP divisions. Consequently, we propose a model whereby Shh provides an instructive signal to overcome the intrinsic asymmetry in neuroepithelial cell divisions, promoting the symmetric PCNT-mediated centrosomal docking of PKA and PP division.

RESULTS

Symmetric proliferative PP divisions are associated with strong Shh/Gli activity

The strength of Shh activity can be determined *in vivo* by measuring the activity of a Gli transcriptional reporter (Gli-BS-RFP). In the developing spinal cord, Shh-responding cells (RFP^+) are restricted to the ventral neural tube (NT), largely within the pMN domain identified by the expression of the MN progenitor marker Olig2 (27 ± 2%$Olig2^+/RFP^+$ cells: Fig. 1a-d). However, endogenous Shh/Gli activity is barely detected in the early differentiated motor neurons identified by the expression of the MN marker Islet1 (MNs, 4 ± 0.5% $Islet1^+/RFP^-$ cells: Fig. 1c,e), suggesting that Shh signalling acts mainly on dividing progenitors and that it does not influence cells committed to neurogenesis.

Neurogenesis is initiated by the switch from progenitor-producing to neuron-producing divisions, which can be monitored with tools that unequivocally identify the three modes of divisions in the chick NT (the Sox2p enhancer element that track proliferative PP progenitors, and the anti-proliferative gene Tis21 whose expression is restricted to neurogenic PN/NN progenitors; Fig. 1f)[11,17].

We investigated whether the strength of endogenous Shh activity is correlated with the mode of division by quantifying Gli transcriptional activity (Gli-BS-Luciferase reporter) after co-electroporation of the pSox2:eGFP and pTis21:RFP reporters, and FACS purification of the PP, PN and NN cell subpopulations (Fig. 1g). Shh/Gli activity was weaker in cells that underwent neuron-generating divisions (PN and NN) than in those that underwent PP divisions (Fig. 1h). These data support the idea that strong canonical Shh/Gli activity is associated with the symmetric PP divisions that expand the pMN pool, prompting us to search for the intrinsic mechanisms driving this Shh activity.

The catalytic and regulatory subunits of PKA localize to centrosomes during mitosis

In neuroepithelial cells, a single primary cilium pointing to the lumen coordinates Shh signalling responses[18]. Shh activation provokes Smo accumulation in the cilia membrane, triggering Gli activation and transcriptional responses (Fig. 2a). Phosphorylation by the cAMP-dependent protein kinase A (PKA) converts a Shh gradient into multiple discrete foci of Gli(A/R) transcriptional activity[19]. The subcellular distribution of Shh signalling components in the NT

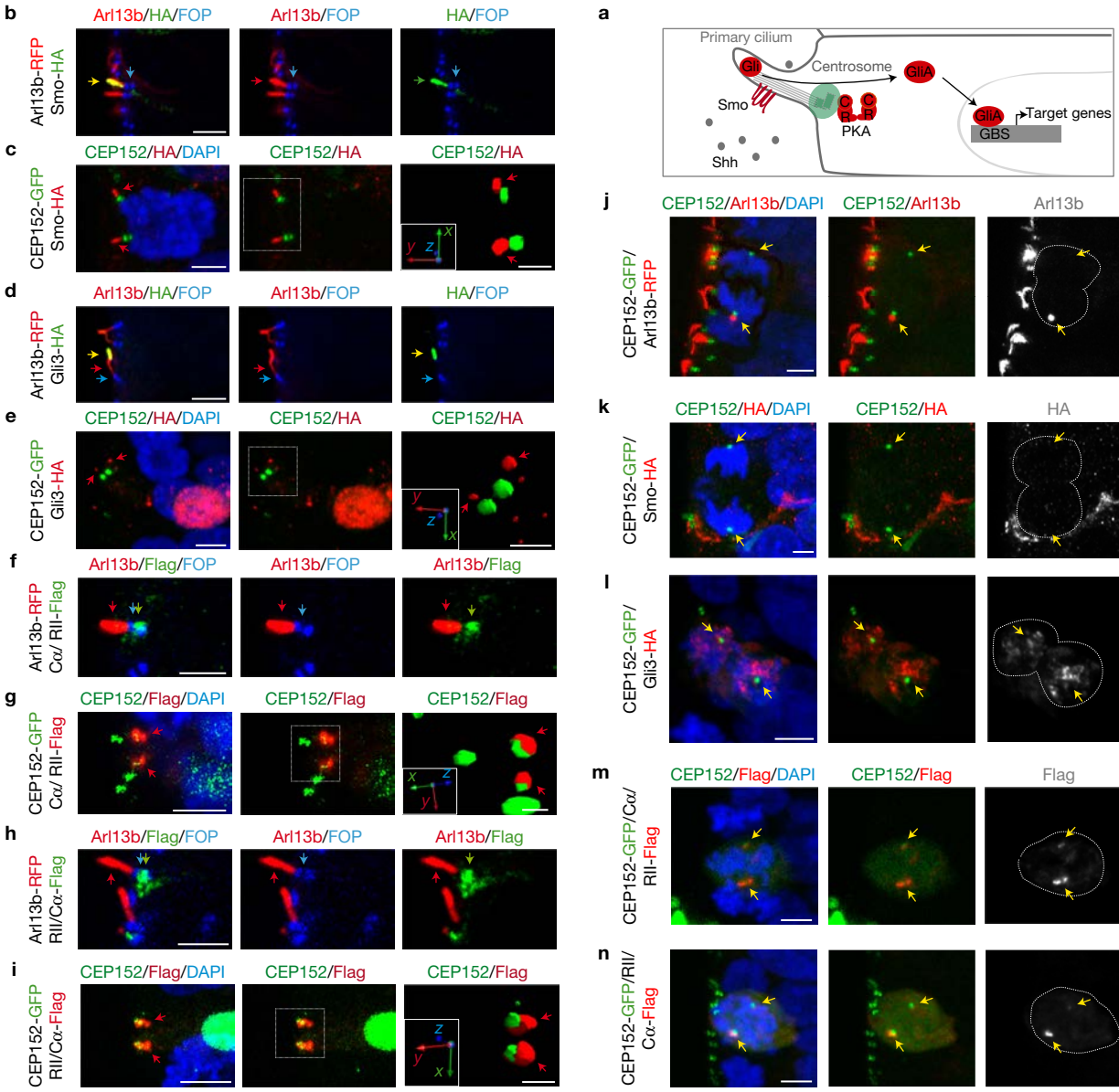

Figure 2 PKA localizes to the centrosome in dividing neural progenitors. (**a**) Scheme showing the Shh pathway associated to the primary cilium. (**b**) Smo-HA (green arrow) localizes to the cilium shaft identified by Arl13b-RFP (red arrow), anti-FOP (blue arrow) stains centrosomes (scale bar, 5 μm). (**c**) Smo-HA (red arrow) localizes distally to the cilium base identified by CEP152-GFP(green). DAPI (blue) stains the nuclei and, in 3D reconstructions, red arrows point to Smo-HA (scale bar 0,5 μm). (**d**) Gli3-HA (yellow arrow) localizes to the tip of the cilium identified by Arl13b-RFP (red arrow), anti-FOP (blue arrow) stains centrosomes (scale bar, 5 μm). (**e**) Gli3-HA (red arrow) localizes distal to the cilium base and the nucleus (scale bar, 5 μm). DAPI (blue) stains the nuclei and, in 3D reconstructions, red arrows point to Gli3-HA (scale bar, 0, 5 μm). (**f**) The regulatory subunit of PKA (RII-PKA-FLAG green arrow) localized to the pair of centrosomes stained by anti-FOP (blue arrow) at the base of the cilium Arl13b-RFP (red arrow), anti-FOP (blue arrow) (scale bar, 5 μm). (**g**) The regulatory subunit of PKA (RII-PKA-FLAG red) localized to the centrosome (CEP152-GFP, green) at the base of the cilium (scale bar, 5 μm). DAPI (blue) stains the nuclei and, in 3D reconstructions, red arrows point to RII-PKA (scale bar, 0,5 μm). (**h**) The catalitic subunit of PKA (RII-PKA-FLAG green arrow) localized to the centrosomes stained by anti-FOP (blue arrow) at the base of the cilium Arl13b-RFP (red arrow), anti-FOP (blue arrow) (scale bar, 5 μm). (**i**) The catalytic subunit of PKA (Cα-PKA-FLAG, red arrow) localizes to centrosomes (CEP152-GFP, green) at the cilium base (scale bar, 5 μm). DAPI (blue) stains the nuclei and, in 3D reconstructions, red arrows point to α-PKA (scale bar, 0,5 μm). (**j**) Arl13b-RFP (red) co-localizes with CEP152-GFP (green) associated to the mother centrosome. DAPI (blue) stains the chromosomes. (**k**,**l**) Smo-HA (red) and Gli3-HA do not localize to the centrosomes identified by CEP152-GFP(green). DAPI (blue) stains the chromosomes, the arrows point to the centrosomes. (**m**,**n**) RII-PKA and Cα-PKA localize to centrosomes. (**m**) Cα-PKA/RII-PKA-FLAG, revealed RII-PKA by anti-FLAG. (**n**) RII⁻PKA/Cα-PKA-FLAG, revealed Cα-PKA by anti-FLAG (scale bars, 5 μm). DAPI (blue) stains the nuclei, the arrows point to centrosomal PKA. Images are representative of three independent experiments.

was examined in neuroepithelial cells by introducing a plasmid encoding the small GTPase ADP-ribosylation factor-like 13b fused to red fluorescent protein (Arl13b-RFP)[10], which specifically associates with the ciliary membrane and marks primary cilia protruding from the two centrosomes, identified as pairs of dots at the VZ surface, that co-localized with the core centrosomal protein

CEP152 (ref. 20) (CEP152-GFP), with FOP (FGFR1 Oncogene Partner[21]), and with α-Tubulin (Supplementary Fig. 1a,b). Both Smo-HA (Fig. 2b,c) and Gli3-HA (Fig. 2d,e and Supplementary Fig. 1c) tagged proteins localized distally to the base of the cilium. In addition, Gli3-HA accumulated in the nucleus (Fig. 2e). Moreover, the regulatory (RII-PKA-FLAG: Fig. 2f,g) and the catalytic (Cα-PKA-FLAG: Fig. 2h,i) subunits of PKA were localized to the base of the cilium (Supplementary Fig. 2a,b). Hence, transient expression of components of the Shh pathway at concentrations insufficient to regulate Shh activity (Supplementary Fig. 2c) reliably indicates their subcellular distribution in neuroepithelial cells.

In neuroepithelial cells, Arl13b-RFP accumulated near one of the centrosomes nucleating the mitotic spindle (Fig. 2j). Thus, as in the developing mouse neocortex[10], the primary cilia was not completely disassembled prior to mitosis (Supplementary Fig. 1d–g). Accordingly, components of the Shh pathway might remain associated to the cilia remnant and/or to the centrosome during mitosis. However, neither the Smo-HA (Fig. 2k) nor Gli3-HA (Fig. 2l) fusion proteins concentrated at the centrosomes nucleating the mitotic spindle, although both PKA subunits did accumulate at these centrosomes (Fig. 2m,n), as suggested previously *in vitro*[22,23]. The docking of PKA to the centrosomes persisted throughout mitosis in neuroepithelial cells (Supplementary Fig. 2d–i). As centrosomes are intrinsically asymmetric (containing either the maternal or daughter centriole), we studied whether PKA accumulated asymmetrically at centrosomes.

The temporal switch in symmetric PKA docking at centrosomes correlates with a switch in the mode of pMN division

The relative accumulation of PKA to centrosomes labelled by CEP152-GFP was assessed to test whether PKA was recruited asymmetrically to centrosomes at the poles of the mitotic spindle in pMN. CEP152-GFP was distributed symmetrically at the two poles (median $=0.009 \pm 0.3$: Fig. 3a–c), as was PKA in expanding pMNs undergoing PP divisions (RII-PKA median $= 0.01 \pm 0.9$, Cα-PKA median $= 0.004 \pm 0.4$, Fig. 3c–e). Interestingly, at 70 hpf, when pMNs switch to asymmetric neurogenic PN divisions[11], the distribution of PKA shifted from symmetric to asymmetric (RII-PKA median $= 0.01 \pm 0.9$; Cα-PKA median $= 0.03 \pm 0.9$: Fig. 3c,f,g and Supplementary Fig. 2j–o). Since the sharp reduction in the number of PP divisions is concomitant with the switch in the symmetric docking of PKA to centrosomes (Fig. 3b,c), the subcellular distribution of PKA might affect the activity of the Shh/Gli pathway. Indeed, PKA docking to the cilium base inhibits its kinase activity, potentially shifting the GliR/GliA balance and activating Shh/Gli responses[24,25].

Activation of the Shh/Gli pathway is correlated to symmetric centrosomal docking of PKA, symmetric inheritance of apical membrane microdomains and the inhibition of neurogenesis

To test whether symmetric docking of PKA to spindle poles is correlated with Gli activity, we electroporated the Gli-BS-RFP reporter together with PKA (RII-PKA-FLAG, or Cα-PKA-FLAG-tagged proteins: Fig. 4a). At 70 hpf, Shh-responding cells (Gli-BS-RFP$^+$) are restricted to the ventral NT where centrosomal recruitment of PKA ranges from symmetric to highly asymmetric (Fig. 4b,c). Interestingly, RII-PKA (median $= 0.06 \pm 0.3$) and Cα-PKA (median $= 0.15 \pm 0.35$) were both associated to centrosomes symmetrically in Gli-BS-RFP$^+$ dividing progenitors (Fig. 4c,e and Supplementary Fig. 3a,b). However, in Gli-BS-RFP$^-$ divisions RII-PKA (median $= 0.1 \pm 0.8$) and Cα-PKA (median $= 0.2 \pm 1.1$, Fig. 4c,f,g and Supplementary Fig. 3c,d) were asymmetrically distributed. Hence, we conclude that when the Shh/Gli pathway is active, PKA was symmetrically recruited to centrosomes during mitosis (Fig. 4h,i), prompting us to test whether this affected daughter cell fate.

The orientation of the mitotic spindle in dividing neuroepithelial cells is tightly regulated to distribute the adhesive and polarity domains between the two daughter cells, thereby influencing their fate[26–30]. N-Cadherin and the PAR complex polarity protein aPKC concentrate at the adherens junction (AJ) in the chick NT, accumulating in discrete microdomains at the apical plasma membrane[26] and distributed in a discrete line along the ventricle (Fig. 5a,b). The partitioning of these microdomains was evaluated by predicting the cleavage plane orientation in anaphase/telophase cells (Fig. 5c). At 54 hpf, the αPKC domain was inherited equally by both daughter cells (mean $= 1.2 \pm 0.02$: Supplementary Fig. 4a–d), and preferentially by one of the two daughter cells at 70 hpf (mean $= 1.7 \pm 0.1$: Supplementary Fig. 4a–d). Next we evaluated the partitioning of these microdomains, co-electroporated with the Gli-BS-RFP reporter and H2B-GFP, in combination with FOP staining (Fig. 5c). Interestingly, the aPKC domain was inherited equally by both daughter cells in H2B-GFP$^+$/Gli-BS-RFP$^+$ divisions (mean $= 1.26 \pm 0.1$: Fig. 5d,e), and preferentially by one of the two daughter cells in H2B-GFP$^+$/Gli-BS-RFP$^-$ divisions (mean $= 3.5 \pm 0.4$; Fig. 5d,f and Supplementary Fig. 4e–g). Thus, we concluded that when the Shh pathway was active, not only centrosomal recruitment of PKA was symmetric but the fate determinant aPKC was also symmetrically distributed (Fig. 5g and Supplementary Fig. 4h–j).

To evaluate the fate of the divisions, we took advantage of the pTis21-RFP reporter that unequivocally identifies neurogenic divisions in the chick NT[11,17]. Neurogenic divisions (Tis21-RFP$^+$) were identified at 70 hpf in the NT (Fig. 6a,b) and both RII-PKA (median $= 0.3 \pm 1.1$) and Cα-PKA (median $= 0.4 \pm 1.15$) were asymmetrically distributed at the centrosomes (identified by the endogenous FOP) in Tis21-RFP$^+$ divisions where one daughter cell is committed to neurogenesis (Fig. 6c,f,g,i and Supplementary Fig. 3e,f). By contrast, RII-PKA (median $= 0.02 \pm 0.3$) and Cα-PKA (median $=0.01 \pm 0.4$) were symmetrically associated to the centrosomes in Tis21-RFP$^-$ divisions (Fig. 6c,d,e,h and Supplementary Fig. 3e,f). Notably, centrosomal docking of PKA at the cilium base was asymmetric in Tis21-RFP$^+$ progenitors committed to neurogenic divisions (Supplementary Fig. 3g–j). Together, there appears to be a strong correlation between high Shh/Gli activity, symmetric centrosomal docking of PKA and the symmetric PP outcome of the division. Hence, we assessed the instructive role of Shh activity in mitotic outcome.

Shh-mediated pericentrin expression contributes to the symmetric docking of PKA at centrosomes and the persistence of proliferative PP divisions

In asymmetrically dividing neuroepithelial cells, PKA is recruited to the mature centrosome identified by Arl13b-RFP and ninein expression (Fig. 7a–c and Supplementary Fig. 3k,l)[10]. Conversely, PP divisions are correlated with symmetric PKA docking at the poles of the mitotic spindle and with Shh/Gli activity. To evaluate the

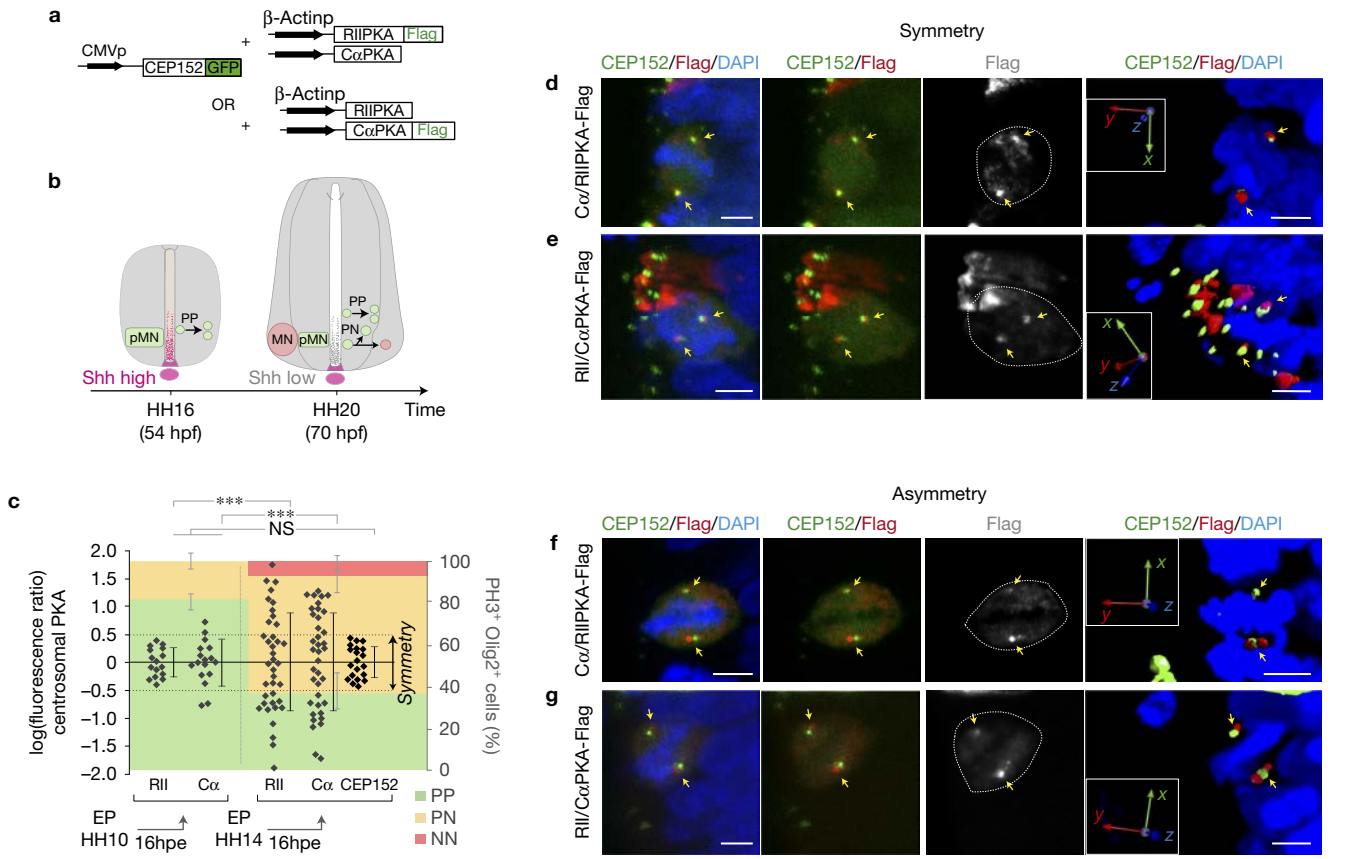

Figure 3 PKA docking to centrosomes changes during NT development. (**a**) Scheme showing the DNAs co-electroporated. (**b**) Scheme showing Shh activity in the developing NT. Shh signalling is strong in the ventral NT at 54 hpf, promoting PP divisions. Shh signalling is weak at 70 hpf and the mode of progenitor division switches from symmetric PP to asymmetric PN[11]. (**c**) Plots of the ratio of fluorescence intensity Rfi between the two centrosomes in individual mitoses. Lines and error bars correspond to the median ± s.d.; three independent experiments; one-way ANOVA; $^{***}P < 0.001$. CEP152-GFP is symmetrically distributed at the two centrosomes (median = 0.009 ± 0.3 $n = 20$ mitoses). At HH10+16hpe, PKA is distributed symmetrically (RII-PKA-FLAG median = 0.03 ± 0.25, $n = 16$ mitoses, Cα-PKA-FLAG median = 0.004 ± 0.4, $n = 17$ mitoses). At HH14+16hpe (70 hpf), a proportion of mitosis also have an asymmetric PKA localization (RII-PKA-FLAG median = 0.01 ± 0.9, $n = 38$ mitoses, Cα-PKA-FLAG median = 0.03 ± 0.9, $n = 38$ mitoses). The background colour code shows the proportion of PH3$^+$/Olig2$^+$divisions that were previously identified as PP (pSox2$^+$/pTis21$^-$, green), PN (pSox2$^+$/pTis21, yellow) and NN (pSox2$^-$/pTis21$^+$, red) at the developmental stages indicated[11]. (**d**,**e**) Selected images show the symmetric centrosomal distribution of PKA. (**d**) Cα-PKA/RII-PKA-FLAG, revealed Cα-PKA by anti-FLAG staining (red) in the centrosomes labelled with CEP152-GFP (green). (**e**) RII-PKA/Cα-PKA-FLAG revealed RII-PKA by anti-FLAG staining (red) in the centrosomes labelled with CEP152-GFP (green). DAPI (blue) labels chromosomes and, in 3D reconstructions, the yellow arrows point to the centrosomes. (**f**,**g**) Selected images showing the asymmetric centrosomal PKA distribution. (**f**) Cα-PKA/RII-PKA-FLAG, revealed Cα-PKA by anti-FLAG staining (red) in the centrosomes labelled with CEP152-GFP (green). (**g**) RII-PKA/Cα-PKA-FLAG, revealed RII-PKA by anti-FLAG staining (red) in the centrosomes labelled with CEP152-GFP (green). DAPI (blue) stains chromosomes and, in 3D reconstructions, yellow arrows point to PKA (scale bars, 5 μm). Images are representative of three independent experiments.

instructive role of Shh in promoting centrosome maturation and mitotic symmetry, we considered an *in vivo* transcriptome analysis of neural progenitors responding to different levels of Shh activity[31,32]. Among the genes over-represented in Shh-responding cells, ~1.9% were associated to centrosomes, including the centriole-associated proteins (CETN2 and SAS6), the pericentriolar proteins (PCNT, PCM1, CNTRL, BBS2) and several centrosome-associated proteins (including ASPM and AKAP9: Fig. 7d,e and Supplementary Table 1). We focused on PCNT and AKAP9, as both proteins are involved in PKA docking to centrosomes through a conserved PCNT–AKAP9 Centrosomal Targeting (PACT) domain[16,33]. *PCNT* expression was seen to be weaker in both neuron-generating divisions (PN and NN) than in PP divisions (Fig. 7f); hence, strong *PCNT* expression might contribute to centrosomal maturation and, therefore, to the maintenance of symmetric PP divisions.

To further test the instructive role of Shh in promoting centrosome maturation—and, hence, mitotic symmetry—we augmented Shh activity by introducing a dominant-active form of the receptor Smoothened (SmoM2: Supplementary Fig. 1c), and decreased Shh activity by introducing a dominant-negative receptor, Patched1 (Ptc1Δloop2; Supplementary Fig. 1c). *PCNT* (but not *AKAP9*; Supplementary Fig. 5a) was significantly over-expressed in cells exhibiting strong Shh activity (Fig. 7g). Conversely *PCNT* expression was significantly reduced in cells exhibiting low Shh activity (Fig. 7g). In addition, in dividing cells responding to high Shh activity, centrosomal recruitment of PCNT was increased (Fig. 7h–j). Moreover, augmenting Shh

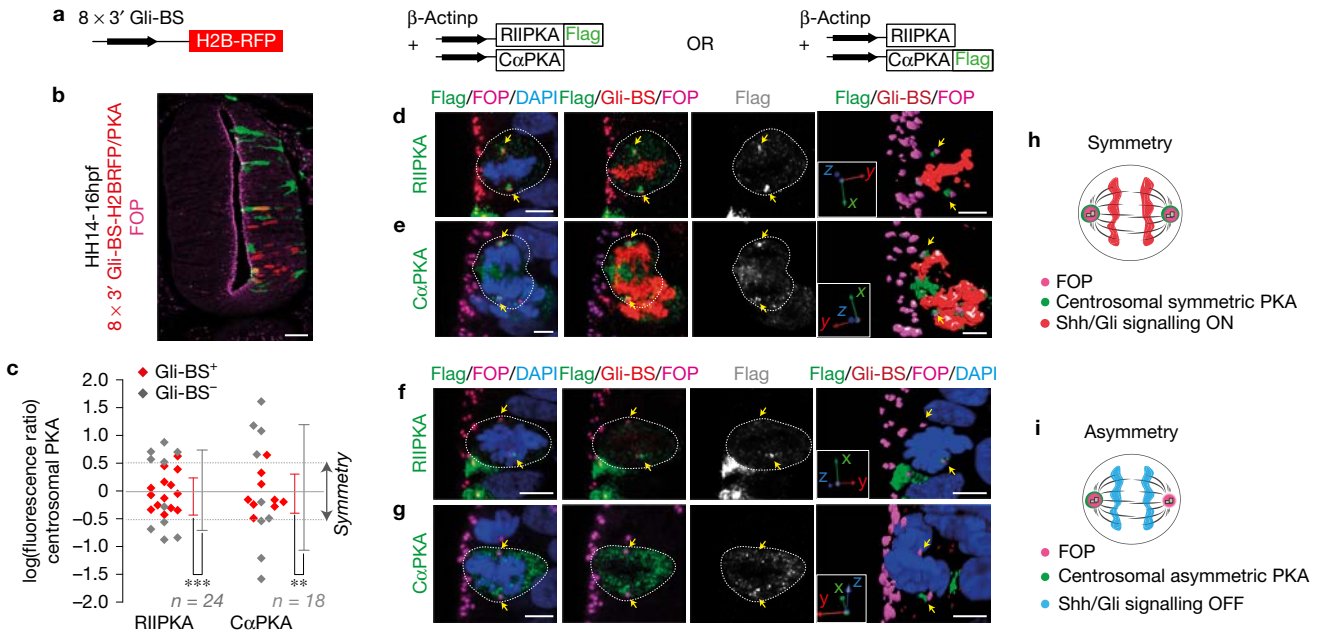

Figure 4 Activation of the Shh/Gli pathway correlates with symmetric centrosomal docking of PKA. (**a**) Scheme showing the co-electroporated DNAs. (**b**) Representative image of a chick NT section at 16hpe of the DNAs indicated, showing Gli-BS-RFP$^+$ (red) cells restricted to the ventral NT, PKA-FLAG (green) expressing cells and FOP (purple) immunostained centrosomes lining the NT lumen (scale bar, 30 μm). (**c**) Plots of the fluorescence ratio between the two centrosomes at individual mitoses, where the lines and error bars correspond to the median ± s.d.; three independent experiments; Mann–Whitney U test; $^{***}P < 0.001$ $^{**}P < 0.01$. RII-PKA distribution was largely symmetric in Gli-BS-RFP$^+$ (red dots) mitosis (RII-PKA-FLAG median = 0.06 ± 0.3 red dots), while it was asymmetric in Gli-BS-RFP$^-$ mitosis (RII-PKA-FLAG median = 0.1 ± 0.7 grey dots, n=24 mitoses). Cα-PKA was also symmetric in Gli-BS-RFP$^+$ mitosis (CαPKA-FLAG median = 0.15 ± 0.35 red dots), while asymmetric in Gli-BS-RFP$^-$ mitosis (Cα-PKA-FLAG median = 0.2 ± 1.1 grey dots, n=18 mitoses). (**d**,**e**) Selected images show symmetric centrosomal PKA localization in Gli-BS-RFP$^+$ mitosis (red). (**d**) Cα-PKA/RII-PKA-FLAG, revealed RII-PKA by anti-FLAG staining (green) in the centrosomes labelled with anti-FOP (purple). (**e**) RII-PKA/Cα-PKA-FLAG, revealed Cα-PKA by anti-FLAG staining (green) in centrosomes labelled with anti-FOP (purple). DAPI (blue) labels the chromosomes and, in the 3D reconstruction, yellow arrows point to PKA (scale bars, 5 μm). (**f**,**g**) Selected images show asymmetric centrosomal PKA localization in Gli-BS-RFP$^-$ mitosis. (**f**) Cα-PKA/RII-PKA-FLAG, revealed RII-PKA by anti-FLAG staining (green) in the centrosomes labelled with anti-FOP (purple), arrows point to centrosomes. (**g**) RII-PKA/Cα-PKA-FLAG, revealed Cα-PKA by anti-FLAG staining (green) in the centrosomes labelled with anti-FOP (purple). DAPI (blue) labels the chromosomes and, in the 3D reconstruction, yellow arrows point to PKA (scale bars, 5 μm). (**h**) Scheme showing a Gli-BS-RFP$^+$ mitosis. (**i**) Scheme showing a Gli-BS-RFP$^-$ mitosis. Images are representative of three independent experiments.

activity increased the symmetric centrosomal docking of PKA (control median 0.014 ± 0.85; SmoM2 median = 0.016 ± 0.4, Fig. 7k,l), while reducing Shh activity disrupted the symmetric centrosomal docking of PKA (control median 0.014 ± 0.85; Ptc1Δloop2 median = 0.12 ± 1.3, Fig. 7k,l). Together these data indicate that Shh signalling regulates the centrosome-specific protein content required for maturation, overcoming the intrinsic asymmetry in order to maintain symmetric PP divisions.

Finally, we tested whether pericentrin-mediated PKA docking to centrosomes was necessary to activate Shh/Gli signalling and inhibit neurogenesis. In addition to the conserved centrosomal targeting (PACT) domain, pericentrin contains a conserved, amino-terminal RII-PKA binding domain (Fig. 8a and Supplementary Fig. 5b–d). Mutant RII-PKA lacks the critical PCNT/AKAP interacting domain (RII$^{\Delta 2-6}$-PKA-FLAG[34]) and it failed to dock RII-PKA to centrosomes in dividing neural progenitors (Fig. 8b,c and Supplementary Fig. 5e). Moreover, this mutant retains the capacity to dimerize with the Cα-PKA subunit[24,34], thereby preventing Cα-PKA recruitment to centrosomes (Fig. 8d). Over-expression of Cα-PKA alone, which directly phosphorylates Gli, prevented Gli transcriptional activation in neural progenitors (Fig. 8e,f), while basal Gli activation was restored in the presence of RII-PKA, which binds to and inhibits Cα-PKA (Fig. 8f). However, while the mutant RII$^{\Delta 2-6}$-PKA retains the capacity to bind Cα-PKA, it was insufficient to restore Gli activation (Fig. 8f). These data support the relevance of the subcellular distribution of PKA for its enzymatic activity, and confirmed that PKA targeting to centrosomes is necessary for Gli activation in neural progenitors. In addition, electroporation of Cα-PKA alone activated the pTis21-Luc reporter in neural progenitors, which served as a readout of neurogenesis (Fig. 8g,h), whereas basal pTis21 activation was restored by co-electroporation of RII-PKA. Co-electroporation of the mutant RII$^{\Delta 2-6}$-PKA with Cα-PKA maintained pTis21-Luc activation (Fig. 8h). To further confirm these results, we introduced a pericentrin variant that contains only the conserved centrosomal targeting (PACT) domain (Fig. 8i), which was sufficient to displace endogenous PCNT (Fig. 8j–l) and PKA (Fig. 8m,n) from centrosomes in dividing neuroepithelial cells. Co-electroporation of the mutant pericentrin (PACT[16]) was sufficient to increase pTis21-Luc activation (Fig. 8o,p), further confirming the impact of PKA docking to centrosomes on neurogenesis.

Based on our results, we propose a model whereby strong Shh/Gli activity regulates *PCNT* expression to promote centrosomal maturation, helping to overcome the intrinsic centrosome asymmetry. In addition, high PCNT levels contribute to the symmetric

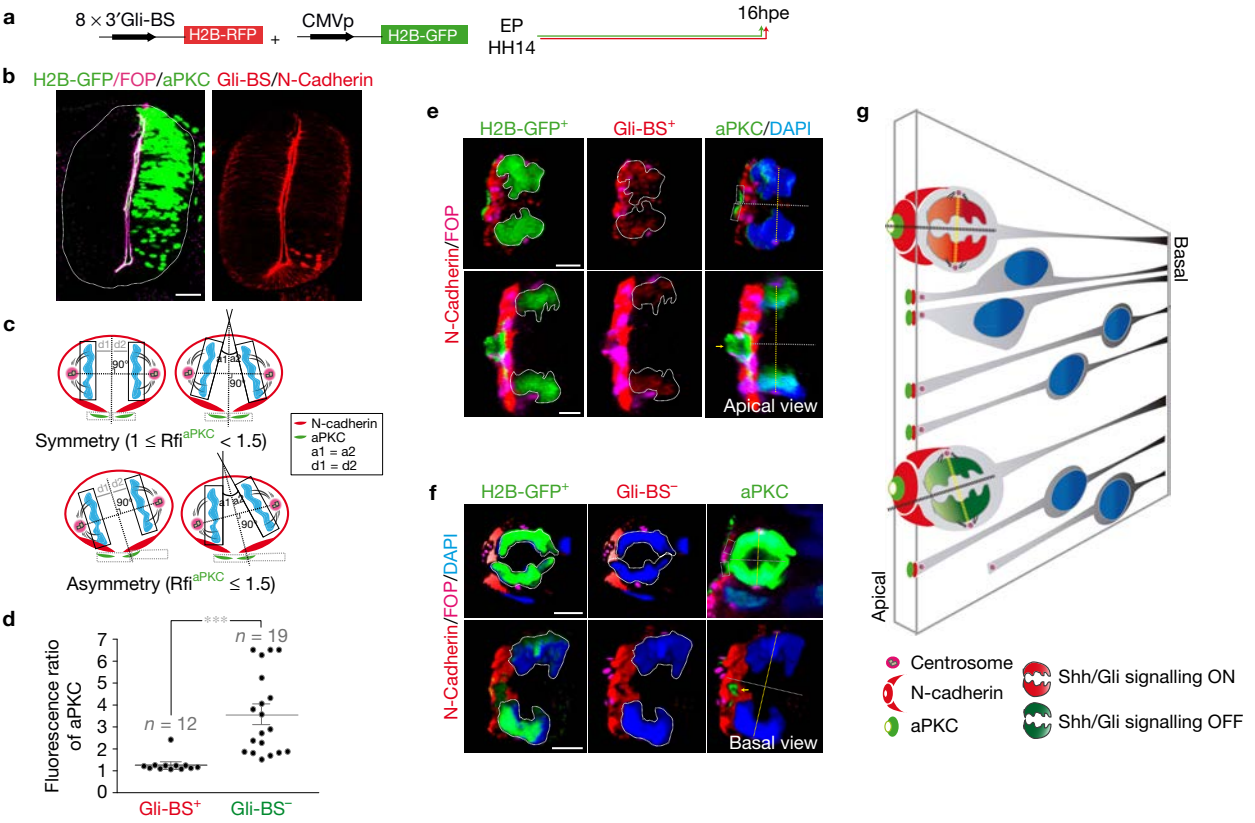

Figure 5 Activation of the Shh/Gli pathway correlates with symmetric inheritance of apical membrane domains. (**a**) Scheme showing the DNAs co-electroporated. (**b**) Representative images of chick NT sections at 16hpe of the DNAs indicated, showing H2B-GFP (green) as a control of electroporation. Anti-aPKC (green) labelled the apical PAR complex and anti-FOP (purple) labelled the centrosomes that line the NT lumen. Gli-BS-RFP$^+$ (red) cells are restricted to the ventral NT, while N-Cadherin immunostaining (red) labelled AJs lining the NT lumen (scale bar, 30 μm). (**c**) Scheme showing the split of AJs by the cleavage plane at anaphase, the cleavage plane being deduced by a line bisecting the two sets of condensed chromatin (blue plates), predicting the type of division made by distributing the N-cadherin hole (red outline) between the two daughter cells, and by partitioning the apical aPKC domain (green). A ratio of fluorescence intensity (Rfi) <1.5 is considered as symmetric inheritance of aPKC, whereas aRfi ≥1.5 is considered asymmetric inheritance of aPKC. (**d**) The Rfi between inherited aPKC apical domains in mitotic cells expressing the DNAs indicated, where the lines and error bars correspond to the median ± s.e.m.; three independent experiments; Mann–Whitney U test; $^{***}P < 0.001$. The partitioning of a PKC was largely symmetric in Gli-BS-RFP$^+$ (red) mitoses (mean = 1.26 ± 0.1, n=12 mitoses), while it was asymmetric in Gli-BS-RFP$^-$ (green) mitoses (mean = 3.5 ± 0.4, n = 19 mitoses). (**e**) Example of two cells in anaphase and telophase in which the cleavage plane is deduced by drawing perpendicular lines (dashed line) bisecting the two sets of condensed chromatin (outlined). Symmetric partitioning of aPKC is correlated with Gli-BS activation (RFP$^+$). GFP represents the control electroporation, FOP (purple) labels the centrosomes, DAPI (blue) labels the chromosomes (yellow arrow points to the N-cadherin hole) (scale bars, 5 μm). (**f**) Example of two cells in anaphase and telophase, in which asymmetric partitioning of aPKC is correlated with Gli-BS inactivation (RFP$^-$, yellow arrow points to the N-cadherin hole) (scale bars, 5 μm). (**g**) Scheme showing dividing neuroepithelial cells. Gli-BS-RFP$^+$ mitoses organize perpendicular to the cleavage plane and the apical complex is inherited symmetrically, while Gli-BS-RFP$^-$ mitoses associate obliquely with respect to the cleavage plane and aPKC is asymmetrically inherited. Images are representative of three independent experiments.

centrosomal docking of PKA which, through a positive feedback loop, maintains Shh activity high and thereby promotes the expansion of the progenitor pool through symmetric PP divisions (Fig. 8q). Adaptation to Shh, including the transcriptional downregulation of Gli, reverts pericentrin expression in neuroepithelial cells and favours asymmetric PKA docking, driving neurogenesis (Fig. 8q).

DISCUSSION

The built-in asymmetry of the centrosomes that nucleate the mitotic spindle has recently generated renewed attention given its impact on the fate of daughter cells. In particular, the daughter cell that retains the maternal centriole[9] and the ciliary membrane remnant[10] persists as a progenitor in the ventricular zone (VZ) of the developing mouse neocortex, whereas the daughter cell containing the new centriole leaves the VZ to initiate differentiation. Moreover, loss of ninein, a mature centriole-specific protein, causes premature depletion of progenitors from the VZ[9]. Hence, for progenitors to expand through symmetric PP divisions during early neural development, these intrinsic asymmetries must be overcome by as yet unexplored mechanisms.

In assessing how Shh signalling maintains proliferative PP pMN divisions in the developing spinal cord[11], we found that symmetric docking of PKA to centrosomes depends on activation of the Shh/Gli pathway in dividing neuroepithelial cells. We show that Shh signalling regulates the expression of several centrosomal proteins, including pericentrin, thereby contributing to centrosomal maturation in neuroepithelial cell divisions. This regulation appears not to be direct, since the Gli1 (ref. 35) and Gli3 (ref. 36) genome binding/occupancy profile in neural progenitors did not identify PCNT as a putative direct

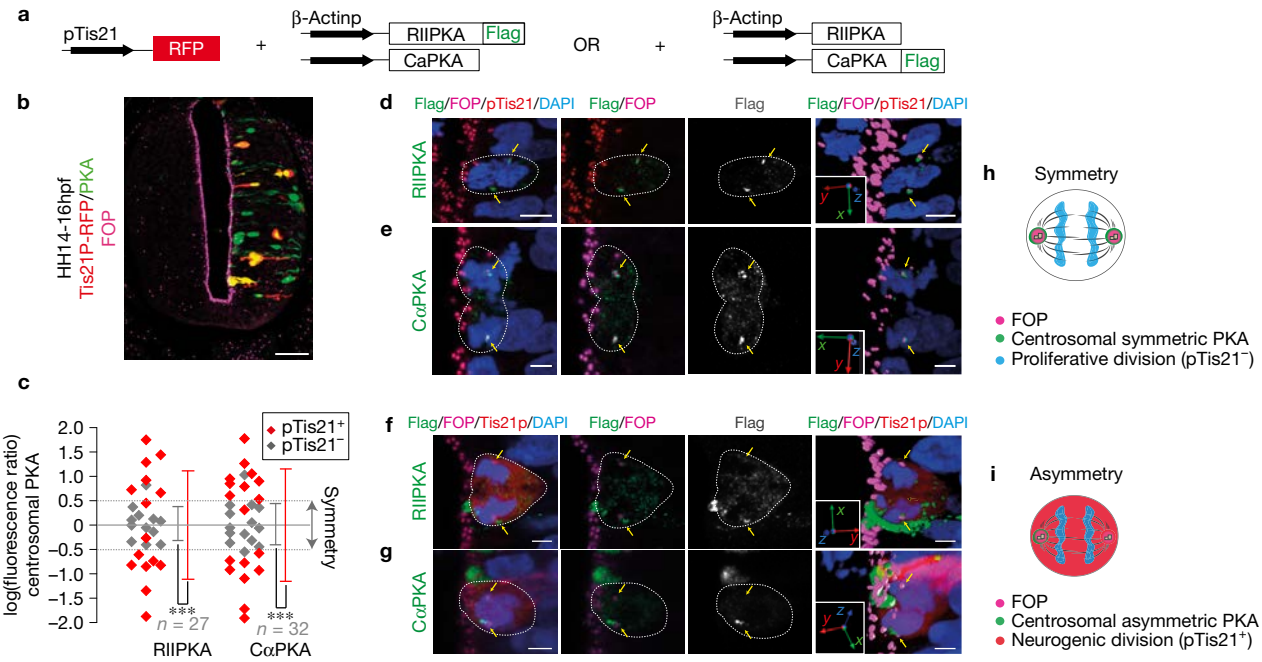

Figure 6 Asymmetric centrosomal docking of PKA is correlated with neurogenic divisions. (**a**) Scheme showing the co-electroporated DNAs. (**b**) Representative image of a chick NT section showing pTis21-RFP (red) cells, PKA-FLAG (green) expressing cells and FOP (purple) immunostaining the centrosomes lining the NT lumen (scale bar, 30 μm). (**c**) Plots of the ratio of fluorescence intensity (Rfi) between the two centrosomes in individual mitosis expressing the DNAs indicated, where the lines and error bars correspond to the median ± s.d.; three independent experiments; Mann–Whitney U test; $^{***}P < 0.001$. RII-PKA and Cα-PKA centrosomal docking is largely symmetric in pTis21-RFP$^-$ (grey dots) mitoses (RII-PKA-FLAG median = 0.02 ± 0.34; Cα-PKA-FLAG median = 0.01 ± 0.4, $n = 27$ mitoses), while it is asymmetric in pTis21-RFP$^+$ (red dots) mitoses (RII-PKA-FLAG median = 0.3 ± 1.1; Cα-PKA-FLAG median = 0.4 ± 1.15, $n = 32$ mitoses). (**d**,**e**) Selected images show symmetric centrosomal PKA localization in pTis21-RFP$^-$ mitoses. (**d**) Cα-PKA/RII-PKA-FLAG, revealed RII-PKA by anti-FLAG staining (green) in the centrosomes labelled with anti-FOP (purple). (**e**) RII-PKA/Cα-PKA-FLAG, revealed Cα-PKA by anti-FLAG staining (green) in the centrosomes labelled with anti-FOP (purple) (scale bars, 5 μm). (**f**,**g**) Selected images show asymmetric centrosomal PKA localization in pTis21-RFP$^+$ mitosis (red). (**f**) Cα-PKA/RII-PKA-FLAG, revealed RII-PKA by anti-FLAG staining (green) in the centrosomes labelled with anti-FOP (purple). (**g**) RII-PKA/Cα-PKA-FLAG, revealed Cα-PKA by anti-FLAG staining (green) in the centrosomes labelled with anti-FOP (purple). DAPI (blue) labels chromosomes and, in 3D reconstructions, the yellow arrows point to centrosomes (scale bars, 5 μm). (**h**) Scheme showing a pTis21-RFP$^-$ mitoses. (**i**) Scheme showing a pTis21-RFP$^+$ mitoses. Images are representative of three independent experiments.

Shh/Gli target. PKA docks to centrosomes through a PACT domain in PCNT[16], which is expressed strongly in symmetric proliferative (PP) divisions relative to neuron-generating (PN or NN) divisions. We propose that a Shh-dependent positive feedback loop operates via centrosomal maturation and targeting of PKA, maintaining strong Shh activity and hence, the symmetric PP mode of division required for pMN expansion. In the ventral NT, dampening Shh activity is required to switch the mode of cell division and drive the onset of neurogenesis[11]. Well-established negative feedback loops are responsible for adaptation to Shh responses, and they involve the transcriptional upregulation of the inhibitory receptor Ptch1, transcriptional down-regulation of Gli, and differential stability of the active/inactive Gli isoforms[37]. Such regulatory loops might drive the switch in the mode of cell division in the ventral NT. Beyond the spatiotemporal influence of Shh activity, a similar role might be fulfilled by other growth factors, as recently reported for BMP/Smad activity in the dorsal NT[17].

The cAMP-dependent PKA is a conserved regulator of Hh signalling that lies downstream of the Ptc and Smo membrane receptors. Activation of PKA completely blocks Hh signalling, even in the presence of the Hh ligand, whereas genetic ablation of PKA shifts the GliR/GliA balance strongly in favour of GliA, fully activating Shh target genes in the developing vertebrate nervous system, ventralizing the NT[25,38]. PKA-dependent phosphorylation of Gli2/3 proteins is a determinant of their transcriptional activity, controlling the production of repressor (Gli2/3R) and activator (Gli2/3A) forms[19]. Shh is a classical morphogen in the NT[39,40], where increasing concentrations of Shh are directly transduced into enhanced Gli2/3 transcriptional activity, mediating the full range of Shh responses in NT patterning[41]. Multi-site phosphorylation converts differences in signal strength into discrete states of Gli2/3 activity[19], transducing the Shh gradient into a gradient of transcriptional activity. PKA activity is primarily controlled by regulatory subunits (R-subunits) that bind to the catalytic (Cα-subunits) in the absence of cAMP, while cAMP binding to the R-PKA displaces it and activates the Cα-PKA. The kinase's activity is further regulated by docking to particular subcellular compartments through association with A-kinase anchoring proteins (AKAPs[16]). We propose that PCNT-mediated centrosomal docking of PKA inhibits its kinase activity on Gli proteins, since symmetric centrosomal recruitment of PKA is correlated with activation of the Shh/Gli pathway. Moreover, the association of mutant RII-PKA, which lacks the critical PACT domain (RII$^{\Delta 2-6}$-PKA), to centrosomes was compromised[24,34] and it failed to inhibit Cα-PKA kinase activity on Gli proteins, thereby promoting neurogenesis. Hence, preventing PCNT-mediated

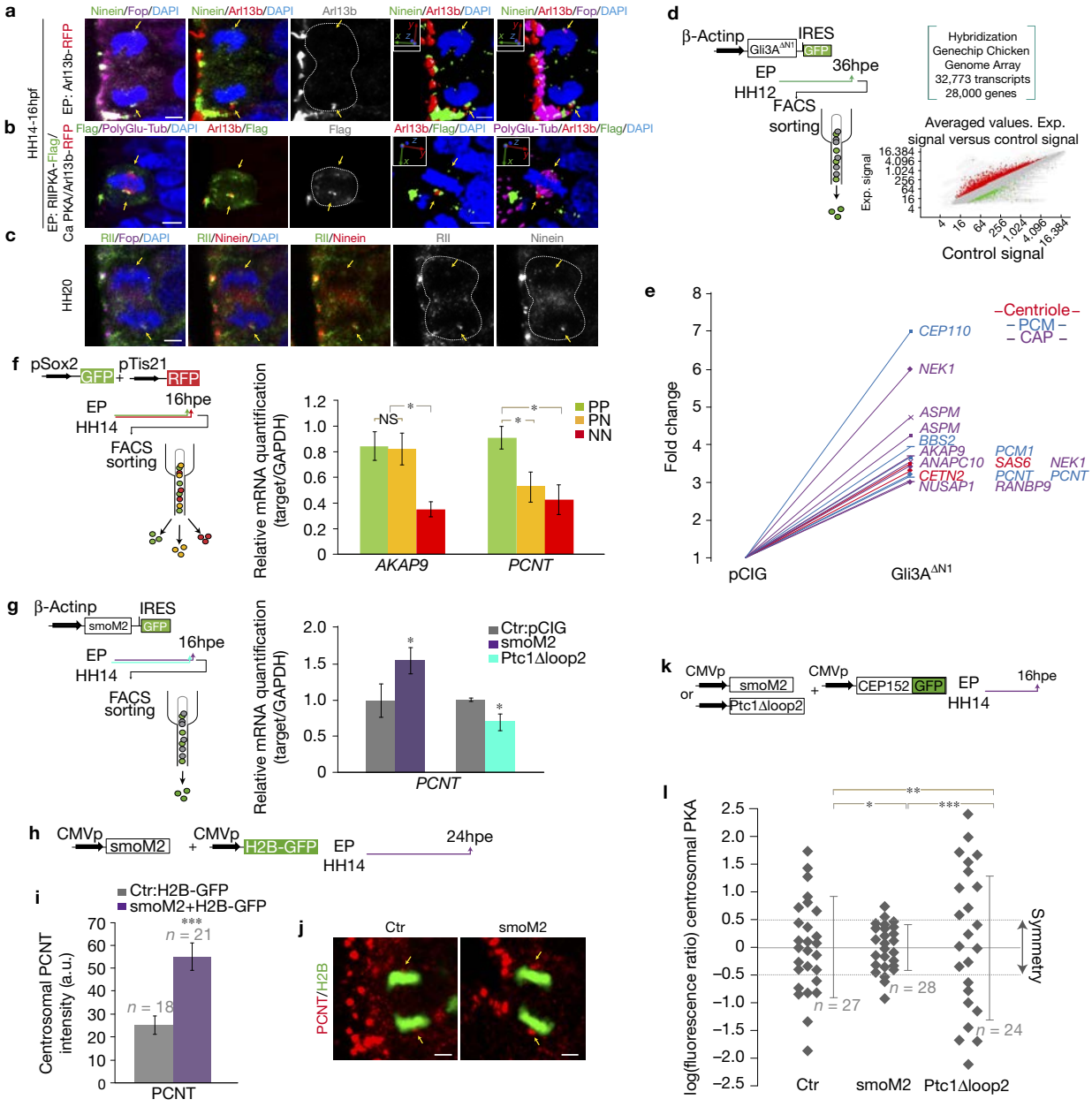

Figure 7 Shh signalling regulates pericentrin expression. (**a**) Asymmetric recruitment of Arl13b-RFP (red) to the mature centrosome identified by the expression of Ninein (green). Anti-FOP (purple) reveals centrosomes. (**b**) Asymmetric recruitment of PKA (green) to the mature centrosome, identified by the expression of Arl13b-RFP (red). Poly-glutamylated tubulin stains the mitotic spindle (purple). (**c**) Asymmetric recruitment of endogenous PKA (green) to the mature centrosome, identified by the expression of Ninein (red). Anti-FOP (purple) reveals centrosomes, DAPI (blue) stains the chromosomes and the yellow arrows point to the centrosomes (scale bars, 5 μm). (**d**) Scheme representing the electroporation experiments at HH12 with the Shh-activator in which the transfected cells expressing GFP were FACs sorted, and their RNA was extracted and hybridized to full genome AFFYMETRIX genechips. (**e**) Centrosome-associated proteins were among the genes differentially expressed in Shh-GOF-GFP cell populations: centriole-associated proteins in red; pericentriolar material (PCM) proteins in blue; centrosome-associated proteins (CAP) in purple ($n=12$ embryos per condition; three independent experiments; two-sided unpaired t-test; $^{**}P<0.01$, $^{***}P<0.001$). (**f**) Scheme showing the sorting of cells co-electroporated with the pSox2:eGFP and pTis21:RFP reporters. PCR analysis of the *AKAP9* and *PCNT* transcripts expressed in the three cell populations (three independent experiments; one-way ANOVA; $^{*}P<0.05$). (**g**) Scheme showing the electroporation at HH14 in which the GFP transfected cells were FACs sorted 16hpe to analyse Shh-regulated gene expression by PCR analysis (three independent experiments; Mann–Whitney U test; $^{*}P<0.05$) (plots show the mean ± s.e.m., 25.000 cells from $n=8$ independent embryos, 5 biological replicates). (**h**) Scheme showing the DNAs electroporated. (**i**) Plots the fluorescence intensity of endogenous PCNT associated to centrosomes in dividing cells (control mean ± s.e.m. = 25 ± 4, $n=18$ mitoses; SmoM2 mean ± s.e.m. = 55 ± 6, $n=21$ mitoses, three independent experiments; Mann–Whitney U test; $^{***}P<0.001$). (**j**) Centrosomal recruitment of endogenous PCNT (red), H2B-GFP (green) stains the chromosomes and the yellow arrows point to the centrosomes (scale bars, 5 μm). (**k**) Scheme showing the DNAs electroporated. (**l**) Plots of the ratio of fluorescence intensity between the two centrosomes at individual mitoses, where the lines and error bars correspond to the median ± s.d.; three independent experiments; one-way ANOVA; $^{*}P<0.05$, $^{**}P<0.01$. SmoM2 enhances the symmetric distribution of PKA (control 48% symmetry/ 52% asymmetry, $n=27$ mitoses; SmoM2 75% symmetry/ 25% asymmetry, $n=28$ mitoses; Ptc1Δloop2 25% symmetry/ 75% asymmetry, $n=24$ mitoses). Images are representative of three independent experiments.

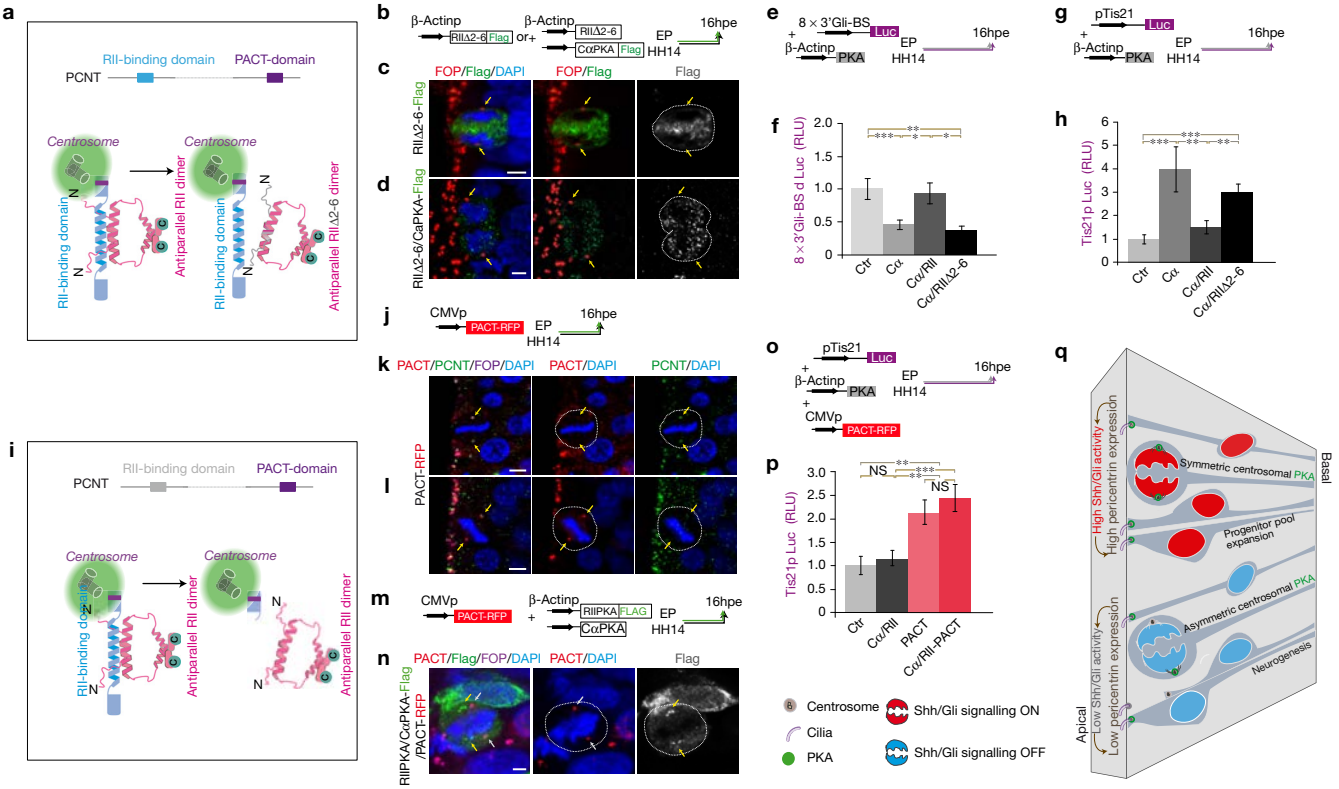

Figure 8 Pericentrin-mediated PKA docking to the centrosomes is necessary for Shh/Gli activation and inhibition of neurogenesis. (**a**) Scheme showing the pericentrin (PCNT) protein. PCNT binds to centrosomes through the conserved PACT domain. PCNT binds RII-PKA through the conserved RII-binding domain. RII-PKA binds Cα-PKA to inhibit the kinase activity of the enzyme. A mutant version of RII-PKAΔ2-6 dimerizes and binds to Cα-PKA, but it impairs binding to PCNT. (**b**) Scheme showing the cDNAs electroporated. (**c**) Images of RIIΔ2-6-PKA electroporation show that RII-PKA (green) does not associate with FOP-labelled centrosomes (yellow arrows). (**d**) Images of RIIΔ2-6-PKA+Cα-PKA co-electroporation showing that Cα-PKA (green) does not associate with centrosomes (yellow arrows). DAPI (blue) stains the chromosome plates (scale bars, 5 μm). (**e**) Scheme showing the cDNAs electroporated. (**f**) Quantification of the Luc/Renilla activity of the Gli-BS-Luc reporter (plot shows the mean ± s.e.m., $n=8$ embryos per condition; three independent experiments; one-way ANOVA; $^{*}P<0.05$; $^{**}P<0.01$; $^{***}P<0.001$). (**g**) Scheme showing the cDNAs electroporated. (**h**) Quantification of the Luc/Renilla activity of the pTis21-Luc reporter (plot shows the mean ± s.e.m., $n=8$ embryos per condition; three independent experiments; one-way ANOVA; $^{**}P<0.01$; $^{***}P<0.001$). (**i**) Scheme showing the mutant PCNT protein that binds to, and displaces RII-PKA from the centrosomes. (**j**) Scheme showing the cDNAs electroporated. (**k**) In the absence of PACT (red), PCNT (green) associate with the centrosomes (purple, yellow arrows). (**l**) In the presence of PACT (red), PCNT (green) was absent from the centrosomes (yellow arrows.) DAPI (blue) stains the chromosome plates (scale bars, 5 μm). (**m**) Scheme showing the cDNAs electroporated. (**n**) In the presence of PACT (red), PKA (green, yellow arrows) was absent from the centrosomes (white arrows.) DAPI (blue) stains the chromosome plates (scale bars, 5 μm). (**o**) Scheme showing the cDNAs electroporated. (**p**) Quantification of the Luc/Renilla activity of the pTis21-Luc reporter after electroporation of the DNAs indicated (plots show the mean ± s.e.m., $n=8$ embryos per condition; three independent experiments; one-way ANOVA; $^{**}P<0.01$; $^{***}P<0.001$). (**q**) Scheme neuroepithelial cells in which high Shh/Gli activity (red) increases PCNT expression, thereby promoting symmetric centrosomal docking of PKA. In turn, this maintains Shh activity high, and therefore contributes to the expansion of the progenitor pool through symmetric PP divisions. In dividing neuroepithelial cells with weak Shh/Gli activity (blue), the intrinsic centrosomal asymmetry drives neurogenesis. Images are representative of three independent experiments.

centrosomal docking of PKA was sufficient to promote neurogenesis. Indeed, depletion of PCNT in neuroepithelial cells reduces progenitor cell number in the ventricular zone of the developing mouse neocortex, while augmenting the differentiated cells in the cortical plate[42]. The importance of centrosomes in brain development is further highlighted in primary microcephalies, a group of diseases involving a dramatically reduced cell number in the brain at birth. Unexpectedly, all primary microcephaly proteins are ubiquitous and they localize to centrosomes for at least part of the cell cycle. Hence, the centrosome would appear to be a hub for the integration of many regulatory pathways affecting prenatal neurogenesis[43,44].

Centrosome function might also affect the final orientation of the metaphase plate during mitosis. Consequently, minor changes in spindle orientation determine whether the cleavage plane bisects or bypasses the small apical domain in dividing neural progenitors. Dividing neural progenitors with strong Shh/Gli activity more frequently establish symmetric cleavage planes than Gli-negative cells, consistent with previous reports where strong Tis21 expression was associated with more frequent asymmetric cleavage planes and, hence, neurogenic divisions[26,45]. However, in the mouse cortex and chick spinal cord, disrupting the cortical effectors of spindle orientation (Gαi, LGN, or NuMA) randomizes spindle orientation; although contrary to the prediction of the model this did not accelerate neurogenesis[46]. Whether the distribution of the apical domain has an instructive role on the fate of the daughter cells is currently unclear[46]. Nevertheless, progenitors committed to differentiate already express neuronal markers, such as class III beta-tubulin, apparently maintaining at least part of the apical AJs and the capacity

to re-organize a primary cilium[47]. Final neuron detachment from the ventricle and withdrawal from the proliferative neuroepithelia is dependent on actin–myosin contraction, which involves the abscission of the apical cell-membrane and dismantling of the primary cilium[47].□

METHODS

Methods, including statements of data availability and any associated accession codes and references, are available in the online version of this paper.

Note: Supplementary Information is available in the online version of the paper

ACKNOWLEDGEMENTS

The authors are indebted to E. Rebollo for her invaluable technical assistance at the AFMU Facility (IBMB). For providing DNAs, we thank S. McKnight (University of Washington, USA), M. Uchikawa (Osaka University, Japan), M. Götz (Ludwig-Maximilians-University Munich, Germany), H. Lickert (GmbH, ISF, Neuherberg, Germany) and S. Pons (IBMB-CSIC). For providing antibodies, we also thank O. Rosnet (CRCM, Marseille, France), M. Bornens (Institut Curie, Paris, France) and S. Pons (IBMB-CSIC). The monoclonal antibodies were obtained from the Developmental Studies Hybridoma Bank, developed under the auspices of the NICHD and maintained by The University of Iowa, Department of Biological Sciences, Iowa City, Iowa 52242. The work in E.M.'s laboratory was supported by grants BFU2013-46477-P and BFU2014-55738-REDT.

AUTHOR CONTRIBUTIONS

M.S. conceived and performed most experiments, analysed the data and discussed results. E.G.-G. contributed to image acquisition, image analysis and quantification, and statistics. R.E. performed the luciferase experiments. S.U. provided technical support to all experiments. E.M. conceived experiments, analysed the data, discussed results and wrote the manuscript.

COMPETING FINANCIAL INTERESTS

The authors declare no competing financial interests.

Published online at http://dx.doi.org/10.1038/ncb3512
Reprints and permissions information is available online at www.nature.com/reprints
Publisher's note: Springer Nature remains neutral with regard to jurisdictional claims in published maps and institutional affiliations.

1. Cajal, R.y. *Textura del Sistema Nervioso del Hombre y de los Vertebrados* Ch. XXI (Nicolás Moya, 1899).
2. Gotz, M. & Huttner, W. B. The cell biology of neurogenesis. *Nat. Rev. Mol. Cell Biol.* **6,** 777–788 (2005).
3. Lui, J. H., Hansen, D. V. & Kriegstein, A. R. Development and evolution of the human neocortex. *Cell* **146,** 18–36 (2011).
4. Franco, S. J. *et al.* Fate-restricted neural progenitors in the mammalian cerebral cortex. *Science* **337,** 746–749 (2012).
5. Franco, S. J. & Muller, U. Shaping our minds: stem and progenitor cell diversity in the mammalian neocortex. *Neuron* **77,** 19–34 (2013).
6. Delattre, M. & Gonczy, P. The arithmetic of centrosome biogenesis. *J. Cell Sci.* **117,** 1619–1630 (2004).
7. Nigg, E. A. & Raff, J. W. Centrioles, centrosomes, and cilia in health and disease. *Cell* **139,** 663–678 (2009).
8. Reina, J. & Gonzalez, C. When fate follows age: unequal centrosomes in asymmetric cell division. *Phil. Trans. R. Soc. B* **369,** 20130466 (2014).
9. Wang, X. *et al.* Asymmetric centrosome inheritance maintains neural progenitors in the neocortex. *Nature* **461,** 947–955 (2009).
10. Paridaen, J. T., Wilsch-Brauninger, M. & Huttner, W. B. Asymmetric inheritance of centrosome-associated primary cilium membrane directs ciliogenesis after cell division. *Cell* **155,** 333–344 (2013).
11. Saade, M. *et al.* Sonic hedgehog signaling switches the mode of division in the developing nervous system. *Cell Rep.* **4,** 492–503 (2013).
12. Lai, K., Kaspar, B. K., Gage, F. H. & Schaffer, D. V. Sonic hedgehog regulates adult neural progenitor proliferation *in vitro* and *in vivo*. *Nat. Neurosci.* **6,** 21–27 (2003).
13. Machold, R. *et al.* Sonic hedgehog is required for progenitor cell maintenance in telencephalic stem cell niches. *Neuron* **39,** 937–950 (2003).
14. Briscoe, J. Making a grade: sonic Hedgehog signalling and the control of neural cell fate. *EMBO J.* **28,** 457–465 (2009).
15. Cayuso, J., Ulloa, F., Cox, B., Briscoe, J. & Marti, E. The Sonic hedgehog pathway independently controls the patterning, proliferation and survival of neuroepithelial cells by regulating Gli activity. *Development* **133,** 517–528 (2006).
16. Wong, W. & Scott, J. D. AKAP signalling complexes: focal points in space and time. *Nat. Rev. Mol. Cell Biol.* **5,** 959–970 (2004).
17. Le Dreau, G., Saade, M., Gutierrez-Vallejo, I. & Marti, E. The strength of SMAD1/5 activity determines the mode of stem cell division in the developing spinal cord. *J. Cell Biol.* **204,** 591–605 (2014).
18. Briscoe, J. & Therond, P. P. The mechanisms of Hedgehog signalling and its roles in development and disease. *Nat. Rev. Mol. Cell Biol.* **14,** 416–429 (2013).
19. Niewiadomski, P. *et al.* Gli protein activity is controlled by multisite phosphorylation in vertebrate Hedgehog signaling. *Cell Rep.* **6,** 168–181 (2014).
20. Dzhindzhev, N. S. *et al.* Asterless is a scaffold for the onset of centriole assembly. *Nature* **467,** 714–718 (2010).
21. Yan, X., Habedanck, R. & Nigg, E. A. A complex of two centrosomal proteins, CAP350 and FOP, cooperates with EB1 in microtubule anchoring. *Mol. Biol. Cell* **17,** 634–644 (2006).
22. Nigg, E. A., Schafer, G., Hilz, H. & Eppenberger, H. M. Cyclic-AMP-dependent protein kinase type II is associated with the Golgi complex and with centrosomes. *Cell* **41,** 1039–1051 (1985).
23. Vandame, P. *et al.* The spatio-temporal dynamics of PKA activity profile during mitosis and its correlation to chromosome segregation. *Cell Cycle* **13,** 3232–3240 (2014).
24. Barzi, M., Berenguer, J., Menendez, A., Alvarez-Rodriguez, R. & Pons, S. Sonic-hedgehog-mediated proliferation requires the localization of PKA to the cilium base. *J. Cell Sci.* **123,** 62–69 (2010).
25. Tuson, M., He, M. & Anderson, K. V. Protein kinase A acts at the basal body of the primary cilium to prevent Gli2 activation and ventralization of the mouse neural tube. *Development* **138,** 4921–4930 (2011).
26. Marthiens, V. & ffrench-Constant, C. Adherens junction domains are split by asymmetric division of embryonic neural stem cells. *EMBO Rep.* **10,** 515–520 (2009).
27. Sabherwal, N. *et al.* The apicobasal polarity kinase aPKC functions as a nuclear determinant and regulates cell proliferation and fate during Xenopus primary neurogenesis. *Development* **136,** 2767–2777 (2009).
28. Lesage, B., Gutierrez, I., Marti, E. & Gonzalez, C. Neural stem cells: the need for a proper orientation. *Curr. Opin. Genet. Dev.* **20,** 438–442 (2010).
29. Brand, A. H. & Livesey, F. J. Neural stem cell biology in vertebrates and invertebrates: more alike than different? *Neuron* **70,** 719–729 (2011).
30. Morin, X. & Bellaiche, Y. Mitotic spindle orientation in asymmetric and symmetric cell divisions during animal development. *Dev. Cell* **21,** 102–119 (2011).
31. Cruz, C. *et al.* Foxj1 regulates floor plate cilia architecture and modifies the response of cells to sonic hedgehog signalling. *Development* **137,** 4271–4282 (2010).
32. Rabadan, M. A. *et al.* Jagged2 controls the generation of motor neuron and oligodendrocyte progenitors in the ventral spinal cord. *Cell Death Differ.* **19,** 209–219 (2012).
33. Gillingham, A. K. & Munro, S. The PACT domain, a conserved centrosomal targeting motif in the coiled-coil proteins AKAP450 and pericentrin. *EMBO Rep.* **1,** 524–529 (2000).
34. Hausken, Z. E., Dell'Acqua, M. L., Coghlan, V. M. & Scott, J. D. Mutational analysis of the A-kinase anchoring protein (AKAP)-binding site on RII. Classification Of side chain determinants for anchoring and isoform selective association with AKAPs. *J. Biol. Chem.* **271,** 29016–29022 (1996).
35. Peterson, K. A. *et al.* Neural-specific Sox2 input and differential Gli-binding affinity provide context and positional information in Shh-directed neural patterning. *Genes Dev.* **26,** 2802–2816 (2012).
36. Nishi, Y. *et al.* A direct fate exclusion mechanism by Sonic hedgehog-regulated transcriptional repressors. *Development* **142,** 3286–3293 (2015).
37. Cohen, M., Kicheva, A. & Ribeiro, A. Ptch1 and Gli regulate Shh signalling dynamics via multiple mechanisms. *Nat. Commun.* **6,** 6709 (2015).
38. Epstein, D. J., Marti, E., Scott, M. P. & McMahon, A. P. Antagonizing cAMP-dependent protein kinase A in the dorsal CNS activates a conserved Sonic hedgehog signaling pathway. *Development* **122,** 2885–2894 (1996).
39. Marti, E., Bumcrot, D. A., Takada, R. & McMahon, A. P. Requirement of 19K form of Sonic hedgehog for induction of distinct ventral cell types in CNS explants. *Nature* **375,** 322–325 (1995).
40. Marti, E., Takada, R., Bumcrot, D. A., Sasaki, H. & McMahon, A. P. Distribution of Sonic hedgehog peptides in the developing chick and mouse embryo. *Development* **121,** 2537–2547 (1995).
41. Stamataki, D., Ulloa, F., Tsoni, S. V., Mynett, A. & Briscoe, J. A gradient of Gli activity mediates graded Sonic Hedgehog signaling in the neural tube. *Genes Dev.* **19,** 626–641 (2005).
42. Buchman, J. J. *et al.* Cdk5rap2 interacts with pericentrin to maintain the neural progenitor pool in the developing neocortex. *Neuron* **66,** 386–402 (2010).
43. Thornton, G. K. & Woods, C. G. Primary microcephaly: do all roads lead to Rome? *Trends Genet.* **25,** 501–510 (2009).
44. Alkuraya, F. S. *et al.* Human mutations in NDE1 cause extreme microcephaly with lissencephaly [corrected]. *Am. J. Hum. Genet.* **88,** 536–547 (2011).
45. Kosodo, Y. *et al.* Asymmetric distribution of the apical plasma membrane during neurogenic divisions of mammalian neuroepithelial cells. *EMBO J.* **23,** 2314–2324 (2004).
46. Peyre, E. & Morin, X. An oblique view on the role of spindle orientation in vertebrate neurogenesis. *Dev. Growth Differ.* **54,** 287–305 (2012).
47. Das, R. M. & Storey, K. G. Apical abscission alters cell polarity and dismantles the primary cilium during neurogenesis. *Science* **343,** 200–204 (2014).

DOI: 10.1038/ncb3512

METHODS

Chick embryos. Eggs from white Leghorn chickens were staged according to the method of Hamburger and Hamilton[48]. *In ovo* electroporation was performed at stage HH14 (54 h post fertilization -hpf-, 22 somite stage) unless otherwise indicated, and the embryos were recovered at the times stipulated (12–72 hpf). Embryos were electroporated with Clontech purified plasmid DNA (2–3 $\mu g\,ml^{-1}$ in H_2O) with Fast Green (50 $ng\,ml^{-1}$). Briefly, the plasmid DNA was injected into the NT lumen and electrodes were placed either side of the embryo to perform electroporation using an Intracel Dual Pulse (TSS10) electroporator, delivering five 50 ms pulses of 20–30 V (ref. 11). Sex is not identified at these stages. No cell lines were used in this study. According to EU animal care guidelines, no IACUC approval was necessary to perform the chick embryo experiments, since the embryos used in this study were all in early stages of embryonic development (between E2 and E3).

DNA constructs. CEP152-GFP (50 $ng\,\mu l^{-1}$: Origene, Clinisciences), encoding a centriolar component required for centriole duplication (ref. 20), was electroporated to label the centrosome. Arl13b-RFP, encoding the ciliary membrane component Arl13b (ref. 49) (50 $ng\,\mu l^{-1}$) was electroporated to label the primary cilia membrane. Full-length cDNAs of mouse CαPKA, RII-PKA and the mutant RIIΔ-6 PKA[24,34] were tagged by PCR and cloned into the pCAGGS_ires_H2B: GFP (pCIG) vector. Full-length Smoothened-HA and HA-Gli were generated by PCR and cloned into the PCS2+ vector. These constructs were electroporated at 0.5 $ng\,\mu l^{-1}$ to track the subcellular distribution of Shh signalling components, without affecting Shh activity. PACT-RFP[33] (0,5 $\mu g\,ml^{-1}$) was electroporated to address PCNT function.

For Luciferase experiments (shown in Supplementary Fig. 1c), PKA constructs were electroporated at 200 $ng\,\mu l^{-1}$ and the inhibition of Shh activity was achieved by overexpressing a mutant form of Patched1 (mPtc1Δloop2, 0.5 $ug\,\mu l^{-1}$: ref. 50). A mutant version of Smoothened (SmoM2: ref. 51) and PKA-R1 (dnPKA: ref. 38) were used (0.7 $ug\,\mu l^{-1}$) to over-activate Shh signalling, as described previously[11,15].

The pTis21:RFP and pTis21:luc reporter were generated by inserting a fragment of the promoter of the mouse Tis21 gene (−442 to 65) into the ptk:RFP and ptk:Luciferase plasmids, respectively, as described elsewhere[11]. The pSox2:EGFP reporter consisted of an EGFP cassette from the ptk2:EGFP plasmid under the control of a fragment of the chicken Sox2 promoter covering 7.6–14 kb of the Sox2 locus[11,52]. Endogenous Shh/Gli activity was assessed using reporter constructs encoding H2B-RFP or luciferase under the control of a promoter containing synthetic 8 × 3′ Gli-BS[11,53].

Immunohistochemistry and microscopy. Embryos were fixed in 4% PFA for 2 h at 4 °C, and immunostaining was performed on vibratome sections (40 µm) following standard procedures. After washing in PBS/0.1% Triton X-100, the sections were incubated with the appropriate primary antibodies (Supplementary Table 2): 1:500 rabbit anti-olig2 (AB9610, Millipore); 1:500 mouse anti-islet1 (402D6, DSHB); 1:500 mouse anti-alpha tubulin (T6199, Sigma); 1:500 mouse anti-aPKC (SC17781-H1, Santa Cruz); 1:1,000 rat anti-N-cadherin (13-2100, Zymed); 1:100 anti-PCNT (AB4448, Abcam); 1:100 anti-Cα-PKA (47825, Cell Signalling Technologies); 1:2,000 rabbit anti-FOP (FGFR1 Oncogene Partner[54]); 1:100 anti-RIIb-PKA (610625, BD Biosciences); 1:10 rabbit anti-Ninein (kindly provided by M. Bornens); 1:2,000 rabbit anti-HA, 1:2,000 rabbit anti-Flag, 1:2,000 mouse anti-Flag and 1:1,000 rat anti-RFP (kindly provided by S. Pons). Alexa Fluor 488, 555 or 633 secondary antibodies were used (Molecular Probes). Sections were stained with 1 $\mu g\,ml^{-1}$ DAPI and mounted in Mowiol (Sigma-Aldrich). Images were acquired at room temperature on a Zeiss LSM-780 confocal microscope system using 25× (Plan-Apochromat 25×/0.8 ImmKorr DIC M27), 40× (Plan-Apochromat 40×/1.3 Oil DIC M27) or 63× (Plan-Apochromat 63×/1.4 Oil DIC M27) lenses. Images were processed in Photoshop CS5 and Illustrator CS4 (Adobe) to merge and resize the images.

Quantification of centrosomal PKA in mitotic cells. The intensity of centrosomal PKA staining was quantified in mitotic progenitors restricted to the ventral part of the NT. HH10 or HH14 embryos were electroporated with PKA subunits (one of the two Flag-tagged), in combination with either the CEP152-GFP, 8 × 3′ Gli-BS-RFP or pTis21-RFP reporters. The NT was recovered at 16 h post-electroporation (hpe), and processed for immunohistochemistry using the rabbit anti-FOP and the mouse or rabbit anti-Flag antibodies.

To calculate the index of symmetry in dividing cells from fixed data, a *z*-projection (0.5 µm spaced optical sections) of the entire mitotic cell was acquired with a confocal microscope (Zeiss LSM-780) and analysed using the ImageJ software. To quantify centrosomal Cα-PKA (Flag-tagged) and RII-PKA (Flag-tagged), the average pixel intensity of Flag staining at (or closely associated with) each centrosome within identical areas (centrosomal fraction) was taken (minus cytosolic Flag staining = non-centrosomal fraction). The ratio of the average intensity of centrosomal Cα-PKA and RII-PKA was calculated according to the dorso-ventral or apico-basal orientation of the centrosome axis in each mitotic cell (with respect to the neural tube lumen). The same analysis was performed to quantify the centrosomal Cα-PKA (Flag-tagged) and RII-PKA (Flag-tagged). When the centrosomal PKA presents a logarithmic value outside of the CEP152 symmetric window it was considered as an asymmetric distribution. Three-dimensional (3D) reconstructed views of the mitotic cells carrying symmetric or asymmetric centrosomal PKA were built from lateral or frontal views of *z*-stacks using the Volocity software, and 5–9 different images of at least 8 different embryos per experimental condition were used for quantification. The data are represented as the ratio of fluorescence intensity between the two centrosomes/mitosis median value ± s.e.m.

Prediction of cleavage plane positioning and the partitioning of Adherens Junction microdomains. To define the inheritance of the apical membrane in mitotic cells, HH14 embryos were co-electroporated with the Gli-BS-RFP reporter together with the pCS2-GFP (as a control of electroporation). The 16 hpe NT was stained for N-cadherin (cadherin–catenin complex marker), aPKC (apical marker) and FOP (centrosomal marker). Only cells in anaphase/telophase were analysed, since the mitotic spindle stops rotating at the end of metaphase in the ventral NT[55,56]. Consecutive optical sections of mitotic cells (3–5), with a 0.5 µm step size (1.5–2.5 µm depth for the stack), were obtained by confocal laser scanning using a ×63 objective lens with a zoom factor of 4. Only mitoses where the two chromosome plates show the same shape in the 3–5 consecutive optical sections were accepted for further analysis. The cleavage plane was deduced from the orientation of two rectangles designed to fit the DNA staining of the sister chromatids[26,45]. When the rectangles were oriented parallel to each other, the cleavage plane was positioned half way in between the rectangles (d1 = d2). When the rectangles were oriented at an angle to each other, the cleavage plane was positioned such that this angle was halved (a1 = a2)[26,45]. In cases where a centrosomal marker was added, the centrosome position always gave a 90° angle to the cleavage plane, confirming the orientation of the cell division axis.

In anaphase/telophase mitosis, the cleavage furrow was identified by N-cadherin staining (marker of cell shape), ingressing from basal to apical[57]. The position of the cleavage furrow about to fuse with the apico-lateral plasma membrane, and relative to the cadherin hole, was used to predict bypass or bisection of the apical membrane[26,45]. To obtain an integral view of the 'cadherin hole', 3D reconstructed views were built from lateral or frontal views of *z*-stacks using the Velocity software.

To quantify the amount of aPKC fluorescence in each presumptive membrane territory, the 1.5–2.5 µm stack of 3–5 consecutive confocal sections showing the position of the two centrosomes and with the same chromosome morphologies was projected as a sum of pixels, and the fluorescence intensity was evaluated in the sum-projected image with the integrated density function of the Image J software. The comparison of fluorescence intensities in the two presumptive membrane territories was expressed as the ratio of the sum of pixel values (ratio of fluorescence intensities, Rfi)—that is, the integrated density. The distribution of the ratios was depicted for each population ($H2B^{-}GFP^{+}/RFP^{-}$ and $H2B^{-}GFP^{+}/RFP^{+}$) and the medians were calculated to compare the distribution in the different populations: 5–9 different images from at least eight different embryos were quantified per experimental condition, and the data were represented as the median Rfi ratio ± s.e.m.

Flow cytometry. HH14 embryos were recovered 16–20 h after co-electroporation with the DNAs indicated. Cell suspensions were obtained from pools of 6–8 NTs after digestion with trypsin-EDTA (10–15 min: Sigma-Aldrich) and they were further processed on a cell sorter (FACS Aria III; BD) for EGFP and RFP fluorescence. At least 25,000 cells for each progenitor cell population were sorted and the data are presented as the mean ± s.e.m. from 4–5 cell pools per experimental condition.

Real-time PCR. Total RNA extracts were obtained following the TRIZOL protocol (Invitrogen) from subpopulations of GFP^{+}/RFP^{-} (PP), GFP^{+}/RFP^{+} (PN), and GFP^{-}/RFP^{+} (NN) cells, segregated and purified by FACS (25,000 cells per pool after co-electroporation of pSox2-GFP/pTis21-RFP). RNAs were also extracted from sorted GFP^{+} populations electroporated with SmoM2, dnPKA, mPtc1Δloop2 or the control empty vector pCIG (25,000 cells). Reverse transcription and real-time PCR were performed according to the manufacturer's instructions (Roche) using a lightcycler (LC 480; Roche). Specific primers for quantitative PCR amplification of PCNT were purchased (QT00662683; QIAGEN) and AKAP9 primer sequences were as follows: forward, 5′-AGGCATTCCTATAGATCCCG-3′; reverse, 5′-GCTCTTTC TGGATCATAGTTCTG-3′. Oligonucleotides specific for chick GAPDH were used for normalization: forward, 5′-CGATCTGAACTACATGGTTTAC-3′ ; reverse, 5′-ATCACAAGTTTCCCGTTCTC-3′. All experimental values were normalized to those obtained for GAPDH and PCR amplifications were assessed from 5 independent cell pools for each experimental condition (biological replicates). The data are expressed in arbitrary units and represent the mean standardized values ± s.e.m.

Luciferase reporter assay. The endogenous Shh/Gli activity was assessed in the NT with the 8 × 3′ GBSs-Luc vector. The activity of Tis21 was assessed in the

NT using the pTis21-Luc vector. Both reporters were co-electroporated with a renilla luciferase reporter construct carrying the cytomegalovirus immediate early enhancer promoter for normalization (Promega). NTs obtained at 16–20 hpe were processed following the Dual Luciferase Reporter Assay protocol (Promega), as described previously[11]. The data are presented as the mean ± s.e.m. from 10–12 embryos per experimental condition (biological replicates).

Microarray analysis of neural progenitors responding to different levels of Shh activity. Plasmid DNA encoding either green fluorescence protein (GFP) alone, or an activated version of Gli3 (Gli3ΔN1 aa 289–1580) were inserted into pCAGGS vector for *in vivo* electroporation into HH11-12 stage embryos[58]. Neural tubes were dissected out at 14 or 36 h later, and single-cell suspension was obtained by 10–15 min incubation on Trypsin-EDTA (Sigma-Aldrich). GFP fluorescence was determined by flow cytometry using a MoFlo flow cytometer (DakoCytomation, Fort Collins). The resulting cell population, consisting of ∼90% of GFP+ cells, was used for total RNA extraction. GeneChip Chicken Genome Arrays (Affymetrix) containing 32,773 chicken transcripts were used for the hybridization of the samples. Unpaired analysis of the data, based on the comparison between the average values of the logRed and logGreen intensities, was performed using SOLAR System v2.0 (Alma Bioinformatics). Results were filtered using unpaired *t*-tests using thresholds of >2-fold change and *P* value <0.01, <0.001 (Supplementary Table 3). Microarray data are available from ArrayExpress with accession E-MEXP-2212. Results have been published elsewhere[31,32].

Bioinformatic analyses of PCNT sequence homology. The *Gallus gallus* Pericentrin (PCNT) homologues (AIU68823) was identified by a reciprocal best-hits BLAST search starting with the isoform 2 of *Homo sapiens* PCNT (NP_001302458) and the isoform a of *Mus musculus* PCNT (NP_032813) protein sequence. Homology protein alignments were carried out using Clustal Omega (http://www.ebi.ac.uk/Tools/msa/clustalo (refs 59,60)). The PACT coiled-coil conserved domain was detected in the corresponding protein sequences using CD-search[61] with a high significant E-value in *Gallus gallus* ($E = 1.44 \times 10^{-22}$) and *Homo sapiens* ($E = 1.15 \times 10^{-26}$) versus $E = 7.12 \times 10^{-27}$ in *Mus musculus*. The PCNT-specific RII-binding domain was determined according to Diviani *et al.*, 2000. The cluster of leucine, shown by site directed mutagenesis to be the specific PKA-anchoring determinant, is highly conserved between the three species (highlighted in blue in Supplementary Fig. 5b).

Statistics and reproducibility. No statistical method was used to predetermine sample size. Quantitative data are expressed as mean or median ± s.e.m. or s.d. All experiments were carried out three independent times, except for Supplementary Fig. 3L in which we quantified divisions from six independent embryos. No samples were excluded from the analysis. All images are representative of three independent experiments.

Statistical analysis was performed using the GraphPad prism6. Each exact *n* value is indicated in the corresponding figure legend. Significance was assessed by performing the Mann–Whitney U test, one-way ANOVA followed by the Student–Newman–Keuls test and an unpaired two-sided Student's *t*-test (NS, $^{*}P < 0.05$, $^{**}P < 0.01$, and $^{***}P < 0.001$), as indicated in individual figures. The experiments were not randomized. The investigators were not blinded to allocation during experiments and outcome assessment.

Data availability. Previously published microarray data that were re-analysed here are available from ArrayExpress with accession E-MEXP-2212 (refs 31,32). All additional data supporting the findings of this study are available from the corresponding author upon reasonable request.

48. Hamburger, V. & Hamilton, H. L. A series of normal stages in the development of the chick embryo. *J. Morphol.* **88,** 49–92 (1951).
49. Caspary, T., Larkins, C. E. & Anderson, K. V. The graded response to Sonic Hedgehog depends on cilia architecture. *Dev. Cell* **12,** 767–778 (2007).
50. Briscoe, J., Chen, Y., Jessell, T. M. & Struhl, G. A hedgehog-insensitive form of patched provides evidence for direct long-range morphogen activity of sonic hedgehog in the neural tube. *Mol. Cell* **7,** 1279–1291 (2001).
51. Hynes, M. *et al.* The seven-transmembrane receptor smoothened cell-autonomously induces multiple ventral cell types. *Nat. Neurosci.* **3,** 41–46 (2000).
52. Uchikawa, M., Ishida, Y., Takemoto, T., Kamachi, Y. & Kondoh, H. Functional analysis of chicken Sox2 enhancers highlights an array of diverse regulatory elements that are conserved in mammals. *Dev. Cell* **4,** 509–519 (2003).
53. Sasaki, H., Hui, C., Nakafuku, M. & Kondoh, H. A binding site for Gli proteins is essential for HNF-3β floor plate enhancer activity in transgenics and can respond to Shh *in vitro*. *Development* **124,** 1313–1322 (1997).
54. Acquaviva, C. *et al.* The centrosomal FOP protein is required for cell cycle progression and survival. *Cell Cycle* **8,** 1217–1227 (2009).
55. Haydar, T. F., Ang, E. Jr & Rakic, P. Mitotic spindle rotation and mode of cell division in the developing telencephalon. *Proc. Natl Acad. Sci. USA* **100,** 2890–2895 (2003).
56. Roszko, I., Afonso, C., Henrique, D. & Mathis, L. Key role played by RhoA in the balance between planar and apico-basal cell divisions in the chick neuroepithelium. *Dev. Biol.* **298,** 212–224 (2006).
57. Kosodo, Y. *et al.* Cytokinesis of neuroepithelial cells can divide their basal process before anaphase. *EMBO J.* **27,** 3151–3163 (2008).
58. Stamataki, D., Ulloa, F., Tsoni, S. V., Mynett, A. & Briscoe, J. A gradient of Gli activity mediates graded Sonic Hedgehog signaling in the neural tube. *Genes Dev.* **19,** 626–641 (2005).
59. Sievers, F. *et al.* Fast, scalable generation of high-quality protein multiple sequence alignments using Clustal Omega. *Mol. Syst. Biol.* **7,** 539 (2011).
60. Goujon, M. *et al.* A new bioinformatics analysis tools framework at EMBL-EBI. *Nucleic Acids Res.* **38,** W695–W699 (2010).
61. Marchler-Bauer, A. *et al.* CDD: NCBI's conserved domain database. *Nucleic Acids Res.* **43,** D222–D226 (2015).

nature cell biology

DOI: 10.1038/ncb3512

In the format provided by the authors and unedited.

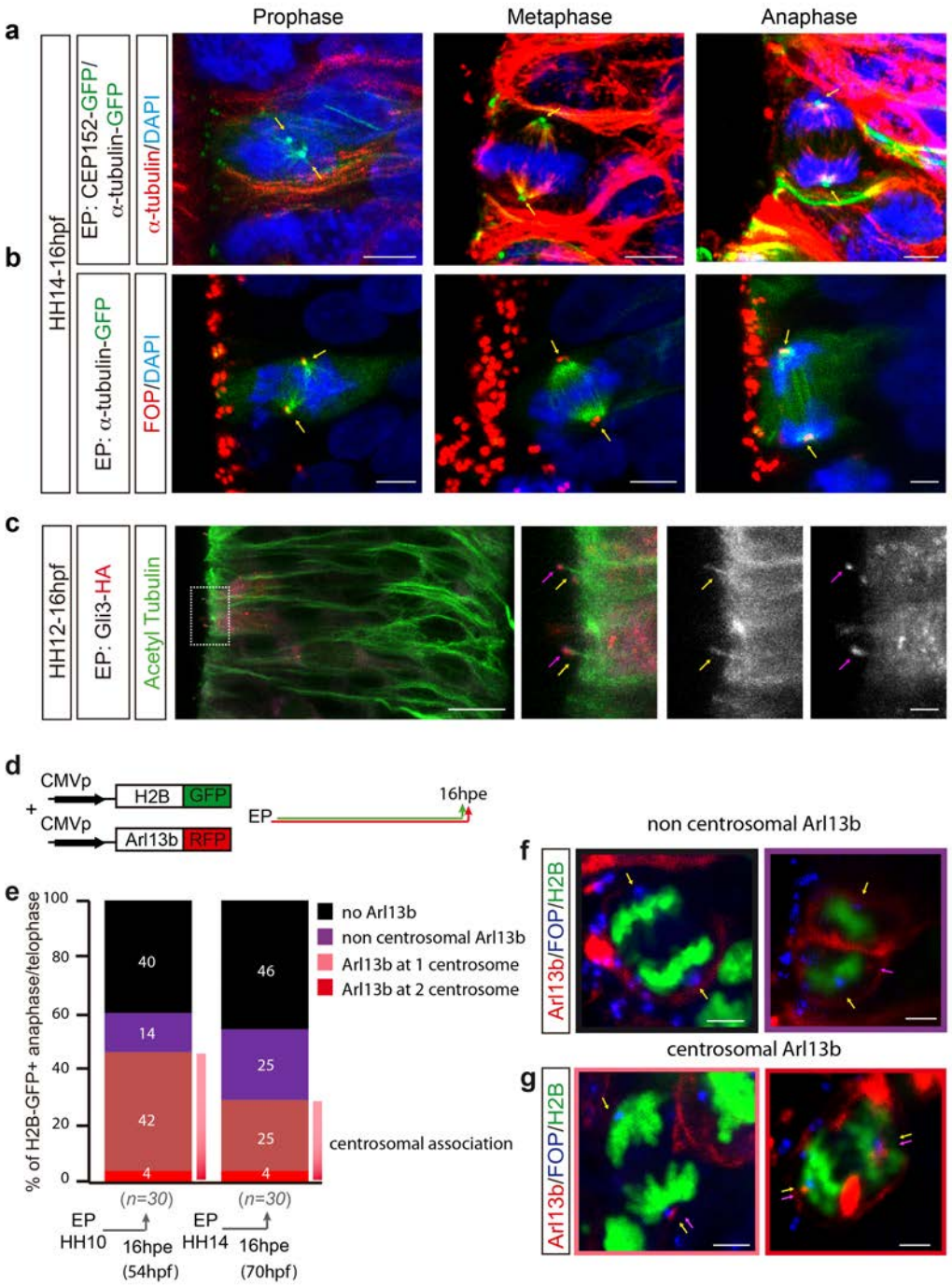

Supplementary Figure 1 In dividing neuroepithelial cells, the primary cilia was not completely disassembled prior to mitosis **(a)** Transient expression of CEP152-GFP in the chick NT after electroporation (HH14, 16 hours post electroporation, hpe) reliably labels the two centrosomes in dividing neural progenitors. CEP152-GFP (green) formed pairs of dots at the spindle poles during mitosis that co-localize with a-Tubulin-GFP (green) and that are immunostained with anti-α-Tubulin (red). DAPI (blue) stains the chromosomes (Scale bars 5μm).**(b)** α-Tubulin-GFP (green) electroporation labelled the mitotic spindle. Immunostaining with anti-FOP (FGFR1 Oncogene Partner, red) revealed the centrosome pairs lining the NT lumen, as well as the nucleating mitotic spindles (Scale bars 5μm). **(c)** Gli3-HA (red) localizes to the cilium tip (pink arrows) and the nucleus. Acetylated tubulin (green) stain the cilium shaft (yellow arrow) **(d)** Scheme showing the DNAs and timing of the co-electroporation (hpe=hours post electroporation)(Scale bars are 10μm and 2μm respectively). **(e)** Quantification of the subcellular Arl13b localization types as percentage of total anaphase/telophase H2B-GFP+ mitoses, at two developmental stages, showing that as neurogenesis progresses, the Arl13b-labelled ciliary remnant can lose its attachment to the old mother centriole during mitosis (HH10, n=30 mitoses; HH14 n=30 mitoses, from three independent experiments). **(f,g)** Selected images showing non-centrosomal (f) and centrosomal (g) Arl13b localization; H2B-GFP (green) labels chromosomes, anti-FOP (blue) revealed the centrosome pairs, Arl13b-RFP (red) labels the ciliary remnant. Yellow arrow shows centrosome localization (FOP+) and purple arrow shows ciliary remnant localization (Arl13b+) (Scale bars 5μm).[. Images are representative of three independent experiments.

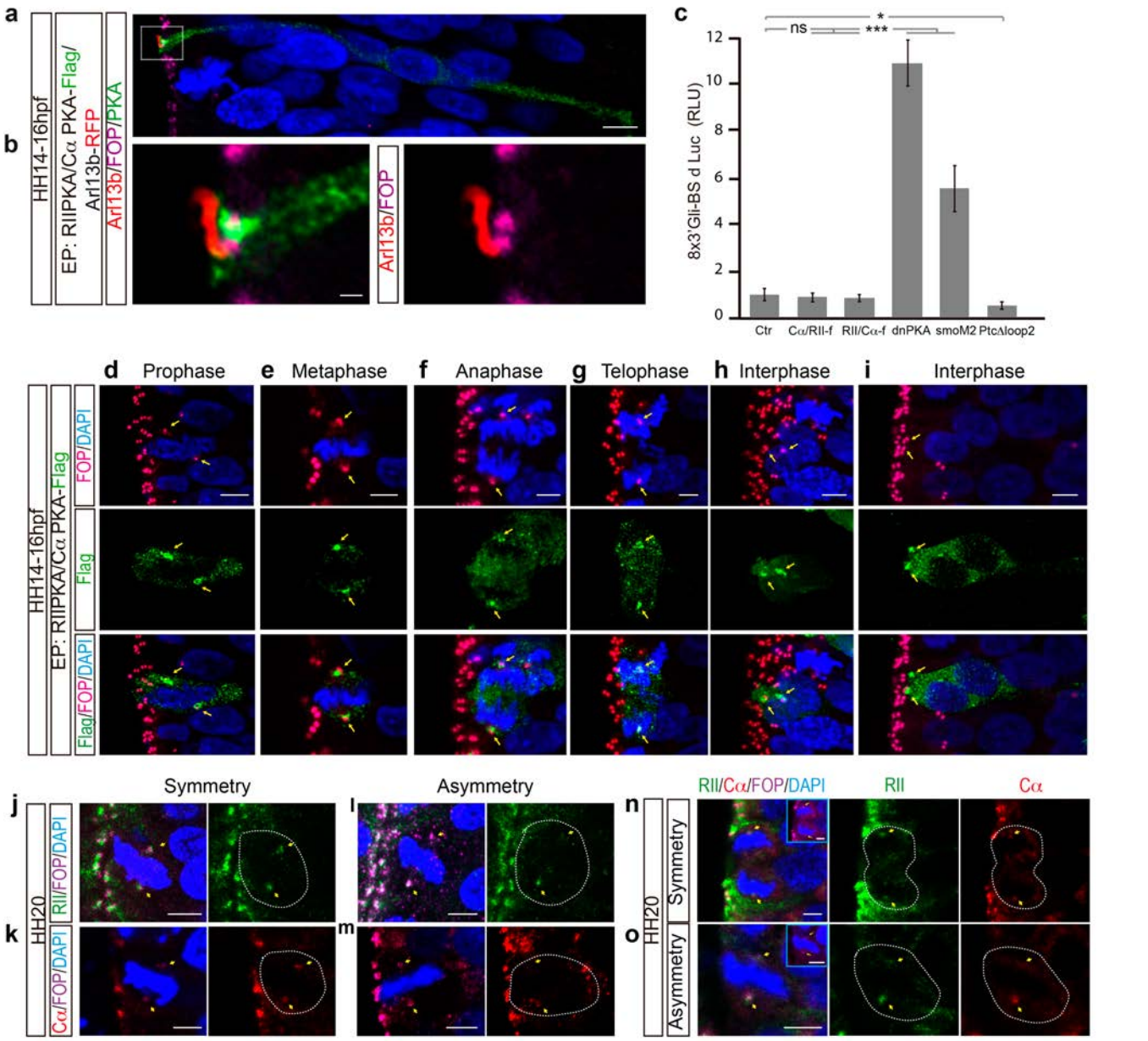

Supplementary Figure 2 PKA localizes to the centrosomes in dividing neural progenitors throughout mitosis. **(a,b)** Transient expression of Arl13b-RFP in the chick NT (HH14, 16 hpe) reliably labels the primary cilia: centrosomes labelled with anti-FOP (purple) line the NT lumen; Arl13b-RFP (red) labels the cilia at the NT lumen; anti-FLAG staining (green) labels PKA; DAPI (blue) labels the nuclei (scale bar 10μm in a; scale bar 0,5μm in b). **(c)** RII-PKA and Cα-PKA are always co-electroporated in order to inhibit the enzyme's kinase activity. Co-electroporation at low concentrations of RII-PKA + Cα-PKA was used to study the subcellular localization, and they do not activate Shh transcriptional responses, as assessed by the Gli-BS-Luc reporter activity. Both dnPKA and SmoM2 are assessed as activators of the pathway, and Ptc Δ Loop2 is studied as an inhibitor of the pathway. Quantification of the Luc/Renilla activity of the Gli-BS-Luc reporter 24 hpe of the DNAs indicated (plots show the mean ±s.e.m., n=8 embryos/condition; three independent experiments; one-way ANOVA; *$p<0.05$, ***$p<0.001$)(Scale bars 5μm). **(d-i)** PKA localizes to the centrosomes at different mitotic phases. RII-PKA + Cα-PKA-FLAG, revealed Cα-PKA by anti-FLAG staining (green) at centrosomes labelled with anti-FOP (red), from prophase to cytokinesis. DAPI (blue) labels the chromosomes. **(j,k)** Endogenous RII-PKA (green) and Cα-PKA (red) subunits symmetrically localize to centrosomes labelled with anti-FOP (purple), during mitosis. DAPI (blue) labels the chromosomes. **(l,m)** Endogenous RII-PKA (green) and Cα-PKA (red) subunits asymmetrically localize to centrosomes labelled with anti-FOP (purple), during mitosis. DAPI (blue) labels the chromosomes. **(n,o)** Endogenous RII-PKA (green) and Cα-PKA (red) subunits co-localize, either symmetrically (n) or asymmetrically (o) to centrosomes labelled with anti-FOP (purple), during mitosis. DAPI (blue) labels the chromosomes (Scale bars 5μm). Images are representative of three independent experiments.

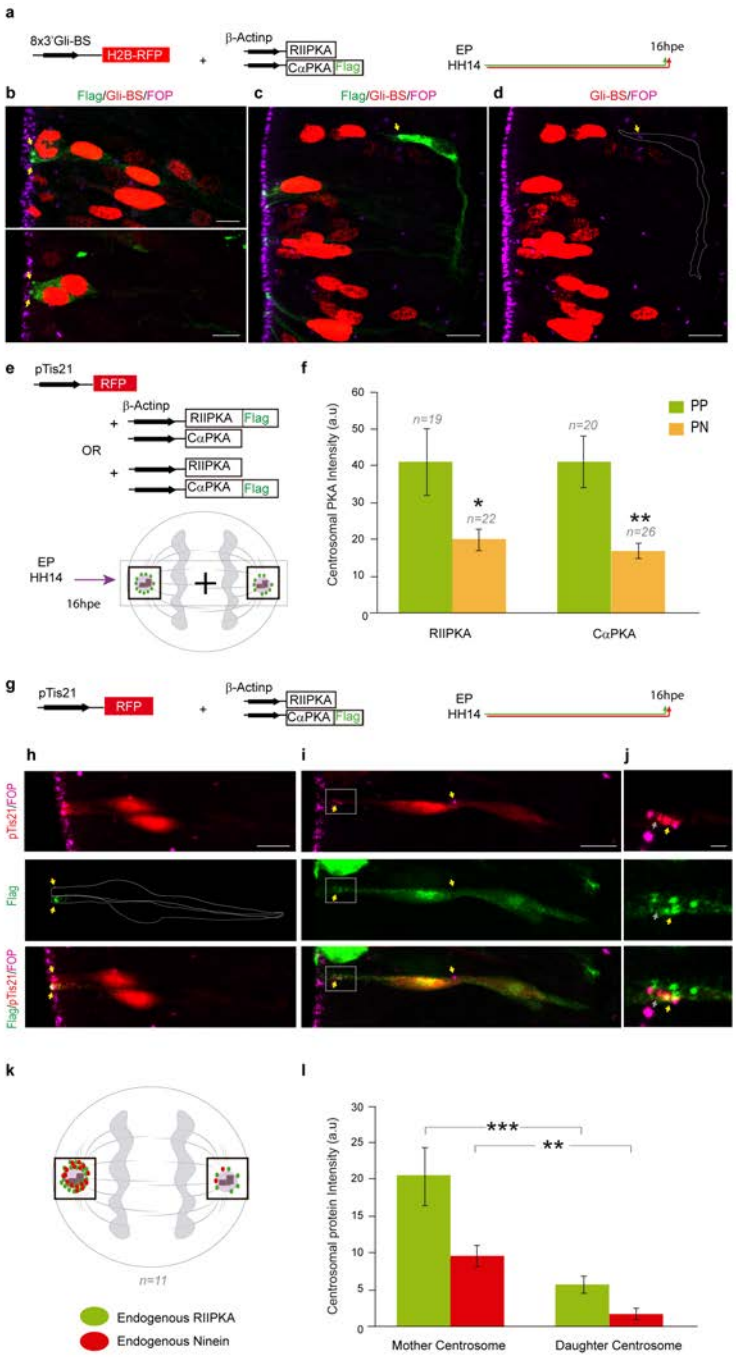

Supplementary Figure 3 PKA dissociates from centrosomes at the onset of neurogenesis **(a)** Scheme showing the DNAs electroporated and the timing of electroporation. **(b)** Selected images showing the symmetric centrosomal docking of PKA at the base of the cilium in Gli-BS-RFP^{+} (red) sister cells. Ca-PKA + RII-PKA-FLAG electroporation revealed Ca-PKA by anti-FLAG staining (green) and the centrosomes were labelled with anti-FOP (purple). **(c,d)** Selected images showing Gli-BS-RFP^{-} cells exiting the ventricular zone in which PKA is distributed in the cytosol but not predominantly associated to the FOP stained centrosome (yellow arrow). **(e)** Scheme showing the DNAs electroporated, the timing of electroporation, and the area (ROI) selected for fluorescence intensity measurement. **(f)** Quantification of centrosomal RII-PKA and Ca-PKA in Tis21-, plots show the mean± s.e.m, Mann-Whitney U test, *$p<0.05$, **$p<0.01$, of cumulative fluoresce intensity in both centrosomes (RII-PKA-FLAG mean=41±9, n=19 mitoses; Ca-PKA mean=41±7, n=20 mitoses) and Tis21+ (RII-PKA-FLAG mean=20±3, n=22 mitoses; Ca-PKA mean=17±2, n=26 mitoses; from three independent experiments) [**(g)** Scheme showing electroporated cDNAs, and the timing of electroporation. **(h)** Selected images showing asymmetric centrosomal docking of PKA in pTis21^{+} sister cells (red). Cα-PKA + RII-PKA-FLAG electroporation revealed Cα-PKA by anti-FLAG staining (green), showing the asymmetric docking of PKA at the centrosomes lining the NT lumen (yellow arrows), labelled with anti-FOP (purple) (Scale bar 0,5μm). **(i)** Selected images showing pTis21^{+} cells exiting the ventricular zone where PKA is distributed in the cytosol and not associated to the FOP (purple) stained centrosomes (yellow arrow). **(j)** High magnification of the apical area in I, showing the centrosomal duplication (two yellow arrows) in the daughter cell that remains as a progenitor, in which PKA remains docked to the apical centrosomes (Scale bars 10μm). **(k)** Scheme showing the area (ROI) selected for fluorescence intensity measurement. **(l)** Quantification of the endogenous centrosomal RII-PKA and endogenous ninein, plots show the mean± s.e.m, Mann-Whitney U test, **$p<0.01$, ***$p<0.001$ of cumulative fluoresce intensity in mother (high ninein) centrosomes (RII-PKA mean=20,6±3,5 ninein mean=9,2±1,6) and in dauther (low ninein) centrosomes (RII-PKA mean=5,8±1,3ninein mean=1,8±0,8 n=11 mitoses) Divisions were analysed from 6 independent embryos in one experiment. . Images are representative of three independent experiments.

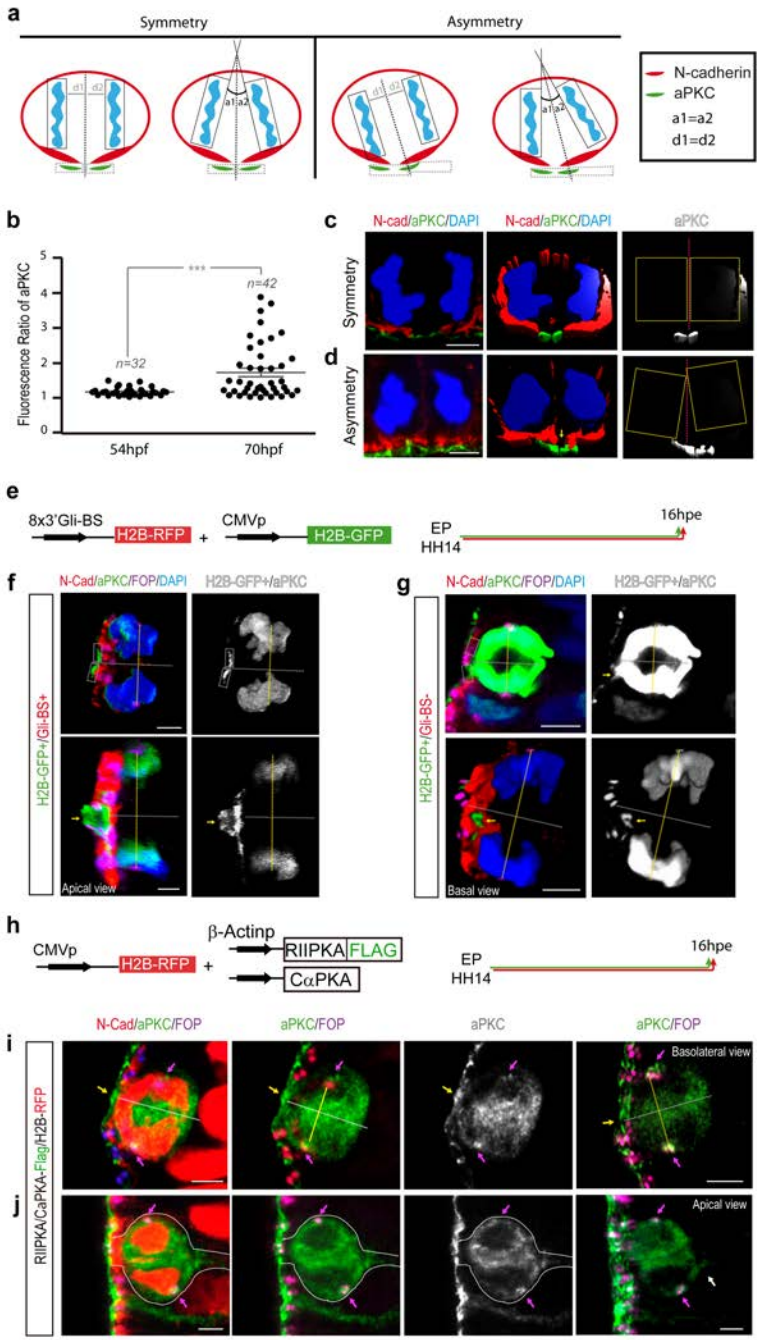

Supplementary Figure 4 Neurogenesis correlates with asymmetric inheritance of apical membrane domains. **(a)** Scheme showing the split of AJs by the cleavage plane at anaphase, the cleavage plane being deduced by a line bisecting the two sets of condensed chromatin (blue plates). When the rectangles were oriented parallel to each other, the cleavage plane was positioned half way in between the rectangles (d1=d2). When the rectangles were oriented at an angle to each other, the cleavage plane was positioned such that this angle was halved (a1=a2), predicting the type of division made by distributing the N-cadherin hole (red outline) between the two daughter cells, and by partitioning the apical aPKC domain (green). **(b)** Quantification of the Rfi between inherited αPKC apical domains in mitotic cells at two developmental stages, where the lines and error bars correspond to the median± s.e.m.; three independent experiments; Mann-Whitney U test; ****p<0.001.* The partitioning of αPKC was largely symmetric at 54hpf; n=32 mitosis), while it was asymmetric at the neurogenic phase 70hpf (n=42 mitosis).**(c)** Example of a symmetric mitosis in which the cleavage plane is deduced by drawing perpendicular lines (dashed line) bisecting the two sets of condensed chromatin (outlined). DAPI (blue) labels the chromosomes, N-cadherin is labelled in red, aPKC in green. **(d)** Example of an asymmetric mitosis(Scale bars 5mm).**(e)** Scheme showing the DNAs electroporated and the timing of electroporation. **(f)** Example of two cells in anaphase and telophase in which the cleavage plane is deduced by drawing perpendicular lines (dashed line) bisecting the two sets of condensed chromatin (outlined). Symmetric partitioning of αPKC is correlated with Gli-BS activation (RFP^+). GFP represents the control electroporation, FOP (purple) labels the centrosomes, DAPI (blue) labels the chromosomes (yellow arrow points to the N-cadherin hole). Black and white panel shows the isolation of aPKC domain for quantification. **(g)** Example of two cells in anaphase and telophase, in which asymmetric partitioning of αPKC is correlated with Gli-BS inactivation (RFP^-, yellow arrow points to the N-cadherin hole)(Scale bars 5μm). **(h)** Scheme showing the DNAs electroporated and the timing of electroporation. **(i)**Example of two cells in telophase, in which asymmetric partitioning of aPKC is correlated with asymmetric centrosomal docking of RII-PKA. FOP (magenta) labels the centrosomes (magenta arrows point to centrosomes). RFP (red) labels the chromosomes (yellow arrow points to the N-cadherin hole)(Scale bars 5μm). Images are representative of three independent experiments.

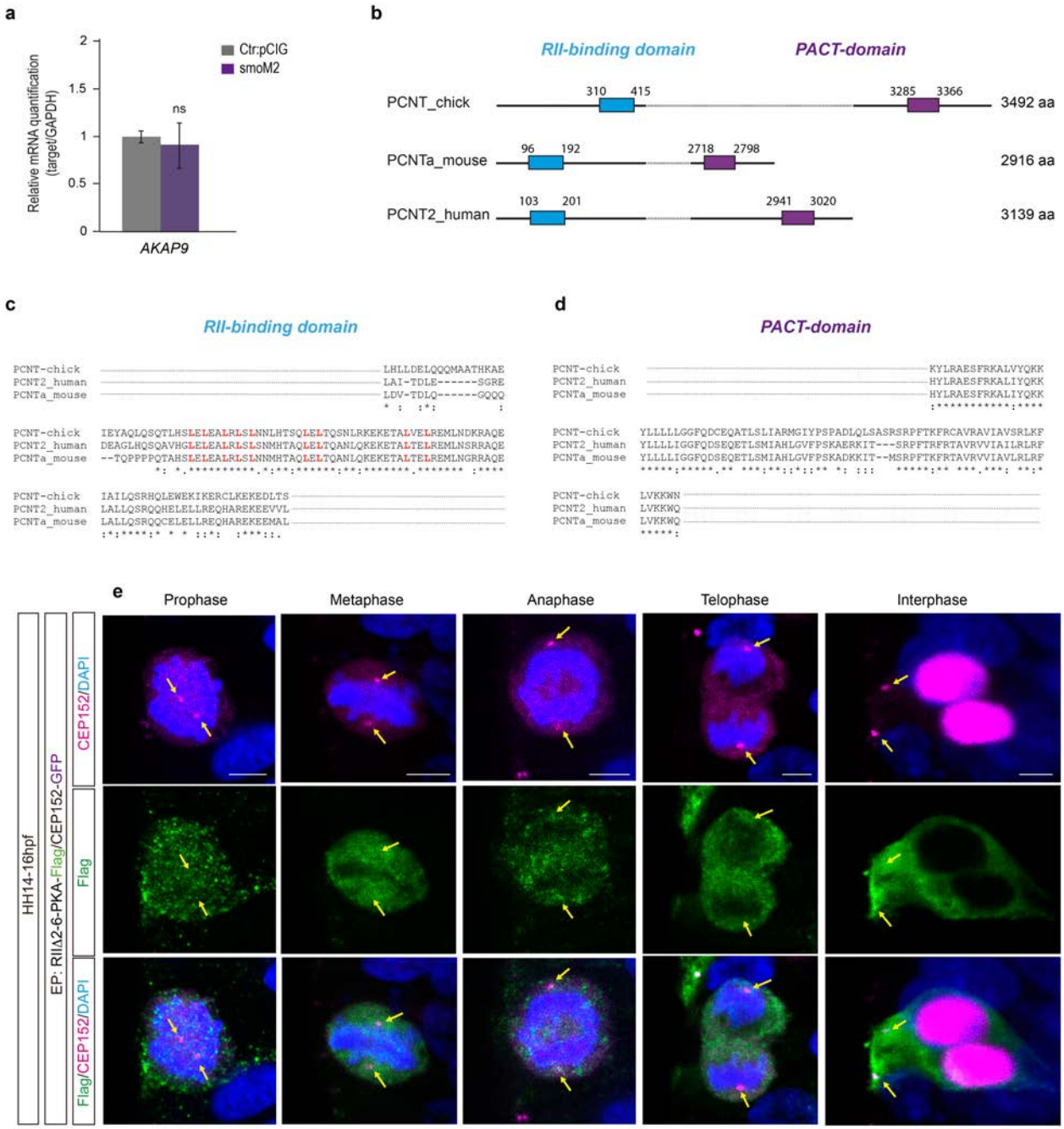

Supplementary Figure 5 Pericentrin mediates PKA docking to the centrosomes **(a)** Semi-quantitative PCR analysis of the *AKAP9* transcripts expressed in control vs SmoM2-EP cells (plot shows the mean±s.e.m, 25.000 cells from n=8 independent embryos, three independent experiments, Mann-Whitney U test; NS). **(b)** Scheme showing the conservation of the PCNT (pericentrin) sequence, highlighting the RII-PKA-binding domain (blue) and the PCNT-AKAP9 Centrosomal Targeting (PACT) domain (purple). **(c)** Multiple sequence alignment of the RII-PKA binding domain of PCNT using Multaling version 5.4.1: red highlights the conserved leucines (L) critical for RII-PKA binding. **(d)** Multiple sequence alignment highlighting the conserved PACT binding domain in PCNT. **(e)** Selected images of RIIΔ2-6-PKA electroporation at mitotic phases: CEP152 (red) labels centrosomes (yellow arrows); DAPI (blue) labels chromosomes. Mutant RII-PKA (green) does not associate with the centrosomes at any phase of mitosis (Scale bars 5µm Images are representative of three independent experiments.

Supplementary Table Legends

Supplementary Table 1 Shh/Gli signalling regulates the expression of centrosomal associated proteins. Table showing transcripts regulated by over-activation of Shh (36 hpe): fold change>2, *p-value **<0.01, ***<0.001*

Supplementary Table 2 Information on Antibodies used. Table contains Information on antibody dilutions/amounts used, company names, catalog numbers and clone numbers for monoclonals.

Supplementary Table 3 Shh/Glisignalling regulated gene expression. Analysis of the transcriptome data, based on the comparison between the average values of the logRed (control) and logGreen (Gli3AΔN1) intensities, results were filtered using unpaired t-tests using thresholds of >2-fold change and P-value **<0.01, ***<0.001.

Supplementary Movie Legends

Supplementary Movie 1 3D reconstruction of symmetric centrosomal docking of PKA in a Gli-BS-RFP$^+$ mitoses. Gli-BS-RFP$^+$ mitosis (red) show symmetric RII-PKA/Cα-PKA-FLAG, revealed Cα-PKA by anti-FLAG staining (green) in centrosomes labelled with anti-FOP (purple). DAPI (blue) labels the chromosomes and yellow arrows point to PKA

Supplementary Movie 2 3D reconstruction of asymmetric centrosomal docking of PKA in a pTis21-RFP$^+$ mitoses. pTis21-RFP$^+$ mitoses (red) show asymmetric RII-PKA/Cα-PKA-FLAG, revealed Cα-PKA by anti-FLAG staining (green) in centrosomes labelled with anti-FOP (purple). DAPI (blue) labels the chromosomes and yellow arrows point to PKA

APPENDIX IV

Review article

A centrosomal view of CNS growth

Murielle Saade, Jose Blanco-Ameijeiras, Elena Gonzalez-Gobartt and Elisa Martí

Development (2018)

Summary:

This review intends to discuss the impact that centrosome-mediated control of cell division has on the size and shape of the overall growing CNS, de-regulation of which can cause neurodevelopmental disorders such as primary microcephaly. We review the intrinsic properties of the centrosome and the emerging notion that centrosome asymmetries can instruct the outcome of NPC division. Moreover, based on recent findings (Le Dreau et al., 2014; Saade et al., 2013; Saade et al., 2017), we highlight that growth factors also contribute to the centrosome maturation and signalling, regulating in this way the mode of NPC division. Finally, we discuss the genetic links between centrosome dysfunction during development and the aetiology of microcephaly.

PhD student contribution: The PhD student made Table 1, discussed, and commented on the manuscript.

© 2018. Published by The Company of Biologists Ltd | Development (2018) 145, dev170613. doi:10.1242/dev.170613

REVIEW

A centrosomal view of CNS growth

Murielle Saade*, Jose Blanco-Ameijeiras, Elena Gonzalez-Gobartt and Elisa Martí

ABSTRACT

Embryonic development of the central nervous system (CNS) requires the proliferation of neural progenitor cells to be tightly regulated, allowing the formation of an organ with the right size and shape. This includes regulation of both the spatial distribution of mitosis and the mode of cell division. The centrosome, which is the main microtubule-organizing centre of animal cells, contributes to both of these processes. Here, we discuss the impact that centrosome-mediated control of cell division has on the shape of the overall growing CNS. We also review the intrinsic properties of the centrosome, both in terms of its molecular composition and its signalling capabilities, and discuss the fascinating notion that intrinsic centrosomal asymmetries in dividing neural progenitor cells are instructive for neurogenesis. Finally, we discuss the genetic links between centrosome dysfunction during development and the aetiology of microcephaly.

KEY WORDS: Organ growth, CNS, Interkinetic nuclear migration, Asymmetric cell division, Centrosome, Growth factors, Primary microcephaly

Introduction

During embryonic development in higher vertebrates, the brain and anterior spinal cord are formed through primary neurulation of the embryonic neural plate, which produces a hollow neural tube (NT) that acts as the primordium of the central nervous system (CNS) (Greene and Copp, 2014). Along its entire anterior-to-posterior axis, the lumen of the NT is covered by a single type of neuroepithelial cell, termed a primary neural progenitor cell (NPC), from which all neural cell types will be generated. NPCs are specified in discrete domains with distinct transcriptional states in response to the activity of secreted proteins (Addison and Wilkinson, 2016; Cohen et al., 2013; Gupta and Sen, 2016; Le Dréau and Martí, 2012; Sousa and Fishell, 2010; Ulloa and Marti, 2010).

During development, primary NPCs proliferate in a tightly controlled manner, exhibiting distinct growth rates along the axis of the NT. The different rates of growth in the anterior and posterior NT are reflected in the enlargement of the brain chambers, which give rise to the primary anatomical structures in the brain. The main divisions initially formed in the anterior part of the CNS are the forebrain (prosencephalon), midbrain (mesencephalon) and hindbrain (rhombencephalon); these are followed caudally by the spinal cord (Fig. 1A). The forebrain comprises two telencephalic vesicles, the dorsal half of which is specified as the primordium of the cerebral cortex (Fig. 1B). At early developmental stages, key features that are important for NPC expansion are conserved along the CNS, including within the cerebral cortex and the spinal cord (Fig. 1B-D). However, later in development, NPCs in the developing cerebral cortex are organized into two germinal layers – the ventricular zone (VZ) and the subventricular zone (SVZ) – and are subject to increasing layers of complexity. These features of cortical NPCs and neurogenesis have been the subject of excellent recent reviews (Florio et al., 2017; Heide et al., 2017; Johnson and Walsh, 2017; Wilsch-Bräuninger et al., 2016) and will not be discussed further here.

Here, we aim to highlight features of primary NPCs that regulate the early growth of the embryonic CNS, de-regulation of which can cause neurodevelopmental disorders such as primary microcephaly. In particular, we discuss mechanisms involving the centrosome – the main microtubule-organizing centre (MTOC) in animal cells. We highlight how the centrosome impacts the process of interkinetic nuclear migration, which not only serves to expose dividing NPCs to the signalling-rich NT lumen environment, but also affects the shaping of the overall growing CNS. We also discuss the intrinsic properties of the centrosome and the emerging notion that centrosome asymmetries can instruct the outcome of NPC division. Moreover, based on recent findings, we highlight how growth factors, known to play a role in the generation of cell diversity during CNS development, also contribute to centrosome maturation and signalling, and thus regulate the mode of NPC division. Finally, given that many of the causative mutations for primary microcephaly affect genes encoding centrosome-related proteins (Gilmore and Walsh, 2013; Jayaraman et al., 2018), we briefly discuss how studies of the centrosome represent an interesting research direction for improving our understanding of neurodevelopmental disorders such as microcephaly.

Centrosome-dependent interkinetic nuclear migration confines mitosis to the apical area

The NPCs that form the embryonic primordium of the CNS are organized as a pseudostratified epithelium in which elongated cells contact both the apical and basal laminae, with their nuclei adopting distinct positions along the apicobasal cell axis (Fig. 2A). During the G1 phase of the cell cycle, the nuclei of NPCs born at the apical surface of the neuroepithelium move toward the basal side. After completing S phase contacting the basal portion of the neuroepithelium, the nuclei return to the apical surface, where they undergo mitoses as their parent cells did. Collectively, these processes are referred to as interkinetic nuclear migration (INM, Fig. 2A) (Langman et al., 1966; Sauer, 1935).

In NPCs, the centrosome is anchored at the apical surface of the cell (Fig. 2B), serving as the base for the primary cilium (Dubreuil et al., 2007; Goetz and Anderson, 2010). Experimental observations indicate that the centrosome behaves as an anchor point for an apical-ward force that pulls the nucleus during G2 phase of the cell cycle. As such, the forces that drive apical nuclear migration within the VZ require the activity of centrosomal proteins, such as SAS-4 (CENPJ in mammals), Cep120, TACCs and Hook3 (Ge et al., 2010; Insolera et al., 2014; Xie et al., 2007). In parallel, and in line with the

Department of Developmental Biology, Instituto de Biología Molecular de Barcelona, Parc Científic de Barcelona, Baldiri i Reixac 20, Barcelona 08028, Spain.

*Author for correspondence (msabmc@ibmb.csic.es)

M.S., 0000-0002-3937-4291; E.M., 0000-0002-0411-0069

Development (2018) 145, dev170613. doi:10.1242/dev.170613

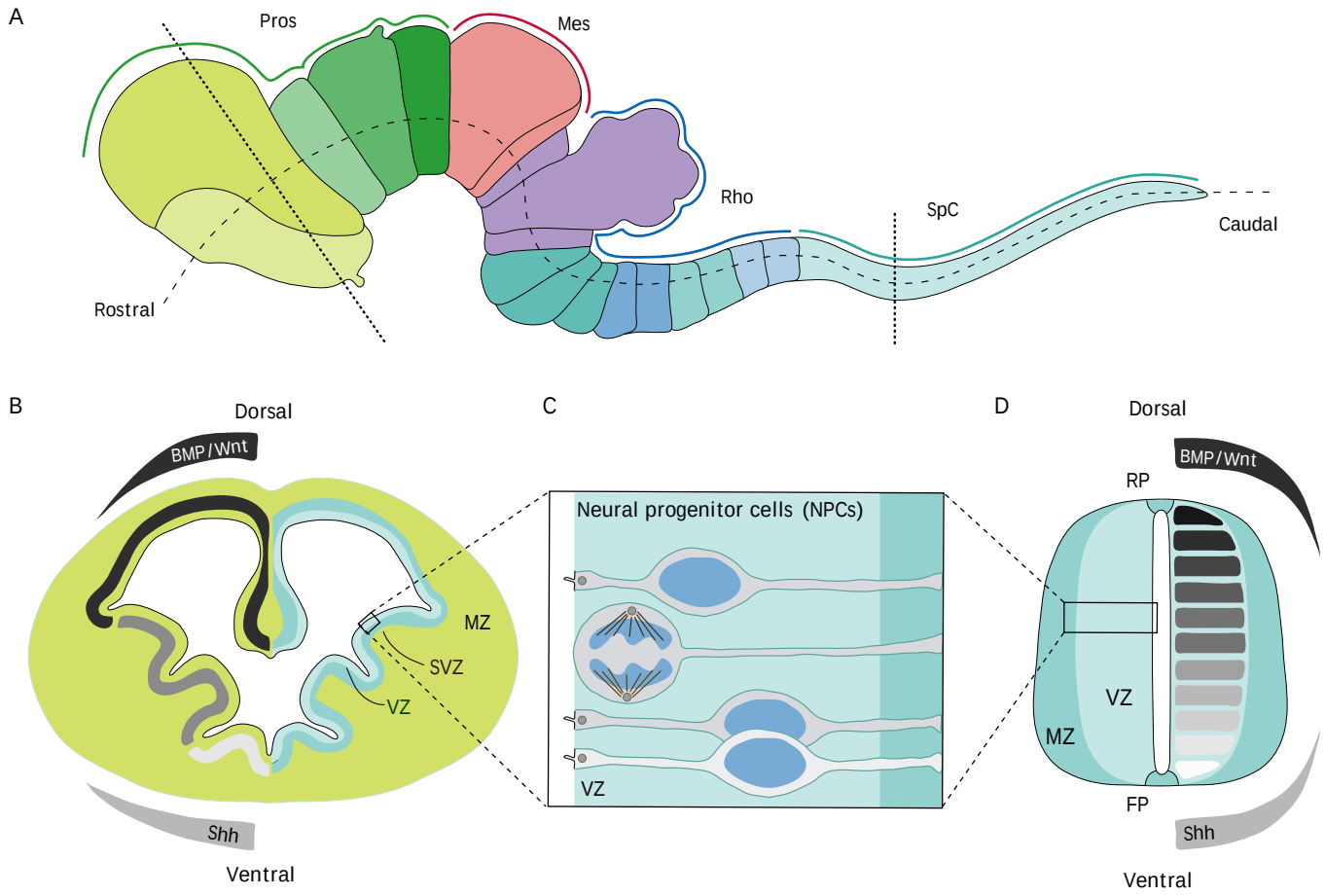

Fig. 1. The embryonic central nervous system. (A) Diagram of a vertebrate embryo (mouse ~E8-10) central nervous system, showing rostral to caudal regionalization into the forebrain (prosencephalon, Pros), midbrain (mesencephalon, Mes), hindbrain (rhombencephalon, Rho), and the caudal spinal cord (SpC). (B) Diagram of a transverse section through the telencephalon. The main telencephalic subdivisions along the dorsal ventral axis are generated in response to dorsal BMP/Wnt and ventral sonic hedgehog (Shh) patterning signals. The relative position of neural progenitor cells (in the ventricular zone, VZ), intermediate progenitors (in the subventricular zone, SVZ) and post-mitotic neurons (in the mantle zone, MZ) are indicated. (C) Detailed view of dividing NPCs that occupy the VZ lining the entire neural tube lumen. NPCs are present as elongated cells that contact both the apical and basal laminae, with their nuclei adopting distinct positions along the apicobasal axis. (D) Diagram showing a transverse section through the spinal cord. The progenitor populations generated along the dorsal-ventral axis, highlighted with a greyscale on the right, are established by the conserved activity of extrinsic secreted signals (dorsal BMP/Wnt and ventral Shh). The relative position of NPCs (in the ventricular zone, VZ) and post-mitotic neurons (in the mantle zone, MZ) is shown. FP, floor plate; RP, roof plate.

role of the centrosome as a MTOC and the observation that intact microtubules are required for INM (Kosodo et al., 2011; Lee and Norden, 2013; Reinsch and Gonczy, 1998), microtubules and their associated motor proteins also contribute to the molecular machinery of INM (Tsai et al., 2010). Indeed, mutations in genes encoding dynein-interacting proteins, such as lissencephaly-1 (Lis1; also known as Pafah1b1), dynactin 1 and laminin γ1 (Lamc1), give rise to perturbed apical-ward nucleokinesis and, consequently, mitoses throughout the neuroepithelium (Del Bene et al., 2008; Feng et al., 2000; Tanaka et al., 2004; Tsuda et al., 2010). Interestingly, in shorter NPCs, such as those in the zebrafish developing retina, there must be some centrosome-independent mechanism of INM, as it appears that once apical INM is triggered a 'point of no return' is passed so that apical mitoses take place independently of centrosome position (Strzyz et al., 2015). Whether this mechanism is conserved in other neuroepithelia is not known.

The connection between the microtubule network controlling INM and the nuclear envelope is mediated by KASH-domain proteins (Syne proteins; also known as nesprin proteins), which form a complex with SUN-domain proteins in the nuclear envelope (Fig. 2B). Following the hypothesis of the centrosome as an anchor point for apical-ward INM, this microtubule network-nuclear envelope connection must be kept intact to allow such a nuclear migration. Indeed, experiments in knockout mice have revealed that the SUN-domain proteins SUN1 and SUN2 and the KASH domain proteins Syne1 and Syne2 are required for the apical migration of nuclei along microtubules toward the apical centrosome (Ge et al., 2010; Schenk et al., 2009; Xie et al., 2007; Zhang et al., 2009) (Fig. 2B).

The rationale behind the striking arrangement and dynamics of NPCs has classically been explained as a mechanism to pack more NPCs into a limited space. As such, INM serves to vary the distances of nuclei from the apical and basal surfaces, thereby allowing more NPCs to remain associated with the limited apical/basal surfaces than would be possible in a columnar epithelium. However, according to the original description of INM, 'the mitoses are confined to the region of the lumen not only because nuclei of that region divide, but because a nucleus that is about to divide moves to the region of the lumen to do so' (Sauer, 1935), indicating that it might be beneficial to send the nucleus to the apical area prior to entering mitosis. One possible advantage of sending the nucleus to the apical area during the G2 phase of the cell cycle is that it makes the centrosome available for entry into division. Supporting

Development (2018) 145, dev170613. doi:10.1242/dev.170613

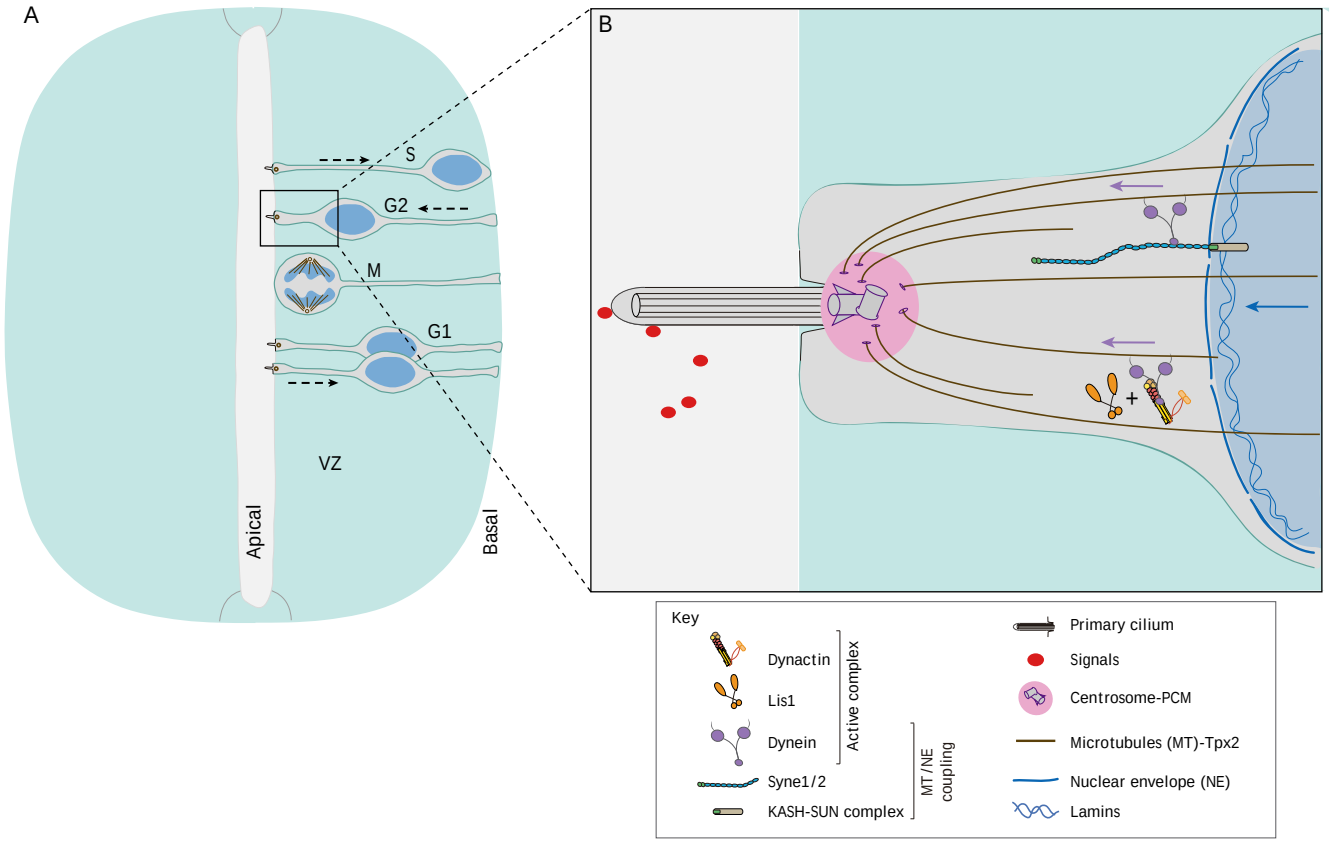

Fig. 2. Interkinetic nuclear migration in NPCs. (A) Diagram of a transverse section through the spinal cord. The nuclei of dividing NPCs occupy different apicobasal positions depending on the phase of the cell cycle (S, G2, M, G1). Dashed arrows indicate the direction of nuclear migration. (B) Diagram of the apical pole of an NPC in the G2 phase of the cell cycle. The primary cilium points to the NT lumen. The centrosome at the cilium base organizes microtubules to pull the nucleus apicalwards (blue arrow). A dynein complex linked to the nuclear envelope activates nuclear apical migration (purple arrows).

this idea, mitosis is in part triggered by a cascade of proteins localized to the centrosome, culminating in the activation of aurora kinase A and, subsequently, in the activation of the cyclin B/Cdk1 complex (Hirota et al., 2003; Jackman et al., 2003), which may function as a checkpoint for centrosome availability for division. The microtubule-dependent apical-ward transition of the nucleus in G2 phase might also facilitate the equal inheritance of apical attachments, thereby ensuring cohesion of the tissue despite a high proliferation rate. Additionally, increasing the exposure of NPCs to signalling pathways and molecules that function at the apical surface, such as Notch, which is known to be required for maintaining the progenitor character of NPCs (Hatakeyama et al., 2014; Ohata et al., 2011), might also be among the benefits of apical mitoses. Hence, besides affecting cell packing, INM could restrict the location of mitosis to particular regions of the NT lumen, thereby impacting the signals received by NPCs. These signals might be instructive for the outcome of cell division, as discussed below, and thus are important for CNS growth.

Intrinsic centrosomal asymmetries in dividing neural progenitor cells are instructive for neurogenesis

Embryonic CNS growth requires a finely tuned balance between the different modes of divisions that NPCs undergo: symmetric proliferative divisions ensure expansion of the progenitor pool by generating two daughter cells with identical progenitor potential, whereas asymmetric divisions generate one daughter cell with progenitor potential and one daughter cell with a more restricted potential, which is then committed to neuronal differentiation (Fig. 3). However, cell division in general is intrinsically asymmetric as a consequence of differences in the centrosomes that are passed on to the daughter cells (Fig. 3). Before entering mitosis, the centrosome replicates in a semi-conservative manner, forming one centrosome that retains the mother centriole and another that receives the daughter centriole. As we discuss below, this centrosome asymmetry, which relates to centrosome age, structure, molecular composition, MTOC capabilities, and the recruitment of signalling components, can influence the fate of NPC divisions and, hence, the expansion of the progenitor pool.

NPCs inherit one centrosome consisting of a pair of centrioles surrounded by amorphous pericentriolar material (PCM). The two centrioles differ in their structure and function. The older ‘mother’ centriole possesses distinct sets of projections at its distal ends called subdistal and distal appendages, which bear specific proteins such as CEP164, CEP170, cenexin (also known as Odf2) and ninein that are implicated in the anchoring of microtubules, cilia formation and docking of the basal body at the plasma membrane (Graser et al., 2007; Ishikawa et al., 2005; Ou et al., 2002; Schmidt et al., 2012; Welburn and Cheeseman, 2012). In contrast to the mother centriole, the younger ‘daughter’ centriole lacks these appendages. Full acquisition of appendages by the daughter centriole is not achieved until at least one and a half cell cycles later (Hoyer-Fender, 2010; Mahen and Venkitaraman, 2012). Importantly for CNS growth, this built-in centrosome asymmetry has an impact on the fate of the daughter cells. Both in the developing mouse cortex (Paridaen et al., 2013; Wang et al., 2009) and in the chick spinal cord (Saade et al., 2017; Tozer et al., 2017) the centrosome retaining

Development (2018) 145, dev170613. doi:10.1242/dev.170613

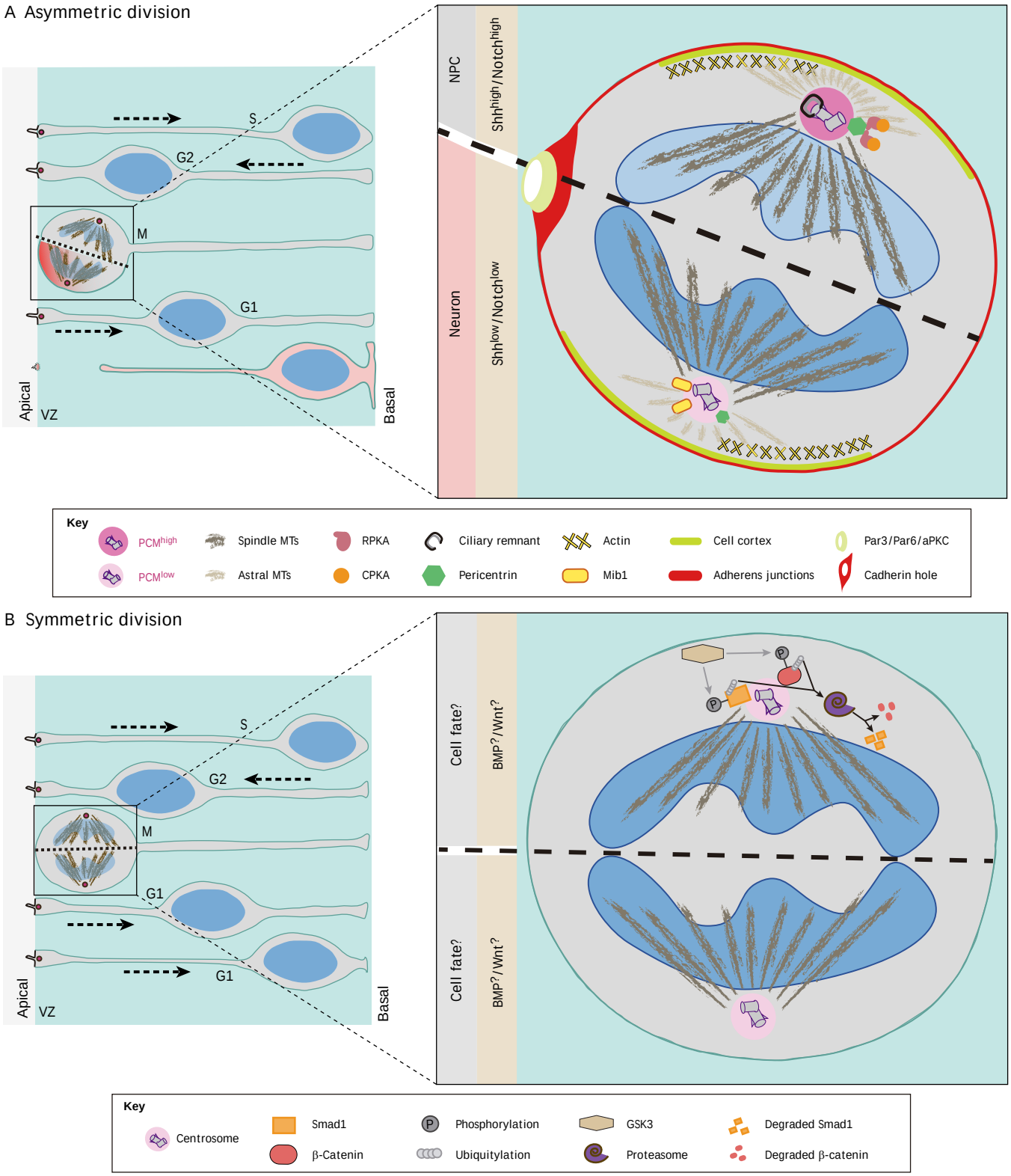

Fig. 3. NPC modes of cell division. (A,B) An asymmetrically dividing NPC generates one NPC and one differentiating neuron (pink, A), whereas a symmetrically dividing NPC generates two NPCs (B). (A) An asymmetrically dividing NPC shows asymmetric recruitment of PKA and Mib1 and asymmetric astral microtubule (MT) nucleation. Association of the astral MTs with the cell cortex defines the positioning of the mitotic spindle relative to the axis of polarity, favouring asymmetric inheritance of cell fate components. CPKA, protein kinase A catalytic subunit; RPKA, protein kinase A regulatory subunit; Mib1, Mind bomb-1. (B) A symmetrically dividing NPC shows centrosomal recruitment of Smad1 and β-catenin and the ubiquitin proteasome system. The final impact of this distribution of BMP and Wnt signalling components on the division mode of NPCs and the cell fate of daughter cells is still not well described. Grey arrows indicate phosphorylation; black arrows indicate proteasome-dependant degradation.

Development (2018) 145, dev170613. doi:10.1242/dev.170613

the old mother centriole is preferentially inherited by the NPC, whereas the centrosome containing the daughter (new mother) centriole is inherited by the delaminating and differentiating neuron, which leaves the VZ.

This centrosomal asymmetry has a number of downstream effects on NPC-derived cells. For instance, maturation of the daughter centriole is required for correct NPC function. The process of centrosome maturation is characterized by drastic expansion of the pericentriolar material and a robust increase in MTOC activity. During this event, proteins such as centrin and ninein are delivered to the centrosome along microtubules via a dynein/dynactin-dependent process (Dammermann and Merdes, 2002). Accordingly, the removal of mature centriole-specific proteins, including ninein (Wang et al., 2009), WDR62 and ASPM (Gai et al., 2016; Jayaraman et al., 2016), is sufficient to cause premature depletion of progenitor cells from the VZ and to impair CNS growth. Other proteins are recruited to the centrosome in a microtubule-independent manner by interacting with scaffold proteins, such as AKAP9 and pericentrin (Gillingham and Munro, 2000), which contain a localization domain (PACT domain) that targets the centrosome and serves to recruit structural and regulatory components such as γ-tubulin, microtubule binding proteins and signalling enzymes involved in microtubule nucleation (Almada et al., 2017). Supporting the relevance of centrosomal scaffold proteins in the control of the mode of NPC division, the removal of pericentrin triggers neurogenic divisions both in the chick spinal cord (Saade et al., 2017) and in the developing mouse cortex (Buchman et al., 2010). Surprisingly, pericentrin expression, together with other genes involved in centrosome maturation, appears to be regulated by the sonic hedgehog (Shh)/Gli signalling pathway (Saade et al., 2017), raising the interesting idea that classical growth factors might contribute to centrosome maturation in dividing NPCs.

Centrosome asymmetry is also reflected in notable differences in the recruitment of signalling components. One of these determinants is the Mind bomb1 (Mib1) protein, which is essential for generating functional Notch ligands (Koo et al., 2005). Mib1 is enriched at the daughter centrosome during mitosis (Fig. 3A) and gets inherited by the prospective neuron in asymmetric divisions (Tozer et al., 2017). This asymmetry is determined through the association of Mib1 with centriolar satellites (Tozer et al., 2017). Asymmetric localization of Mib1 at the daughter centrosome is accompanied by an unexpected asymmetric enrichment of the satellite markers PCM1 and AZI1 (CEP131) at the daughter centrosome (Tozer et al., 2017). Disruption of this interaction leads to symmetric Mib1 localization in mitosis, reciprocal Notch activation between sister cells, and a reduction in asymmetric NPC divisions and neurogenesis. Interestingly, centriolar satellite proteins have also been shown to assemble with microcephaly-associated proteins and promote centriole duplication (Kodani et al., 2015).

Centrosome asymmetry also impacts on the capacity to reassemble a primary cilium; the daughter cell that inherits the mother centriole reassembles a cilium and responds to external stimuli, such as Shh and other growth factors, prior to its sister cell (Anderson and Stearns, 2009). In dividing NPCs, a portion of the ciliary membrane that is preferentially attached to the mother centriole is endocytosed at the onset of mitosis, persists through mitosis at one spindle pole (Fig. 3A), and is asymmetrically inherited by one daughter cell; this cells retains progenitor character (Paridaen et al., 2013; Saade et al., 2017; Wang et al., 2009). Hence, it appears that the presence of this ciliary membrane remnant speeds up primary cilium assembly and facilitates the integration of signals, which in turn helps to maintain asymmetric NPC division.

Centrosomes, and hence centrosome asymmetry, also determine the organization and final orientation of the mitotic spindle relative to the cell cortex during cell division (Negishi et al., 2016; Rebollo et al., 2007). As discussed above, mother and daughter centrosomes differ notably in the expansion of their PCM and in their MTOC activity at mitosis entry. As such, the mother centrosome organizes a microtubule aster that is larger than that of the daughter centrosome (Fig. 3A) (Negishi et al., 2016; Rebollo et al., 2007; Yamashita et al., 2007). Astral microtubules connect to the cell cortex via the NuMA/LGN/Gai protein complex, which, by recruiting motor proteins of the dynein/dynactin complex, pulls on astral microtubules; this, in turn, drives mitotic spindle movements and orientation (Konno et al., 2008; Lesage et al., 2010; Morin et al., 2007; Saadaoui et al., 2017). In dividing NPCs, mitotic spindle orientation is associated with the partitioning of apical membrane subdomains. At the luminal surface, membrane subdomains organize to form the apical junction complex where, among other proteins, Par3/6 and atypical protein kinase C (aPKC) localize (Kosodo et al., 2004; Marthiens and ffrench-Constant, 2009). By contrast, the junctional proteins N-cadherin (Cdh2), α-catenin and β-catenin are found in the sub-apical domain (Fig. 3A) (Kosodo et al., 2004; Marthiens and ffrench-Constant, 2009; Saade et al., 2017). During interphase, the apical junction complex drives the positioning of NPCs within the epithelium. However, when NPCs divide, the components of the apical junction complex redistribute depending on the orientation of the mitotic spindle and the fate of the daughter cells. As such, a symmetric distribution of apical membrane subdomains is associated with proliferative divisions in which both daughter cells remain within the VZ as NPCs. Minor changes in spindle orientation determine whether the cleavage plane bisects or bypasses the small apical domain of dividing NPCs (Fig. 3A) and hence determine the outcome of the division (Saade et al., 2017). Importantly, it has been shown that progenitors retaining the old mother centriole reorganize a new apical polarity complex and remain within the VZ (Das and Storey, 2014). By contrast, NPCs that inherit the daughter centrosome also inherit the old apical polarity complex, which becomes disorganized upon differentiation (Das and Storey, 2014; Kasioulis et al., 2017). Together, these findings suggest that asymmetric spindle orientation is associated with a reduction in symmetric divisions, premature cell cycle exit and premature neurogenesis, potentially leading to a microcephaly phenotype (Bultje et al., 2009; Lancaster and Knoblich, 2012; Shitamukai et al., 2011; Shitamukai and Matsuzaki, 2012; Wilcock et al., 2007).

Hence, all of the findings discussed above reinforce the idea that, from a centrosomal perspective, the default outcome of any cell division should be asymmetric. Overcoming these various centrosomal, and associated, asymmetries would be required to promote symmetric proliferative divisions and embryonic CNS growth, and failure to do so might lead to neurodevelopmental defects such as microcephaly. This is an important point to note, especially as much of the effort in this field has focused on the search for signals that instruct the switch to asymmetric division, which instead appears to be the default state for NPC division (and possibly for other dividing cells).

New roles for classic growth factors in centrosome maturation during embryonic CNS growth

In the growing CNS, the morphogenetic activity of secreted proteins that generate cell diversity (e.g. members of the Shh, Wnt and BMP families) is combined with their capacity to coordinate cell cycle progression by directly regulating discrete sets of genes that are key

Development (2018) 145, dev170613. doi:10.1242/dev.170613

components of the cell cycle machinery (Alvarez-Medina et al., 2009; Cayuso et al., 2006; Molina and Pituello, 2017; Ulloa and Briscoe, 2007). In addition to such activities that ensure the maintenance of progenitor cell proliferation, these factors appear to modulate the mode of cell division adopted by NPCs and neurons.

Shh signalling, for example, has been shown to regulate the mode of motor neuron progenitor cell division within the developing spinal cord (Saade et al., 2013). By combining experimental data with mathematical modelling, it has been shown that the cell division mode switches sharply, from proliferative divisions to neurogenic divisions, with the sudden loss of Shh activity (Saade et al., 2013). In addition, maintaining Shh signalling artificially high is sufficient to prevent this developmental switch and to maintain symmetric proliferative divisions. This observation raised the question as to whether this Shh activity might impact on centrosome biology during NPC division. As introduced above, Shh/Gli activity in NPCs is sufficient to activate the expression of a cluster of centrosomal proteins, including centriolar and pericentriolar material and centrosome-associated proteins, that might contribute to centrosomal maturation and hence overcome intrinsic centrosome asymmetries (Saade et al., 2017). Among them, pericentrin, the expression of which is activated by Shh/Gli signalling, serves to dock an equal amount of protein kinase A (PKA) to both the mother and daughter centrosomes. PKA also exerts a downstream effect on processing of the Gli transcription factors so, at early developmental stages when Shh/Gli activity is high and proliferative divisions are predominant, the centrosomal localization of PKA becomes symmetric, leading to equal Shh activity in both daughter cells. As development proceeds, however, Shh/Gli activity decreases, pericentrin expression becomes low, and PKA remains associated with only the mother centrosome, leading to asymmetric Shh activity and neurogenic divisions (Fig. 3A). Disrupting the interaction of pericentrin with the centrosome leads to PKA mislocalization in mitosis and an increase in asymmetric neurogenic divisions (Saade et al., 2017). The expression of a number of additional centrosome proteins appears to be regulated by the Shh/Gli signalling pathway. These include CEP110 (CNTRL), which colocalizes with ninein and is involved in maturation of the daughter centrosome (Ou et al., 2002); ASPM, which concentrates at NPC mitotic spindle poles and is downregulated at the switch from symmetric proliferative to asymmetric neurogenic divisions (Fish et al., 2006); and PCM1, which is a component of centriolar satellites involved in the redistribution of molecular determinants (Tozer et al., 2017). Hence, centrosome maturation and the consequent regulation of the mode of NPC division should be added to the already long list of multiple roles played by Shh/Gli signalling during CNS development (Martí and Bovolenta, 2002).

The BMP/Smad and Wnt/β-catenin signalling pathways also play major roles in regulating growth of the developing vertebrate nervous system (Le Dréau and Martí, 2012). Indeed, the mode of cell division adopted by interneurons in the developing spinal cord is dictated by different levels of activity of the canonical BMP effectors Smad1/5 (Le Dréau et al., 2014). Thus, analogous mechanisms regulating cell division, similar to those controlled by Shh, might be foreseen, particularly as signalling components of both pathways localize to centrosomes. Phosphorylated Smad1 (pSmad1), the effector of canonical BMP signalling, appears to be localized to centrosomes during cell division, although this pool of Smad1 protein (which is subjected to sequential phosphorylation by MAPK and glycogen synthase kinase 3) is targeted for degradation (Fuentealba et al., 2007). Moreover, pSmad proteins specifically targeted for proteasomal degradation are asymmetrically inherited preferentially by one daughter cell during cell division (Fig. 3B) (Fuentealba et al., 2008). Indeed, the proteasomal degradation of pSmad1 in the centrosome regulates the duration of the BMP signalling pathway, which in turn is known to maintain stem cell identity (Fuentealba et al., 2007; Le Dréau et al., 2014). This suggests that degradation mechanisms might be associated with the mother centrosome during asymmetric divisions (Fig. 3B).

Dividing NPCs in the mouse embryonic midbrain also show centrosomal localization of phosphorylated β-catenin – the effector of the canonical Wnt signalling pathway (Chilov et al., 2011) (Fig. 3B). Whether β-catenin is asymmetrically recruited to mitotic centrosomes in these cells, however, has not yet been addressed. Phosphorylated β-catenin also shows centrosomal localization in human embryonic stem cells (Fuentealba et al., 2008) and, *in vitro*, a localized Wnt signal can induce oriented cell divisions that generate distinct cell fates in embryonic stem cells (Habib et al., 2013). Moreover, in *Caenorhabditis elegans*, SYS-1/β-catenin localizes to mitotic centrosomes in mother cells and is subjected to dynamic proteasome degradation (Vora and Phillips, 2015). In this context, the centrosomal localization negatively regulates SYS-1/β-catenin levels and Wnt-dependent cell fate in daughter cells after division.

Hence, beyond age and structure, mother and daughter centrosomes appear to have different abilities to serve as hubs for the integration, duration and coordination of signalling pathways that are important for CNS growth.

Centrosome dysfunction and microcephaly

The consequences of centrosome dysfunction during development and how they contribute to human diseases are highlighted by the study of autosomal recessive primary microcephaly (MCPH). MCPH is a genetically heterogeneous neurodevelopmental disorder characterized by a small CNS at birth and non-progressive intellectual disability. Many of the causative genes for the 20 loci mapped to date (MCPH1-MCPH20) in various populations around the globe encode centriole/centrosome or kinetochore/spindle pole proteins that are involved in centriole biogenesis, centrosome maturation, cytokinesis, centromere and kinetochore function (Table 1). This indicates that centrosome dysfunction is one of the main causes of MCPH (Jayaraman et al., 2018; Nano and Basto, 2017). Moreover, additional microcephaly phenotypes are associated with centrosome proteins, including CEP63, PCNT, NIN, POC1A (Table 1), establishing a strong genetic link between centrosome dysfunction during development and the aetiology of microcephaly. What remains to be resolved, however, is why brain size in particular is so vulnerable to centrosome mutations; centrosome dysfunction found in MCPH mostly leads to architecturally normal but smaller brains, in most cases without affecting body size. It thus appears that, compared with other organs, size regulation in the CNS might rely more on the tightly controlled mode of cell divisions that occur during developmental stages.

Conclusions

As we have reviewed here, recent research in animal models has started to reveal the multiple roles played by centrosomes during embryonic CNS growth and neurogenesis. Centrosomes are confined to the apical pole of NPCs where they serve as a basal body for the primary cilium. As such, they regulate the exposure of cells to the growth factor signalling-rich microenvironment of the NT lumen. The subsequent integration of growth factor signals during the G1 phase of the cell cycle results in the regulated

Development (2018) 145, dev170613. doi:10.1242/dev.170613

Table 1. The MCPH1-20 loci, their gene products and protein functions

Locus	Gene product	Alternative names and symbols	Protein function and localization	OMIM
MCPH1	MCPH1	Microcephalin; BRCT-repeat inhibitor of TERT expression 1; BRIT1	Regulates chromosome condensation	607117
MCPH2	WDR62	WD repeat-containing protein 62	Localizes to the centrosome and to the nucleus	613583
MCPH3	CEP215	Centrosomal protein, 215-kD; CDK5 regulatory subunit-associated protein; CDK5RAP2	Localizes to the centrosome and to the spindle poles during mitosis	608201
MCPH4	CASC5	Kinetochore scaffold 1; KNL1	Localizes to the kinetochore	609173
MCPH5	ASPM	Abnormal spindle-like, microcephaly-associated	Essential for mitotic spindle assembly/function	605481
MCPH6	CENPJ	Centromeric protein J; centrosomal P4.1-associated protein; CPAP	Localizes to the centrosome, regulates microtubule assembly and nucleation	609279
MCPH7	STIL	SCL/TAL1-interrupting locus	Localizes to PCM, regulates centriole duplication	181590
MCPH8	CEP135	Centrosomal protein, 135-kD	Forms the core centriole structure, regulates early centriole assembly	611423
MCPH9	CEP152	Centrosomal protein, 152-kD	Core protein of the centrosome	613529
MCPH10	ZNF335	Zinc finger protein 335; NRC-interacting factor; NIF1	Component of the trithorax H3K4-methylation chromatin remodelling complex	610827
MCPH11	PHC1	Polyhomeotic-like 1	Component of the polycomb repressive complex-1 (PRC1)	602978
MCPH12	CDK6	Cyclin-dependent kinase 6	Localizes to the centrosome, plays a role in cell cycle progression	603368
MCPH13	CENPE	Centromeric protein E	Kinetochore-associated kinesin-like motor protein	117143
MCPH14	SASS6	SAS-6 centriolar assembly protein	Functions in procentriole formation	609321
MCPH15	MFSD2A	Major facilitator superfamily domain-containing protein 2A	Sodium-dependent lysophosphatidylcholine transporter	614397
MCPH16	ANKLE2	Ankyrin repeat- and LEM domain-containing protein 2; LEM domain-containing protein 4; LEM4	Regulates reassembly of the nuclear envelope at anaphase	616062
MCPH17	CIT	Citron RHO-interacting serine/threonine kinase; serine/threonine protein kinase 21; STK21	Essential for cytokinesis	605629
MCPH18	WDFY3	WD repeat- and FYVE domain-containing protein 3	Organizes misfolded ubiquitylated proteins into bodies to be degraded by autophagy	617485
MCPH19	COPB2	Coatomer protein complex, subunit β2	Subunit of the Golgi coatomer complex, necessary for retrograde intracellular trafficking	606990
MCPH20	KIF14	Kinesin family member 14	Microtubule-associated motor, plays an important role in cell division	611279
SCKL6	CEP63	Centrosomal protein, 63-kD	Centrosomal protein	614724
SCKL7	NIN	Ninein; GSK3B-interacting protein	Centrosomal protein, re-forms interphase centrosomal architecture after mitosis	608684
MOPD2	PCNT	Pericentrin; kendrin; KEN	Localizes to the centrosome	605925
SOFT	POC1A	POC1 centriolar protein, chlamydomonas, homolog of, A	Localizes to centrioles, functions in centriole duplication and/or maintenance	614783

OMIM, Online Mendelian Inheritance in Man

Loci beneath the line relate to other centrosome proteins with associated microcephaly phenotypes.

expression of multiple targets including genes involved in centrosome maturation. Hence, by controlling symmetric centrosomal protein assembly, growth factors can overcome the intrinsic asymmetry of the centrosome during NPC division, thereby promoting self-expanding symmetric divisions and CNS growth. Importantly, the failure to overcome such intrinsic cell division asymmetries, and thus the failure to ensure appropriate cell divisions during early CNS growth, may be responsible for neurodevelopmental disorders such as primary microcephaly.

Moving forward, we propose that we should turn our attention to the search for instructive signals that can overcome these intrinsic asymmetries in NPC divisions. As we have highlighted here, classical growth factors might be key players. For example, a role for Shh has recently been revealed and requires further investigation. It will also be important to understand how molecular components of the Wnt and BMP signalling pathways are integrated into the mitotic centrosome and whether they affect NPC modes of division. It is likely that additional regulatory mechanisms that remain to be discovered are also involved, and their characterization might expand our knowledge of how, from a centrosomal perspective, classical growth factors contribute to defining the division mode of NPCs. Do such components participate directly in the intrinsic functions of the centrosome? Does the centrosome serve as a hub for the integration, duration and distribution of these signals in NPCs after division? These key open questions need to be answered in order to fully understand CNS growth from a centrosomal point of view.

Acknowledgements

We apologize to colleagues whose work is not included owing to space constraints. We thank the E.M. laboratory members for useful discussions.

Competing interests

The authors declare no competing or financial interests.

Funding

The work in E.M.'s laboratory is supported by grants from Ministerio de Economía, Industria y Competitividad, Gobierno de España (BFU2016-77498-P and BFU2016-81887-REDT). E.G.-G. holds a Predoctoral Scholarship BES-2014-068589, J.B.-A. holds a Predoctoral Scholarship BES-2017-080050 from Ministerio de Economía, Industria y Competitividad, Gobierno de España.

References

Addison, M. and Wilkinson, D. G. (2016). Segment identity and cell segregation in the vertebrate hindbrain. *Curr. Top. Dev. Biol.* **117**, 581-596.

Almada, E., Tonucci, F. M., Hidalgo, F., Ferretti, A., Ibarra, S., Pariani, A., Vena, R., Favre, C., Girardini, J., Kierbel, A. et al. (2017). Akap350 recruits Eb1 to the spindle poles, ensuring proper spindle orientation and lumen formation in 3D epithelial cell cultures. *Sci. Rep.* **7**, 14894.

Alvarez-Medina, R., Le Dreau, G., Ros, M. and Marti, E. (2009). Hedgehog activation is required upstream of Wnt signalling to control neural progenitor proliferation. *Development* **136**, 3301-3309.

Anderson, C. T. and Stearns, T. (2009). Centriole age underlies asynchronous primary cilium growth in mammalian cells. *Curr. Biol.* **19**, 1498-1502.

Buchman, J. J., Tseng, H.-C., Zhou, Y., Frank, C. L., Xie, Z. and Tsai, L.-H. (2010). Cdk5rap2 interacts with pericentrin to maintain the neural progenitor pool in the developing neocortex. *Neuron* **66**, 386-402.

Bultje, R. S., Castaneda-Castellanos, D. R., Jan, L. Y., Jan, Y.-N., Kriegstein, A. R. and Shi, S.-H. (2009). Mammalian Par3 regulates progenitor cell asymmetric division via notch signaling in the developing neocortex. *Neuron* **63**, 189-202.

Cayuso, J., Ulloa, F., Cox, B., Briscoe, J. and Marti, E. (2006). The Sonic hedgehog pathway independently controls the patterning, proliferation and survival of neuroepithelial cells by regulating Gli activity. *Development* **133**, 517-528.

Chilov, D., Sinjushina, N., Rita, H., Taketo, M. M., Mäkelä, T. P. and Partanen, J. (2011). Phosphorylated beta-catenin localizes to centrosomes of neuronal progenitors and is required for cell polarity and neurogenesis in developing midbrain. *Dev. Biol.* **357**, 259-268.

Cohen, M., Briscoe, J. and Blassberg, R. (2013). Morphogen interpretation: the transcriptional logic of neural tube patterning. *Curr. Opin. Genet. Dev.* **23**, 423-428.

Dammermann, A. and Merdes, A. (2002). Assembly of centrosomal proteins and microtubule organization depends on PCM-1. *J. Cell Biol.* **159**, 255-266.

Das, R. M. and Storey, K. G. (2014). Apical abscission alters cell polarity and dismantles the primary cilium during neurogenesis. *Science* **343**, 200-204.

Del Bene, F., Wehman, A. M., Link, B. A. and Baier, H. (2008). Regulation of neurogenesis by interkinetic nuclear migration through an apical-basal notch gradient. *Cell* **134**, 1055-1065.

Dubreuil, V., Marzesco, A.-M., Corbeil, D., Huttner, W. B. and Wilsch-Bräuninger, M. (2007). Midbody and primary cilium of neural progenitors release extracellular membrane particles enriched in the stem cell marker prominin-1. *J. Cell Biol.* **176**, 483-495.

Feng, Y., Olson, E. C., Stukenberg, P. T., Flanagan, L. A., Kirschner, M. W. and Walsh, C. A. (2000). LIS1 regulates CNS lamination by interacting with mNudE, a central component of the centrosome. *Neuron* **28**, 665-679.

Fish, J. L., Kosodo, Y., Enard, W., Paabo, S. and Huttner, W. B. (2006). Aspm specifically maintains symmetric proliferative divisions of neuroepithelial cells. *Proc. Natl. Acad. Sci. USA* **103**, 10438-10443.

Florio, M., Borrell, V. and Huttner, W. B. (2017). Human-specific genomic signatures of neocortical expansion. *Curr. Opin. Neurobiol.* **42**, 33-44.

Fuentealba, L. C., Eivers, E., Ikeda, A., Hurtado, C., Kuroda, H., Pera, E. M. and De Robertis, E. M. (2007). Integrating patterning signals: Wnt/GSK3 regulates the duration of the BMP/Smad1 signal. *Cell* **131**, 980-993.

Fuentealba, L. C., Eivers, E., Geissert, D., Taelman, V. and De Robertis, E. M. (2008). Asymmetric mitosis: unequal segregation of proteins destined for degradation. *Proc. Natl. Acad. Sci. USA* **105**, 7732-7737.

Gai, M., Bianchi, F. T., Vagnoni, C., Vernì, F., Bonaccorsi, S., Pasquero, S., Berto, G. E., Sgrò, F., Chiotto, A. M. A., Annaratone, L. et al. (2016). ASPM and CITK regulate spindle orientation by affecting the dynamics of astral microtubules. *EMBO Rep.* **17**, 1396-1409.

Ge, X., Frank, C. L., Calderon de Anda, F. and Tsai, L.-H. (2010). Hook3 interacts with PCM1 to regulate pericentriolar material assembly and the timing of neurogenesis. *Neuron* **65**, 191-203.

Gillingham, A. K. and Munro, S. (2000). The PACT domain, a conserved centrosomal targeting motif in the coiled-coil proteins AKAP450 and pericentrin. *EMBO Rep.* **1**, 524-529.

Gilmore, E. C. and Walsh, C. A. (2013). Genetic causes of microcephaly and lessons for neuronal development. *Wiley Interdiscip. Rev. Dev. Biol.* **2**, 461-478.

Goetz, S. C. and Anderson, K. V. (2010). The primary cilium: a signalling centre during vertebrate development. *Nat. Rev. Genet.* **11**, 331-344.

Graser, S., Stierhof, Y.-D., Lavoie, S. B., Gassner, O. S., Lamla, S., Le Clech, M. and Nigg, E. A. (2007). Cep164, a novel centriole appendage protein required for primary cilium formation. *J. Cell Biol.* **179**, 321-330.

Greene, N. D. E. and Copp, A. J. (2014). Neural tube defects. *Annu. Rev. Neurosci.* **37**, 221-242.

Gupta, S. and Sen, J. (2016). Roof plate mediated morphogenesis of the forebrain: new players join the game. *Dev. Biol.* **413**, 145-152.

Habib, S. J., Chen, B.-C., Tsai, F.-C., Anastassiadis, K., Meyer, T., Betzig, E. and Nusse, R. (2013). A localized Wnt signal orients asymmetric stem cell division in vitro. *Science* **339**, 1445-1448.

Hatakeyama, J., Wakamatsu, Y., Nagafuchi, A., Kageyama, R., Shigemoto, R. and Shimamura, K. (2014). Cadherin-based adhesions in the apical endfoot are required for active Notch signaling to control neurogenesis in vertebrates. *Development* **141**, 1671-1682.

Heide, M., Long, K. R. and Huttner, W. B. (2017). Novel gene function and regulation in neocortex expansion. *Curr. Opin. Cell Biol.* **49**, 22-30.

Hirota, T., Kunitoku, N., Sasayama, T., Marumoto, T., Zhang, D., Nitta, M., Hatakeyama, K. and Saya, H. (2003). Aurora-A and an interacting activator, the LIM protein Ajuba, are required for mitotic commitment in human cells. *Cell* **114**, 585-598.

Hoyer-Fender, S. (2010). Centriole maturation and transformation to basal body. *Semin. Cell Dev. Biol.* **21**, 142-147.

Insolera, R., Bazzi, H., Shao, W., Anderson, K. V. and Shi, S. H. (2014). Cortical neurogenesis in the absence of centrioles. *Nat. Neurosci.* **17**, 1528-1535.

Ishikawa, H., Kubo, A., Tsukita, S. and Tsukita, S. (2005). Odf2-deficient mother centrioles lack distal/subdistal appendages and the ability to generate primary cilia. *Nat. Cell Biol.* **7**, 517-524.

Jackman, M., Lindon, C., Nigg, E. A. and Pines, J. (2003). Active cyclin B1-Cdk1 first appears on centrosomes in prophase. *Nat. Cell Biol.* **5**, 143-148.

Jayaraman, D., Kodani, A., Gonzalez, D. M., Mancias, J. D., Mochida, G. H., Vagnoni, C., Johnson, J., Krogan, N., Harper, J. W., Reiter, J. F. et al. (2016). Microcephaly proteins Wdr62 and Aspm define a mother centriole complex regulating centriole biogenesis, apical complex, and cell fate. *Neuron* **92**, 813-828.

Jayaraman, D., Bae, B.-I. and Walsh, C. A. (2018). The genetics of primary microcephaly. *Annu. Rev. Genomics Hum. Genet.* **19**, 177-200.

Johnson, M. B. and Walsh, C. A. (2017). Cerebral cortical neuron diversity and development at single-cell resolution. *Curr. Opin. Neurobiol.* **42**, 9-16.

Kasioulis, I., Das, R. M. and Storey, K. G. (2017). Inter-dependent apical microtubule and actin dynamics orchestrate centrosome retention and neuronal delamination. *eLife* **6**, e26215.

Kodani, A., Yu, T. W., Johnson, J. R., Jayaraman, D., Johnson, T. L., Al-Gazali, L., Sztriha, L., Partlow, J. N., Kim, H., Krup, A. L. et al. (2015). Centriolar satellites assemble centrosomal microcephaly proteins to recruit CDK2 and promote centriole duplication. *eLife* **4**.

Konno, D., Shioi, G., Shitamukai, A., Mori, A., Kiyonari, H., Miyata, T. and Matsuzaki, F. (2008). Neuroepithelial progenitors undergo LGN-dependent planar divisions to maintain self-renewability during mammalian neurogenesis. *Nat. Cell Biol.* **10**, 93-101.

Koo, B.-K., Lim, H. S., Song, R., Yoon, M. J., Yoon, K. J., Moon, J. S., Kim, Y. W., Kwon, M. C., Yoo, K. W., Kong, M. P. et al. (2005). Mind bomb 1 is essential for generating functional Notch ligands to activate Notch. *Development* **132**, 3459-3470.

Kosodo, Y., Röper, K., Haubensak, W., Marzesco, A.-M., Corbeil, D. and Huttner, W. B. (2004). Asymmetric distribution of the apical plasma membrane during neurogenic divisions of mammalian neuroepithelial cells. *EMBO J.* **23**, 2314-2324.

Kosodo, Y., Suetsugu, T., Suda, M., Mimori-Kiyosue, Y., Toida, K., Baba, S. A., Kimura, A. and Matsuzaki, F. (2011). Regulation of interkinetic nuclear migration by cell cycle-coupled active and passive mechanisms in the developing brain. *EMBO J.* **30**, 1690-1704.

Lancaster, M. A. and Knoblich, J. A. (2012). Spindle orientation in mammalian cerebral cortical development. *Curr. Opin. Neurobiol.* **22**, 737-746.

Langman, J., Guerrant, R. L. and Freeman, B. G. (1966). Behavior of neuro-epithelial cells during closure of the neural tube. *J. Comp. Neurol.* **127**, 399-411.

Le Dréau, G. and Martí, E. (2012). Dorsal-ventral patterning of the neural tube: a tale of three signals. *Dev. Neurobiol.* **72**, 1471-1481.

Le Dréau, G., Saade, M., Gutiérrez-Vallejo, I. and Martí, E. (2014). The strength of SMAD1/5 activity determines the mode of stem cell division in the developing spinal cord. *J. Cell Biol.* **204**, 591-605.

Lee, H. O. and Norden, C. (2013). Mechanisms controlling arrangements and movements of nuclei in pseudostratified epithelia. *Trends Cell Biol.* **23**, 141-150.

Lesage, B., Gutierrez, I., Martí, E. and Gonzalez, C. (2010). Neural stem cells: the need for a proper orientation. *Curr. Opin. Genet. Dev.* **20**, 438-442.

Mahen, R. and Venkitaraman, A. R. (2012). Pattern formation in centrosome assembly. *Curr. Opin. Cell Biol.* **24**, 14-23.

Marthiens, V. and ffrench-Constant, C. (2009). Adherens junction domains are split by asymmetric division of embryonic neural stem cells. *EMBO Rep.* **10**, 515-520.

Martí, E. and Bovolenta, P. (2002). Sonic hedgehog in CNS development: one signal, multiple outputs. *Trends Neurosci.* **25**, 89-96.

Molina, A. and Pituello, F. (2017). Playing with the cell cycle to build the spinal cord. *Dev. Biol.* **432**, 14-23.

Morin, X., Jaouen, F. and Durbec, P. (2007). Control of planar divisions by the G-protein regulator LGN maintains progenitors in the chick neuroepithelium. *Nat. Neurosci.* **10**, 1440-1448.

Nano, M. and Basto, R. (2017). Consequences of centrosome dysfunction during brain development. *Adv. Exp. Med. Biol.* **1002**, 19-45.

Negishi, T., Miyazaki, N., Murata, K., Yasuo, H. and Ueno, N. (2016). Physical association between a novel plasma-membrane structure and centrosome orients cell division. *eLife* **5**, e16550.

Ohata, S., Aoki, R., Kinoshita, S., Yamaguchi, M., Tsuruoka-Kinoshita, S., Tanaka, H., Wada, H., Watabe, S., Tsuboi, T., Masai, I. et al. (2011). Dual roles

of Notch in regulation of apically restricted mitosis and apicobasal polarity of neuroepithelial cells. *Neuron* **69**, 215-230.
Ou, Y. Y., Mack, G. J., Zhang, M. and Rattner, J. B. (2002). CEP110 and ninein are located in a specific domain of the centrosome associated with centrosome maturation. *J. Cell Sci.* **115**, 1825-1835.
Paridaen, J. T. M. L., Wilsch-Bräuninger, M. and Huttner, W. B. (2013). Asymmetric inheritance of centrosome-associated primary cilium membrane directs ciliogenesis after cell division. *Cell* **155**, 333-344.
Rebollo, E., Sampaio, P., Januschke, J., Llamazares, S., Varmark, H. and González, C. (2007). Functionally unequal centrosomes drive spindle orientation in asymmetrically dividing Drosophila neural stem cells. *Dev. Cell* **12**, 467-474.
Reinsch, S. and Gonczy, P. (1998). Mechanisms of nuclear positioning. *J. Cell Sci.* **111**, 2283-2295.
Saadaoui, M., Konno, D., Loulier, K., Goiame, R., Jadhav, V., Mapelli, M., Matsuzaki, F. and Morin, X. (2017). Loss of the canonical spindle orientation function in the Pins/LGN homolog AGS3. *EMBO Rep.* **18**, 1509-1520.
Saade, M., Gutiérrez-Vallejo, I., Le Dréau, G., Rabadán, M. A., Miguez, D. G., Buceta, J. and Martí, E. (2013). Sonic hedgehog signaling switches the mode of division in the developing nervous system. *Cell Rep.* **4**, 492-503.
Saade, M., Gonzalez-Gobartt, E., Escalona, R., Usieto, S. and Martí, E. (2017). Shh-mediated centrosomal recruitment of PKA promotes symmetric proliferative neuroepithelial cell division. *Nat. Cell Biol.* **19**, 493-503.
Sauer, F. C. (1935). Mitosis in the neural tube. *J. Comp. Neurol.* **62**, 377-405.
Schenk, J., Wilsch-Brauninger, M., Calegari, F. and Huttner, W. B. (2009). Myosin II is required for interkinetic nuclear migration of neural progenitors. *Proc. Natl. Acad. Sci. USA* **106**, 16487-16492.
Schmidt, K. N., Kuhns, S., Neuner, A., Hub, B., Zentgraf, H. and Pereira, G. (2012). Cep164 mediates vesicular docking to the mother centriole during early steps of ciliogenesis. *J. Cell Biol.* **199**, 1083-1101.
Shitamukai, A. and Matsuzaki, F. (2012). Control of asymmetric cell division of mammalian neural progenitors. *Dev. Growth Differ.* **54**, 277-286.
Shitamukai, A., Konno, D. and Matsuzaki, F. (2011). Oblique radial glial divisions in the developing mouse neocortex induce self-renewing progenitors outside the germinal zone that resemble primate outer subventricular zone progenitors. *J. Neurosci.* **31**, 3683-3695.
Sousa, V. H. and Fishell, G. (2010). Sonic hedgehog functions through dynamic changes in temporal competence in the developing forebrain. *Curr. Opin. Genet. Dev.* **20**, 391-399.
Strzyz, P. J., Lee, H. O., Sidhaye, J., Weber, I. P., Leung, L. C. and Norden, C. (2015). Interkinetic nuclear migration is centrosome independent and ensures apical cell division to maintain tissue integrity. *Dev. Cell* **32**, 203-219.
Tanaka, T., Serneo, F. F., Higgins, C., Gambello, M. J., Wynshaw-Boris, A. and Gleeson, J. G. (2004). Lis1 and doublecortin function with dynein to mediate coupling of the nucleus to the centrosome in neuronal migration. *J. Cell Biol.* **165**, 709-721.
Tozer, S., Baek, C., Fischer, E., Goiame, R. and Morin, X. (2017). Differential routing of mindbomb1 via centriolar satellites regulates asymmetric divisions of neural progenitors. *Neuron* **93**, 542-551.e544.
Tsai, J.-W., Lian, W.-N., Kemal, S., Kriegstein, A. R. and Vallee, R. B. (2010). Kinesin 3 and cytoplasmic dynein mediate interkinetic nuclear migration in neural stem cells. *Nat. Neurosci.* **13**, 1463-1471.
Tsuda, S., Kitagawa, T., Takashima, S., Asakawa, S., Shimizu, N., Mitani, H., Shima, A., Tsutsumi, M., Hori, H., Naruse, K. et al. (2010). FAK-mediated extracellular signals are essential for interkinetic nuclear migration and planar divisions in the neuroepithelium. *J. Cell Sci.* **123**, 484-496.
Ulloa, F. and Briscoe, J. (2007). Morphogens and the control of cell proliferation and patterning in the spinal cord. *Cell Cycle* **6**, 2640-2649.
Ulloa, F. and Marti, E. (2010). Wnt won the war: antagonistic role of Wnt over Shh controls dorso-ventral patterning of the vertebrate neural tube. *Dev. Dyn.* **239**, 69-76.
Vora, S. and Phillips, B. T. (2015). Centrosome-associated degradation limits beta-catenin inheritance by daughter cells after asymmetric division. *Curr. Biol.* **25**, 1005-1016.
Wang, X., Tsai, J.-W., Imai, J. H., Lian, W.-N., Vallee, R. B. and Shi, S.-H. (2009). Asymmetric centrosome inheritance maintains neural progenitors in the neocortex. *Nature* **461**, 947-955.
Welburn, J. P. I. and Cheeseman, I. M. (2012). The microtubule-binding protein Cep170 promotes the targeting of the kinesin-13 depolymerase Kif2b to the mitotic spindle. *Mol. Biol. Cell* **23**, 4786-4795.
Wilcock, A. C., Swedlow, J. R. and Storey, K. G. (2007). Mitotic spindle orientation distinguishes stem cell and terminal modes of neuron production in the early spinal cord. *Development* **134**, 1943-1954.
Wilsch-Bräuninger, M., Florio, M. and Huttner, W. B. (2016). Neocortex expansion in development and evolution - from cell biology to single genes. *Curr. Opin. Neurobiol.* **39**, 122-132.
Xie, Z., Moy, L. Y., Sanada, K., Zhou, Y., Buchman, J. J. and Tsai, L.-H. (2007). Cep120 and TACCs control interkinetic nuclear migration and the neural progenitor pool. *Neuron* **56**, 79-93.
Yamashita, Y. M., Mahowald, A. P., Perlin, J. R. and Fuller, M. T. (2007). Asymmetric inheritance of mother versus daughter centrosome in stem cell division. *Science* **315**, 518-521.
Zhang, X., Lei, K., Yuan, X., Wu, X., Zhuang, Y., Xu, T., Xu, R. and Han, M. (2009). SUN1/2 and Syne/Nesprin-1/2 complexes connect centrosome to the nucleus during neurogenesis and neuronal migration in mice. *Neuron* **64**, 173-187.